Mechanisms of Shallow Rainfall-induced Landslides in Residuali Soils in Humid Tropical Environments

Kit Ying Ng,

Mechanisms of Shallow Rainfall-induced Landslides in Residual Soils in Humid Tropical Environments

Kit Ying Ng

PhD thesis

This thesis is submitted in accordance with the regulations for the degree of Doctor of Philosophy in Durham University, Department of Geography, 2007

Declaration

I confirm that no part of the material offered has previously been submitted by me for a degree in this or in any other University. In all cases, where it is relevant, material from the work of others has been acknowledged.

Signed: K.Y.Ng

Date: 18/7/2007

Abstract

Landslide mechanisms and processes, particularly within the basal deformation region during failure, are poorly understood in the current knowledge. The aim of this research is to understand the initiation processes of shallow rainfall-triggered landslides under humid, tropical conditions. The major objectives are (1) to investigate the actual processes of rainfall-triggered landslides; and (2) to examine the relationship between the rates of pore water pressure increase and the rates of soil movement.

Field sampling has been undertaken at two landslide sites on weathered volcanic slopes on Lantau Island, Hong Kong (22°N, 114°E). Reinflation tests have been conducted on the undisturbed soil samples using a triaxial stress path cell to replicate the field conditions during rainstorm events. Various rates of increasing pore water pressure have been designed with reference to the field monitoring data. Landslide initiation processes have been deduced by examining the relationship between the increasing pore water pressures and soil deformation.

The results demonstrate that rainfall-induced landslide development on weathered slopes undergoes three stages with distinctive movement patterns towards failure. The key controlling mechanism appears to be plastic deformation. The varied velocities are dependent on the stress state (changes in the mean effective stress, under constant shear stress), the pore water pressure reinflation rate and soil permeability. Stage 1 represents a perfectly plastic state below yield. Velocity remains low or at zero as the soil particles are strongly interlocked. The fluctuating to constant strain rates at Stage 2 are primarily controlled by the reinflation rate and permeability after exceeding the yield state, with localised interparticle sliding. Rapid acceleration to failure occurs at Stage 3, facilitated by the general remoulding process.

The systematic movement patterns have also been observed in shallow rainfall-induced landslides in plastic soil materials. The steady-state behaviour could be a precursor for the acceleration to the final failure.

Acknowledgements

I would like to express my deepest gratitude for the Croucher Foundation, a charitable organization based in Hong Kong, that has granted me a 3-year scholarship with generous support for my tuition fees, living expenses, conference attendance, thesis preparation and return air fare. An exceptional 3-month extension of the scholarship has also been kindly approved to support my living costs during the writing-up period. Their comprehensive and continuous support enables me to pursue my interest in landslide research and fulfils my dream of studying for a PhD overseas. Thanks are extended to the prestigious Overseas Research Student Award Scheme (ORSAS) funded by the Universities UK that lowers my tuition fees to the home rate for three years. I am also grateful to Mr William C.L. Hui, donor of the Hui Yin Hing Fellowship 2003/04, who supports my PhD studies. The International Landslide Centre at Durham University has provided financial support for my fieldwork in Hong Kong.

I am very grateful to my main supervisor Professor David Petley for his professional guidance, intellectual stimulations and encouragement throughout my studies. Dave is always enthusiastic and positive about my work and has been my constant source of research support. At personal level, I am particularly impressed by his kind hospitality and caring approach in my first year that helps me adapt quickly to UK life. I would also like to thank my former second supervisors, Dr Toru Higuchi for his assistance with soil sampling in Hong Kong and advice on the laboratory work; and Professor Robert Allison for the insightful discussions on the geomorphological aspects in this research.

A lot of help has been kindly provided by the Department of Geography at the University of Hong Kong (HKU) which enables me, a former student, to complete the fieldwork successfully. Professor C.Y. Jim has offered me helpful advice on permit application and geological sampling within country parks. The sampling permission on Lantau Island granted by the Agriculture, Fisheries and Conservation Department of the Hong Kong SAR Government is gratefully acknowledged. Dr Mervyn Peart allowed me to borrow field sampling equipment from the department and kindly provided space for the sample preparation and storage in the laboratory. Miss Jeannette Liu gave me practical advice on field sampling and technical help with testing density for Hong Kong soils.

I would also like to thank Professor Andrew Malone from the Department of Earth Sciences at HKU for his insightful and encouraging discussions on landslide

mechanisms. Dr Mark Ruse, a consultant geomorphologist, has shared information and his working experience on natural landslides in Hong Kong.

The Geotechnical Engineering Office (GEO) of the Hong Kong SAR Government has provided the latest information on natural landslides specifically for this research. I am especially grateful to Dr Samuel K.C. Ng for his suggestions on the relevant official publications and permission to use the monitoring data of pore pressures and rainfall at the Tung Chung site (Geotechnical Observations Ltd., 2002; Evan and Lam, 2003). This allows the calculation of the rate of increasing pore water pressure as a field reference for the design in this study. Further discussions with Dr Samuel Ng and Dr Steve Parry on the project have been stimulating. Mr Philip W.K. Chung has shared his expertise on triaxial testing and practical skills in soil preparation. Mr W.L. Shum and the staff in the Planning Division have provided landslide location maps from the updated Natural Terrain Landslide Inventory (1999-2002), geological data and aerial photos of the study area.

The laboratory programme would not be made possible without the expertise of several people. I would like to give special thanks to Dr David Toll from the Department of Engineering at Durham University, who has very kindly provided his user-friendly TRIAX windows software for running the triaxial stress path system that greatly increases the frequency of data logging. I am also benefited from his lectures on soil mechanics and tropical soils engineering which provide fundamental background knowledge for my research. Mr Ian Bushell, manager of the Services Department at ELE International, offered technical advice for the triaxial cell. Assistance has been provided by a team of friendly laboratory technicians in the Geography Department at Durham. I am very grateful to Derek Coates who always gives me good advice and extends my help resource to his friends for specific support: Bernie McEleavey from the applied mechanics laboratory in the Department of Engineering who gave advice on calibration; and Barry Barker from the electronic workshop in the Department of Chemistry who kindly fixed the transducers and provided the electrical interference check in the Environmental Laboratory. Eddie Million provided constant attention on the maintenance of the air compressor. The friendliness and humour of Derek and Eddie, Alison Clark, Amanda Hayton, Frank Davies, Neil Tunstall, Mervyn Brown, Martin West and Dave Hodgson have formed my joyful memories working in the laboratory.

My friends within the department, at college, and in Hong Kong have helped me through various stages of my studies. Ann Le-mare always motivates me with her excellent research progress. Dr Jian-Yong Xiang, Fengling Yu, Irene Oi Ning Lai and

Lu Dong gave me tutorials on physics. Sérgio Lourenço shared his experience in landslide research using the triaxial cell. Pauline Hau Ming Tse and my sister Kit Wing Ng kindly provided me very efficient inter-library loan service from Hong Kong. Jimmy Lam is always very helpful and professional in solving computer problems and enhances performance of my laptop. Sarah Carter, Janice Ching Yu Tse, Linda Whelan, Joanna Yee Man Lai and Shu Tan shared my ups and downs with enormous support and care.

This thesis is dedicated to my loving parents who always give me full support to follow my interest in my studies.

Table of Contents

List of Tables

List of Figures

List of Notations

The following symbols (BSI, 1990a; Head, 1998) have been used in the thesis, with the term and the International System (SI) of Units defined where appropriate. An asterisk indicates no unit or dimensionless.

Symbol	Description	Unit
DIS	Drained initial shear	*
ICD	Isotropic consolidated drained triaxial test	*
ICU	Isotropic consolidated undrained triaxial test	*
FSP	Field stress path	*
TC	Tung Chung	*
PO	Pui O	*
PPR	Pore pressure reinflation test	*
Λ	Inversed velocity	s/μs
B	Skempton's pore pressure coefficient $\frac{\delta u}{\delta \sigma_3}$	*
F	Factor of Safety	*
C_u	Coefficient of uniformity	*
c'	Effective cohesion	kPa
c_{vi}	Coefficient of consolidation	m^2/year
c (subscript)	Consolidation	*
D_{10}, D_{30}, D_{60}	Particle diameter at which 10, 30, 60% is finer	μm
dis (subscript)	Drained initial shear	*
e	Void ratio	*
G_s	Specific gravity	*
I_P, PI	Plasticity index	%
k	Coefficient of permeability	m/s
m_{vi}	Coefficient of volume compressibility	m^2/MN
p'	Mean normal effective stress $(\sigma_1 + \sigma_2 + \sigma_3)/3$	kPa
p'_c	Mean normal effective stress, after consolidation	kPa
p'_{dis}	Mean normal effective stress, after drained initial shear (i.e. the start of the reinflation test)	kPa
q	Deviatoric stress $(\sigma_1 - \sigma_3)$	kPa
sat (subscript)	Saturation	*

t	Time (in seconds)	sec
u	Pore water pressure	kPa
w	Moisture content	%
w_L, LL	Liquid limit	%
w_P, PL	Plastic limit	%
ε, Ω	Strain	μs
ε_a	Axial strain	%
ε_v	Volumetric strain	%
$\dot{\varepsilon}, \dot{\Omega}$	Strain rate; velocity	μs/s
$\ddot{\Omega}$	Acceleration	$\mu s/s^2$
ρ	Bulk density	Mg/m^3
ρ_d	Dry density	Mg/m^3
σ	Total normal stress	kPa
σ'	Effective normal stress	kPa
σ_1'	Effective major principal stress; effective axial stress	kPa
σ_3'	Effective minor principal stress; effective confining pressure	kPa
τ	Shear resistance; shear stress	kPa
τ_{max}	Maximum shear stress	kPa
ϕ'	Effective frictional angle	degrees

List of Appendices

Chapter 1 Introduction

1.1 Landslides in a global context and in tropical regions

Landslides are a major geomorphological process affecting many countries over the world. They involve mass movement of materials downslope under the force of gravity (Cruden and Varnes, 1996). Landslides are a significant natural hazard that cause substantial economic loss and extensive loss of life in both developing and developed countries (Rosenfeld, 1994). The annual landslide-associated economic losses cost US$ 2.6 billion in Italy (Schuster, 1996), US$ 1.6-3.2 billion in the United States, more than 1 billion in Japan and US$ 62 million in Venezuela (Petley *et al.*, 2005a). In many developing countries, notably in Southeast Asia, the annual losses from landslides are estimated to amount to 1 or 2 % of the gross national products, according to the UN Disaster Relief Co-ordinator (Hutchinson, 1995). In terms of fatalities, landslides claim globally more than 5,000 lives per year (Petley *et al.*, 2005a). Most of the fatalities (excluding the events causing more than 1000 deaths) have been found in tropical regions including East and Southeast Asia, South America and South Asia (Petley and Bulmer, 2004) (Figure 1.1).

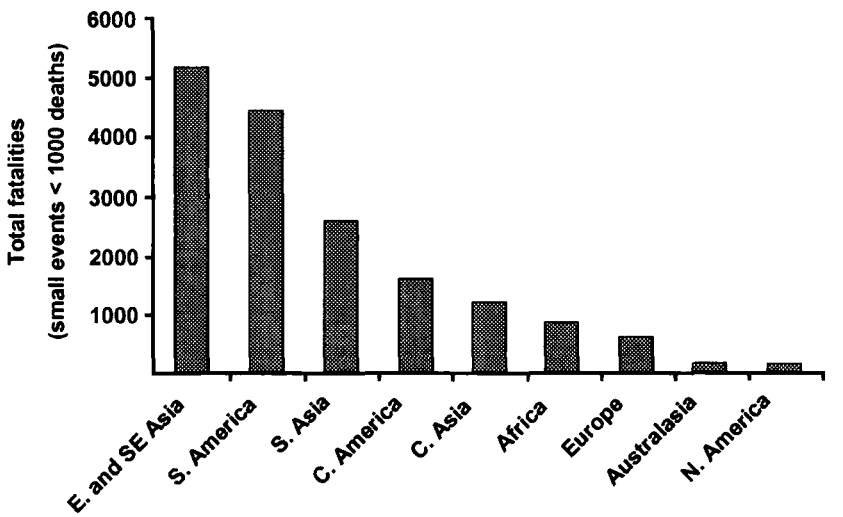

Figure 1.1 Geographical distribution of landslide fatalities on major continents between 1980 and 2000 (after Petley and Bulmer, 2004)

Rainfall-induced landslides triggered by severe rainfall associated with typhoons or low pressure troughs are particularly extensive and frequent on humid tropical and subtropical slopes, such as in Brazil (Vieira and Fernandes, 2004), Hong Kong (Zhou *et al.*, 2002), Malaysia (Lee and Talib, 2005), Mexico (Alcantara-Ayala,

2004), Puerto Rico (Larsen and Torres-Sánchez, 1998), Singapore (Toll, 2001) and Taiwan (Yu *et al.*, 2006). The high amount and intensity of rainfall, deeply weathered soils and steep slope gradients are generally recognised as the main causal factors of slope instability in these environments.

1.2 Mechanisms of rainfall-induced landslides

Previous studies aimed at revealing the underlying mechanisms of rainfall-induced landslides in tropical regions have tended to focus on hydrological and geotechnical aspects, mainly through: (1) field monitoring and measurement of the hydrological response to rainfall (e.g. Rezaur *et al.*, 2002; Tsaparas *et al.*, 2003); and (2) experimental simulation of the field conditions (e.g. Zhu and Anderson, 1998; Dai *et al.*, 1999a). These studies have generally recognised that pore pressure increase is the key landslide triggering mechanism in rainfall-induced landslides. Stability analysis based on the factor of safety, which is the ratio of shear strength to shear stress, has been the dominant research theme. However, the deformation behaviour of slope materials during landslide initiation has not been well-addressed. The actual processes leading to landslide initiation within the shear zone of a landslide remain poorly understood (Iverson, 2005).

Recent research has increasingly enhanced our understanding of the mechanisms of landslides through examining their movement records (e.g. Petley *et al.*, 2002, 2005b, 2005c; Kilburn and Petley, 2003; Petley, 2004; Petley and Petley, 2006). Most importantly, these studies have identified the "linear" and "asymptotic" patterns of landslide movement through $\Lambda - t$ space analyses (where Λ is inverse velocity and t is time) (Saito, 1965) and their relationship to the underlying mechanisms (Petley *et al.*, 2002). Linearity indicates rupture surface development (crack growth), dominated by brittle failure mechanisms (Kilburn and Petley, 2003; Petley, 2004; Petley *et al.*, 2005b; Petley and Petley, 2006); while the asymptotic trend suggests sliding on pre-existing weak surfaces (crack nucleation) or as a result of ductile deformation processes (Petley *et al.*, 2005c). Such relationships have been validated in large-scale, deep-seated landslides that have occurred in a wide variety of slope materials in temperate environments. The applicability of these observations to small-scale, shallow landslides in tropical residual soils is yet to be tested.

1.3 Aim and objectives

This research aims to understand the processes and mechanisms of the initiation of rainfall-induced landslides within natural hillslopes of humid tropical environments.

The major objectives of the research project are as follows:

(i) To analyse pore pressure changes in response to rainstorm events from field monitoring data on natural hillslopes in the humid tropics that are prone to shallow rainfall-induced landslides;

(ii) To conduct field sampling of undisturbed residual soils on natural hillslopes;

(iii) To simulate the field stress conditions of rainfall-induced landslides using a stress path triaxial cell;

(iv) To design representative rates of increasing pore water pressure with reference to the field data;

(v) To examine the movement of residual soil when subjected to different rates of increasing pore water pressure through the $\Lambda - t$ space analysis; and

(vi) To investigate the relationship between the movements of shallow rainfall-induced landslides and the underlying mechanisms and processes.

1.4 Scope of the study

The initiation processes of rainfall-induced landslides on natural slopes are investigated which directly leads to research objectives (i)-(iv). Post-failure and landslide re-activation mechanisms are not within the scope of this study. In order to closely simulate the actual field conditions, undisturbed soil samples have been collected from natural hillslopes that have been prone to rainfall-induced landslides. Moreover, the rates of pore water pressure increase are designed with reference to the field monitoring data.

Hong Kong is chosen as the study area for an investigation on landslide mechanics in residual soil materials in humid tropical environments. Landslides are extensive on steep natural hillslopes, often triggered in weathered residual soil by heavy and intense rainstorms related to typhoons or low-pressure troughs. Natural hillslopes, in the local context, are defined as "terrain that has not been modified substantially by human activity but including areas where grazing, hill fires and deforestation may have occurred" (King, 1999: 9-10).

This research is specifically focused on examining the relationship between changes of pore water pressure increase and deformation behaviour of tropical soil materials, achieving objectives (v) and (vi). A process approach has been adopted through conducting a systematic series of modified triaxial experiments (pore pressure reinflation tests) which simulate the field stress conditions. Movements of soil are monitored by the displacement transducer of the stress path system. Different increasing rates of field-referenced pore water pressure, including linear, stepped and logarithmic rates have been designed. The application of the $\Lambda - t$ technique permits a detailed investigation of the response of the tropical materials to the increasing pore pressures to achieve the aim of the study.

1.5 Structure of the thesis

The thesis is centred upon the theme of understanding the mechanisms of shallow rainfall-triggered landslides in residual soils in the humid tropics.

Chapter 2 reviews previous research on the landslide mechanisms in humid tropical environments and pre-failure movements of landslides. Particular focus will be placed on the current understanding of the deformation behaviour of soil materials in relation to pore pressure changes based on recent field and laboratory studies.

Chapter 3 describes the physical setting of the study area which represent the key landslide governing factors in the humid tropical environments on natural hillslopes, including relief and slope gradient, geology, climate and vegetation.

Chapter 4 explains the rationale for the methodology adopted in field sampling, laboratory testing and the methods of analyses for revealing landslide deformation mechanisms. This chapter further illustrates the processing of the displacement data using the $\Lambda - t$ technique, which allows interpretation of the underlying failure mechanisms (Petley *et al.*, 2002; Kilburn and Petley, 2003; Petley *et al.*, 2005b, 2005c; Petley and Petley, 2006). The design of rainstorm associated pore water pressure increase rates with reference to the field monitoring data collected from the Geotechnical Engineering Office (Evans and Lam, 2003) is also discussed.

Chapter 5 presents the experimental findings obtained from the soil samples collected at Tung Chung (TC) and Pui O (PO) including physical properties, conventional triaxial tests and the reinflation tests. The soil classification, strain development prior to failure, failure envelopes and stress-strain behaviour are

demonstrated. The chapter further presents the response of the soil materials to different rates of increasing pore water pressure. Systematic patterns of soil deformation behaviour towards failure have been noted.

Chapter 6 discusses the key findings on the nature of the residual soils and the sample volumetric behaviour during pore water reinflation. The underlying deformation mechanism is diagnosed through critical analyses and evaluation of the fundamental properties of soil behaviour: elasticity, plastic deformation and creep. Plastic deformation has been identified as the dominant mechanism. The systematic relationships between the soil movements and variations of pore water pressures further imply three successive stages of rainfall-induced landslide development towards failure. The distinctive style and rates of movements of each stage have been further validated by field observations.

Chapter 7 concludes the thesis by highlighting the principal findings. Recommendations for further research are also made.

Chapter 2 Literature review

2.1 Type of landslides

The types of landslides can be defined by a range of classification schemes (Sharpe, 1938; Skempton and Hutchinson, 1969; Carson and Kirkby, 1972; Varnes, 1978; Hutchinson, 1988; Cruden and Varnes, 1996). Most of these schemes are based on the three key elements: the type of movement, the kind of material, and the rate of movement (Varnes, 1978). The classification proposed by Varnes (1978) is the most widely accepted and utilized (Table 2.1). The main landslide types include falls, topples, slides, spreads and flows, which can occur on rock, debris and earth materials. The rate of movement ranges from "extremely slow" (< 16 mm/year) to "extremely rapid" (> 5 m/sec) (Varnes, 1978). A recent comprehensive review on the terminology used in the classifications is provided by Shroder *et al.* (2004).

The typical shallow landslides in humid and subtropical regions are flows and slides, which often occur in weathered debris or earth materials (Maharaj, 1993; Larsen and Torres-Sánchez, 1998; Zhu and Anderson, 1998; Dai *et al.*, 1999a; Capra *et al.*, 2003; Vieira and Fernandes, 2004; Yu *et al.*, 2006).

Table 2.1 Varne's (1978) classification of landslide types

Type of movement		**Type of material**		
		Bedrock	Engineering soils	
			Predominantly coarse	Predominantly fine
Falls		Rockfall	Debris fall	Earth fall
Topples		Rock topple	Debris topple	Earth topple
Slides	Rotational	Rock slump	Debris slump	Earth slump
	Translational	Rock back slide	Debris back slide	Earth back slide
		Rock slide	Debris slide	Earth slide
Lateral spreads		Rock spreads	Debris spread	Earth spread
Flows		Rock flow	Debris flow	Earth flow
		(Deep creep)	(Soil creep)	
Complex	Combination of two or more principal types of movement			

However, for the purpose of this research, which aims to understand the processes and mechanisms of shallow rainfall-induced landslides, Hutchinson's (1988) geotechnical classification (Table 2.2) appears particularly relevant, as the mechanism of slope movements is also considered. Landslide type is classified by (1) the shearing conditions (first time; reactivated) with reference to soil fabric (undisturbed; disturbed)

and shear strength parameters (peak; between peak and residual) and (2) pore-water pressure conditions over time (short-term, undrained; intermediate, partial equalisation of excess pore water pressures; and long-term, drained) (Hutchinson, 1988).

Table 2.2 Hutchinson's (1988) geotechnical classification of landslides based on (a) soil fabric and (b) pore water pressure conditions

(a) Soil fabric (affecting c' and ϕ')		**(b) Pore-water pressure on the slip surface (affecting u)**	
1.	FIRST-TIME SLIDES IN PREVIOUSLY UNSHEARED GROUND: soil fabric tends to be random (or partly orientated as a result of depositional history) and shear strength parameters are at peak or between peak and residual values.	1.	SHORT TERM (undrained) – no equalisation of excess pore-water pressure set up by the changes in total stress.
2.	SLIDES ON PRE-EXISTING SHEARS associated with:	2.	INTERMEDIATE – partial equalisation of excess pore-water pressures. Delayed failures of cuttings in stiff clay are usually in this category.
2.1	Re-activation of earlier landslides	3.	LONG-TERM (drained) – complete equalisation of excess pore-water pressures to steady seepage values.
2.2	Initiation of landsliding on pre-existing shears produced by processes other than earlier landsliding, i.e.: (a) Tectonics (b) Glacitectonics (c) Gelifluction of clays (d) Other periglacial processes (e) Rebound (f) Non-uniform swelling In these cases the soil fabric at the slip surface is highly orientated in the slip direction, and shear strength parameters are or about residual value.		Note that combinations of drainage conditions 1, 2, 3 can occur at different times in the same landslide. A particularly dangerous type of slide is that in which long-term, steady seepage conditions (3) exist up to failure but during failure undrained conditions (1) apply, i.e. a drained/undrained failure.

Under this classification, this research examines first-time landslides which occur in largely unsheared geomaterials. Pore-pressure conditions are simulated with reference to the field conditions to investigate the deformation behaviour of rainfall-induced landslides in tropical slope materials.

2.2 The triggering mechanism of rainfall-induced landslides

Landslides initiate when shear stress (the driving force that causes downslope movement of slope materials, or the "external" force) is greater than the shear resistance of the material (the resistance of movement, or the "internal" force) (Terzaghi, 1950). Hence slope instability can be caused by either increasing shear stresses or decreasing resistance or both. Their relative relationship is expressed as a ratio of shear resistance to shear stress, known as the factor of safety, F:

$$\text{Factor of Safety},\ F = \frac{\text{Shear resistance } (\tau_f)}{\text{Shear stress } (\tau)}$$

(Eq. 2.1)

Failure occurs when F = 1. The slope is in a stable condition when F > 1 but unstable when F < 1. The stability analysis has been incorporated with the Coulomb equation as:

$$F = \frac{c' + (\sigma_n - u)\tan\phi'}{\tau}$$

(Eq. 2.2)

where c' is the effective cohesion, σ_n is the total normal stress, u is the pore-water pressure, ϕ' is the effective angle of internal friction and τ is the shear stress. c' and ϕ' are the strength parameters, $(\sigma_n - u)$ is the effective stress, as defined by Terzaghi (1936), in its original form:

$$\sigma' = \sigma_n - u$$

(Eq. 2.3)

where σ' is effective stress.

For shallow translational slides on natural slopes (< 5 m thick), the factor of safety can be analysed through an infinite slope analysis (Fell *et al.*, 2000), expressed as:

$$F = \frac{c' + (\gamma - m\gamma_w) z \cos^2\beta \tan\phi'}{\gamma z \sin\beta \cos\beta}$$

(Eq. 2.4)

where γ is the unit weight of the soil at the natural moisture content, m is a fraction of the soil thickness above the slide plane, γ_w is the unit weight of water, β is the slope inclined angle and z is the depth.

The Coulomb-Terzaghi shear strength equation (Eq. 2.2) clearly indicates that slope resistance mainly comes from the effective cohesion (c') and the angle of internal friction (ϕ') due to the interlocking of particles which depends on the normal force (σ_n). Slope disturbance (the shear force), as revealed from Eq. 2.4, depends on the weight of the slope material which is directly proportional to its density, slope angle and thickness.

Based on this equation, the triggering mechanism of rainfall-induced landslides on shallow hillslopes can be attributed to the increase of pore water pressure. This has been termed "hydrological triggering" by Terlien (1998). On a natural soil slope receiving rainfall, the shear stress is approximately constant due to gravity. However, the increase of pore pressure as a result of rainfall infiltration progressively reduces the normal effective stress of the slope materials acting on a potential shear surface. The shear resistance decreases as the inter-particle friction is reduced by the buoyancy force and eventually reaches a critical value equal to the shear stress (i.e. F = 1), which triggers a landslide. The failure condition (F = 1) can be expressed using the Mohr-Coulomb failure envelope (Figure 2.1).

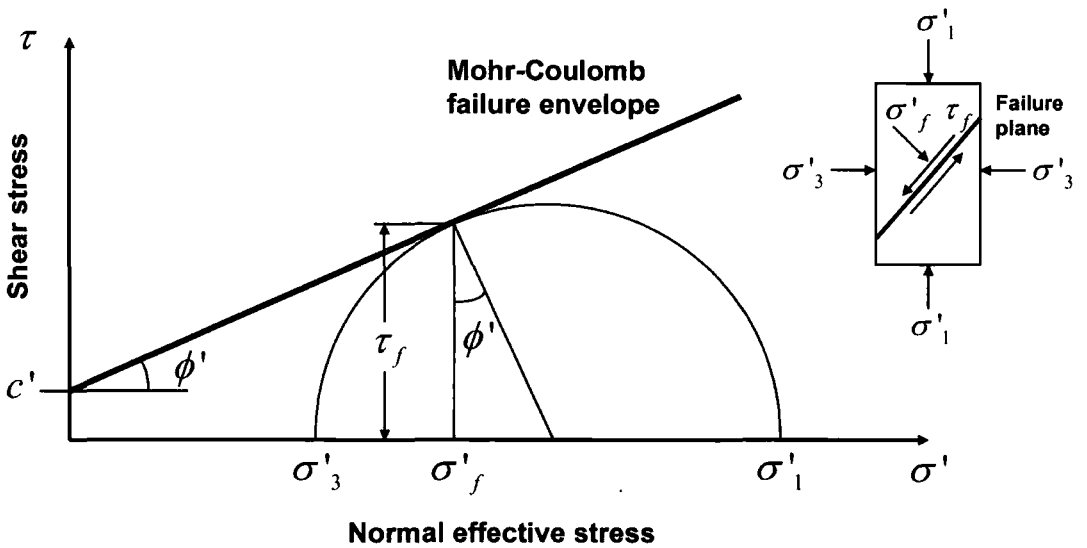

Figure 2.1 Stress conditions at failure (after Craig, 1997)

The above conventional limit equilibrium analyses, therefore, only determine the landslide triggering conditions through the identification of the relationship between the material strength and the stress on the potential sliding plane. As such, the factor of safety has been criticized as an "all-or-nothing" approach that simply defines slopes as either stable or unstable (Helmstetter *et al.*, 2004; Sornette *et al.*, 2004). The preparatory stage leading to catastrophic failure is not considered (Sornette *et al.*, 2004).

Moreover, the failure that determines the shear strength of soil could be defined by one of the five criteria, namely (1) critical state, (2) residual state, (3) peak deviator stress, (4) maximum principal stress ratio or (5) limiting strain (Head, 1998). The failure envelope itself does not indicate which criterion is used unless clearly stated. The

failure envelope derived from the residual strength, for example, cannot represent the failure conditions of a first-time landslide that exhibits a peak deviator stress.

Most importantly, the Mohr-Coulomb criterion does not explain the landslide kinematics, the movement style, and displacement rates (Qin *et al.*, 2006), or the velocity and the acceleration (Helmstetter *et al.*, 2004; Sornette *et al.*, 2004) at the shear zone as failure develops (Cristescu *et al.*, 2002). This is because such analyses do not address the pre-failure strains (Craig, 1998).

Another slope stability analysis approach, known as the finite element method, places more emphasis on assessing slope stresses and strains (Duncan, 1992, 1996a, 1996b). The analysis places more emphasis on small deformations (Sitar *et al.*, 2005). However, these approaches are insufficient to understand landslide development, as the underlying mechanisms and processes for the wide range of movement rates and styles are not accounted for (Iverson, 2005).

2.3 Material deformation behaviour

The underlying mechanisms for the rate and styles of landslide movements are explained in more detail with reference to the typical stress-strain behaviour of materials at various levels of effective stresses (Petley, 1996; Petley and Allison, 1997) (Figure 2.2). Rapid, catastrophic failure is often associated with brittle deformation, prevailing in bonded or cemented materials at low effective stresses; while the steady, continual creep movement is often attributed to ductile deformation mechanisms, commonly found in materials with little or no interparticle bonding at higher effective stresses. The changing behaviour from creep to sudden failure is often the result of a transition from ductile to brittle deformation mechanisms (Petley and Allison, 1997).

Both brittle and ductile deformation initially undergo an elastic phase in which the inter-particle bonds within the material are being loaded without breaking and strain is recoverable (Stage I) (Figure 2.2). This is followed by the elastic-plastic deformation when the shear stress continues to increase, involving the breakage of the weakest or highly stressed bonds between particles (Stage II) (Petley and Allison, 1997).

However, brittle failure is characterised by a peak where strain is localised to initiate shear surface development, and followed by a sudden drop where the shear surface is fully developed through strain weakening (Stage VI) to residual strength (Stage V) (Figure 2.2a). The loss of cohesion from the peak to the residual stress state

during the development of the shear surface can be responsible for rapid movement rates. This is due to shear stress being much greater than the shear strength and thus providing the large imbalance force required to drive the catastrophic failure (Petley and Allison, 1997; Kilburn and Petley, 2003; Petley *et al.*, 2005b).

Ductile deformation, on the other hand, involves no peak strength but purely plastic failure at a constant stress due to internal restructuring of the material in which the strain cannot localize (Stage III) (Figure 2.2b). The strain rate increases as a result of the progressive destructuring and pore water pressure fluctuations.

These research findings have improved understanding of the mechanics underlying the various movement types of large, comparatively deep-seated landslides in cohesive materials. Caution has to be made in interpreting the results as they were derived from standard strain rate controlled triaxial tests, which might not replicate the field stress condition (Petley and Allison, 1997). However, later experimental research using a stress-controlled method, known as the "pore pressure reinflation" test (Petley *et al.*, 2005b), has also identified the movement styles and successfully explained the progressive development of deep-seated landslides in cohesive materials through damage mechanics. The applicability for understanding shallow rainfall-induced landslide mechanisms on tropical weathered soils is yet to be examined.

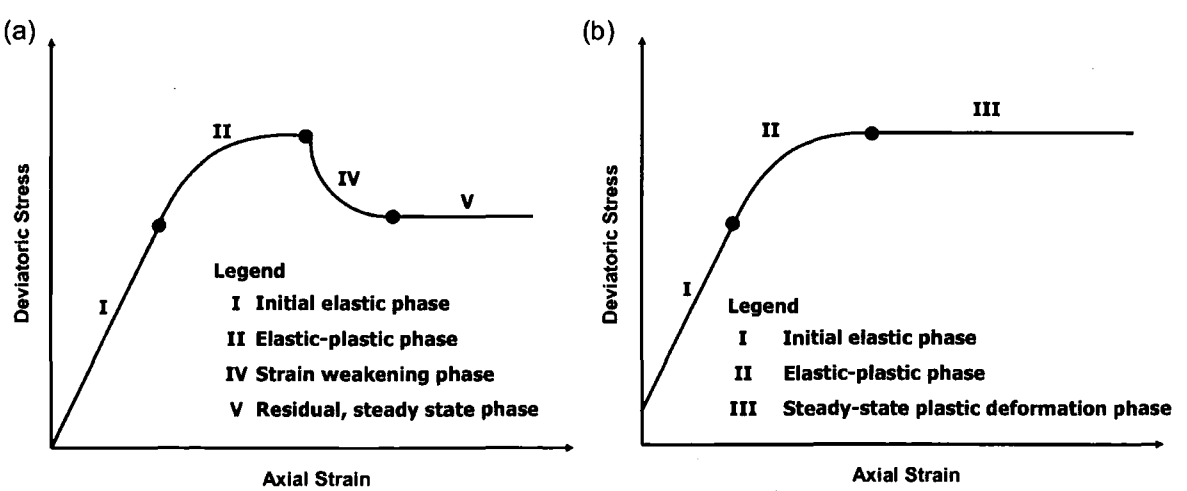

Figure 2.2 Typical stress-strain behaviour for materials: (a) brittle deformation; (b) ductile deformation (after Petley and Allison, 1997)

2.4 Landslide mechanisms in humid tropical environments

Landslides are caused by the interactions of many factors (Terzaghi, 1950; Crozier, 1986; Selby, 1993). In the humid tropical or subtropical regions, most landslides are found on weathered soil slopes, and are triggered by heavy and intense rainfall (Zhu and Anderson, 1998; Franks, 1999; Faisal, 2000; Toll, 2001; Alcantara-Ayala, 2004). It is essential, therefore, to examine specifically the relationship between the nature of pore water pressure increase and the deformation behaviour of residual soil materials, which is of primary importance and directly relevant to the understanding of their initial mechanisms and processes.

2.4.1 Slope environments in the humid tropics

2.4.1.1 Residual soils

Most shallow landslides in tropical regions occur in intensely weathered or residual soils (Rahardjo *et al.*, 1995; Au, 1998; Zhu and Anderson, 1998). Residual soil can be generally defined as "a soil-like material derived from the in situ weathering and decomposition of rock which has not been transported from its original location" (Blight, 1997: 1). Most residual soils are found in tropical regions with high temperatures and rainfall (Fookes, 1997; Faisal, 2000). They are formed in situ from bedrock, by physical, chemical and biological weathering processes (Blight, 1997; Fookes, 1997).

The term "residual soil" has been considered as Grade VI in many classification schemes of the weathering profile relevant to tropical and sub-tropical climatic environments (e.g. Fookes, 1997; Irfan, 1999; GEO, 2000) (Table 2.3). However, the Geological Society of London also broadly considers tropical residual soils to include weathering Grades IV and V as they possess the "soil-like" mass and material properties derived from the in-situ weathering processes (Fookes, 1997: 12).

The engineering properties of residual soils, including mineralogy, particle size distribution and void ratio, vary at different weathering grades (Vaughan, 1988; Fookes, 1997; Queiroz de Carvalho and Simmons, 1997; Aung *et al.*, 2000). In the most intensely weathered grades such as Grades IV-VI, kaolinite has been found to be the dominant clay mineral (Irfan, 1994, 1999; Rahardjo *et al.*, 2004). The percentage of fines also increases as the soils are more intensely weathered (Lumb, 1962, 1965; Rahardjo *et al.*, 2004). Tropical weathering processes have been shown to increase the pore volume and moisture content of argillaceous rocks (Fan *et al.*, 1994; 1996) and the void ratio of granitic and sedimentary rocks (Rahardjo *et al.*, 2004). These findings appear to indicate that residual soils (Grade IV-VI) can be typically

characterised by a highly decomposed structure that is heterogeneous, fine-grained and highly porous.

Table 2.3 Classification of a weathered rock mass profile (after Fookes, 1997)

Grade	Term	Description
I	Fresh	No visible sign of rock material weathering; perhaps a slight discoloration on major discontinuity surfaces
II	Slightly weathered	Discoloration indicates weathering of rock material and discontinuity surfaces. All the rock material may be discoloured by weathering
III	Moderately weathered	Less than half of the rock material is decomposed or disintegrated to a soil. Fresh or discoloured rock is present either as a continuous framework or as corestones.
IV	Highly weathered	More than half of the rock material is decomposed or disintegrated to a soil. Fresh or discoloured rock is present either as a discontinuous or as corestones.
V	Completely weathered	All rock material is decomposed and or disintegrated to soil. The original mass structure is still largely intact.
VI	Residual soil	All rock material is converted to soil. The mass structure and material fabric are destroyed. There is a large change in volume, but the soil has not been significantly transported.

The increased pore-size as a result of weathering may lead to a higher permeability. For example, a study in Hong Kong showed an increase in the average permeability from 0.9×10^{-6} m/s in Grade I-III volcanics to a value of 4×10^{-6} m/s in Grade IV-VI decomposed volcanics (GCO, 1982). Similarly, the saturated permeability increased from 1.0×10^{-10} m/s in the weathered sedimentary bedrock (> 2.5 m deep) to 1.0×10^{-6} m/s in the silty clay residual soils in the upper 1.5 m of a slope in Singapore (Gasmo *et al.*, 2000).

2.4.1.2 Pore water pressures during rainstorms

It is well-established that the rise of pore pressure as a result of rainfall decreases the mean effective stress of the slope, which lowers the soil strength and eventually triggers rainfall-induced landslides (section 2.2). Thus, pore pressure responses to rainfall directly affect the location, timing and rates of landsliding on tropical hillslopes (Iverson, 2000).

Field monitoring of groundwater or pore pressure response is an important way to investigate hillslope hydrological conditions during rainstorms. Recent studies in the tropics have been undertaken in Hong Kong (e.g. GOL, 2002; Evans and Lam, 2003; Li *et al.*, 2005), Singapore (e.g. Deutscher *et al.*, 2000; Rezaur *et al.*, 2002, 2003; Tsaparas *et al.*, 2003; Rahardjo *et al.*, 2005), Taiwan (Chang *et al.* 2005), Sikkam Himalaya (Bhasin *et al.*, 2002) and Brazil (e.g. Vieira and Fernandes, 2004; Gerscovich *et al.*, 2006). These studies are often equipped with field instrumentation consisting of piezometers or tensiometers, and rain gauges. The main alternative approach uses physical modelling (Gasmo *et al.*, 2000; Ng *et al.*, 2001; Tsaparas *et al.*, 2002; Lan *et al.*, 2005; Jiao *et al.*, 2005).

Despite these efforts, our understanding of soil slope response to rainfall infiltration remains poor (Li *et al.*, 2005; Rahardjo *et al.*, 2005). Comparatively little is known about the nature and variability of pore pressure response over time and space. This is crucial to slope instability (Rezaur *et al.*, 2002).

(a) Positive change of pore pressures

Positive change or increasing pore pressures is commonly observed during rainstorms. Pore pressure increases have been found mainly associated with either rainfall infiltration (e.g. Tsaparas *et al.*, 2003; Chen *et al.*, 2005a; Rahardjo *et al.*, 2005) or the rise of the groundwater table (Rahardjo *et al.*, 1998; Chang *et al.*, 2005). The former process is pre-dominant in tropical slopes during rainstorms, frequently associated with the development of a perched water table (Irfan, 1994; Lim *et al.*, 1996; Dai *et al.*, 1999a; Dykes and Thornes, 2000; Deutscher *et al.*, 2000; GOL, 2002; Capra *et al.*, 2003; Li *et al.*, 2005; Rahardjo *et al.*, 2005).

Increases in pore pressure could fall into one of these regimes: (A) an increase from an initially positive value to a higher positive value (commonly termed "excess pore water pressure"), (B) an increase from negative to zero or a positive value ("loss of suction") or (C) an increasing but always negative value ("changes in suction"). This can be illustrated by the pore pressure response observed from an instrumented residual soil slope in Singapore (Figure 2.3).

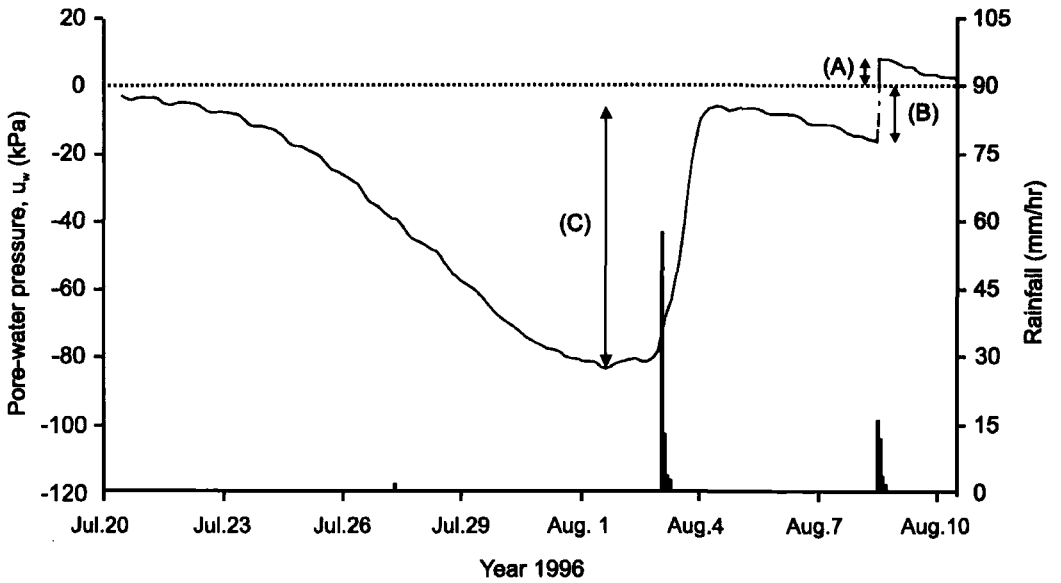

Figure 2.3 Rainfall and pore water pressure measurements in a weathered sedimentary slope in Singapore (after Gasmo *et al.*, 2000), illustrating the three scenarios of increasing pore pressure: (A) excess pore water pressure; (B) loss of suction; (C) changes in suction

Having identified these scenarios, it should also be noted there are divided views over the triggering cause for tropical landslides, with regard to scenarios (A) and (B). Scenario (C) is not considered here as there is no empirical evidence suggesting that it is associated with the actual triggering of failures.

Many studies of rainfall-induced landslides in the humid tropics observe that failure is triggered when pore water pressure is positive (i.e. scenario A) (e.g. Baum and Reid, 1995; Capra *et al.*, 2003; Vieira and Fernandes, 2004; Gerscovich *et al.*, 2006). For example, in Hawaii, the main body of a slow-moving landslide within the year-round saturated weathered material only moves during periods with intense rainfall ($\geq$ 25 mm/day) when the pore water pressure increases 10-30 kPa at the slip surface (Baum and Reid, 1995). Development of positive pore water pressures associated with a perched water table has been reported as the trigger for shallow soil slides and debris flows in clay-rich volcanic paleosols in Mexico (Carpa *et al.*, 2003), whilst high positive pore pressures within deep weathered soils often lead to slope failures in Brazil (Vieira and Fernandes, 2004; Gerscovich *et al.*, 2006).

Loss of suction (scenario B) can trigger failure in unsaturated residual soils due to the drop in apparent cohesion as a result of water infiltration (Lumb, 1965, 1975; Brand *et al.*, 1983). A large drop in cohesion in unsaturated decomposed rhyolite was observed upon full saturation, from 215 kPa to zero (Lumb, 1965) (Figure 2.4). Foss

(1973) also reported a more than 50% drop in cohesion on andisol in Kenya due to saturation. Similar effects have also been reported in other tropical soils (Tsutiya *et al.*, 1992; Rao, 1996). The reduction in the apparent cohesive strength and effective stress associated with the loss of suction upon saturation may decrease shear strength on the potential failure zone and trigger a landslide, especially in the absence of the true cohesion (Rao, 1996).

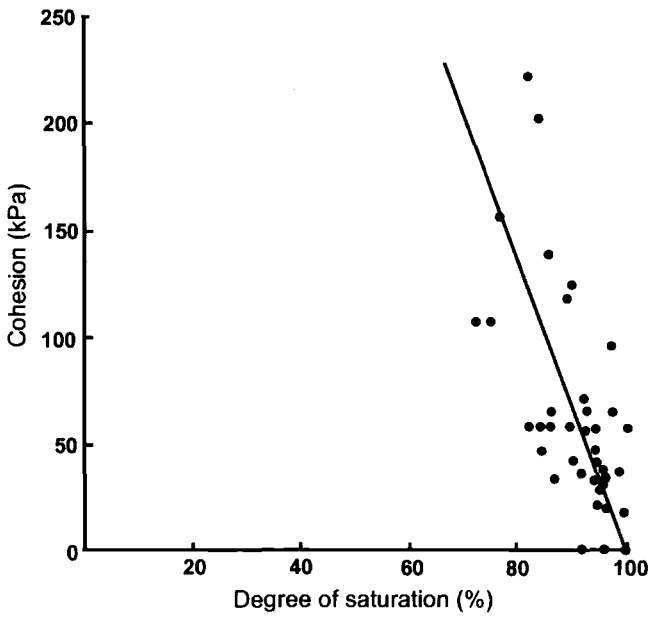

Figure 2.4 Negative relationship between drained cohesion and the degree of saturation for decomposed rhyolite, Hong Kong (after Lumb, 1965)

Nevertheless, there is very little field evidence to suggest that the loss of suction directly leads to landslides. Lim *et al.* (1996) studied the role of matric suction on tropical slopes and concluded that shallow landslides occurred during rainstorms as a result of the development of perched water tables. This is consistent with Farooq *et al.* (2004) who suggested that dissipation of suction by rainfall infiltration was insufficient to cause landslides and a positive pore water pressure was required. Recent field studies have shown that the negative pore pressures that develop at shallow depths during prolonged dry periods reduce dramatically the process of water infiltration during rainfall (Deutscher *et al.*, 2000; Faisal, 2000; Rezaur *et al.*, 2002). These studies have not demonstrated that loss of suction alone causes landslides. Recent tropical slope studies have been mainly focused on the role of suction on unsaturated soil slope stabilisation (e.g. Lim *et al.*, 1996; Ng and Pang, 2000; Zhang *et al.*, 2004; Babu and Murthy, 2005) rather than the failure mechanism. Hence, the role of loss of suction as a landslide trigger on unsaturated tropical slopes appears to be uncertain.

In summary, the evaluation of the positive pore pressure scenarios suggests that scenario A (or "excess pore water pressure") is more likely to represent the field conditions during rainstorms and act as a triggering cause for tropical landslides. Scenario B (or "loss of suction") alone may not be sufficient to cause landslides.

(b) Temporal variations

The three scenarios of increasing pore pressure are often associated with seasonal variation. Excess pore pressures (scenario A) may be common during the wettest season (e.g. Dykes and Thornes, 2000; Rezaur *et al.*, 2002, 2003; Rahardjo *et al.*, 2005). Loss of suction (scenario B) often relates to moderate wet periods (Deutscher *et al.*, 2000; Evans and Lam, 2003) or to rainfall after a long dry period (e.g. Tsaparas *et al.*, 2003), when the soil is initially unsaturated (Fredlund and Rahardjo, 1993). Changing suction (scenario C) mainly occurs during the dry season when the groundwater level is low (e.g. Lim *et al.*, 1996; Deutscher *et al.*, 2000; GOL, 2002; Evans and Lam, 2003).

Following the onset of a rainstorm, studies on tropical slopes have often observed that pore pressures increased rapidly (GCO, 1982; Dykes and Thornes, 2000; GOL, 2002; Rezaur *et al.*, 2002, 2003; Evans and Lam, 2003; Tsaparas *et al.*, 2003). For example, shallow tensiometers at 1-2 m were seen to respond within 10 mins of the onset of rainfall in Singapore (Rahardjo *et al.*, 2005). Instantaneous response was also observed in shallow piezometers during rainstorm periods in Hong Kong (Evans and Lam, 2003) (Figure 2.5). Moreover, in some cases, the change of positive pore pressure was significant. For example, rainfall-related infiltration was observed to trigger an increase in pore pressure of 70 kPa on a residual soil slope in Singapore (Gasmo *et al.*, 2000) (Figure 2.3). Positive changes in pore pressure of 30 kPa have been reported on weathered hillslopes in Hong Kong (GOL, 2002). Therefore, the temporal pore pressure variations in humid environments have been described as highly transient (Anderson and Sitar, 1995; Lan *et al.*, 2005). It has also been noted that shallow pore water pressures rapidly reach a maximum and remain relatively constant till the end of a rainfall event (Tsaparas *et al.*, 2003), although it is not really known whether this is universally applicable.

Whilst some studies have provided detailed descriptions on the variations of pore pressure during rainfall events, surprisingly, few studies have quantified the actual rate of pore pressure increases over time.

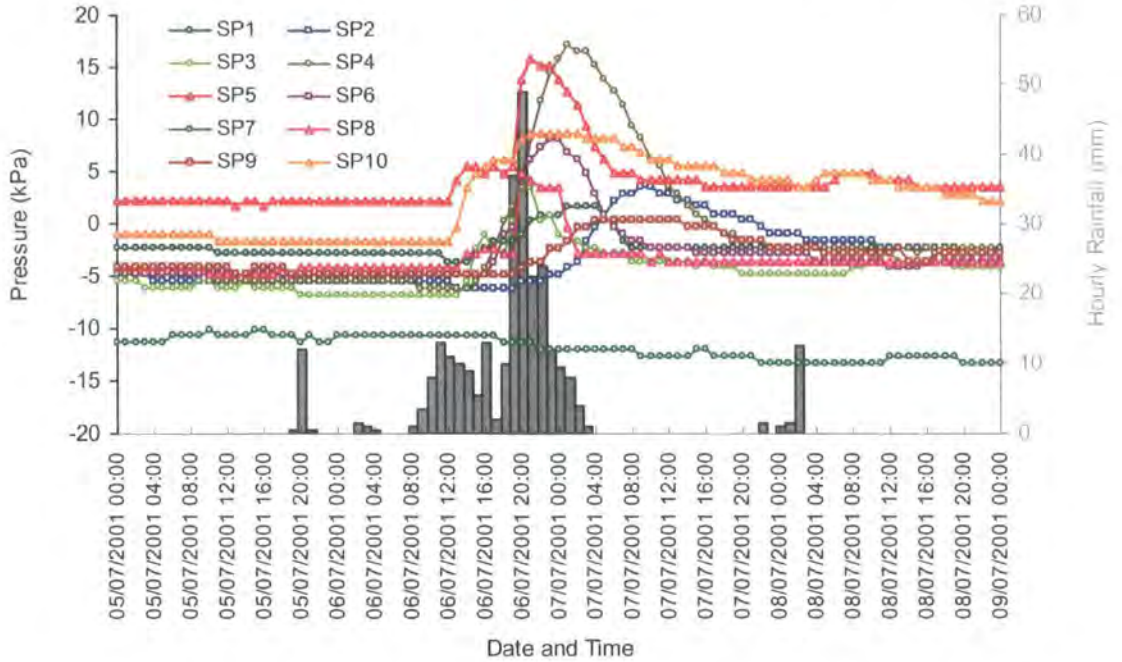

Figure 2.5 Rapid pore pressure responses during the rainstorm on 5-8 July 2001 on Lantau Island, Hong Kong. The depth of the shallow piezometers is indicated by the symbols: triangles (< 2 m deep), circles (2-3 m deep), squares (3 m deep) (after Evans and Lam, 2003)

(c) Spatial variations

Under a particular rainstorm, the rate and style of the pore pressure responses also appears to vary across a slope, depending on the soil depth and soil permeability (Ng *et al.*, 2001; GOL, 2002; Evans and Lam, 2003; Rezaur *et al.*, 2002, 2003; Tsaparas *et al.*, 2003; Vieira and Fernandes, 2004; Lan *et al.*, 2005; Rahardjo *et al.*, 2005). These recent field studies have demonstrated that the largest and most rapid changes in rainfall-induced pore pressure are generally observed at shallow depths (< 3 m) and/or in soils with low permeability.

In contrast, slower rates of increase in pore pressure occur at greater depths (> 3 m) (Tsaparas *et al.*, 2003; Rahardjo *et al.*, 2005). For example, under a rainstorm with maximum intensity at 75 mm/hr on a natural hillslope in Hong Kong, shallow piezometers (less than 2 m deep) showed the greatest increase in pore pressure, whilst a much more gentle or no response was noted for deeper piezometers at 3 m (Figure 2.5) (Evans and Lam, 2003). Similarly, extensive development of positive pore water pressures within the entire shallow soil slope was also observed during a rainfall event in Singapore, as revealed by the spatial distribution of pore pressure contours (Tsaparas *et al.*, 2003) (Figure 2.6).

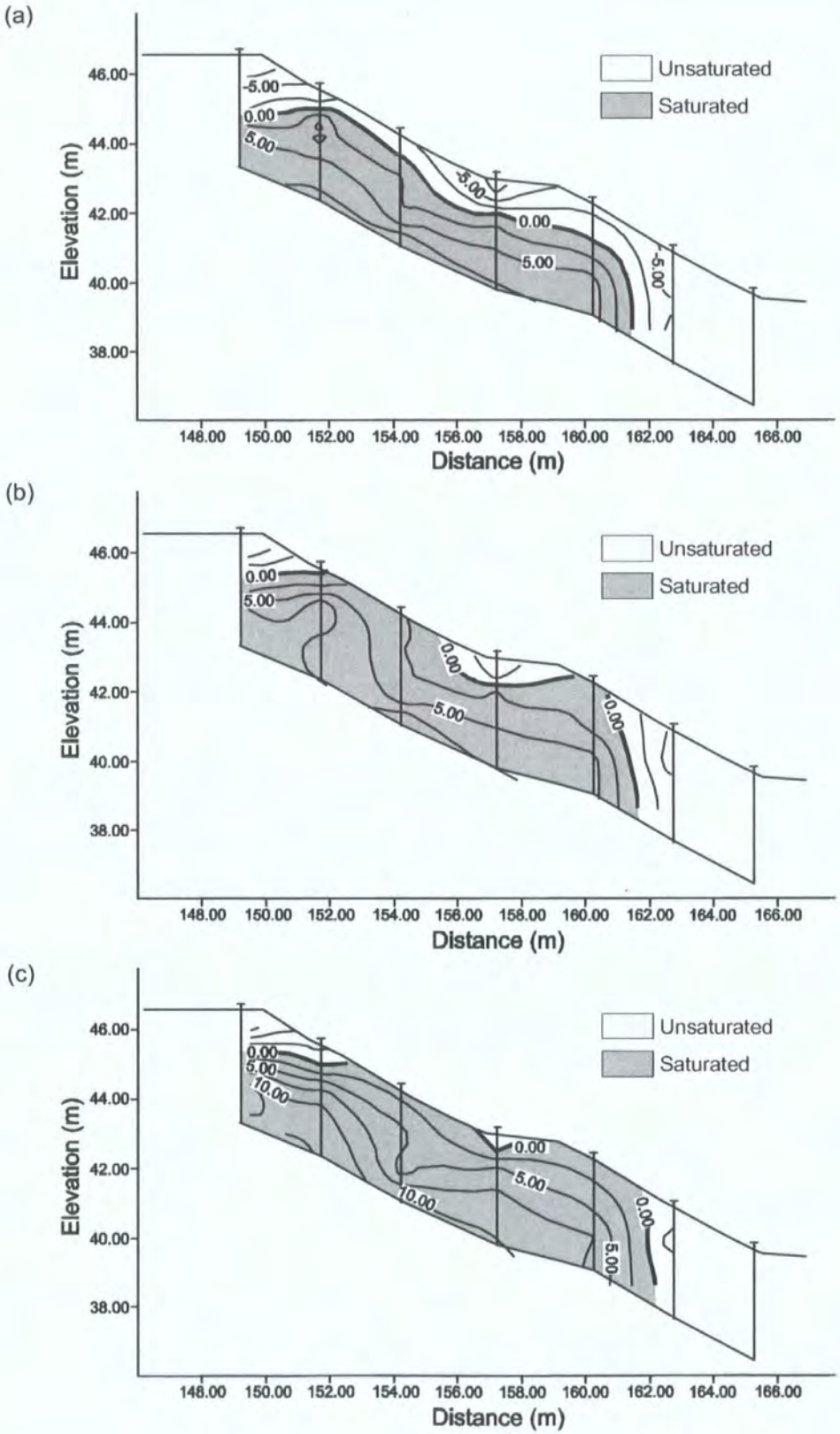

Figure 2.6 Spatial distribution of pore pressure in contours (kPa) within the NTU-CSE residual soil slope on 6 December 1999 during a rainfall event in Singapore: (a) start of rainfall at 00:10; (b) at 01:03 after 65 mm of rainfall; (c) 86 mm at the end of the rainfall (after Tsaparas *et al.*, 2003)

2.4.1.3 Pre-failure slope movements

The relationship between the variations of pore water pressure and pre-failure displacements in the humid tropics is not clear. Nevertheless, creep movements on residual soil slopes have been reported. For example, rapid acceleration (tertiary creep) was observed in June, 2003 towards the final failure of the 626 landslide in Taiwan (Chang *et al.* 2005) (Figure 2.7). In Hawaii, landslides are frequently triggered by creep (Nicholson *et al.*, 1996). Creep rates of 0.5 cm/year to 1 cm/year were observed on many hillsides in Honolulu (Nicholson *et al.*, 1996). In Honolulu, the long-term average rates of twelve "slow-moving landslides" ranged from 6 to 25 mm/day, characterised by rapid stepped-like movements with intermittent periods of slow creep or zero displacement (Kwong *et al.*, 1999). In Sabah, east Malaysia, displacement rates recorded on the natural slopes (up to 30 m deep) are between 2 and 14 mm/week, with a maximum at 21 mm/week in association with the development of shear surfaces (Shaw-Shong, 2004).

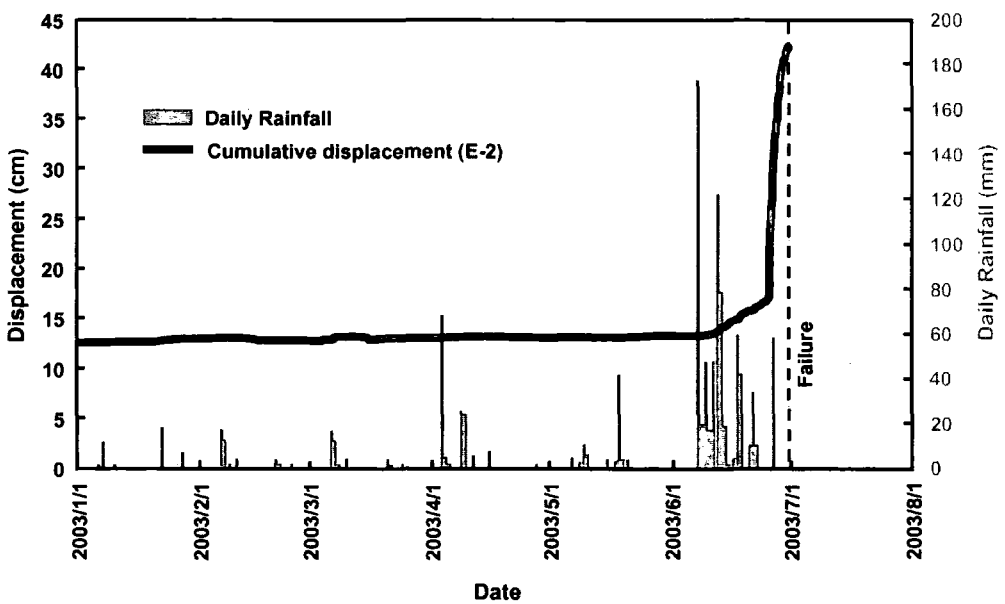

Figure 2.7 Displacements before the final failure of the 626 landslide in Taiwan (after Chang *et al.*, 2005)

In Hong Kong, however, the presence of creep before failure is unclear as most of the evidence of creep is indirect. The key studies on the creep mechanism have been undertaken by Irfan (1994, 1998a) on saprolitic soils based on post-failure examination of geological features, which concluded that the swelling of halloysite clay minerals and the opening up of relict discontinuities contributed to the formation and development of creep. In contrast, Au (1998) asserted that a majority of rainfall-induced landslides in Hong Kong occurred in a sudden manner, without signs of warning or progressive failure.

2.4.2 Experimental studies

Previous research on the mechanisms of rainfall-induced landslides in the humid tropics has been largely based on experimental studies simulating the field conditions on hillslopes (section 2.4.1). This section reviews the key laboratory testing approach and its applications, the main findings on the deformation behaviour under increase of pore water pressure, and the resulting key issues.

2.4.2.1 Simulating the mechanisms of rainfall-induced landslides

The experimental procedures that simulate failure processes caused by increasing pore pressure were first described by Bishop and Henkel (1962). However, the test idea was not developed further until Brand (1981), who conceptualised the mechanism of rainfall-triggered landslides represented by the "field stress path" (FSP) (Figure 2.8). In terms of soil mechanics parameters, the initial stress state of the test is represented by (p'_i, q'_i), where $p' = (\sigma'_1 + \sigma'_3)/2$ is the mean effective stress, and $q = (\sigma'_1 - \sigma'_3)/2$ is the deviatoric stress. The increase of pore water pressure decreases the mean effective stress from (p'_i, q_i) to (p'_f, q_f) while the total normal stresses, σ_1 and σ_3, remain constant. Failure is assumed to occur at (p'_f, q_f) when reaching the Mohr-Coulomb failure envelope.

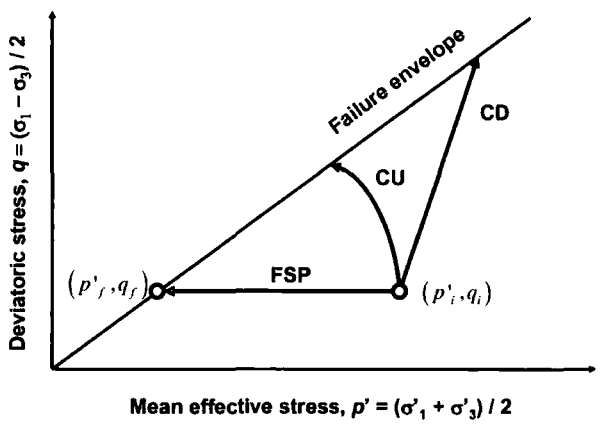

Figure 2.8 Comparison between field stress path (FSP) and conventional consolidated undrained (CU) and drained (CD) stress paths (after Brand, 1981)

The key features of FSP include (1) increasing pore pressure at a constant total normal stress (and hence decreasing the effective stress) and (2) constant shear stress. The former simulates the main process leading to rainfall-triggered landslides (section 2.4.1.2), whilst the latter is related to the approximately constant gravity-induced shear stress on a planar slope and the negligible load of infiltrating rainfall (Zhu and Anderson, 1998).

In contrast, the stress paths derived from the conventional triaxial compression tests such as the consolidated drained (CD) test or the consolidated undrained (CU) test (Figure 2.8) fail to replicate the field conditions. Instead, they are undertaken with the application of increasing axial load, σ_1 (shear stress), at constant displacement rates. As a result, these strain-controlled conventional tests are mainly used for determination of the shear strength of slope materials (e.g. Gan and Fredlund, 1996), but are irrelevant to understand pre-failure soil deformation behaviour within a landslide (Kalaugher *et al.*, 2000).

2.4.2.2 Test applications

Concerning the test conditions, the FSP has been also named as the "constant dead load (DL) test" (GCO, 1982; Brenner *et al.*, 1985; GEO, 1994a; Chen *et al.*, 2000; 2004), "constant shear drained (CSD) test" (Anderson and Sitar, 1995; Anderson and Riemer, 1995; Santos *et al.*, 1996; Zhu and Anderson, 1998; Chu *et al.*, 2003; Springman *et al.*, 2003; Farooq *et al.*, 2004; Lourenço *et al.*, 2006), "constant deviatoric stress path (CQD)" (Dai *et al.*, 1999a, 1999b) and "pore pressure reinflation (PPR) test" (Petley *et al.*, 2005b). Previous tests have used both undisturbed and disturbed samples under saturated and unsaturated conditions. However, this review focuses on the main characteristics of the studies using undisturbed, saturated samples (Table 2.4), as they best represent the field conditions of first time failures on shallow hillslopes under rainstorms.

These tests have been mostly undertaken on tropical or subtropical soils (Table 2.4). Weathered hillslope materials have mostly been tested at a low mean effective stress ($\leq$ 200 kPa), while studies from temperate areas have generally been conducted at higher effective stresses (100 - 1000 kPa) due to the different dominant failure types. Moreover, most of the tropical studies were undertaken at a low pore pressure increase rate (less than 2 kPa/hr), whereas much higher increase rates of pore pressure (5 - 60 kPa/hr) were applied to temperate areas.

The rationale behind the choice of the rate of pore pressure increase is generally not clearly stated, although some studies have made reference to the field hydrological conditions (e.g. Anderson and Sitar, 1995; Zhu and Anderson, 1998), and the "dead load" tests, which restricted the rate to maintain pore pressure equalisation within the sample (GCO, 1982; GEO, 1994a).

Table 2.4 Laboratory simulation of rainfall-induced landslide on saturated undisturbed soils

Test	Location	Soil material	Mean effective stress, p'	Pore pressure increase rate	Axial strain development	Deformation behaviour	References
Pore-pressure reinflation test (PPR)	Selborne, Hampshire, UK	Gault Clay	200 kPa	0.42, 60 kPa/hr	Linear trend in $\Lambda - t$	Brittle (shear surface)	Petley *et al.*, 2005b
	Tessina, northern Italy	Highly fractured molasse deposits	200-210 kPa	10, 15 kPa/hr	Asymptotic trend in $\Lambda - t$	Ductile	Petley *et al.*, 2005b, 2005c
	Black Ven, Lyme Regis	Foxmould (66.4% sand, 28.3% slit, 5.3% clay)	100-400 kPa 600, 1000 kPa	5, 10, 20 kPa/hr	Linear trend Asymptotic trend	Brittle Ductile	Karintzis, 2005
Constant deviatoric stress path (CQD)	South Lantau, Hong Kong	Colluvial clayey silt / silty clay sand	< 60 kPa	0.9 kPa/hr	Strain increases very slowly initially but sharply increases after yield	Dilative	Dai *et al.*, 1999a
Constant shear drained test (CSD)	Honolulu, Hawaii	Residual soil, high plasticity silt or silty sand (65-75% sand, 25-25% silt/clay)	10-45 kPa	1 kPa/hr	Axial strain rapidly increase when yield is reached	Dilative (bulging with slight shear surface)	Zhu and Anderson, 1998
	Berkeley, California	Clayey residual/colluvial soil (< 5% sand, 55-70% silt; 25-40% clay)	13-35 kPa	0.67 kPa/hr	Little axial strain in early stage followed by rapid increase to 1.5-6% per hour (ε_f < 0.5%)	Dilative	Anderson and Riemer, 1995
		Clayey residual/colluvial soil (< 5% sand, 55-70% silt; 25-40% clay)	7-20 kPa	0.67 kPa/hr	Sudden strain rate 3-6%/hr	Dilative	Anderson and Sitar, 1995
Dead load triaxial test (DL) / stress-path tests	Hong Kong	Decomposed volcanics (18% gravel, 42% sand, 40% silt-clay)	60-100 kPa	2 kPa/hr	Little deformation before failure ε_f = 0.5-1%	Dilative Stiff and brittle	GEO, 1994a
	Mid-levels, Hong Kong	Colluvium, decomposed volcanic, decomposed granite	50-98 kPa 55-117 kPa 63-137 kPa	Not specified	ε_f = 0.3-2.5% 0.1-7.8% 0.4-2.8%	Dilative (75%, 83% and 100%)	GCO, 1982

2.4.2.3 Deformation behaviour during increasing pore water pressure

The analysis of deformation in stress path tests commonly involves general descriptions of the axial and volumetric strains, with particular emphasis on the failure conditions (Table 2.4). Typical deformation behaviour is shown in plots of axial strain against mean effective stress ($\varepsilon_a - p'$) and volumetric strain against mean effective stress ($\varepsilon_v - p'$) (Figure 2.9).

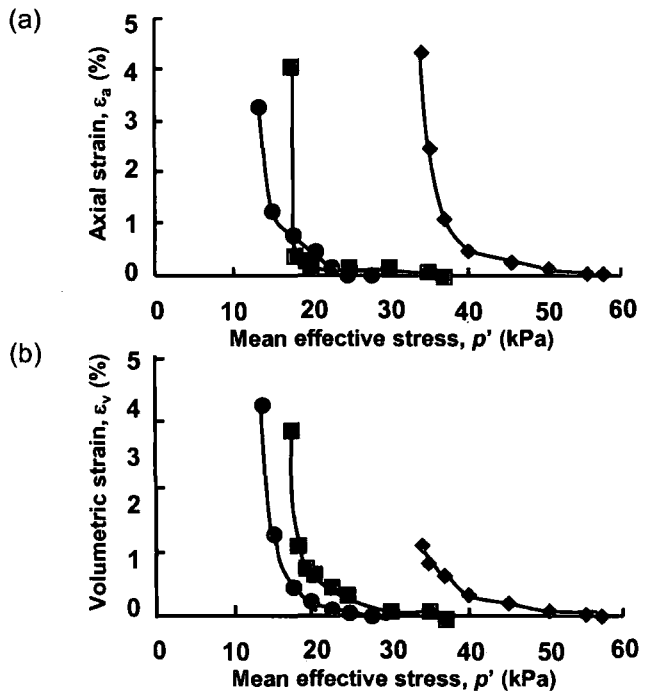

Figure 2.9 Typical deformation behaviour of simulation tests: (a) plots of $\varepsilon_a - p'$; (b) plots of $\varepsilon_v - p'$ (after Dai *et al.* 1999a)

Most studies have reported (1) little axial and volumetric deformation during initial pore water increase, but followed by (2) rapid and large increase in strains at failure. The transition, which is indicated by the sudden change of slope of strain, has been termed "yield" (Zhu and Anderson, 1998: 78). After yield is reached, the strain rate has been found to increase at 1.5 - 6% per hour (Anderson and Riemer, 1995; Anderson and Sitar, 1995). The strain at yield was found to be in the range of 0.1 and 7.8% (Table 2.4).

(a) Dilative behaviour

Dilative behaviour has been observed in almost all of the FSP experiments (Anderson and Riemer, 1995; Anderson and Sitar, 1995; Zhu and Anderson, 1998; Dai *et al.*, 1999a; Chen and Yang, 2000; Gabet and Mudd, 2006). The key mechanism of dilation involves the rearrangement of soil particles (Atkinson, 1993; Terzaghi *et al.*,

1996; Craig, 1997). Dilatancy is regarded as the most important characteristic in plastic deformation (Mitchell and Soga, 2005). The explanation has been grounded in Casagrande's (1936) critical state theory, which concludes that dense soils dilate and loose soils contract to reach the same critical void ratio during drained shear (Figure 2.10). Based on this widely accepted principle, it follows that dilatancy is associated with both shear and volumetric deformations (Wood, 1990; Atkinson, 1993; Mitchell and Soga, 2005).

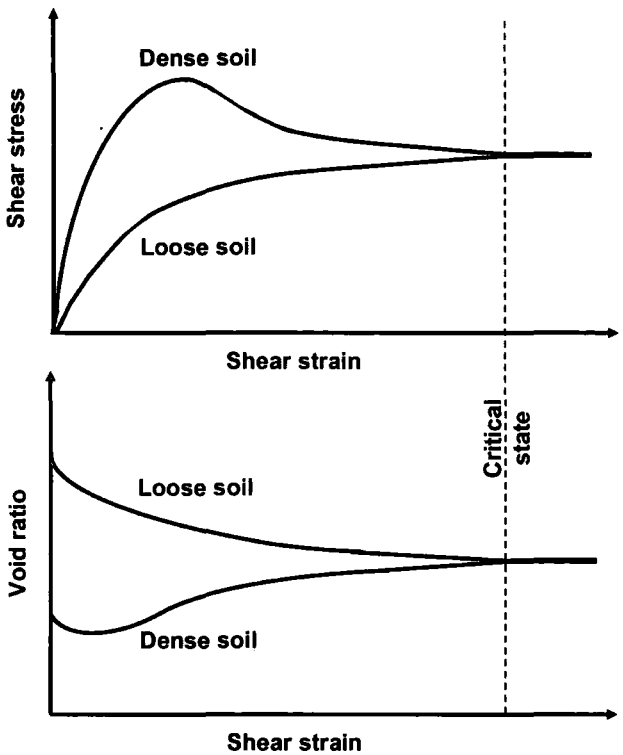

Figure 2.10 Dilative and compressive soil behaviour under drained shear, as revealed by the changes in void ratio within dense and loosely packed soils (after Atkinson, 1993)

The dilative soil behaviour has been further explained in relation to the inter-particle movements subjected to shear. These include (1) particle pushing and climbing (Crozier, 1986; Wood, 1990; Atkinson, 1993; Selby, 1993; Terzaghi *et al.*, 1996), (2) particle sliding (Wood, 1990) and (3) breaking of interparticle bonds, especially for overconsolidated clays (Terzaghi *et al.*, 1996). The push and climb movement, which is also been referred as "geometrical interference or interlocking" (Terzaghi *et al.*, 1996: 147), is the most commonly accepted explanation for dilation. The interlocked or densely packed of soil particles cause dilation because some particles have to push and ride over the adjacent grains to deform in the direction of shear (Wood, 1990)

(Figure 2.11a). The mechanical interlocking of particles also facilitates the sliding movement within the soil on inclined planes as illustrated by the saw blade model (Figure 2.11b) (Wood, 1990).

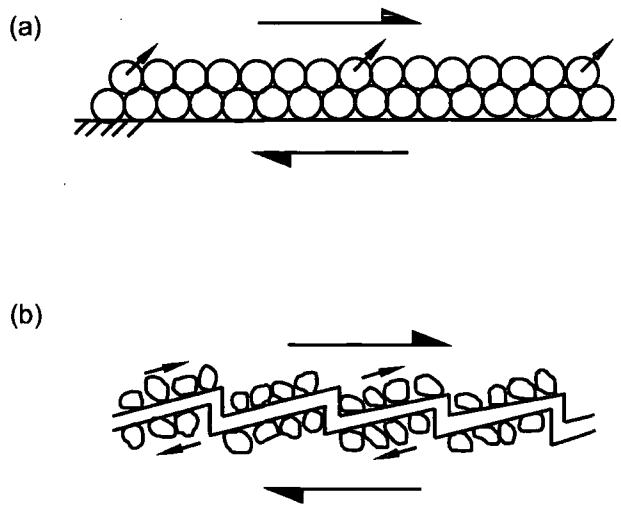

Figure 2.11 Interparticle movements in dense soils resulting in dilation during shear: (a) push and climb, (b) sliding movements (after Wood, 1990)

Interestingly, there has been no consensus on the fundamental explanation for the dilative soil behaviour observed in the FSP experiments, especially on undisturbed soils with initial high void ratio, when the classic critical state theory appears to be inapplicable. For example, Zhu and Anderson (1998) considered that dilation was very uncommon within undisturbed Hawaiian residual soil samples with a high void ratio. Difficulties have been reported in defining the steady-state (Anderson and Sitar, 1995). These might be due to the fact that the critical state theory was established from results of remoulded or reconstituted soils without taking into account the micro and macro structure of natural soils (Burland, 1990). Thus research has tended to concentrate more on the effect of dilation after failure, replicating for example liquefaction and the mobilization of debris flows (e.g. Dai *et al.*, 1999a; Gabet and Mudd, 2006), which is beyond the scope of this study.

Nevertheless, most of the FSP studies have directly attributed the cause of the volume increase to the increase of pore water pressure (or reduction of the mean effective stress), which loosens the interparticle contacts (e.g. Anderson and Riemer, 1995; Dai *et al.*, 1999a; Chen and Yang, 2000). This explanation, however, does not taken into account shear deformation. Very few experimental studies have considered the contribution of interparticle movements. One key exception is Gabet and Mudd

(2006), which noted that dilation is associated with particles overriding each other. Recent research on the microstructure of a slip zone within a landslide further confirms that dilation is one of the deformation processes (Wen and Aydin, 2004).

(b) Axial strain development

Petley *et al.* (2005b) analysed the development of axial strain during PPR tests on landslide materials from temperate environments. Two distinctive patterns of movements in $\Lambda - t$ space (where Λ is inverse velocity and t is time), the "linear" and "asymptotic" trends, have been identified (Figure 2.12). The linear $\Lambda - t$ behaviour shown by Gault clay was attributed to brittle deformation, while the asymptotic trend exhibited by disaggregated molasse material revealed ductile deformation (Petley *et al.*, 2005b). The former is the dominant mechanism for first-time landslides characterised by rapid, catastrophic movements; while the latter implies continual, creep-like plastic failure within ductile materials or landslide re-activation on an existing shear surface (Petley *et al.*, 2002). Most importantly, these findings have revealed for the first time the fundamental relationship between the rate and style of landslide movements and the underlying mechanisms.

Preliminary studies have been further undertaken on the relationship between the rate of pore water pressure and deformation in large, deep-seated landslides (Karintzis, 2005; Petley *et al.*, 2005b), but the results are not conclusive. Petley *et al.*, (2005b) found a negative relationship between the rates of pore pressure increase and the gradient of the line in $\Lambda - t$ space in both brittle (Gault clay) and ductile (highly fractured molasse deposits) (Figure 2.12). This may imply a change of failure mechanism (and hence different rates and styles of movements) under different rainfall conditions. In contrast, the relationship was not clear in Foxmould (glauconitic sandstone) from the Black Ven landslide, which was masked by the variability of sample densities (Karintzis, 2005).

These studies clearly demonstrate the need for more research to clarify the role of the rates of increasing pore pressure on landslide mechanisms that control the rate and style of landslide development.

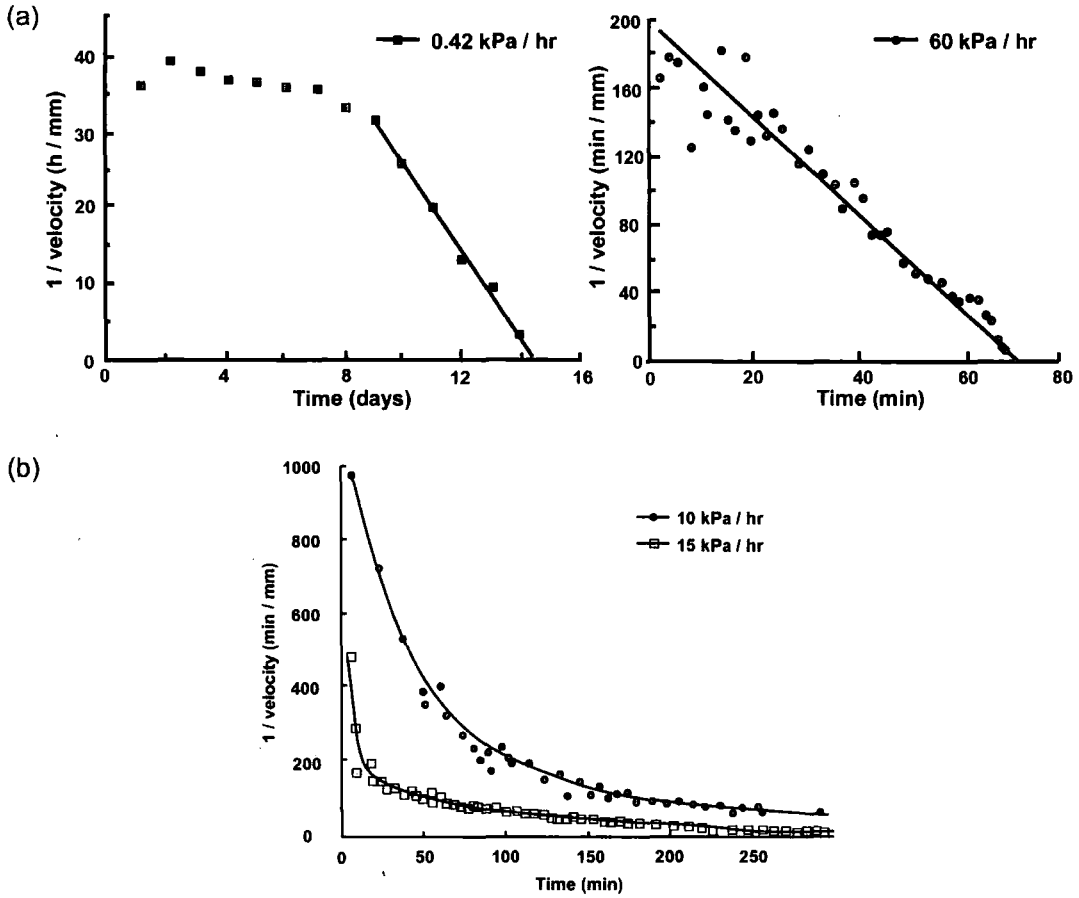

Figure 2.12 Relationship between increase rates of pore water pressure and gradient in $\Lambda - t$ space tested at mean effective stress 200-210 kPa at the start of the reinflation: (a) Gault clay; (b) Tessina mudslide matrix (after Petley *et al.*, 2005b)

2.4.2.4 Key issues

Analyses of laboratory data often emphasize the "dilative" or "contractive" behaviour of samples during pore pressure increases (GCO, 1982; GEO, 1994a; Anderson and Riemer, 1995; Anderson and Sitar, 1995; Zhu and Anderson, 1998; Dai *et al.*, 1999a). This may be attributed to the application of critical state theory, which predicts that loose samples will contract and dense samples dilate to the same void ratio and volume during shear (Atkinson and Bransby, 1978). However, the results from the FSP/PPR tests suggest that most samples, if not all, show dilative behaviour regardless of the initial sample density. Therefore, the usual volumetric strain analyses appear inadequate in the interpretation of the actual material behaviour.

In particular, the processes controlling the development of axial strain during the initiation of failure have not been fully analysed. The utilisation of kinematic

parameters, such as velocity and acceleration, allow quantitative assessment of soil movement behaviour with emphasis on the rates and styles through time.

The most important issue is that there have been very few experimental studies focusing on how patterns of increasing pore water pressure affect soil behaviour. Most studies have applied just one rate, but at different mean effective stresses, and/or have limited testing to linear rates at similar effective stresses (Table 2.4). Moreover, the rate and style of increase in pore water pressure used in the experiments surprisingly have not been designed with reference to the field data. For most studies, the design of pore pressure changes appears to be arbitrary. The tests performed at constant linear pore pressure rates (Table 2.4) may have oversimplified the changing nature of pore water pressures in the field (section 2.4.1.2). Therefore, more advanced testing focussing on pore pressure variations, which represent different rainfall conditions, is essential and is particularly relevant to the understanding of the behaviour of shallow failures on tropical slopes (section 2.4.1.3).

2.5 Pre-failure movements of landslides and the mechanisms

This section focuses on the creep phenomenon as an early phase of landslide development. Two key models, the progressive failure model (Bjerrum, 1967) and the three creep phase model (Varnes, 1983), are explored. The movement patterns of landslides and the underlying physical mechanisms are examined.

2.5.1 The creep phenomenon

The creep phenomenon has been studied under different disciplines including geomorphology (e.g. Selby, 1993), engineering (e.g. Varnes, 1983), materials science (e.g. De la Cruz-Reyna and Reyes-Dávila, 2001), and rheology (e.g. Ranalli, 1995). A comprehensive classification of creep in landslides has been given by Hutchinson (1988: 3) namely: (1) "superficial, predominantly seasonal creep or mantle creep", (2) "deep-seated, continuous creep or mass creep", (3) "pre-failure creep or progressive creep", and (4) "post-failure creep". The main characteristics of each creep type are shown in Table 2.5. A further analysis of the literature on the study of creep movements in landslides demonstrates that the term "creep", unsurprisingly, has multiple meanings (Table 2.5).

In this research, the complimentary definitions based on engineering (type II) and material science (type III) are the most relevant. They have the common fact that

they both consider deformation below maximum shear stress/strength. The key distinction between these two creep types is that the former emphases the time-dependent dimension of the deformation, while the latter involves the dynamic nature of pre-failure movement, highlighting the changing stress distribution within materials. For this study, creep can be defined as the deformation of slope materials under constant shear stress towards failure.

Table 2.5 Definitions of creep (modified after Hutchinson, 1988)

Type	Key approach	Type of creep described	Key characteristics	References
I	Geomorphology	Superficial, predominantly seasonal creep; mantle creep	Confined to surface layer (less than 1 m deep); involves changes of volume due to changes in water content and temperature	Terzaghi (1953); Carson and Kirkby (1972); Selby (1993)
II	Engineering	Deep-seated, continuous creep; mass creep	Occurs at constant stress below the maximum strength of the material	Terzaghi (1953); Varnes (1978, 1983); Selby (1993); Fell *et al.* (2000)
III	Materials science	Pre-failure creep; progressive creep	Accelerating displacements towards shear failure; involves progressive development of shear structures from imperfect shear zones to continuous displacement shears	Terzaghi (1950); Bjerrum (1967); Ter-Stipanian (1980); De la Cruz-Reyna and Reyes-Dávila (2001)
IV	Rheology	Post-failure creep	Involves small renewals of failure on a pre-existing slip surface	Van-Asch (1984); Ranalli (1995)

2.5.2 Progressive failure model

The precursory movements of landslides were first conceptualised as a creep phenomenon by Terzaghi (1950), who described progressive deformation and thus downslope movements in the shear zone. This can be expressed using the displacement-time curve (OA in Figure 2.13). Terzaghi (1950) illustrated the process of creep as a gradual decrease in the factor of safety (i.e. the ratio of shear strength to shear stress) through time. Shear failure occurs (AB) when the shear resistance decreases until the factor of safety reaches unity, characterized by an increasing strain rate.

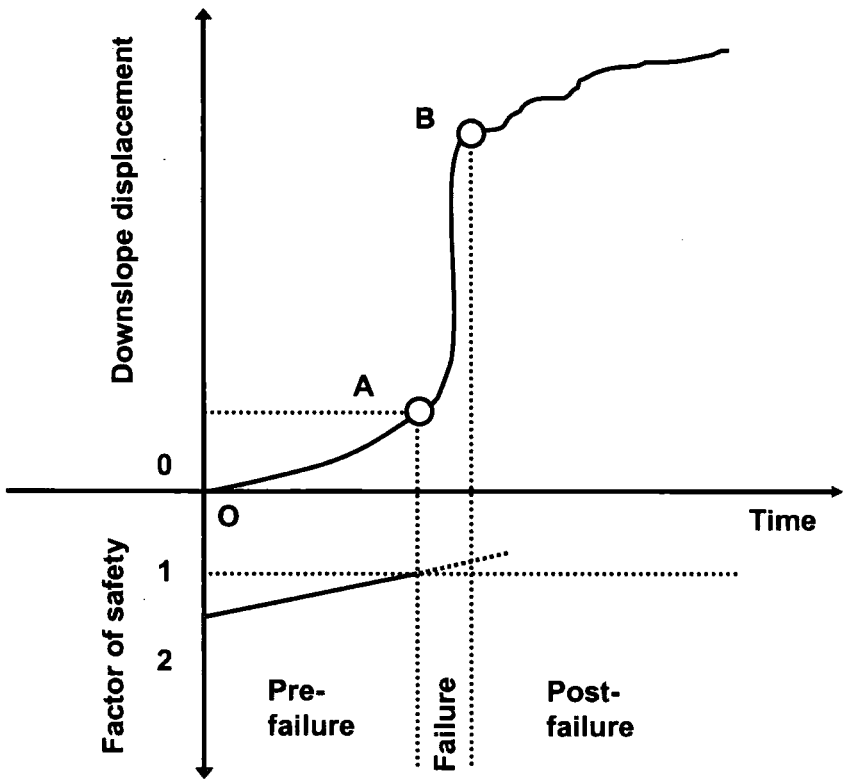

Figure 2.13 Pre-failure movements of a landslide through time (modified after Terzaghi, 1950)

However, the process of progressive failure in landslides was not explained until Bjerrum (1967), who observed a transition between the peak and residual strengths of cohesive materials within the shear zone before the landslide occurred. The mechanism of progressive failure was proposed in association with the development of a continuous shear surface (Bjerrum, 1967). The key condition was the presence of the "recoverable strain energy" in the shearing materials (Bjerrum, 1967: 44). The formation of the shear surface, accordingly, required the deformation of heavily overconsolidated (bonded) materials which liberated elastic strain energy by expansion under loading. The growth of the shear surface was facilitated by stress concentrations in the front of an advancing sliding surface as a result of the progressive decrease of shear strength from the peak to the residual value (Bjerrum, 1967).

This model might also imply that progressive failure within non-cohesive or normally consolidated materials, or in heavily weathered soils, may not develop into a slide. Instead, it will experience steady, slow creep, as most of the stored elastic strain energy has already been released, and shear stresses are equal to the residual shear strength within the failure zone (Bjerrum, 1967).

Nevertheless, only limited research has been done to test the validity of these concepts on the actual mechanisms of shear plane development, and hence the development of progressive failure (Petley *et al.* 2005b).

2.5.3 Three phase creep model

The pre-failure creep deformation of materials under constant stress conditions has been shown to undergo three different phases of movement (Varnes, 1983). The three phases are referred as primary (transient), secondary (steady-state) and tertiary (accelerating) creep, which are characterised by decreasing, constant and increasing strain rates respectively (Figure 2.14).

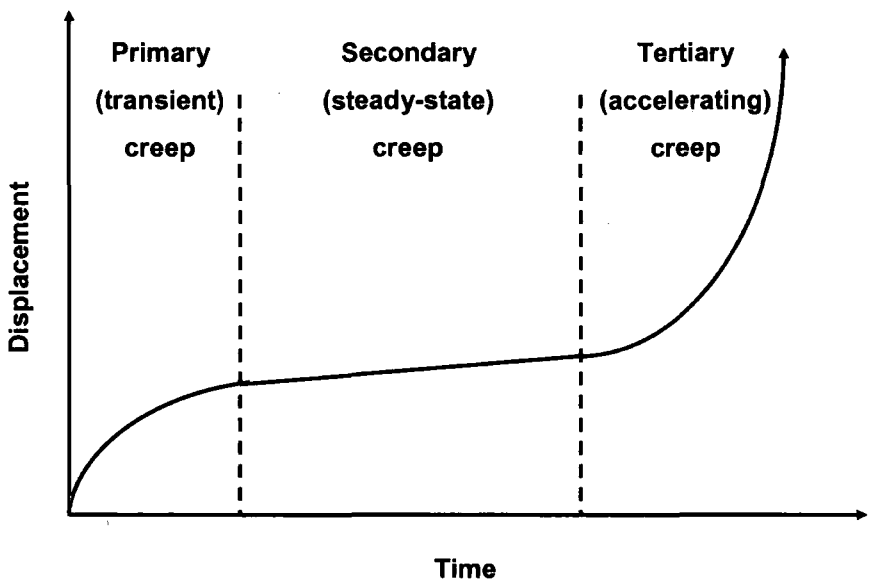

Figure 2.14 Creep deformation expressed in primary, secondary and tertiary phases under constant stress (after Varnes, 1983)

The three phase creep model has been explained by Main (2000) in the light of damage mechanics and non-linear constitutive equations for time-dependent subcritical crack growth. According to Main's (2000) hybrid model, the primary creep represents the early stages of damage, dominated by the local hardening mechanism at the tip of the crack. Crack growth at this stage is stable and decelerating as a result of stress relaxation and dilatancy hardening on the grain scale. Tertiary creep, by contrast, dominates the later stages of damage with local softening feedback mechanisms. It shows macroscopic brittle behaviour. Crack growth is unstable and accelerating, leading to ultimate failure by progressive localisation of deformation onto a single plane.

Secondary creep can be explained by the linear superposition of the local hardening and softening processes with a power law rheology (Main, 2000). This supports Varnes' (1983) observation in which the period of secondary creep may be the result of the primary and tertiary creep processes (Fell *et al.*, 2000).

The accelerating creep behaviour for slope failures was characterised mathematically by Saito (1969) who first observed an inversely proportional relationship between the reciprocal of strain rate and the rupture time:

$$\dot{\varepsilon}\,(t_f - t) = a$$

(Eq. 2.5)

where $\dot{\varepsilon}$ is strain rate, $(t_f - t)$ is time remaining to failure and a is a constant. This implies a linear relationship between the logarithm of the time to failure and logarithm of acceleration (Federico *et al.*, 2004). This derived relation was modified from load-controlled triaxial compression experiments of secondary creep (Saito and Uezawa, 1961; Saito, 1965).

However, the approach was not widely applied until Fukozono (1985), who put forward a simple method using the reciprocal of mean velocity to predict the failure time, based on large-scale slope failure experiments. This differed from Saito (1969) in that the logarithm of acceleration was considered proportional to the logarithm of velocity of surface displacement towards failure, expressed by:

$$\frac{d^2x}{dt^2} = A\left(\frac{dx}{dt}\right)^{\alpha}$$

(Eq. 2.6)

where x is surface displacement, t is time, A and α are empirical constants. (d^2x/dt^2) and (dx/dt) therefore represent acceleration and velocity respectively. This equation can also be written as:

$$(dx/dt)^{-1} = \left[A(\alpha - 1)\right]^{(\alpha-1)^{-1}} (t_{f_0} - t)^{(\alpha-1)^{-1}}$$

(Eq. 2.7)

where $(dx/dt)^{-1}$ is the reciprocal of velocity, and $(t_f - t)$ is the time remaining to failure. The equation can be expressed by different functions based on the constant α (Figure 2.15). The reciprocal of velocity is the exponential function of time at α = 1, and a power function of time when α is between 0 and 1 (Fukuzono, 1990). However, most of the reported slope movements were characterised by the generalised or the pure Saito form, for which α = 2 (Campanella and Vaid, 1974; Varnes, 1983; Fukozono, 1985), which implies a hyperbolic increase of strain rate during the tertiary creep (De la Cruz-Reyna and Reyes-Dávila, 2001). In this case, a linear relationship occurs between inverse velocity and time (Figure 2.15). The prediction of failure time is then estimated by extrapolating the creep curve to intercept the time abscissa (Fukuzono, 1985, 1996) (Figure 2.15).

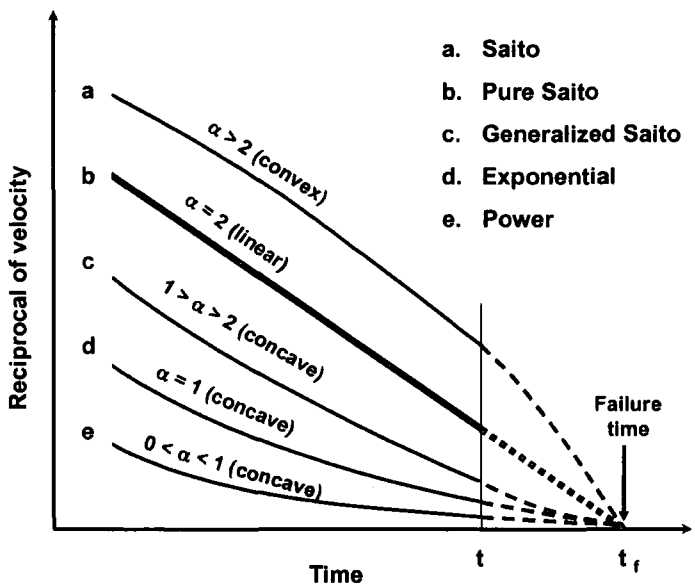

Figure 2.15 Relationships between reciprocal of velocity of surface displacement and time to failure in the tertiary creep phase (after Fukuzono, 1985, 1996)

The graphical method was regarded as a fundamental physical material science law by Voight (1988a, 1988b, 1989a, 1989b). Most importantly, the law appears to control both first-time and reactivated failure behaviour of various materials during the tertiary creep stage, under conditions of constant stress and temperature. Voight (1988a) integrated Eq 2.6 to put first emphasis on the influence of the rate of failure, $\dot{\Omega}$, on failure time:

$$\ddot{\Omega} = A\dot{\Omega}^{\alpha}$$

(Eq. 2.8)

where Ω is an measurable parameter of deformation such as strain or displacement of soil materials, $\dot{\Omega}$ and $\ddot{\Omega}$ are strain rate (velocity) and acceleration respectively, A and α are empirical constants.

Voight's proposal is similar to Fukuzono (1985) (Figure 2.15) and the reciprocal rate is expressed by:

$$\dot{\Omega}^{-1} = \left[A(1-\alpha)(t-t_0) + \dot{\Omega}_0^{\,1-\alpha} \right]^{(\alpha-1)^{-1}}$$

(Eq. 2.9)

The reciprocal rate decreases continuously with time showing a linear relationship for α = 2, a concave upward curve for α < 2 and a convex upward curve for α > 2. Voight (1989b) further noted that slope failures generally gave α = 1 to 3, and α = 1.9 to 2.1 for various soils.

While the above empirical equations have been successful in estimating the failure time of most geological phenomena (e.g. Voight, 1988a; Main, 1999), the key criticism has been the lack of physical basis concerning the nature and shape of the creep curves (Fell *et al.*, 2000; Hutchinson, 2001; Federico *et al.*, 2002, 2004). The reason why most materials fail at α = 2 is poorly understood (Voight, 1988b). More specifically, regarding landslides, the approach has not yet explained how landslides develop in the light of soil mechanics (Federico *et al.*, 2002). In particular, the mechanisms involved in tertiary creep behaviour have not yet been interpreted (Fell *et al.*, 2000).

It should also be noted that the equations or the relationships were based on the results derived from conventional drained or undrained triaxial tests (e.g. Singh and Mitchell, 1968; Campanella and Vaid, 1974). Samples tested under increasing monotonic loads or constant strain rates, however, do not necessarily represent the actual stress conditions within a slope.

In addition, this approach does not take into account the irregularities of pre-failure movements which have been noted in relation to the changing internal or external variables in real landslide systems (Hutchinson, 2001) such as intermittent

rainfall which could decrease the strength of soil rapidly (Voight, 1989a). As Fell *et al.* (2000) point out, creep behaviour can be induced by changes in pore pressure or slope softening by seepage in addition to shearing of materials itself. For example, saturated soft sensitive clays are most likely to lose strength during creep due to increasing pore water pressure over time, whilst heavily overconsolidated clays are prone to creep rupture by softening in relation to moisture increase caused by dilation and swelling (Mitchell and Soga, 2005). As the climatic disturbances over time have not been considered by the mathematical descriptions (Saito, 1969; Fukuzono, 1985; Voight, 1988a), long-term prediction of landslide development cannot be made accurately (Qin *et al.*, 2002).

2.5.4 Landslide movement patterns

Progressive landslide development with the three phase creep has been shown through field monitoring worldwide. A notable example of progressive failure is the Selborne cut slope failure in Hampshire, United Kingdom, occurring within Gault clay subjected to increasing pore pressures (Figure 2.16). Initial investigation suggested that the landslide initiated at the toe of the slope (inclinometer 9) and advanced upslope, as indicated by measurements of the movements (Cooper *et al.*, 1998) (Figure 2.16).

The displacement records within all parts of the slope (except inclinometer 4) clearly show the primary, secondary and tertiary creep phases before the final failure (Figure 2.16). The three creep phases have also been found in recent studies in the Jimingsi landslide in China (Qin *et al.*, 2006) (Figure 2.17) and the Roesgrenda landslide district in Norway (Okamoto *et al.*, 2004) (Figure 2.18). The former was explained by assuming a planar shearing surface with elastic-brittle (or strain hardening) and strain softening media (Qin *et al.*, 2006). The latter study reported an interesting observation that precipitation did not directly influence the final failure as no landslide occurred under the same mean precipitation in the study area (Okamoto *et al.*, 2004). For the Xintan landslide in China, which shows both the primary and the secondary creep phases (Figure 2.19), the Saito method was criticised as "ineffective" for precise prediction of catastrophic landslide movements and an additional parameter, surface vector angle, was proposed (He and Wang, 2006: 696).

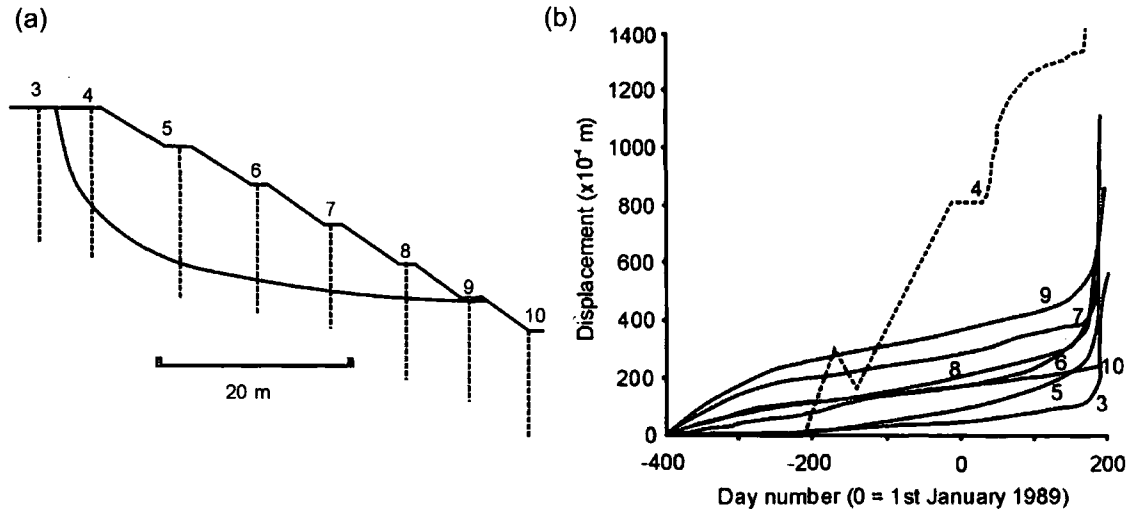

Figure 2.16 The Selborne landslide experiment in Gault clay: (a) location of inclinometers (3-10) across the cut slope; (b) displacement records revealed by the inclinometers (pore pressure increased on Day 0) (after Cooper *et al.* 1998; in Petley, 2004)

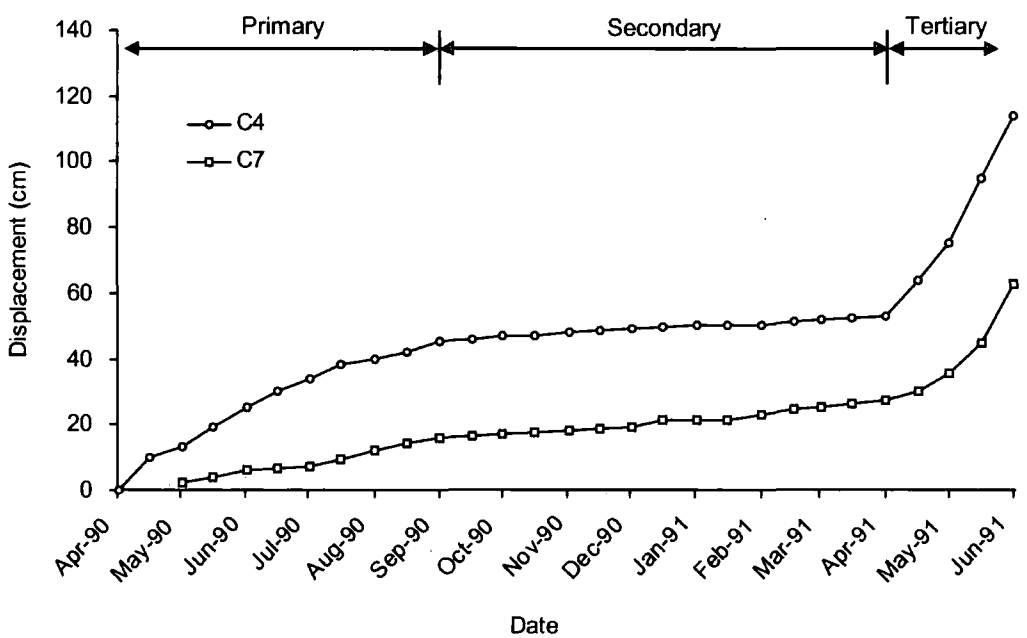

Figure 2.17 Displacement records at observations points C4 and C7 of the Jimingsi landslide in China, comprising hard limestone with soft and thin marlite intercalations (after Qin *et al.*, 2006)

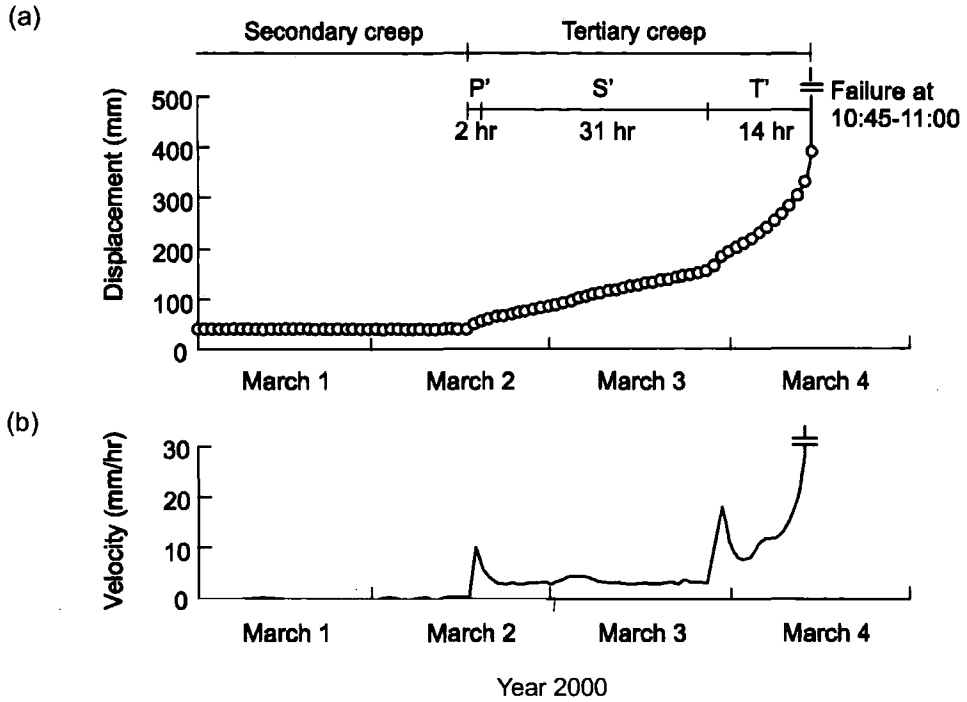

Figure 2.18 Short primary (P'), secondary (S') and tertiary (T') creep phases before the final failure of Slide-B, which is composed of river sediments, in Roesgrenda landslide district, Norway: (a) displacement –time; (b) velocity-time (after Okamoto *et al.*, 2004)

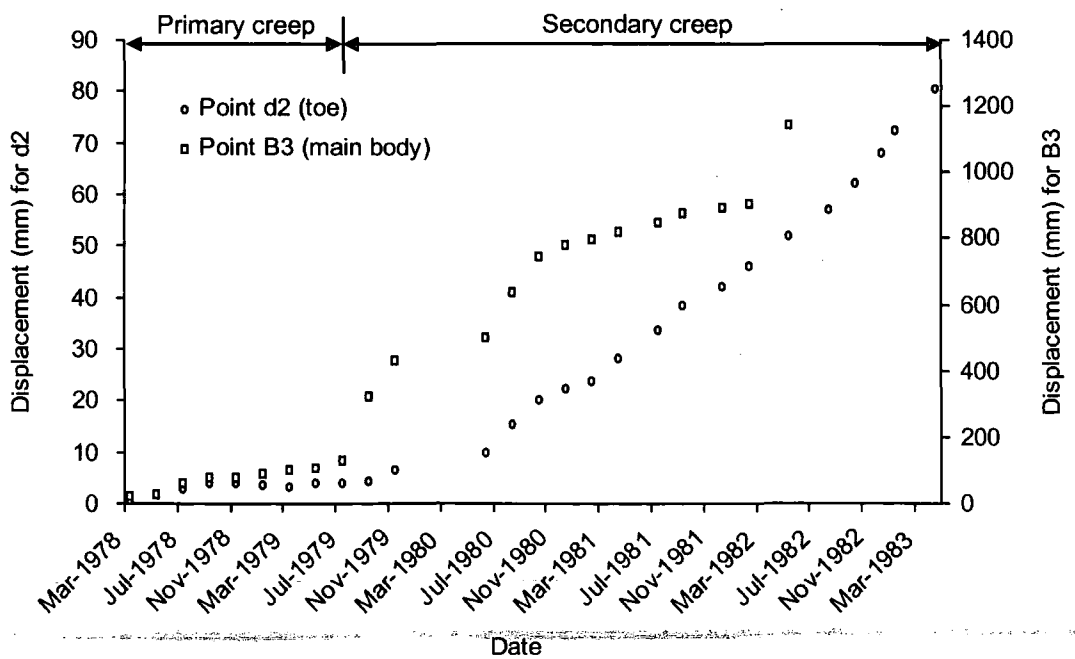

Figure 2.19 Primary and secondary creep phases in the colluvial Xintan landslide, China (after He and Wang, 2006)

Landslide movement patterns have also been classified into different types based on velocities and cumulative displacements related to seasonal fluctuations of pore water pressure (e.g. Bhandari, 1988; Allison and Brunsden, 1990; Petley *et al.*, 2005c). In general, four distinctive types have been recognised, namely "multiple stick-slip", "graded slip", "surge" and "random" movements (Allison and Brunsden, 1990) (Table 2.6).

Table 2.6 Patterns of mudslide movement in relation to pore water pressures, in the Wealden Beds of the Isle of Purbeck, Dorset (extracted from Allison and Brunsden, 1990)

Movement type	**Displacement characteristics**	**Related pore water pressures (PWP)**
Stick slip	Small individual spatial movements < 1 cm Total displacement up to 0.08 m	Slowly rising PWP
	Separated by varying time intervals with zero displacement	Slowly declining PWP
Graded slip	Larger gradual spatial movements over proportionally shorter time periods (maximum displacement record: 35 cm in 17 hrs)	Gradual rise in PWP Rapid rise followed by declining PWP
Surge	Large spatial displacement over short time periods (3 m in 20 mins)	Highest rate of increase in PWP
Random	Small, irregular slips through space and time	Related to other factors, such as internal deformation with the mudslide, effects of plasticity, seasonal cycles and gravitational forces

The characteristics of the former three patterns appear to be comparable with the classification proposed by Petley *et al.* (2005c): "Type II", "Type III" and "Type IV" movements respectively (cf. Tables 2.6, 2.7), schematically illustrated in Figure 2.20.

Both classifications suggest a model of which landslides develop through these patterns, that is, from "stick slip" to "graded" and then "surge" (Allison and Brunsden, 1990) or from Type I to Type IV (Petley *et al.*, 2005c). The transition behaviour has been mainly attributed to the changes in pore water pressure conditions within the landslide, showing seasonal variations (Allison and Brunsden, 1990; Petley *et al.*, 2005c).

Table 2.7 Patterns of landslide movement in relation to pore water pressures, Tessina, Italy (extracted from Petley *et al.*, 2005c)

Movement type	Displacement characteristics	Related pore water pressures
Type I	Very slow movements at less than 1 mm/day; consist of slow creep	Increase in velocity associated with wetter winter months
Type II	Low velocity movements 2-3 mm/day Typical block movements; highly variable movement rate	Gradual rise in PWP Faster movements occur during months with high groundwater levels
Type III	Movement rates at 10 mm/day; creep occurs at similar, continuous rates	Relatively small seasonal fluctuations
Type IV	Episodic, very rapid movements Movements initiated rapidly and terminates abruptly, but static in between movement events Peak rates more than 1-2 m/day	

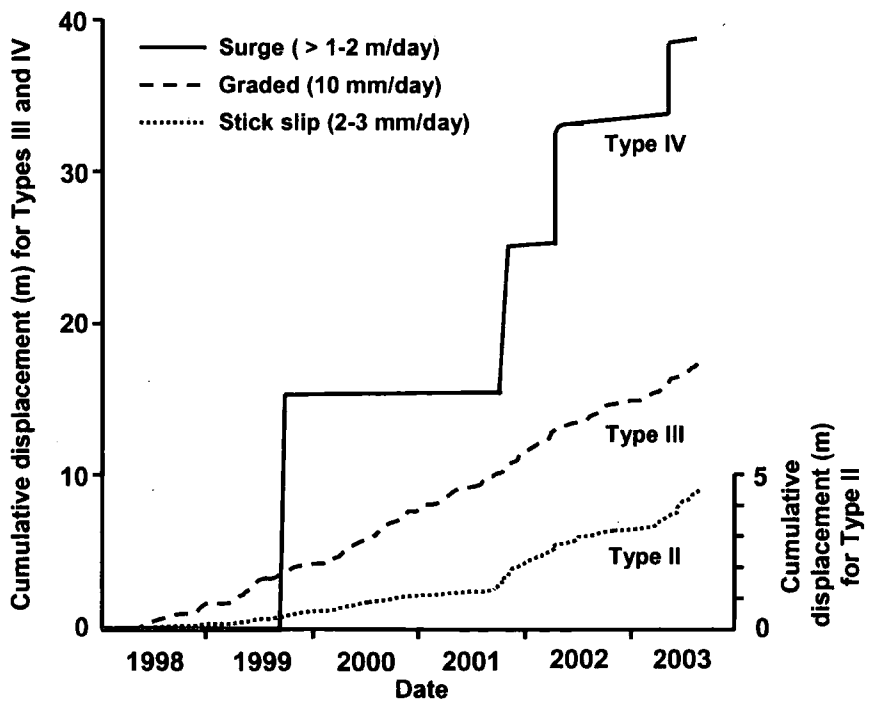

Figure 2.20 Schematic representation of the movement types in Tessina landslide, Italy (modified from Petley *et al.*, 2005c)

Significant progress on the understanding of accelerating landslide movements was made by Petley *et al.* (2002) who identified the basal deformation mechanisms for both linear and non-linear landslide accelerating movement patterns revealed by the inverse velocity (Λ) against time (t) plots (section 2.5.3). They proposed that a linear trend in $\Lambda - t$ space is associated with crack growth undergoing rupture surface formation through brittle failure mechanisms, resulting in rapid, catastrophic movements, whereas the asymptotic trend implies ductile deformation processes or sliding on pre-existing shear surfaces (reactivations) exhibiting steady-state movements with rates increasing to a constant (Petley *et al.*, 2002, 2005b, 2005c; Kilburn and Petley, 2003; Petley, 2004; Petley and Petley, 2006) (Table 2.8).

The proposed mechanisms were further validated by post-failure investigations (Cooper *et al.*, 1998; Petley *et al.*, 2002) and revealed through PPR stress path testing (Petley *et al.*, 2005b). A slow microscopic cracking model has also been established mathematically in Kilburn and Petley (2003) to explain the precollapse accelerating slope movements relating to crack growth and nucleation, expressed as:

$$(dx/dt)^{-1} = (dx/dt)_0^{-1} - \psi(t - t_0) \qquad \text{(Eq. 2.10)}$$

where $(dx/dt)^{-1}$ is the reciprocal of the rates of downslope displacement, the subscript 0 represents conditions when crack growth first dominates crack nucleation, and ψ is an inverse length scale that depends on applied stress, rock properties and the length of the crack array (Kilburn and Petley, 2003).

Similar to Eq. 2.7 (Fukuzono, 1985) and Eq. 2.9 (Voight, 1988a), failure occurs at $(dx/dt)^{-1}$ = 0, as velocity becomes infinitely large. This model at least partially verifies previous proposals that a linear trend in $\Lambda - t$ space indicates crack growth. In addition, it also implies crack nucleation processes for the asymptotic trend in $\Lambda - t$ space (Kilburn and Petley, 2003). Their work has provided fundamental physical explanations for the previous empirically-based velocity-failure time relations for slope failures (e.g. Saito, 1969; Fukuzono, 1985; Voight, 1989a).

Table 2.8 Summary of the $\Lambda - t$ analyses and their implications on landslide behaviour (Extracted from Petley *et al.*, 2002; Kilburn and Petley, 2003)

Landslide movement styles/ patterns	**Type I**	**Type II**
Landslide acceleration behaviour in $\Lambda - t$ space	Linear trend 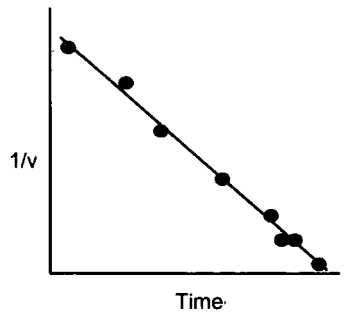	Exponential trend 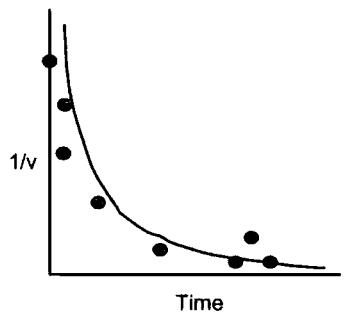
Deformation rate	Bulk movement accelerates linearly with time Hyperbolic growth	Bulk movement accelerates exponentially with time Increasing to a constant velocity value
Dominant basal deformation process	Crack propagation/growth New cracks join together (micro-cracking process) Development of discrete shear/rupture surface Shear surface generation Brittle failure mechanisms	Crack nucleation New cracks remain isolated Sliding on existing planes of weakness Reactivation of existing landslide systems Ductile deformation processes
Material behaviour	Brittle	Ductile/ plastic/ non-brittle
Stress-strain relationship	Commonly occurs in bonded or cemented materials at relatively low mean effective stresses	Shown by materials with little or no interparticle bonding at high mean effective stresses
Failure	First-time failure Catastrophic Sudden and rapid displacement	Landslide reactivation Not catastrophic / not intrinsically dangerous Continual, slow, creep-like movement

The $\Lambda - t$ space technique has successfully revealed the underlying mechanism in various landslide types and materials from a wide range of environments (Petley *et al.*, 2002) (Table 2.9) (Figure 2.21). It provides insights for the processes occurring within a basal region of a landslide, the underlying mechanism and possibly the effects of pore water pressure. For example, a detailed evaluation of the inclinometer data derived from the Selborne landslide using the $\Lambda - t$ technique further revealed that the development of the rupture surfaces initiated in the midslope (inclinometer 6, Figure 2.16a) (instead of the toe slope as suggested by Cooper *et al.*, 1998) and then propagated upslope and downslope leading to the final failure (Petley, 2004). The asymptotic $\Lambda - t$ trend within the Tessina landslide indicated its plastic nature and more importantly showed the close relationship between the different styles of movements and the changing pore pressure conditions (Petley *et al.*, 2005b, 2005c).

However, it is also noted that these findings are largely obtained from large-scale, deep-seated landslides in temperate environments. The applicability of the $\Lambda - t$ technique for small-scale, shallow landslides occurring on tropical weathered slopes is yet to be tested. It will be particularly valuable to investigate the inter-relationships between the highly variable pore pressures and the deformation of weathered materials (section 2.4.1).

Table 2.9 Examples of linear and asymptotic landslide movements in $\Lambda - t$ space

Landslide location	Material	Failure mechanism	Movement pattern in Λ - t	References
Black Ven landslide, UK	Foxmould	First-time	Linear / asymptotic (transitional)	Karintzis (2005)
Selborne, UK*	Gault clay	First-time progressive failure	Linear	Petley (2004); Petley *et al.* (2005b)
Vajont, Italy (1963)	Limestone and clay beds	First-time or reactivation (controversial)	Linear	Kilburn and Petley (2003)
Abbotsford, New Zealand*	Highly plastic, smectitic clay	Ductile deformation	Asymptotic	Salt (1985)
Giau Pass, Italy*	Glacial moraine	Sliding on pre-existing shear surface	Asymptotic	Angeli *et al.* (1989)
Kunimi, Japan*	Clay breccias	Reactivation	Asymptotic	Shuzui (2001)
Tessina, Italy*	Highly fractured molasse deposits	Reactivation	Asymptotic	Petley *et al.* (2005b)
Xintan, China	Colluvium	Unknown	Asymptotic	He and Wang (2006)

*Data reinterpreted in Petley *et al.* (2002)

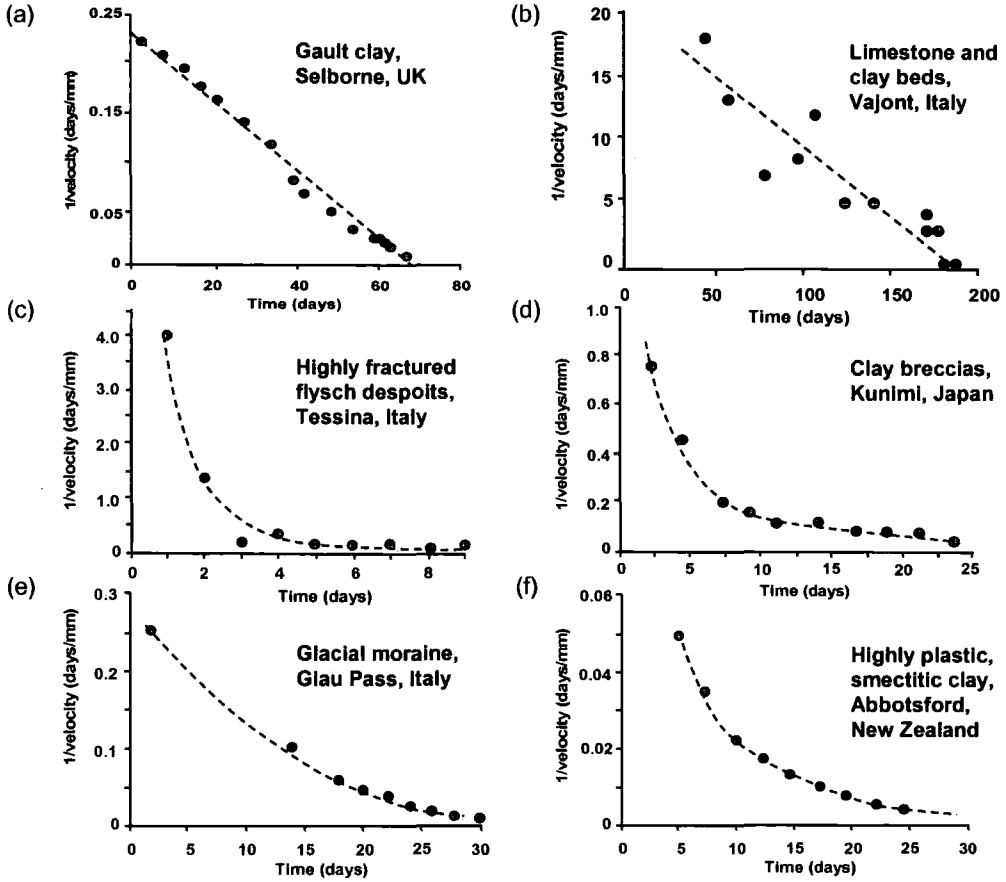

Figure 2.21 Deformation patterns of landslides in $\Lambda - t$ space: (a-b) linear trend (brittle failure); (c-f) asymptotic trend (ductile failure) (after Petley *et al.*, 2002; Petley and Petley, 2006)

2.5.5 The physical mechanisms for landslide development

Recent progress has been made in the understanding of the relationship between the rates and styles of pre-failure landslide movements and the underlying mechanisms. Physical theories are centred upon two themes relating to (1) progressive failure mechanism associated with the micro-cracking process grounded in damage mechanics (Petley *et al.*, 2005b), and (2) the slider-block model based on the state- and velocity-dependent frictional law (Helmstetter *et al.*, 2004; Brückl and Parotidis, 2005; Iverson, 2005).

2.5.5.1 Micro-cracking process

Early attempts in explaining the accelerating creep phase on a physical basis were reviewed in Varnes (1983), who suggested that tertiary creep was largely related to the progressive production and extension of microcracks. This appears consistent with Cornelius and Scott's (1993) damage accumulation theory, which implies crack

propagation as well as plasticity processes. The mechanisms involve void growth during creep fracture by stress corrosion, and void concentration or localization governed by power law lattice deformation. The accelerating strain is controlled by the stress increase due to the decreasing cross sectional area of crystalline solids within the deformed material (Cornelius and Scott, 1993). Picarelli (2000) similarly related the increasing strain rate to the propagation of a shear zone as a result of stress redistribution after a local soil failure.

However, the underlying mechanics for the development of progressive landslide failure in brittle materials had not been conceptualized until Petley *et al.* (2005b), who developed a new model which synthesised Bjerrum's (1967) observations of strain weakening (section 2.5.2), the damage mechanics theories (Main *et al.*, 1993) and the Saito analyses (Fukuzono, 1990) associated with the classic three phase creep behaviour (section 2.5.3).

The main idea was that the typical hyperbolic increase in strain rate in $\Lambda - t$ space exhibited by the three phase progressive creep indicated a fracturing mechanism for brittle failure in damage mechanics (Cornelius and Scott, 1993). This involved a stress-transfer process involving a progressive loss of cohesion (De La Cruz-Reyna and Reyes-Davila, 2001) and growth of micro-cracks (Petley *et al.*, 2005b). The model has explained the pre-failure development of a landslide in four stages, with reference to the factor of safety, the Saito linearity and shear plane development (Figure 2.22).

Interestingly, the model also noted the increasing irrelevance of pore pressures through the landslide development stages (Petley *et al.*, 2005b). In the first stage (Figure 2.22a), the variation of pore pressures triggers the growth of micro-cracks when a critical factor of safety (depending on slope morphology and materials) is reached (i.e. 1.x). The creep strains are small and the slope is largely stable without initiating shear surface development (Figure 2.22a). In the second stage (Figure 2.22b), the microcracks grow to a high density and start to interact and coalesce after reaching a critical strain leading to the formation of the shear surface within the shear zone. The factor of safety drops further as the strength of the material decreases from the peak to residual strength. Secondary creep prevails within the landslide mass, but can be stopped by decreasing pore pressure (Figure 2.22b). The third stage (Figure 2.22c) is dominated by the rapid growth of the shear surface facilitated by the hyperbolic increase in shear stress transferred to the unsheared materials within the shear zone due to their reduced surface area (Kilburn and Petley, 2003). The factor of safety drops

rapidly through time. The acceleration (tertiary creep) is indicated by the linear trend in $\Lambda - t$ space. However, changes in pore pressure have little influence in the rupture-surface development process which is primarily controlled by crack growth (Petley *et al.*, 2005b). The final failure (factor of safety equals unity) is marked by a fully-developed shear plane surface just before $\Lambda = 0$ (Figure 2.22d). The rate of movement depends on other processes such as smoothing and polishing of the shear surface (Petley *et al.*, 2005b).

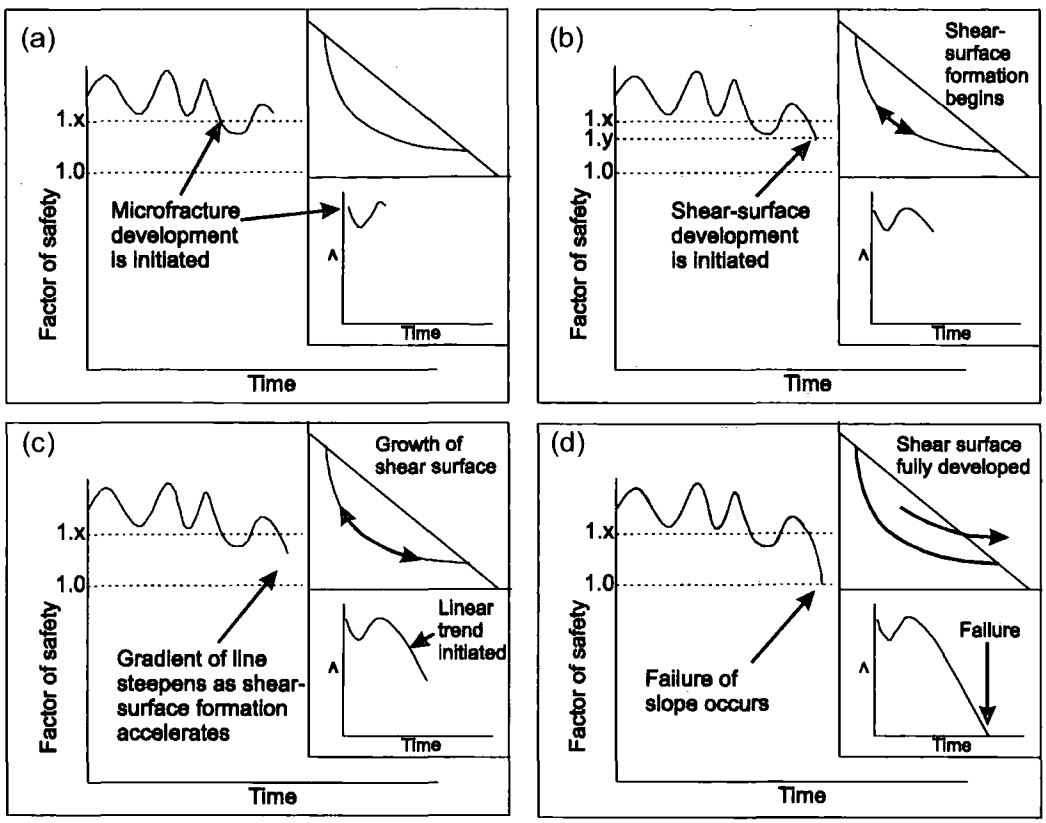

Figure 2.22 Development of progressive failure (a-d) in cohesive materials, illustrated by the factor of safety, shear surface formation and strains in $\Lambda - t$ space (after Petley *et al.*, 2005b)

This model provides new insights for the progressive development of rainfall-triggered landslides. It also effectively explains the non-responsive landslide behaviour to the changes in pore-pressure conditions based on damage mechanics (Petley *et al.*, 2005b). However, current explanations are largely limited to landslides in cohesive or brittle materials. Modifications of the micro-cracking model may be required to fully explain the evolution of landslides within non-cohesive or plastic materials without shear surface development.

2.5.5.2 Slider-block friction model

An alternative physical explanation for the accelerating creep phase for landslides, known as the "slider block friction model", was initially put forward by Helmstetter *et al.* (2004). This model assumed the landslide to be a rigid sliding block over a slope surface on which the motion was governed by the friction law under a constant gravity. It was based on the state- and velocity-dependent friction law established from laboratory experiments. The dynamic friction coefficient (as opposed to the constant Mohr-Coulomb friction coefficient) was used to replicate the yield-plastic behaviour of a brittle material (Helmstetter *et al.*, 2004).

The sliding block model exhibited four different regimes to explain landslide displacements, as a function of the state- and velocity-dependent friction law parameters, A, B, and of the initial frictional state of the sliding surfaces denoted as X_i (Helmstetter *et al.*, 2004). The B/A ratio, which is a material property, indicates that the sliding is either "always stable" ($0<B/A<1$) or "always unstable" (>1), while the initial state variable, X_i, reveals if the sliding velocity increases ($X_i>1$) or decreases ($X_i<1$) towards a constant value. The model produced good fit with the displacement records for the Vaiont and La Clapière landslides, suggesting that they were in the "unstable velocity weakening" and the "stable velocity-strengthening" sliding regimes respectively (Helmstetter *et al.*, 2004) (Table 2.10). The predictability of the model on the movements of the two landslides was further validated by Sornette *et al.* (2004), which concluded that the Vaiont landslide could be predicted 20 days before the failure, while the deceleration observed in the La Clapière landslide implied a stable condition.

This model, however, does not take into account the effects of pore pressure on landslide behaviour (Iverson, 2005). The application of the friction law for landslides in ductile materials without a sliding surface is also unknown (Helmstetter *et al.*, 2004).

Table 2.10 Landslide displacement regimes based on the slider-block model (after Helmstetter *et al.*, 2004)

Regime	Rate and state friction ratio, B/A	Initial frictional state, X_i	Sliding movements	Landslide example
I	>1	<1	Velocity weakening Unstable acceleration	Vaiont landslide
II	<1	>1	Velocity strengthening Stable (constant) acceleration	La Clapière
III	<1	<1	Deceleration	
IV	>1	>1	Deceleration	

More recent slider block models have considered the role of pore pressures in addition to the variable friction effects on landslide movements (e.g. Brückl and Parotidis, 2005; Iverson, 2005). In particular, Iverson (2005) asserted that the rates and styles of landslide motion were dependent on the effects of the pore pressure feedback, which was in turn regulated by the Coulomb friction through dilation or contraction within the saturated basal shear zones. Soil properties played an important role in the relationship between the pore pressure feedback and the landslide motion (Iverson, 2005). In summary, the model suggests that the contracting shear zone of sand-rich landslides during failure would lead to elevated pore pressure (positive feedback) which resulted in a rapid transition from slow, steady motion to a runaway acceleration. For clay-rich landslides, the dilation within the shear zone and the negative feedback of pore pressure would lead to slow, steady landslide movements which might ultimately stabilise the slope. However, the model fails to replicate the stick-slip movement pattern (Iverson, 2005).

Similarly, the rotational slider block model proposed by Brückl and Parotidis (2005) cannot explain stick-slip motion during the periods of high velocities. Most interestingly, this model suggests that the process and the velocity of deep-seated creep in rock slopes was controlled by both subcritical crack growth and progressive smoothing of the sliding surface (Brückl and Parotidis, 2005). Their model appears to be largely consistent with the micro-cracking model proposed by Petley *et al.* (2005b), as both of which have been built on the concept of crack growth in damage mechanics. However, the focus of the rotational slider block model was to understand the relationship between the smoothing of the sliding surface and the change in stresses due to rotation (Brückl and Parotidis, 2005). The key process for rapid failure was attributed to a progressive smoothing of the sliding surface which facilitated crack growth at all asperities as a result of stress concentrations. A proportional relationship between the velocity of the rock mass movements and the velocity of subcritical crack growth was found (Brückl and Parotidis, 2005). The smoothing process of the shear surface, according to Petley *et al.* (2005b), was more likely to develop at or after the final failure of progressive landslides.

The review of the physical mechanisms of landslide development has shown that the latest research has advanced understanding on the rate and styles of pre-failure creep in the light of damage mechanics and Coulomb friction. The main focus has been on the accelerating phase of progressive failure within brittle materials on a sliding surface. The mechanisms for landslide development on ductile materials without a sliding surface have not been investigated in detail.

2.6 Chapter summary

This chapter has reviewed the literature on the mechanisms of rainfall-triggered landslides, centred upon two themes: (1) landslide mechanisms in humid tropical environments, and (2) pre-failure movements of landslides.

The first theme of the literature review focused on identifying the unique characteristics of tropical slope environments including the nature of residual soils, the temporal and spatial variations of positive pore pressures, and the pre-failure slope movements. Previous experimental approaches simulating field conditions were evaluated in terms of their applicability and the main findings on the deformation behaviour.

The second theme reviewed the pre-failure movements of landslides and the underlying mechanisms. The creep phenomenon was defined. The associated progressive failure model (Bjerrum, 1967) and the three phase creep model (Varnes, 1983) were examined. Landslide movement patterns observed in a wide range of slope environments in relation to pore pressure changes through the $\Lambda - t$ space technique were analysed. Previous explanatory models of the physical mechanisms for landslide development, including the progressive failure model (Petley *et al.*, 2005b) and the slider-block friction model (Helmstetter *et al.*, 2004; Brückl and Parotidis, 2005; Iverson, 2005), were assessed.

The literature review has identified the following research gaps, which will be addressed in this research:

(1) In terms of the experimental design, very few studies simulate the actual field conditions using undisturbed samples collected from natural hillslopes, and taking into account the variability of rainfall-induced pore pressures by referencing the rate of change in pore pressure in the field. The understanding between changing rates of pore pressure and landslide movements remains poor.

(2) The strain data obtained from the laboratory simulation studies have been under-analysed, which could have revealed the underlying deformation mechanism through the Saito approach (Fukuzono, 1990).

(3) There is a lack of research and physical explanation on the processes and mechanisms of shallow landslide development in ductile materials or landslides without a sliding surface.

Chapter 3 Physical setting of Lantau Island, Hong Kong

3.1 Introduction

Lantau Island is chosen as the study area because it represents typical environmental conditions favourable for the occurrence of rainfall-induced shallow landslides in the humid tropics. Landslides occur in the steep, chemically weathered slopes under the hot and wet climate, and are often triggered by heavy and intense rainstorms. Previous studies have further identified the major governing factors for the natural landslides on the island including the relief and slope gradient; geology; climate; and vegetation (Wong *et al.*, 1998; Dai *et al.*, 1999a, 2001, 2004; Dai and Lee, 2002; Franks, 1999; Ng, 2001; Zhou *et al.*, 2002). This setting provides a context for the understanding of landslide mechanisms on tropical slopes. Moreover, the availability of the rainfall and pore water pressure monitoring data on largely undeveloped natural hillslopes with high landslide frequency and density (GOL, 2002; Evans and Lam, 2003) permits an investigation of the actual processes and mechanisms of rainfall-induced landslide initiation, achieving the research aim.

3.2 An overview of landslides on Lantau Island, Hong Kong

Hong Kong is located in the southeast part of China (22°N, 114°E), south of Guangdong Province (Figure 3.1). The total land area is 1104 km^2, comprising Hong Kong Island, Kowloon, the New Territories and 262 outlying Islands (HKSAR government, 2006) (Figure 3.1). Rainfall-induced landslides occur extensively on steep natural hillslopes.

A total number of 26,780 natural terrain landslides occurred in Hong Kong between 1945 and 1994, according to the Natural Terrain Landslide Inventory (NTLI) compiled by the Geotechnical Engineering Office (GEO) (Evans, 1998; Evans *et al.*, 1999) (Figure 3.2). The resulting average landslide density on natural hillslopes is approximately 38.5-39.5 per square kilometre (Evans *et al.*, 1999), or one each year for every 2 km^2 (Ng *et al.*, 2002). These landslides are generally triggered in weathered soils by rainstorms related to typhoons and low pressure troughs.

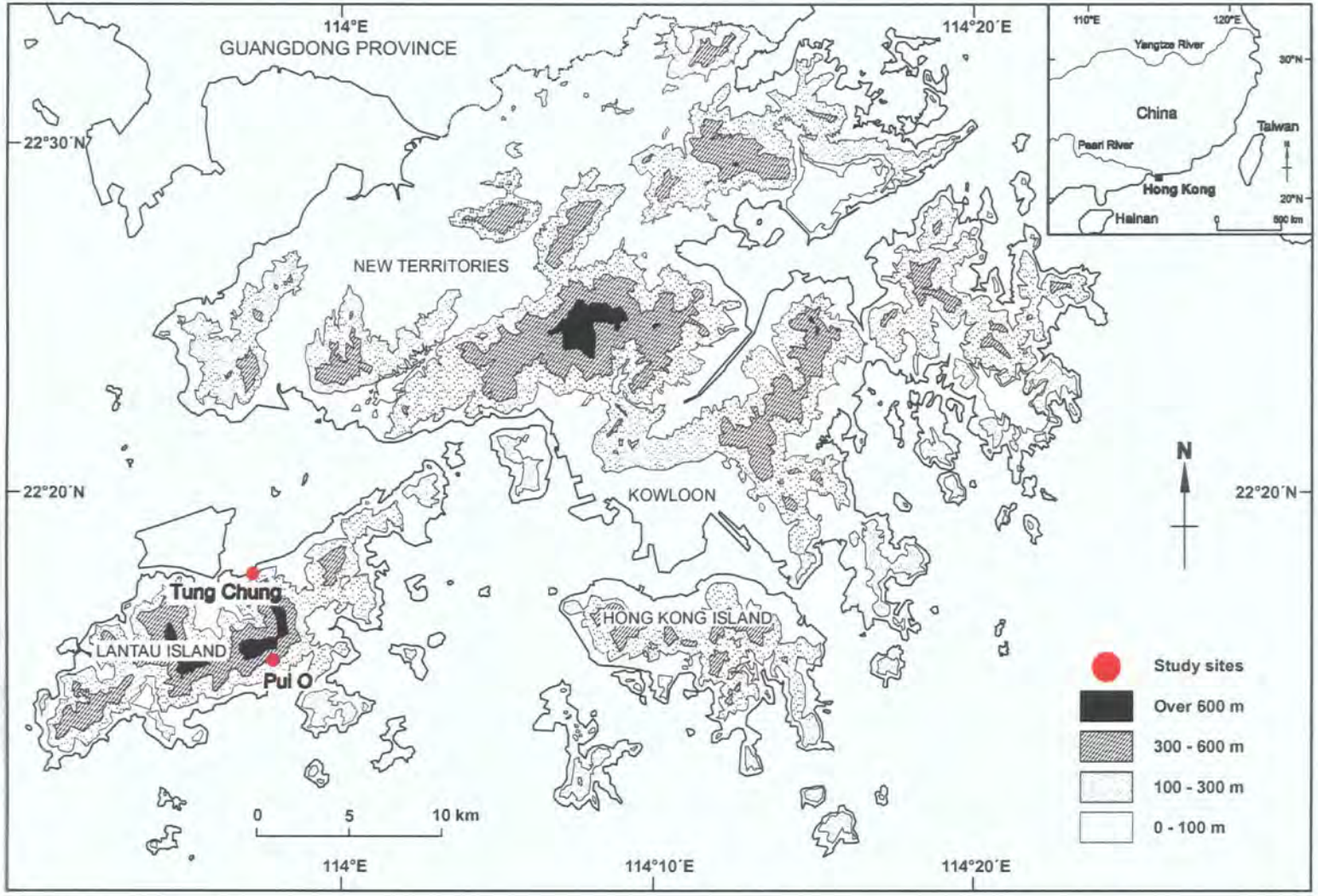

Figure 3.1. Location of the study sites on Lantau Island, Hong Kong

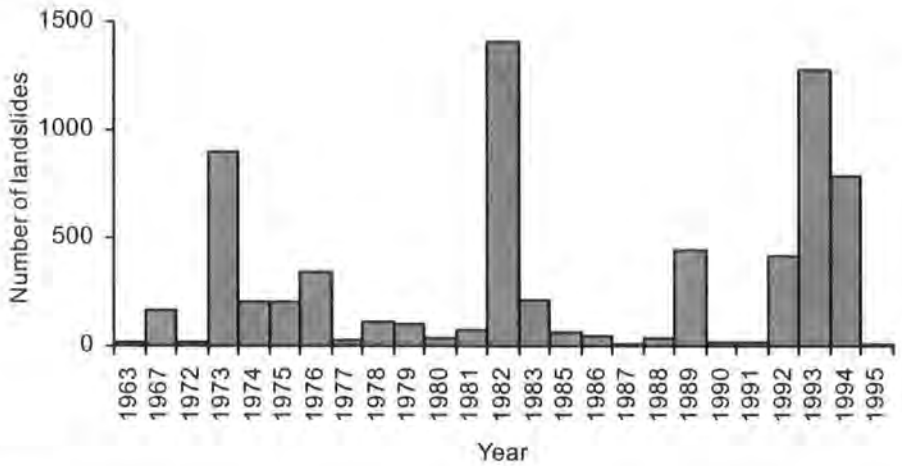

Figure 3.2 Landslide frequency recorded in the NTLI (after Evans, 1998). The exceptionally high number of landslides that occurred in the year 1945 (9094 landslides) and the year 1964 (10742 landslides) is not presented.

The largest island, Lantau, is situated in the southwestern part of Hong Kong with a total area of 146.5 km^2 (Figure 3.1), 78.4 km^2 (54%) of which is designated as country park. Most of the island is undeveloped and uninhabited because of the steep slopes. Landslides occur frequently on the hilly terrain (Wong *et al.*, 1997, 1998; Dai *et al.*, 1999a, 2001; Franks, 1999; Ng, 2001; Dai and Lee, 2002; Zhou *et al.*, 2002). The updated NTLI for the period 1999-2002 further demonstrates the high frequency and spatial clusters of recent landslide activities on the island (Figures 3.3, 3.4), for example, around Tung Chung and Pui O.

Most of the landslides on the island are shallow debris slides and flows (Wong *et al.*, 1997, 1998) of less than 3 metres deep (Franks and Woods, 1993; Wong *et al.*, 1998; Dai *et al.*, 1999a). The scar width is generally less than 20 m (Dai and Lee, 2002; Dai *et al.*, 2004). These characteristics are consistent with a detailed field study of 52 landslides undertaken in the Tung Chung area, with the majority having scar dimensions of less than 1.5 m depth, 5-30 m width and less than 400 m^3 in volume (Franks, 1999).

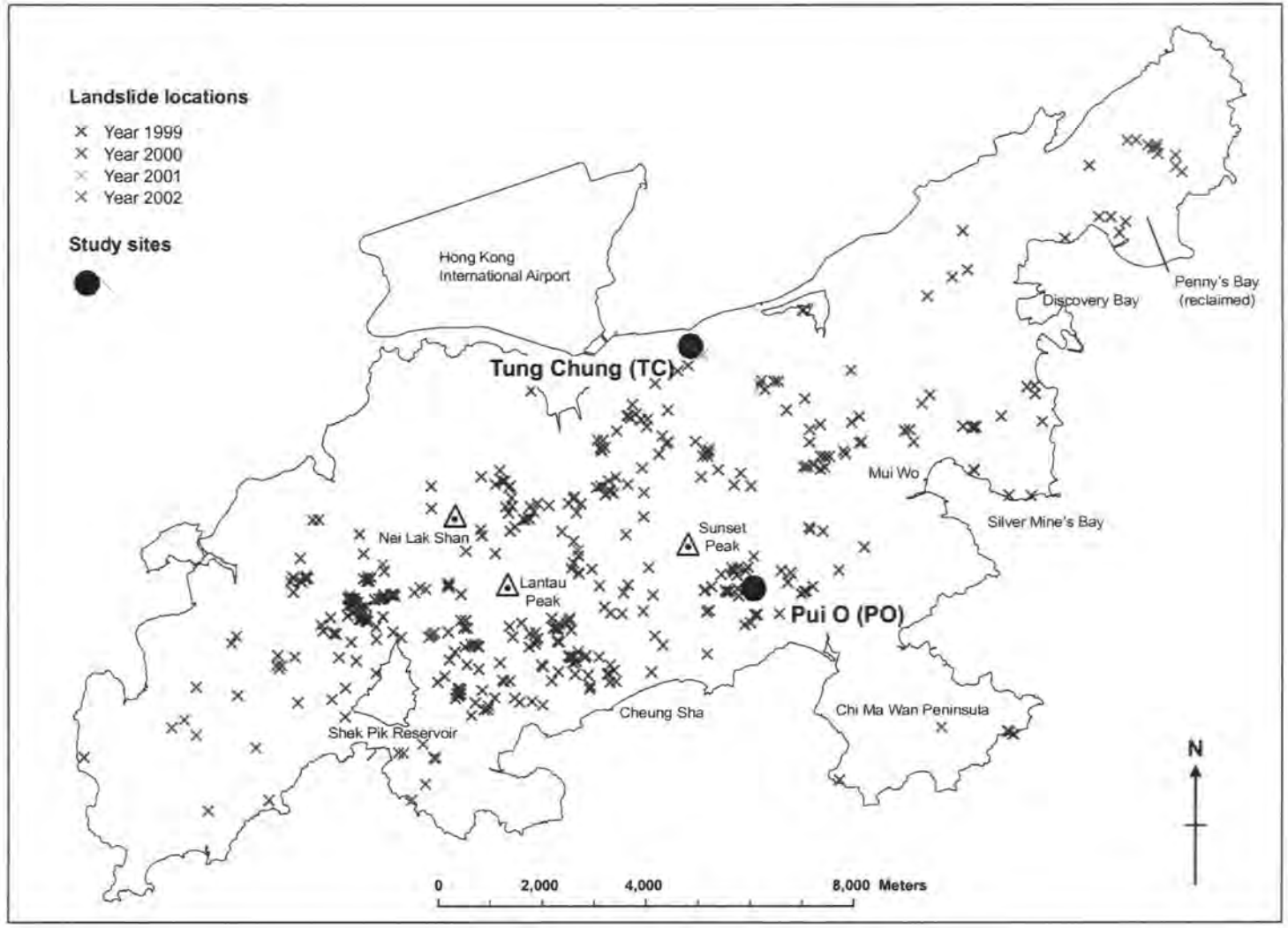

Figure 3.3 Distribution of landslides on Lantau Island for the period 1999-2002 (modified after GEO, 2004)

Figure 3.4 Shallow debris slides and flows are widespread on Lantau Island. The gentle slopes (foreground) are located on the northeast flanks of Lantau Peak. The steep hill in the background is Nei Lak Shan

3.3 Relief and slope gradient

The highest peaks, Lantau Peak and Sunset Peak, which reach 934 m and 869 m respectively (Figure 3.3), form the landscape of the island. Low and flatlands are restricted to areas along the coastline, housing clusters of urban development. The topographic relief is mainly controlled by the underlying rock types (Langford *et al.*, 1995). The more resistant volcanics form the higher and rugged relief with elongated, ridge-like crests while the more deeply eroded granites form the lower and more rounded terrains (Langford *et al.*, 1995). The island mainly consists of steep slopes, with more than 70% of the land being steeper than 15°, and over 20% steeper than 30° (Dai *et al.*, 1999a).

Most landslides occur at mid-elevations between 250-400 m (Dai and Lee, 2002) (Figure 3.5a). Moderately steep slopes with gradient of 30°-40° have the highest frequency and density of landslides (Wong *et al.*, 1998; Dai *et al.*, 1999a; Ng, 2001; Dai and Lee, 2002) (Figure 3.5b). Lower landslide density occurs at higher elevations which are composed of steeper slopes > 40° as the slope materials are the most

resistant to weathering. Few landslides are also found at the lower elevations as they comprise mainly gentle, flat areas (Langford *et al.*, 1995; Wong *et al.* 1999).

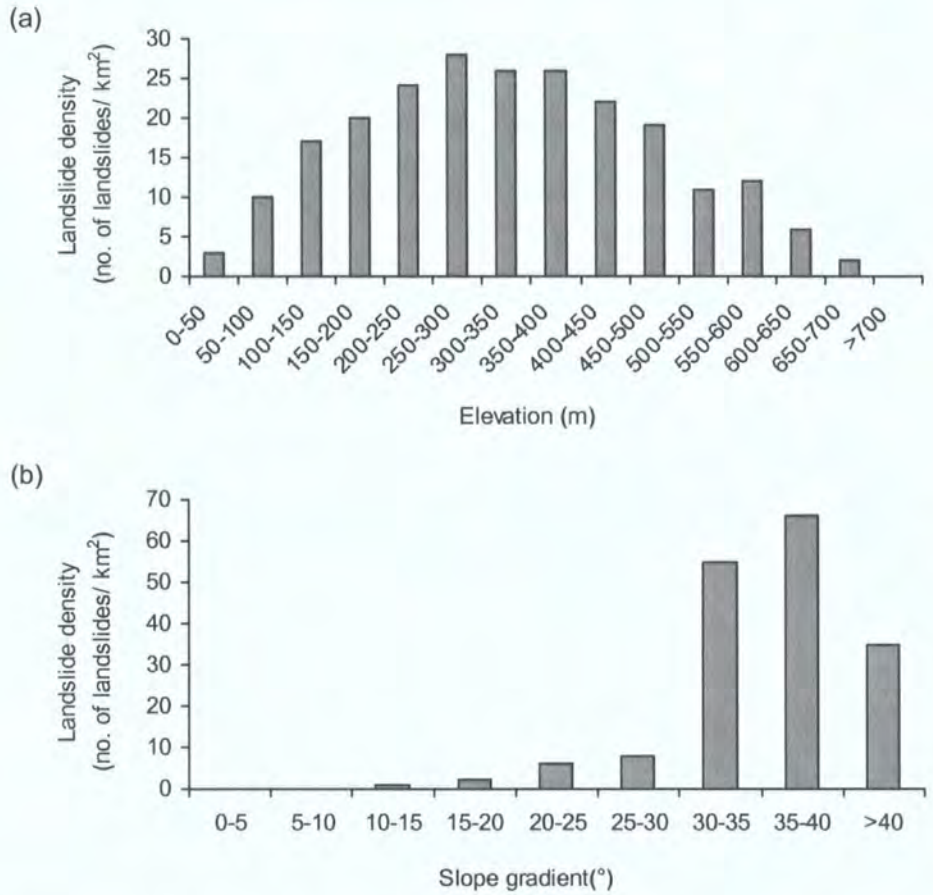

Figure 3.5 Landslide density (no. of landslides/km^2) on Lantau Island in relation to (a) elevation and (b) slope gradient (Dai and Lee, 2002)

3.4 Geology

Mesozoic volcanics and granite are the dominant rock types on Lantau Island, and are structurally affected by NE-SW and NW-SE faulting systems (Figure 3.6). Volcanic rocks are widespread over the central and western part of the island, and are composed of fine to coarse ash, tuffs and lavas. They also have the highest landslide frequency and density (Wong *et al.*, 1998; Ng, 2001). For example, the total number of landslides triggered by a rainstorm on 4 and 5 November 1993 on volcanic hillslopes was six times greater than on the granitic terrain (Wong *et al.*, 1998). Granite is exposed extensively on the eastern part of the island, and is characterised by its pinkish colour and porphyritic texture, with a medium to coarse grain size between 3-5 mm (Langford *et al.*, 1995; Hong Kong Geological Survey, 1999). Middle to Lower Jurassic sedimentary rocks, composed of thinly bedded siltstones, black silty shales and sandstones, are limited to the northwest coast (GCO, 1988b).

The sampling sites at Tung Chung (TC) and Pui O (PO) lie on the volcanics, which are classified as the Repulse Bay volcanic group of Late Jurassic-Early Cretaceous age (Langford *et al.*, 1995). The principal materials at the TC site are rhyolite lava and tuff while the PO site is mainly composed of crystal tuff (GCO, 1988b; GEO, 1994b).

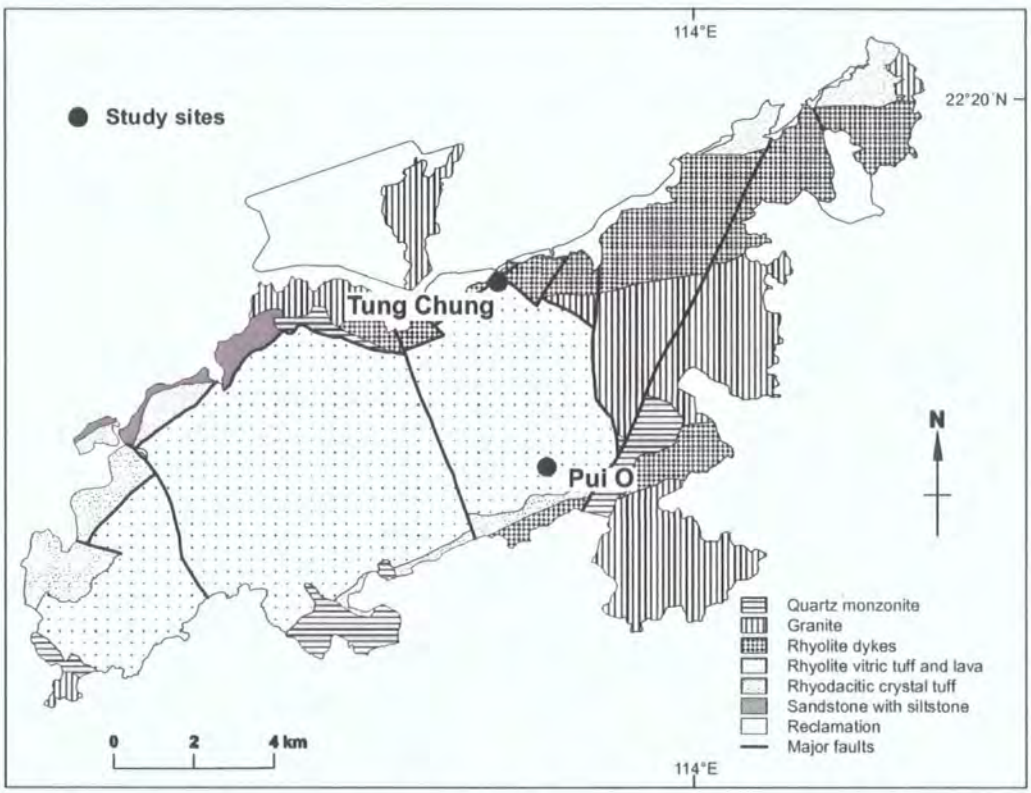

Figure 3.6 Major rock types of Lantau Island (Hong Kong Geological Survey, 1999)

However, it is more essential to note the nature of the soils derived from the bedrock which form the key materials of landslides on the island. In general, these materials include in-situ weathered rock (residual soils) developed from the Late Pliocene (Bennett, 1984) and the Quaternary superficial deposits (transported materials) such as colluvium, alluvium and beach deposits (GCO, 1988a, 1988b; Langford *et al.*, 1995). Previous studies on Lantau Island found that most landslides involved residual soils and colluvium of volcanic origin (Wong *et al.*, 1997, 1998; Dai *et al.*, 1999a; Franks, 1998, 1999) (Figure 3.7). Low incidence of slope instability has been reported on alluvium and beach deposits as they are generally associated with low slope angles (GCO, 1988a, 1988b).

Figure 3.7 A landslide that occurred in weathered volcanics overlain by a thin layer of colluvium, Ngong Ping, Lantau Island

The bedrock has been subjected to various degrees of intense weathering that form regolith of different thickness over most parts of the island (Langford *et al.*, 1995). The finer-grained and narrowly-jointed volcanic rocks are more resistant to weathering than the coarse-grained, widely-jointed granites. The average weathering depth of volcanics is between 10 and 20 m, but commonly two times deeper on granitic terrain due to their higher porosity and permeability (GCO, 1988a, 1988b). This is confirmed by recent studies at Tung Chung where the reported thickness of weathered volcanics is between 5 m and 10 m (Franks, 1998; 1999), and between 4 m and 25 m (Evans and Lam, 2003) respectively. The weathered materials comprise mainly quartz within a clay matrix (Langford *et al.*, 1995). Clayey silt and silty sand are the main products of the decomposed volcanics and granites respectively (Lumb, 1975; GCO, 1988a, 1988b). Laboratory tests on plasticity of the fines further showed that the silty volcanic saprolitic soils had an intermediate to high plasticity (liquid limit: 35-60%; plasticity index: 10-30%), while a slightly lower plasticity was found in the sandy granitic saprolites (liquid limit: 35-50%; plasticity index: 10-25%) (Franks and Woods, 1993).

Most importantly, a majority of landslides appear to occur within the in-situ soils. In a detailed regolith survey on Lantau, it was found that the summit region of Lantau Peak, which had a high landslide density of 60.5/km^2 recorded on the NTLI, was predominantly composed of saprolite (40%) and mixed saprolite/corestones (16%) derived

from volcanic tuff. Moreover, 85% of natural landslides were initiated in granitic saprolite in the Penny's Bay area with a landslide density of 11.2/km^2 (Sewell and Fletcher, 2000). The field survey further noted that many of these weathered areas were misinterpreted as colluvium on the 1:20000-scale (GEO, 1994b) and 1:5000-scale terrain classification and geological maps (GEO, 1996; Sewell and Fletcher, 2000).

Colluvium is the main type of superficial deposit commonly found in valley floors and footslopes (GCO, 1988a, 1988b). Instability of low-angle (< 15°) colluvial sideslopes near drainage lines appears to be related to the increase of pore water pressures during rainfall periods and a concentration of surface runoff (GCO, 1988a, 1988b). Colluvium is composed of mass movement deposits of Early Pleistocene to Holocene age, including creep debris, rock falls, debris slides and debris flows (Langford *et al.*, 1995). The Pleistocene slope deposits have a stiff, mottled, reddish-brown or white matrix with highly weathered clasts. The Holocene slope deposits are composed of softer, light yellowish-brown, sandy silt to gravelly silty sand with moderately weathered cobbles and boulders (Langford *et al.*, 1995). In general, the slope deposits are poorly-sorted and highly subangular in shape, and typically consist of cobbles and boulders in a matrix of gravely, sandy silt (Langford *et al.*, 1995). They are highly permeable and largely unconsolidated (GCO, 1988a, 1988b).

A detailed mapping of colluvium at the landslide-prone Tung Chung area has similar findings and further shows that the slope deposits are thin (less than 3 m thick), characterised by the mottled nature, a relatively high bulk density (1.7-2.3 Mg/m^3) and the presence of a patina up to 50 mm thick which is likely of Late Pleistocene age (Franks, 1998, 1999). The thick (> 20 m) and extensive accumulation of colluvial deposits are found along the major drainage networks below the steep volcanic slopes on the island (Langford *et al.* 1995; Franks and Woods, 1993; Franks, 1998). These observations suggest that mass movement processes have been active throughout the Quaternary period. Rockfall, however, played a limited role as talus deposits are rarely found, except near the Lantau Peak where small accumulations of large, angular boulders fell from the cliffs (Langford *et al.* 1995).

Alluvial deposits are generally limited to the flat, low-lying areas of larger valleys (e.g. Tung Chung, Mui Wo, Shek Pik) (Figure 3.3) with small patches on the hillsides due to the steep, rugged terrain of the island (Langford *et al.*, 1995). The deposits are grey to yellowish-brown in colour and generally semi-sorted to well-sorted downstream. The pre-dominant particle size of the alluvium depends on the parent rock, where volcanic rocks tend to derive clayey, clast-rich deposits, and granitic rocks produce

more sand-size material (Langford *et al.*, 1995). Upper Pleistocene alluvial deposits may also form fluvial terraces. An example can be found at Tung Chung Valley where the extensive Pleistocene alluvial terrace is about 400-500 m wide and 2000 m long, reaching an elevation of about 20 m. The Holocene alluvium is more low-lying (about 10 m), and is confined to the recent stream networks that are incised up to 7 m into the Pleistocene terraces (Langford *et al.*, 1995).

Beach deposits, composed of mainly uniform medium to fine-grained sand, are confined to the sheltered inlets and bays along the Lantau coastline (GCO, 1988a, 1988b; Langford *et al.*, 1995). They form many long, narrow sandy beaches especially along the south coast of the island, such as Cheung Sha, Pui O, Discovery Bay and Silver Mine Bay (Figure 3.3). Cheung Sha is the longest sandy beach in Hong Kong which extends for almost 3 kilometres, comprising clean, pale yellow sand up to 50 metres wide (Langford *et al.*, 1995). The headlands prevent the sediments from being transported or eroded away by incoming waves or currents from the South China Sea. However, the size and width of beaches are not large because of the limited supply of local sediments from rock weathering and erosion due to the small scale of the surface drainage systems on the island. Marine sediments such as shell fragments can be found at more exposed coasts which are composed of pebbles, cobbles and boulder-sized deposits (Langford *et al.*, 1995).

3.5 Climate

The climate is sub-tropical and monsoonal, characterised by hot, wet summers, and cool, dry winters. These can be illustrated by the annual distribution of rainfall and temperatures during the time period between 1971 and 2000 (Figure 3.8). The mean annual rainfall was 2281 mm and the average monthly temperature was 23.1°C. However, most of the rainfall and the highest temperatures were unevenly distributed throughout the year, with the monthly mean rainfall ranging from 24.9 mm (in January) to 444.6 mm (in August) and the monthly mean temperatures between 16.1°C (in January) and 28.7°C (in July) (HKO, 2003).

The rainfall amount and temperatures are slightly lower and highly seasonal comparing with other humid equatorial areas (Figure 3.9, Table 3.1). The seasonality is mainly driven by the monsoon system associated with the summer heating and winter cooling of the Asia mainland. The temperature contrast between the land and sea gives rise to the cold, dry, north to northeasterly winds from mainland China, and the warm, moist, southerly or southwesterly winds from the Pacific (Chin, 1986, Fyfe *et al.*, 2000).

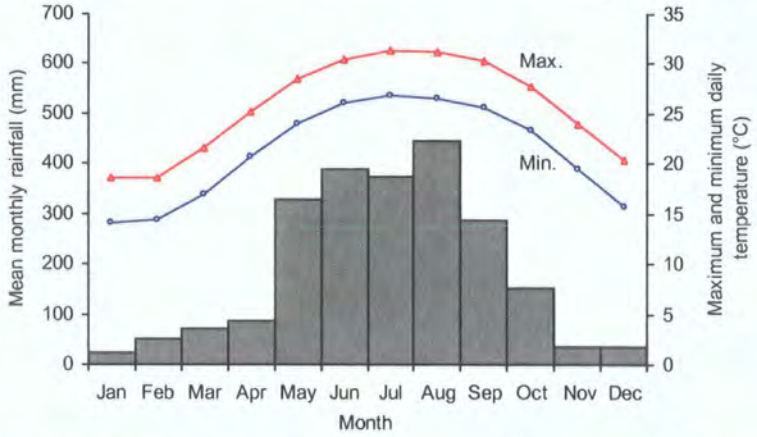

Figure 3.8 Mean monthly rainfall and the maximum and minimum daily temperature of Hong Kong, 1971-2000 (HKO, 2003)

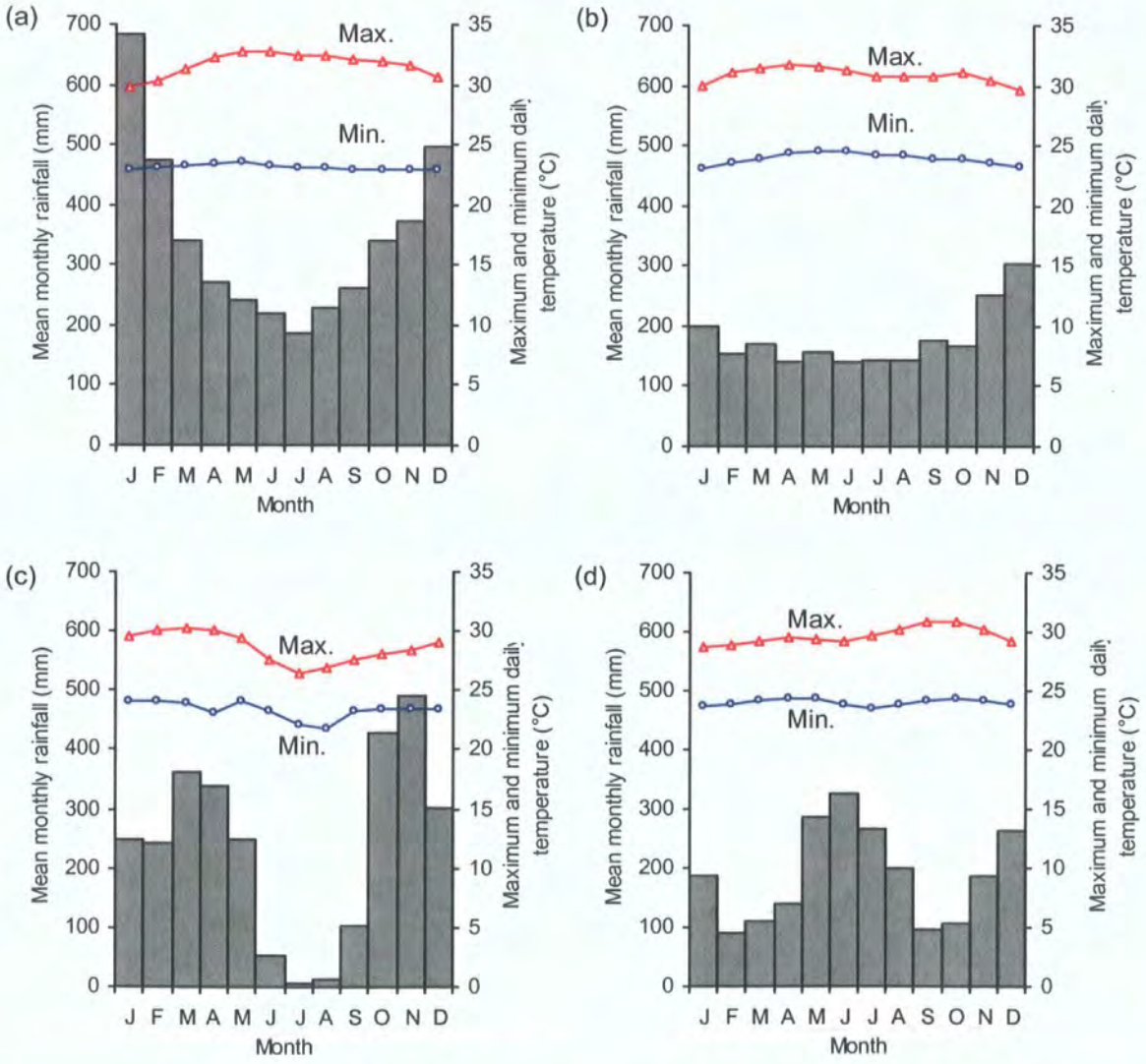

Figure 3.9 Mean monthly rainfall and the maximum and minimum daily temperature in humid equatorial regions: (a) Kuching, Malaysia; (b) Singapore; (c) Libreville, Gabon; (d) Georgetown, Guyana (after NMHSs, 2007)

Table 3.1 Rainfall and temperature characteristics of Hong Kong in comparison with humid equatorial regions (after NMHSs, 2007)

Location	Data period	Annual rainfall (mm)	Minimum daily temperature (°C)	Maximum daily temperature (°C)
Hong Kong (22.11°N, 114.14°E)	1971-2000	2281	14.1	31.3
Kuching, Malaysia (1.32°N, 110.20°E)	1971-2000	4117	22.9	32.7
Singapore (1.17°N, 103.51°E)	1961-1990	2150	23.1	31.7
Libreville, Gabon (0.25°N, 9.26°E)	1961-1990	2842	21.8	30.2
Georgetown, Guyana (6.46°N, 58.10°W)	1961-1990	2260	23.5	30.8

Summer (the wet season), from May to September, accounts for 80% of the annual rainfall with the monthly mean ranging from 287.5 mm (in September) to 444.6 mm (in August) (HKO, 2003). The large amount of rainfall is mainly brought by typhoons and low pressure troughs. The mean monthly temperatures in this wet period are often above 25°C, with the maximum daily reaching the highest at 31.3°C (in July) (HKO, 2003) (Figure 3.8).

In winter (the dry season), from October to April, the mean monthly rainfall records are usually much lower. In the period 1971-2000, the mean monthly rainfall was between 24.9 mm (in January) and 151.9 mm (in October) (HKO, 2003). The average monthly temperature during this dry period was 19.8°C, with the highest and lowest monthly average at 16.1°C (in January) and 25.3°C (in October). The daily minimum was at 14.1°C in January (HKO, 2003) (Figure 3.8).

The seasonally hot and humid climate favours active chemical weathering processes such as oxidation, hydration, hydrolysis and solution of rock minerals which contribute to the formation of a deep soil profile (section 3.4). Physical disintegration of rocks, such as exfoliation, by repeated wetting and drying is also noted (Fyfe *et al.* 2000).

Spatially, the mean annual rainfall is unevenly distributed where the highest amount of rainfall has been mainly found on the hilly areas such as Tai Mo Shan (the highest peak in Hong Kong) and Lantau Island, as shown in the years 1961-1990 (Figure 3.10).

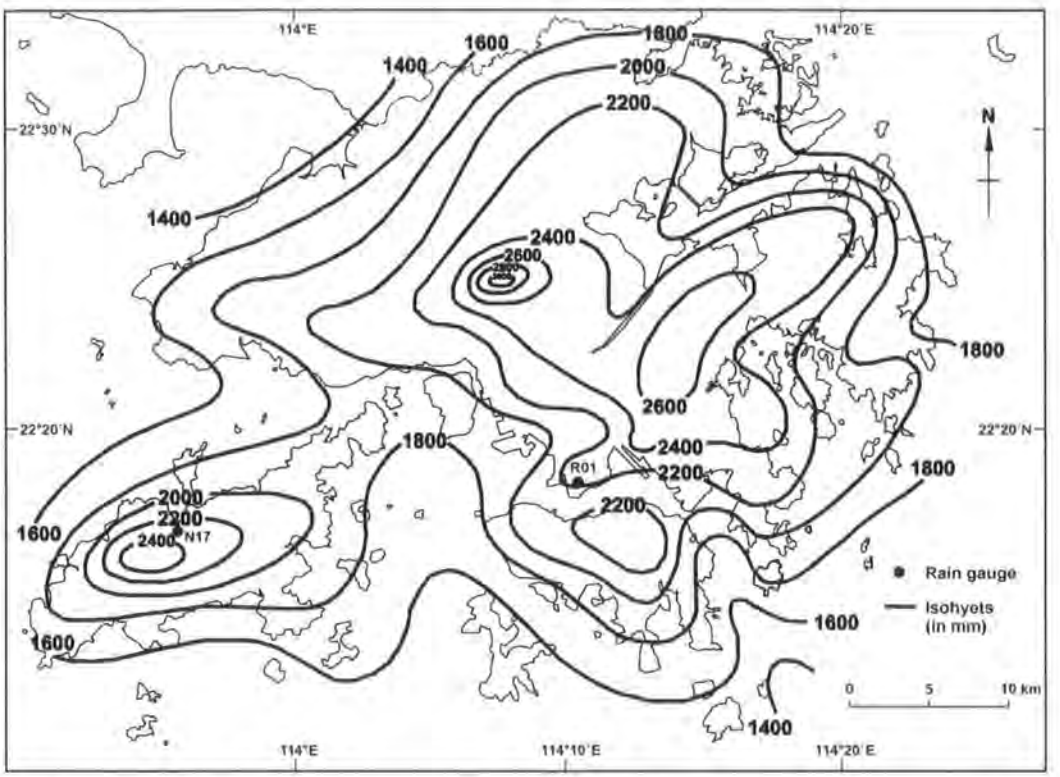

Figure 3.10 Spatial distribution of mean annual rainfall in Hong Kong, 1961-1990 (HKO, 2003)

The reported landslide-triggering rainfall events on the island are summarised in Table 3.2. The actual number of the landslide-triggered rainstorms may be largely underestimated as there have been very limited studies on the relationship between rainfall and natural terrain landslides until the 1990s. Most detailed studies were focused on the severe rainstorm event that occurred on November 4-5, 1993 which triggered over 800 landslides on the island. The peak 1-hour rainfall was 114 mm which largely exceeded the landslide-triggered rainfall threshold of 70 mm/hr for Hong Kong established by Brand *et al.* (1984). The 24-hour rainfall exceeded 400 mm for most parts of the island and reached 742 mm (the return period was 857 years) in Tung Chung (Brand, 1994; Wong *et al.*, 1998) (Figures 3.11, 3.12). The magnitude of this rainfall event was associated with high landslide density (> 10 /km^2) over natural terrain in Hong Kong based on the 1985-1994 data (Evans and Lam, 1999). However, the landslide density on Lantau as a result of the 1993 rainstorm (i.e. about 6 /km^2) was lower than the expected.

Table 3.2 Landslide triggering rainfall events reported on Lantau Island

Rainstorm	Maximum rolling rainfall (mm)			Rain gauge*	Study area	Landslides triggered	References
	1 hr	12 hr	24 hr				
14-15 June 1959			308.9	R01	North Lantau	Widespread landslides on thin vegetated slopes	Franks, 1999
18-19 August 1972 (Typhoon Betty)			186.8	R01	North Lantau	Many landslides occurred on the hillslopes, northeast and east of Tai Po	Franks, 1999
28-29 May 1982	44		394.3	R01	Lantau Island	233 landslides	Franks, 1998; Dai *et al.* 2004
17 June 1983			346.7	R01	Lantau Island	151 landslides	Franks, 1998; Dai *et al.* 2004
18-19 July 1992	115	423.5	454	N17	Lantau Island / Tung Chung East	263 landslides / multiple high mobility shallow failures to the south of Tai Po, north Lantau	Franks, 1999; Evans and Lam, 2003; Dai *et al.* 2004
4-6 Nov 1993 (Typhoon Ira)	114	579	742	N17	Lantau Island	838 shallow landslides on Lantau island (about 600 of which occurred on natural hillslopes)	Brand, 1994; Wong and Ho, 1995; Wong *et al.*, 1997, 1998; Dai *et al.*, 1999a; Franks, 1999; Evans and Lam, 2003; Dai *et al.* 2004; Lan *et al.* 2005
22-27 Aug 1999 (Typhoon Sam)	54.5	205	310.5	N17	Tung Chung East	Shallow, low-mobility slab sliding to moderately-sized high mobility slump type failures	Evans and Lam, 2003
6-8 July 2001 (Typhoon Utor)	32/ 27	208/ 196.5	254.5/ 242.5	R1/R2	Tung Chung East	Minor single high mobility shallow failure	Evans and Lam, 2003; Lan *et al.* 2005

* Rain gauge location: N17 at Tung Chung; R1/R2 at Tung Chung East; R01 at Kowloon

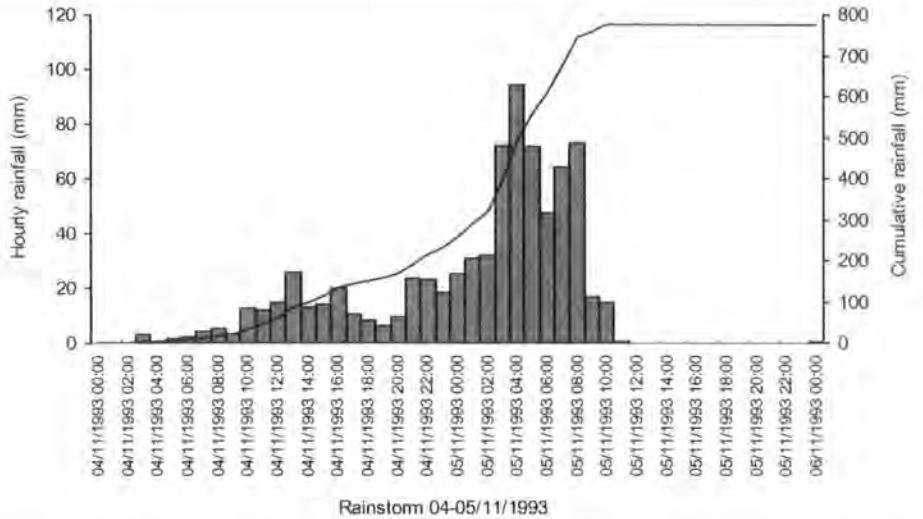

Figure 3.11 Characteristics of the November 1993 rainstorm which triggered over 800 landslides on Lantau Island, in terms of hourly and cumulative rainfall (Evans and Lam, 2003)

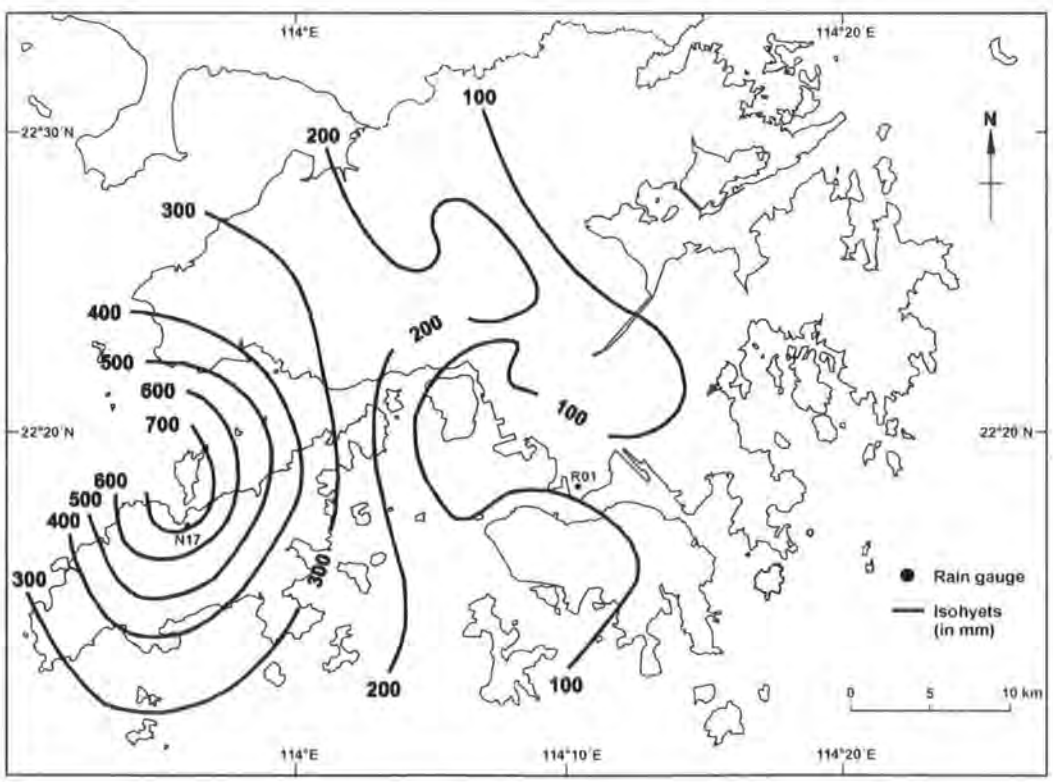

Figure 3.12 The spatial distribution of 24-hr rainfall of the 4-5 November 1993 rainstorm over Hong Kong. The maximum rainfall amount fell at Tung Chung area (after Brand, 1994)

The 1993 rainstorm, also surprisingly, did not trigger a landslide or slope movement within the Tung Chung east area, which reflected a complex relationship between rainfall and groundwater response or movement (Evans and Lam, 2003). Instead, the landslides there were assumed, based on aerial photo interpretation and post-failure survey, to occur during the less severe rainstorms in 1992, 1999 and 2001 (Table 3.2) (Figure 3.13) which were characterised by an initial period of moderately intensity rainfall (7.5-9 mm/hr), followed by a period of higher rainfall intensity (> 40 mm/hr) (Evans and Lam, 2003).

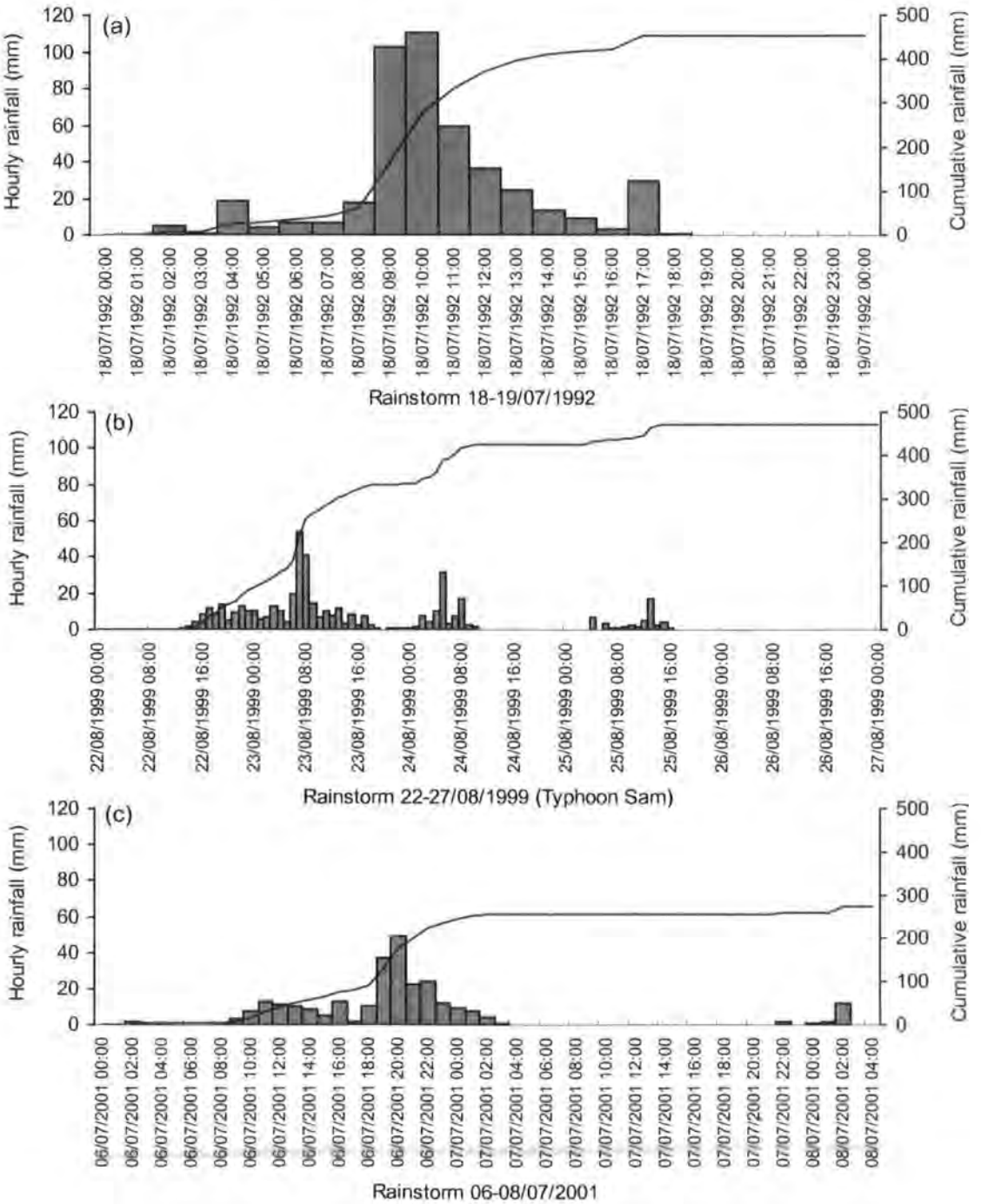

Figure 3.13 Characteristics of three rainstorms on natural slopes at Tung Chung area in terms of hourly and cumulative rainfall (after Evans and Lam, 2003)

These presumably landslide-triggering rainstorm events at Tung Chung and other parts of the island are associated with a maximum 24-hour rolling rainfall of at least 200 mm (Table 3.2). This appears to be consistent with the minimum natural terrain landslide threshold suggested by Evans *et al.* (1999). The rainstorm-associated hydrological conditions on natural hillslopes are spatially and temporally variable (section 2.4.1.2) (Figure 2.5). Shallow piezometer records (< 3 m) at the Tung Chung east area showed that intense short-period rainfall generally led to rapid and positive groundwater responses near the ground surface. Full saturation of the surface layer (about 1 m) and seepage pressures were observed. In contrast, rainfall of a longer-duration mainly affected greater depths of regolith with a slower groundwater response (Evans and Lam, 2003). However, the rainfall-landslide relationship is largely uncertain as the actual timing of the landslides is unknown and the hydrological conditions within the natural hillslopes leading to and during the failure have not been identified.

Hydrogeological studies further suggest that the regional groundwater table in north Lantau lies within the slightly to moderately weathered rock (50-90% unweathered rock) or within the saprolite (less than 30% unweathered rock) (Franks and Woods, 1993; Franks, 1998; GEO, 2000). During or after intense rainfall, transient perched water tables are also observed at the interface between the saprolite and the more permeable colluvium deposits (Franks, 1998, 1999). In south Lantau, groundwater flow in the bedrock is concentrated in open and closely-spaced joints and fissures by sheeting or conduit flow (GCO, 1988b). However, groundwater flow in superficial deposits, such as colluvium, appears to have been affected by piping as observed on the western coast of (the former) Penny's Bay (Franks and Woods, 1993) and the colluvial footslopes in south Lantau (GCO, 1988b).

Heavy and prolonged rainfall also supplies water for the numerous small and ephemeral streams which deeply dissect the hillslopes (Franks, 1998, 1999). Dai and Lee (2002) further noted that landslide frequency generally increased as the distance from the drainage lines became shorter. This could be related to the extension and expansion of drainage network development (Yau, 2001). The rainfall associated stream discharge has been described as "flashy" reaching a peak in a short time in the steep catchments in south Lantau with thin soils and high drainage density (GCO, 1988b). The catchment size over Lantau varies from less than 1 km^2 to about 11.2 km^2 (Tung Chung south catchment) and the catchments have a dendritic drainage pattern (GCO, 1988a, 1988b).

3.6 Vegetation

Lantau Island is covered by three main types of vegetation including woodland (20.5%), shrubland (28%) and grassland (24.6%). Bare ground makes up 26.9% of the island (Zhou *et al.* 2002). The woods are mainly found on the valley floors and lower to midslopes, including both native and introduced broadleaf species (GCO, 1988a, 1988b). They are largely secondary forests as a result of the post-war afforestation programmes during the 1960s and 1970s. The original vegetation was largely removed by man for fuel and timber (Catt, 1986) and/or by hill fires (GCO, 1988a, 1988b). Extensive woodlands are located in the Chi Ma Wan Peninsula and around the water catchment areas of Shek Pik reservoir in South Lantau (AFCD, 2006) (Figures 3.3, 3.14). Shrubs cover most of the island at the lower slopes of drainage basin and in stream valleys (AFCD, 2004) and occasionally on mid and upper slopes as regrowth of the disturbed terrain cleared by hill fires (GCO, 1988a, 1988b). Grasslands dominate the upper slopes, perhaps due to the strong winds on the exposed high grounds or as a result of the clearing of woodland or shrubland (GCO, 1988a, 1988b).

Figure 3.14 Extensive woodlands around the catchment area of Shek Pik reservoir due to the post-war afforestation programme. Scattered shrubs and grasslands cover upper slopes

The effect of the deforestation on landslide occurrence on the island has not been studied. Previous research findings on the relationship between vegetation and landslides are not conclusive (e.g. Dai *et al.*, 1999a; Evans *et al.*, 1999; Zhou *et al.*, 2002). Landslides have occurred in different types of vegetation cover (Figure 3.15). For example, landslides observed in 1995 on Lantau Island were more or less evenly

distributed between woodland and non-woodland areas (Ng, 2001). However, Dai and Lee (2002) reported the highest landslide density on densely grassed land (less than 40% scrub coverage) in the time period 1945-1994. At Tung Chung, the highest landslide frequency was noted on grasslands and low scrub following the two heavy rainstorms in 1992 and 1993 (Franks, 1999). These different results probably reflect the temporal variability of landslide occurrence and vegetation growth as well as the areal coverage of the study sites. Moreover, the findings may have also been largely affected by the different classification of vegetation defined by the researchers.

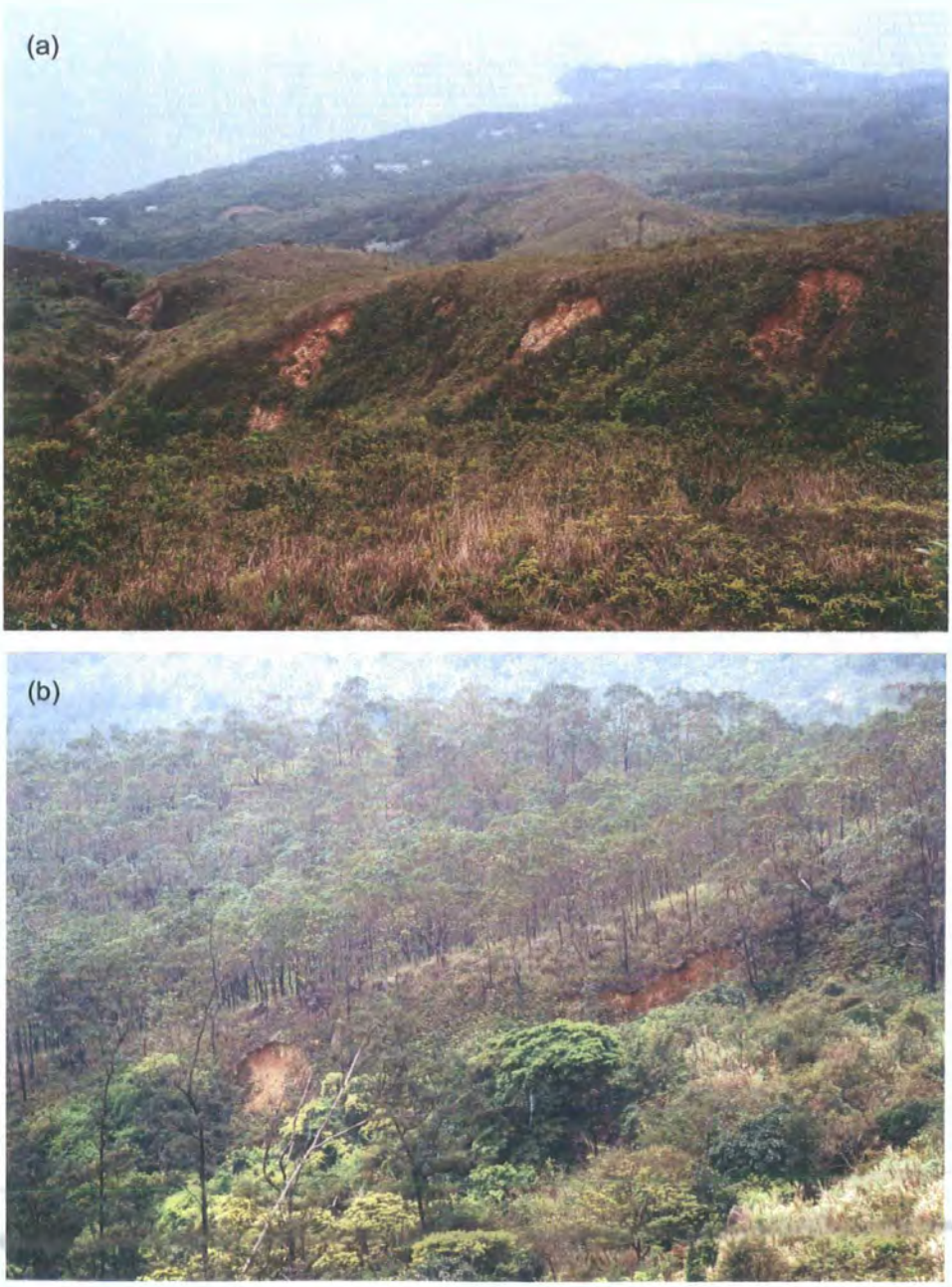

Figure 3.15 Landslides occur on (a) shrub / grasslands and (b) in woodlands at the south flank of Sunset Peak, Lantau Island

3.7 Chapter summary

Lantau Island has been chosen as the study area as it represents the typical environmental setting in the humid tropics which favours the occurrence of rainfall-induced landslides. The availability of rainfall and pore pressure monitoring data on the landslide-prone hillslopes at Tung Chung further allows an investigation on the rainfall-triggered landslide initiation processes to achieve the research aim.

This chapter has described the characteristics of landslides on the island and the landslide governing factors including relief and slope gradient, geology, climate and vegetation. In overview, most landslides on Lantau occur on moderately steep, weathered volcanic, vegetated slopes of 30°-40° at mid-elevations triggered by intense rainstorms with 24-hr rainfall of more than 200 mm. Previous studies have provided background information on the environmental controls of the natural landslides on the island. However, a process approach is fundamental towards the understanding of landslide movement behaviour.

Chapter 4 Methodology

4.1 Field sampling

4.1.1 Site selection

The selection of landslide sites on Lantau was based on the following criteria:

(i) Representativeness—the selected landslide sites should represent the typical conditions of landslide occurrence under tropical environments: triggered by rainfall on intensely weathered soil slopes within the tropics, upon which this research is primarily focused. Weathered natural slopes, which have the highest density of rainfall-induced landslides (Evans *et al.*, 1999), have been considered.

(ii) Natural landslides—only landslides on natural hillslopes were selected to allow examination of their natural mechanisms. Man-made slope failures were not included.

(iii) Accessibility—the selected landslide sites should be accessible in consideration of safety of the field workers. In addition, the sites should render collection and transportation of the soil samples feasible.

(iv) Recent landslides—soil samples of recently occurred landslides should be less affected by soil erosion. The landslides chosen on the island were based on the latest landslide inventory (1999-2002) available from the Hong Kong Geotechnical Engineering Office (Figure 3.3).

Two sites were selected on Lantau Island, namely Tung Chung (TC), located at 22°17'N, 113°57'E and Pui O (PO), at 22°15'N, 113°57'E. Both landslides occurred on natural tropical slopes formed from intensely weathered volcanic soils, triggered by rainstorms in year 1999 (Figure 3.3). They were chosen also because of their good accessibility using hiking trails.

4.1.1.1 Tung Chung (TC) site

The Tung Chung (TC) landslide site is located in a small gully on a hillslope adjacent to the North Lantau Highway, east of Tung Chung (Figure 4.1). The slope angle is about 30°. The main vegetation cover is grass with scattered bushes. The landslide scar dimension is about 20 m wide, 27 m long and less than 2 m deep, with a runout of 33 m in length (Figure 4.1). The elevation of the head scarp is at 38 m and the toe of the runout is about 17 m above sea level. The cross section of the landslide shows that it has involved mainly highly or completely decomposed weathered tuff (Grade IV/V) (Figure 4.2). The study undertaken by Evans and Lam (2003) further

indicates that the landslide mass at the main body is composed of topsoil, colluvium and Grade V ash tuff which can be best described as sandy/clayey silt, based on the trial pit (up to 3 m deep) and Mazier sample records. The landslide was probably triggered on August 22-27, 1999 during the rainstorm brought by Typhoon Sam, based on aerial photo interpretation and ground observation (Evans and Lam, 2003).

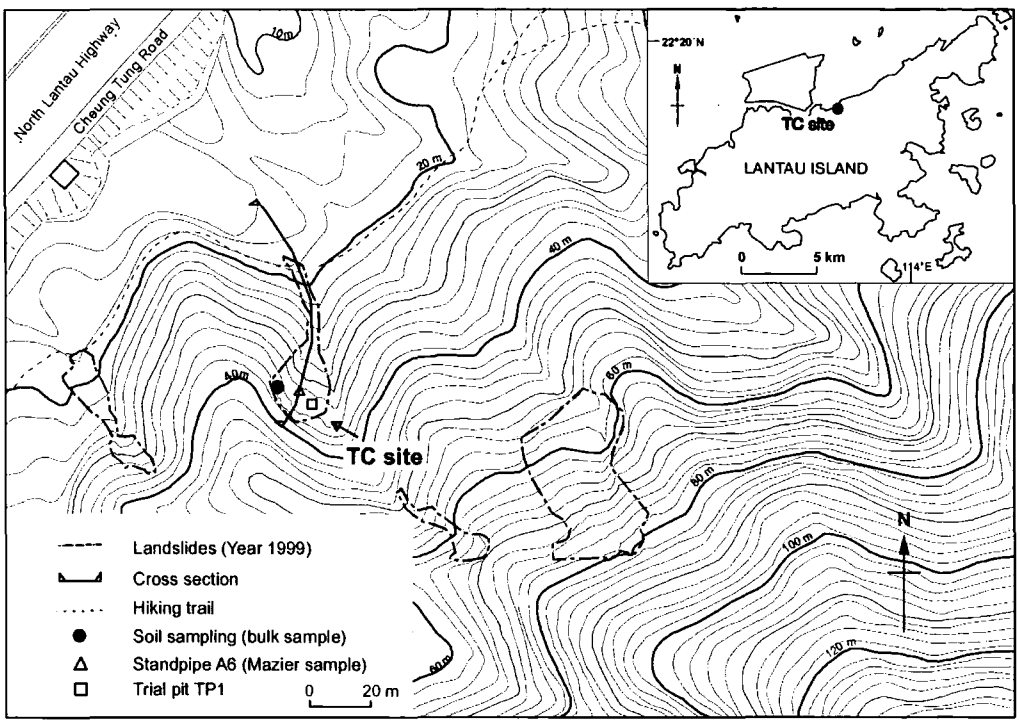

Figure 4.1 Location of the Tung Chung (TC) landslide site, Lantau Island (modified from Evans and Lam, 2003)

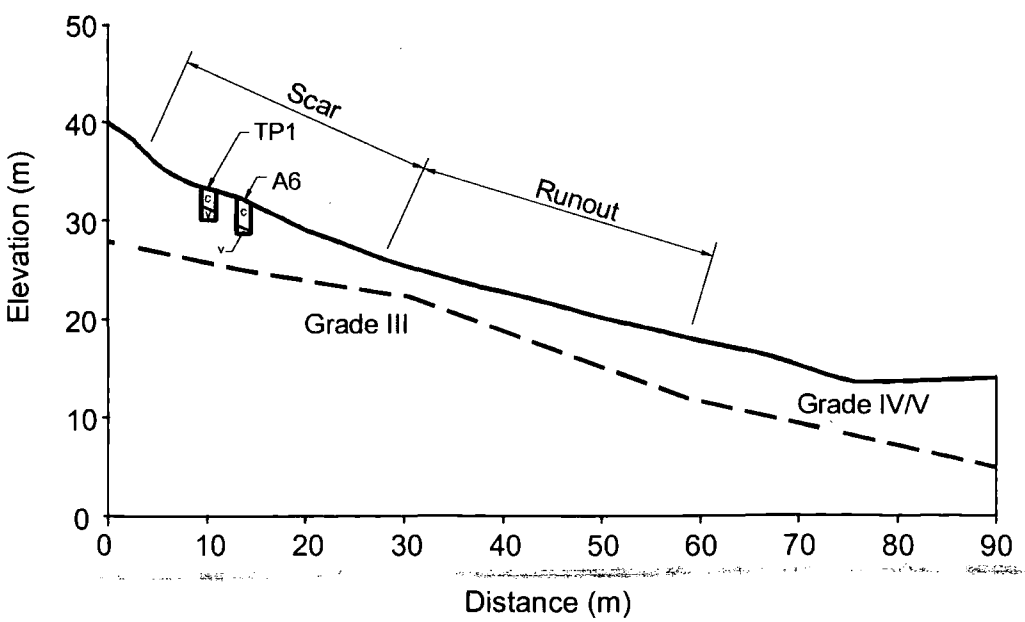

Figure 4.2 Cross-section of the TC landslide showing the distribution of colluvium and the weathering grades of rocks in the area (modified from Evans and Lam, 2003)

4.1.1.2 Pui O (PO) site

The Pui O (PO) landslide site is located on a valley sideslope of Sunset Peak at an elevation of 330 m above sea level, northwest of Pui O village (Figure 4.3). The slope angle is about 35°. The area is densely covered with shrubs. The landslide scar dimension is about 11 m wide, 13 m long and less than 2 m in depth. The underlying solid bedrock at the site is crystal tuff (GEO, 1994b). However, the landslide materials are intensely weathered showing the deep-red, orange colour (Figure 4.4). The debris from the PO site joins the runout of two landslides that occurred in the upper valley in the same year (1999), forming a long debris trail of about 280 m downslope (Figures 4.3, 4.4).

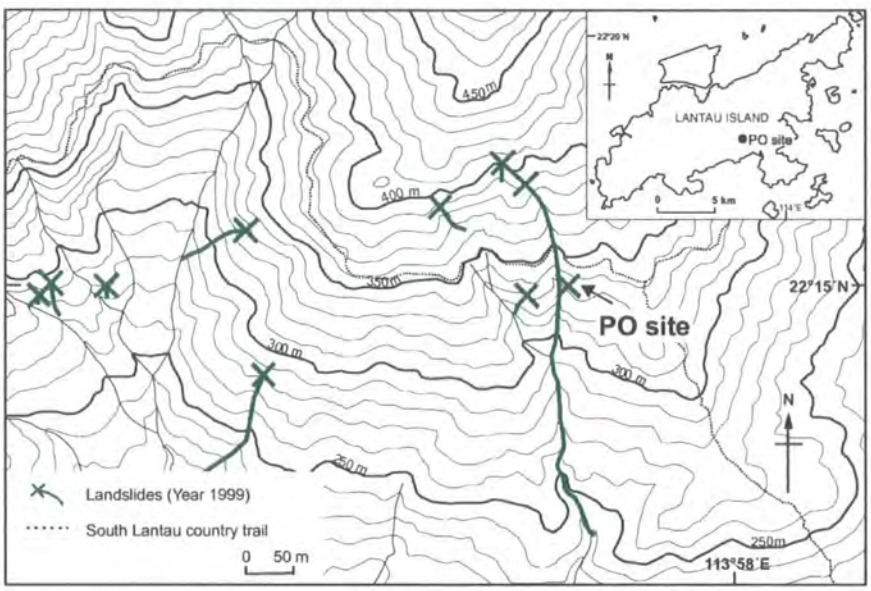

Figure 4.3 Location of the Pui O (PO) landslide site, Lantau Island (modified from GEO, 2004)

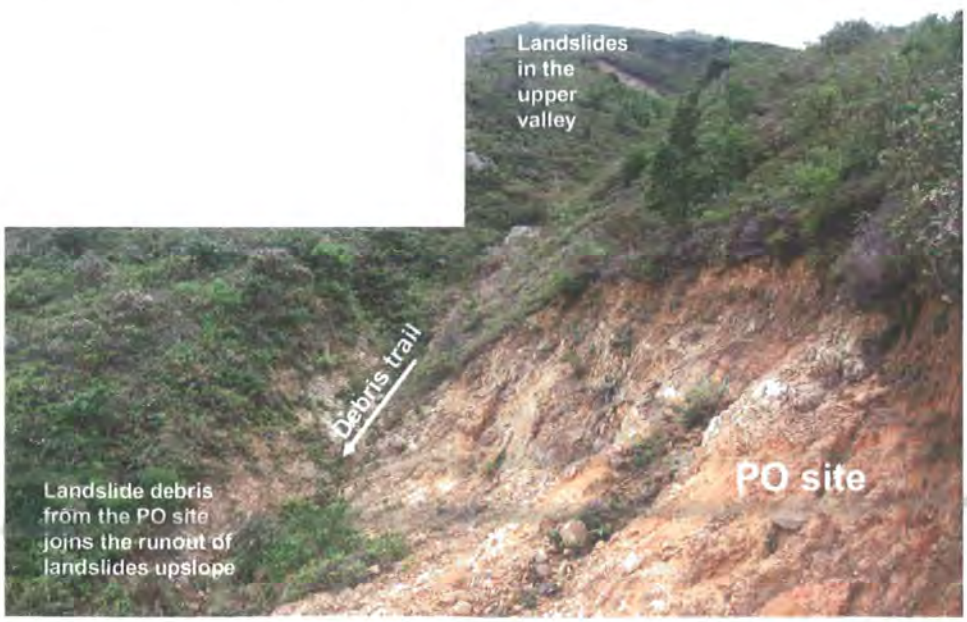

Figure 4.4 Geomorphology of the PO landslide site

4.1.2 Sampling method

Soil sampling was undertaken at the main scarp or the head of the exposed landslide slope at a depth of about one metre (Figures 4.5, 4.6). This position was chosen for three main reasons. Firstly, the soil at the main scarp is the least affected by landslide movement, as compared with the main body or the toe of the landslide where disturbance by transportation and deposition of the displaced soils have occurred. The relatively undisturbed soils from the main scarp allow closer simulation of the pre-failure slope condition. Secondly, the exposed, nearly vertical soil surface provides a natural pit for soil sampling. The samples can be readily taken by hand-carving using a trowel after removing the surface soils with a spade, which minimises the disturbance of soils as opposed to pit excavation by heavy digging. Thirdly, samples collected at a depth of about one metre, which is composed of intensely weathered soils without signs of discontinuities, represent a common location of shallow landslide occurrence. Soils at shallower depths are not considered as they are more likely to be disturbed by vegetation roots and other organic processes.

Both undisturbed (in blocks) and disturbed (loose) samples were collected from the landslide scar at the TC and PO sites in late May and early June 2004 (Figure 4.6). At each sampling site, a total of 40 undisturbed hand-cut soil samples of a size twice as large as the testing requirements (38 mm in diameter and 76 mm in height) were taken. The disturbed samples were used for the physical property tests.

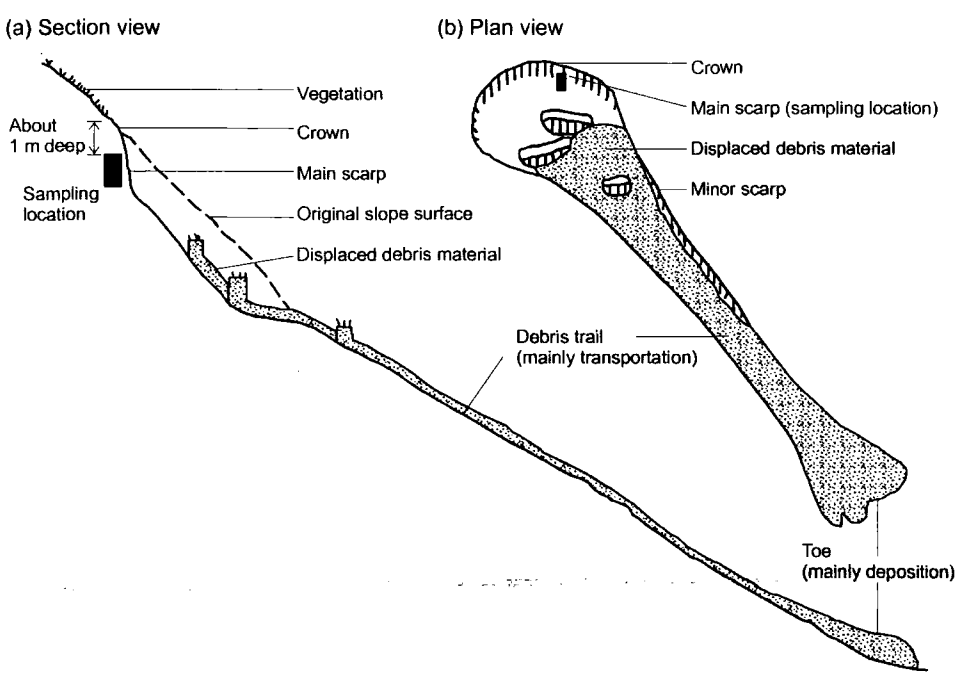

Figure 4.5 Location of soil sample collection at the main scarp of a typical landslide on Lantau Island: (a) section view; (b) plan view (modified after Franks, 1999)

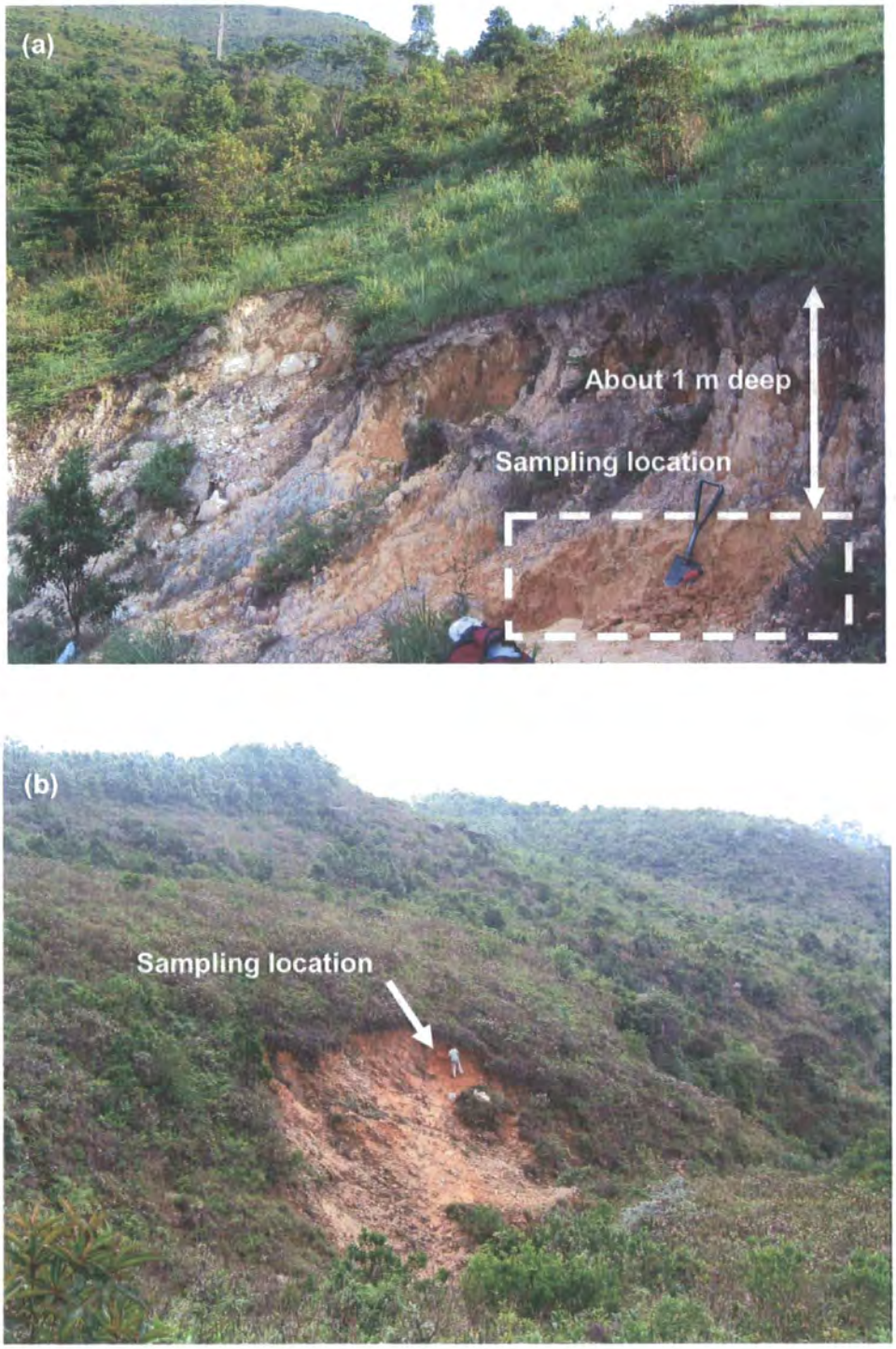

Figure 4.6 Collection of undisturbed weathered volcanic samples at the landslide sites: (a) Tung Chung (TC); (b) Pui O (PO)

4.1.3 Sample preservation, transportation and storage

The undisturbed samples were initially trimmed and wrapped in several layers of "cling film" to preserve the moisture content immediately after they were extracted from the site. The sample orientation was recorded so that the soil sample could be put in the same position as in the field during laboratory testing. The disturbed samples were put into sealed polythene bags.

Each undisturbed sample was cushioned by bubble foam and placed in an air-tight and water-proof plastic box to minimise disturbance during carriage. For transport by sea freight, the undisturbed samples were further wrapped by additional layers of bubble foam and packed into card board boxes with shock-absorbent sponge.

Upon arrival to Durham University, the samples were stored in the fridge at a constant temperature and humidity until required for laboratory testing.

4.2 Laboratory testing

The purpose of the laboratory tests was to simulate the conditions of the rainfall-induced natural landslides during the development of failure. The experimental programme involved three test stages: (1) characterisation, (2) conventional isotropic consolidated undrained (ICU) and drained (ICD) triaxial testing and (3) pore pressure reinflation (PPR) tests.

4.2.1 Stage 1: Physical property tests

Standard classification tests were undertaken to determine the physical properties of the collected field samples. A representative mass of samples from the two sites was defined by assessment of soil grouping before testing (BSI, 1990a), including particle size analysis (distribution of gravel, sand, silt and clay in percentage), specific gravity, loss on ignition and the Atterberg limits. The water content, void ratio, bulk density and dry density of each undisturbed sample were further determined during triaxial testing (Table 4.1). In some of the physical property tests, special procedures for tropical soils are required during the soil preparation stage. The modified details and the justifications are described in Table 4.2.

Table 4.1 Basic physical properties of soil and the related test methods

Properties	Measurements / Descriptions	Test method used
Particle size analysis	Expresses the different size grades of particles in a soil in terms of percentages, by weight	Coulter™ particle size method
Specific gravity	Ratio of soil weight to an equal volume of water	BSI ,1990b: 8.3 (Small pyknometer method)
Loss on ignition	Indicator of organic matter content	BSI ,1990c: 4.3
Atterberg limits	Consistency limits describe the four states (solid, semi-solid, plastic, liquid) of cohesive soils depending on their moisture content, while the boundaries between these states are referred to as the shrinkage limit (SL), the plastic limit (PL) and the liquid limit (LL).	BSI ,1990b: 4.3 (Cone penetrometer method for liquid limit) BSI ,1990b: 5 (Plastic limit)
Water content	Ratio of mass of water to mass of solids / the amount of water contained in a soil	BSI ,1990b: 3.2 (Oven-drying method)
Void ratio	Ratio of volume of voids to volume of solids	
Bulk density	Ratio of total mass of soil to total volume	BSI ,1990b: 7.2 (Linear measurement method)
Dry density	Mass of the solid particles divided by the total volume	BSI ,1990b: 7.2.5 (calculated from bulk density with known moisture content)

Table 4.2 Special procedures taken for the residual soil samples

Test	Special procedures taken	Rationale
Particle size analysis	1. Pretreatment of the soil by oven-drying at 105°C was not carried out, but was tested in its natural state.	1. High temperature can cause residual soils to form aggregations (Chen, 1996). The structure and physical behaviour of tropical residual soils may be altered by drying (Fookes, 1997). Irreversible changes take place when dried at 105°C or even when air-dried (BSI ,1990a).
	2. Chemical pretreatment of soil by hydrogen peroxide was avoided.	2. The pre-treatment of soil samples for organic matter is unnecessary for most Hong Kong soils (Chen, 1996)
	3. Wet-sieving was replaced by using the Coulter™ laser diffraction particle size analyser.	3. Enables a continuous particle size distribution curve from sand to clay size particles to be plotted.
Specific gravity	Oven-drying at 45°C instead of 105°C in soil preparation	Oven drying may change particle density due to loss of water of hydration (BSI ,1990a) for residual soil
Plasticity tests	Soil was mixed for at least 40 mins instead of 10 mins before testing	To obtain reliable results for residual soils (BSI ,1990b)
Moisture content	Determined at the lower temperature of 45°C. However, comparative tests at 105°C were also undertaken.	Residual soils in Hong Kong contain minerals with water of hydration, or 'structural' water, which will release when the temperature exceeds 50°C. (Chen, 1996; Fookes, 1997)

4.2.2 Stage 2: Isotropic consolidated undrained (ICU) and drained (ICD) triaxial testing

The main purpose of the isotropic consolidated undrained (ICU) and drained (ICD) tests is to provide a standard and comparable reference for the design of the reinflation test (Stage 3). This is achieved through constructing the Mohr-Coulomb envelope or the failure envelope, which is derived from at least three ICU and ICD tests respectively carried out at different confining pressures. With reference to the failure envelope, the initial stress conditions (i.e. before failure) of the reinflation test can be designed, and the failure conditions can be compared after the test.

In addition, the ICU and ICD tests are also used to determine shear strength parameters including the effective frictional angle (ϕ') and the effective cohesion (c'), stress-strain soil behaviour and provide information on pre-failure strain development which reveals how the samples fail under conventional tests (and how different this process is compared with the reinflation tests).

4.2.2.1 Test equipment

The soil samples underwent saturation, consolidation and compression in a hydraulic triaxial stress path cell apparatus (Figure 4.7). The key difference between these two standard triaxial tests lay in the compression phase, in that drainage was not permitted for the undrained tests.

The triaxial stress path system is manufactured by ELE International, based on the design of Bishop and Wesley's (1975) hydraulic stress path cell developed at Imperial College, London. The pressure system is controlled by a motorised compressed air system, consisting of a constant rate of strain (CRS) pump, motorised cell pressure (CP), back pressure (BP) and ram pressure (RP) regulators and three corresponding bladder type air-water pressure cylinders. The cylinders could provide more immediate response and maintenance of pressures during sudden failures than the GDS pressure-volume controller (Junaideen, 2005). The working pressure of the motors and the cylinders ranges from 0 to 1000 kPa. The compressed air is supplied from a compressor tank manufactured by Fini. The compressor has a maximum capacity of 1000 kPa and is regulated by the air motors before entering to the bladders to provide pressurised water for the stress path cell.

The triaxial stress path system is capable of performing both strain rate controlled (ICU, ICD tests) and stress rate controlled (PPR) tests at positive total and

effective stresses for 38 mm diameter samples. The stress path cell can support lateral pressures ranging from 0 to 1000 kPa and is fitted with a stationary 4.5 kN submersible load cell measuring the axial load. Axial load can be applied to the sample through a piston fixed to the pedestal, of which the vertical movement can be controlled by the ram pressure in the bottom pressure chamber (Figure 4.7). The rolling diaphragm which separates the upper cell and the bottom pressure chamber minimises the effects of piston friction upon loading (Menzies, 1988). The axial strain of the sample is measured by the displacement transducer (0-50 mm range), also known as the "linear variable differential transformer" (LVDT) (Head, 1998: 94), on the extension rod of the cross arm attached to the moving piston (Figure 4.7). The volume change transducer, which is of a rolling diaphragm type and measures the movement of water in the back pressure line, has a maximum capacity of 80 cm^3 and is readable to 0.1 cm^3 under the working pressure up to 1700 kPa (ELE, 2004).

The measurements of the changes in pressures (CP, BP, RP and pore pressure), displacement, load, and volume change are conducted by the transducers. The maximum capacity of the CP, BP, RP and PP transducers is at 700 kPa. All of the transducers are energised by a stable electric supply at 10 V d.c. and their electric output signals (in voltage) are amplified and read by the ELE autonomous data-acquisition unit (ADU). The 8-channel ADU (one of them is a spare channel) forms the key part of the ELE stress path control system that directly controls the CRS pump and the CP, BP, and RP motors.

The computer software package used for the data acquisition and control of the stress path triaxial tests was TRIAX version 4.2, developed by Dr. David Toll of the Geotechnical Systems Group at Durham University (Toll, 1999, 2002). The program ran under Microsoft® Windows 98 and provided a display on screen for the transducer readings, data logging and storage at regular time intervals (a minimum of every 10 seconds) as well as the automatic/manual control over the BP, CP, RP and CRS pump devices through user-defined equations and tolerance band. Tolerance values were set at +/-0.5 kPa for the pressure controllers (i.e. CP, BP, RP), and +/-0.01 mm for the CRS pump which were found to be suitable for the ELE stress path system without overshooting for the target value.

The de-aired water required for the triaxial testing was supplied by the ELE de-aired water apparatus. The apparatus is a self-contained unit with its own electrical and water supply that consists of an upper assembly (the control panel), a suction pipe and a water tank with a maximum capacity of 15 litres. The water stored in the tank was de-

aired and maintained through continuous vacuum generated by the internal pump above the water level.

Calibration of transducers was performed using the calibration program in TRIAX 4.2. The best-fit (linear) line for the calibration data of each transducer including two coefficients and the maximum percentage error (the maximum deviation from linearity) were calculated by the TRIAX program using the regression function, or (for the new load cell) entered manually to the program with reference to the calibration records supplied by ELE International. The coefficients were stored in the program to provide corrected display of transducer readings during the stress path tests.

The PP, CP, BP and RP transducers were calibrated against a GDS digital controller which could control pressure to 0.5 kPa with measurement resolved to 0.2 kPa at pressures ranging from 0 to 2000 kPa (Menzies, 1988). The pressure transducer reading (in kPa) was set to zero against the atmospheric pressure, followed by an application of three cycles of pressure changes. In each cycle, the pressure was increased successively to 50, 100, 200, 400, 600 kPa within the working range and then decreased to 300, 150, 74, 37, and 10 kPa. A total of 31 data points (including the zero point) were recorded for each transducer. The linear coefficients (R^2) for the PP, CP, BP and RP transducers were ≥ 0.9999 and their maximum percentage error were 0.26%, 0.14%, 0.11% and 0.46% respectively.

The calibration for the original load cell was carried out manually using a hanger by adding or reducing squares of slotted cast iron of known dead weight of about 10 kg each (measured up to 0.01 N using a balance) at a range from 0-700 N for three cycles (46 data points). The linear coefficient (R^2) was 0.9997. The new load cell (which replaced the original) was calibrated by the ELE International. The linear coefficient (R^2) was 0.9999 with the maximum percentage error at 0.37%.

The displacement transducer was calibrated against a dial gauge (maximum travel at 50 mm, measured up to 0.01 mm). The calibration range for the transducer was from 10.00 to 41.00 mm (98 data points, measured in every 2.00 mm). The linear regression coefficient was 1.000, with the maximum percentage error at 0.25%.

The volume change transducer was calibrated by weighing the de-aired water moving out of the transducer (measured up to 0.01 ml) between 45 and 65 ml of piston travel in upward and downward directions respectively. The calibration file was unfortunately not recorded in TRIAX.

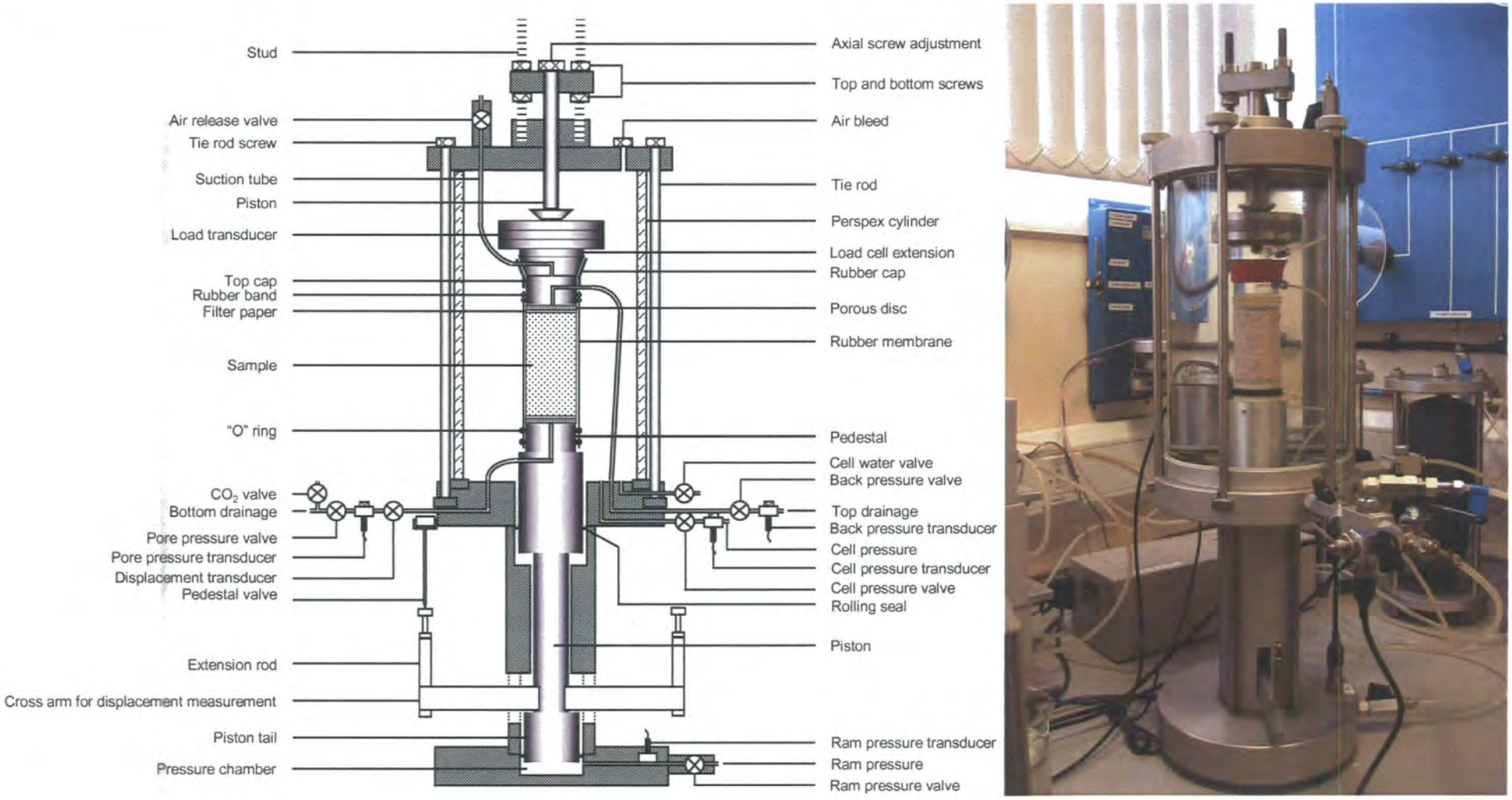

Figure 4.7 The triaxial stress path apparatus for the conventional triaxial (Stage 2) and the reinflation (Stage 3) tests in this research

4.2.2.2 Soil preparation

To prepare for the triaxial tests, the undisturbed soil samples were trimmed to 38 mm in diameter and 76 mm in height using a straight-edged knife, wire saw and scalpel. The TC samples were trimmed in a hand-operated soil lathe. For the PO samples with larger particles, the trimming process was aided with a cylindrical aluminium split mould of the required dimension. Three of them, however, were slightly damaged (cracked) including POD14, POD16 and POD17. The trimmings were weighed for the moisture content analysis. The diameter and the height of the trimmed samples were measured using a calliper (up to 2 decimal places, in millimetres).

4.2.2.3 Saturation

Saturated tests were performed to simulate the nearly and fully saturated soil conditions at shallow depths during a rainstorm on tropical slopes (section 2.4.1.2). The saturated state was also justified based on the field monitoring data at Tung Chung East because no failure occurred at the site even though the pore pressures were not positive (Evans and Lam, 2003). Moreover, saturation could eliminate the unnecessary complication of the pore air pressure which differs from the pore water pressure (Head, 1998).

Full saturation was achieved using three steps. Firstly, each sample was flushed very slowly with carbon dioxide for at least one hour. Subsequently, de-aired water was introduced to fill the pore air voids. Thirdly, cell pressure and back pressure were increased simultaneously until the pressures reached 210 kPa and 200 kPa respectively to dissolve the CO_2 into solution. A positive effective stress of 10 kPa was maintained throughout the saturation process to avoid sample swelling. The pressures were kept constant overnight until the Skempton's pore pressure parameter (the B-value) (Eq. 4.1) was equal to or greater than 0.95 (BSI, 1990d):

$$B = \frac{\delta u}{\delta \sigma_3} \qquad \text{(Eq. 4.1)}$$

where δu is the increment of pore water pressure (in kPa);

$\delta \sigma_3$ is the increment of normal stress (in kPa);

B is the Skempton's pore pressure parameter.

4.2.2.4 Consolidation

The consolidation process was then undertaken on the saturated samples by the application of isotropic confining pressure ($\sigma_1 = \sigma_2 = \sigma_3$). The aim of consolidation is to bring the soil samples back to the field stress state associated with the weight of the overlying and surrounding soil material at original sample depth.

This research consolidated the samples at effective stresses (p'_c) between 50 and 200 kPa, with a large majority being tested at 200 kPa with regard to the functional capacity of the triaxial cell. Low effective stresses of up to 200 kPa were considered appropriate to simulate shallow landslide conditions in residual soils (GCO, 1982, 1988b; Brand, 1985, 1995; GEO, 1994a). Recent experimental studies on shallow rainfall-induced landslides undertaken in Hawaii (Zhu and Anderson, 1998) and Hong Kong (Dai *et al.*, 1999a) have applied effective confining pressure at a range from 10 to 60 kPa.

Standard isotropic consolidation was conducted by ramping the cell pressure from 210 kPa to a desired value at the rate of 1 kPa/min while the back pressure was kept at 200 kPa. Isotropic consolidation is justified for practical purposes, as the result is similar to the K_0 consolidation (σ_1', $\sigma_3' = K_0\sigma_1'$) (Brenner *et al.*, 1997). Consolidation was completed when there was no further significant volume change, and the excess pore pressure due to the applied stress was dissipated (BSI, 1990d).

During the isotropic consolidation process, the coefficient of consolidation (c_{vi}) and the coefficient of volume compressibility (m_{vi}) were calculated to determine the value of the coefficient of vertical permeability (k). This value was used for comparing the degree of permeability in the TC and PO samples.

The coefficient of consolidation, c_{vi}, can be obtained (BSI, 1990d) by:

$$c_{vi} = \frac{1.65 D_c^2}{\lambda t_{100}} \text{ m}^2\text{/year} \qquad \text{(Eq. 4.2)}$$

where D_c is the diameter of the sample after consolidation (in mm);

λ = 4, which is the coefficient for consolidation with drainage from both ends; and a sample length:diameter ratio of 2:1;

t_{100} is the time for theoretical 100% consolidation (in min).

The coefficient of volume compressibility, m_{vi}, is calculated (Head, 1998) from:

$$m_{vi} = \frac{\Delta V_c}{V_0} \times \frac{1000}{\Delta \sigma'} \text{ m}^2/\text{MN}$$

(Eq 4.3)

where ΔV_c is change in sample volume during consolidation (in cm^3);

V_0 is the sample volume at the beginning of consolidation (in cm^3);

$\Delta \sigma'$ is the change of effective stress during consolidation (in kPa).

With these two consolidation parameters, c_{vi} and m_{vi}, the coefficient of vertical permeability, k, can be determined by the equation:

$$k = 0.31 c_{vi} m_{vi} \times 10^{-9} \text{ m/s}$$

(Eq. 4.4)

4.2.2.5 Undrained and drained compression

After consolidation, the sample was either subjected to undrained or drained shear compression at a constant axial strain rate (strain-controlled compression). For undrained testing, the sample was sheared at approximately 0.1% of the initial axial length per minute until failure (typically when the axial strain reached 30%). For example, the calculated strain rate of drained shear for samples of 76 mm in height was approximately 0.076 mm/min. This slow rate of axial deformation was applied to ensure adequate equalisation of excess pore pressures (BSI, 1990d). No drainage was allowed during undrained shear. For drained tests, the applied strain rate (in mm/min) was slower at 0.01% of the initial sample length per minute as drainage was permitted. These tests were performed to define the sample failure envelopes under undrained and drained conditions, as a reference for the design of the pore pressure reinflation tests.

4.2.3 Stage 3: Pore pressure reinflation (PPR) tests

The pore pressure reinflation (PPR) test was designed to simulate the actual rainfall-induced landslide initiation process in the field by keeping the total normal stress and the shear stress constant while increasing the pore water pressure (Figure 4.8). These stress-controlled tests aimed to examine the strain development of the soil samples in response to changes of pore water pressure. The rates were chosen with reference to the field pore pressure monitoring data available on Lantau Island, Hong

Kong (Evans and Lam, 2003). The displacement data under each of the specified increasing rates of pore-water pressure (i.e. linear, stepped and logarithmic) were logged during the reinflation. It should be noted that the axial strains, probably replicating the vertical slope movements in the field, could be accurately and directly measured by the triaxial stress path system using the displacement transducer. Although shear strain could indicate the actual deformation in the shear zone of a landslide, it could only be indirectly estimated, as the radial strain gauge was not available in the standard triaxial testing system.

For the reinflation tests, the saturation and consolidation phases were the same as the conventional tests described above in 4.2.2.3 and 4.2.2.4. However, they were followed by drained initial shear (DIS) phase until reaching the desired deviatoric stress, q , which represented the pre-failure slope condition below the maximum sample strength. The chosen effective stress after drained initial shear, p'_{dis} , and deviatoric stress, q , were 233 kPa and 100 kPa respectively for most reinflation tests. These values represent a soil depth of approximately 20 m with a gradient below 35°. The p'_{dis} value will overestimate the field stress condition of the samples collected at about 1 m depth and results in overconsolidation. However, the selection of the high p'_{dis} value was justified to minimise the "noise" due to the high working range of the triaxial stress path system (with a 4.5 N load cell). At this point, (p'_{dis} , q), the pore pressure was increased at the designed rates under constant deviatoric stress until failure occurred (Figure 4.8).

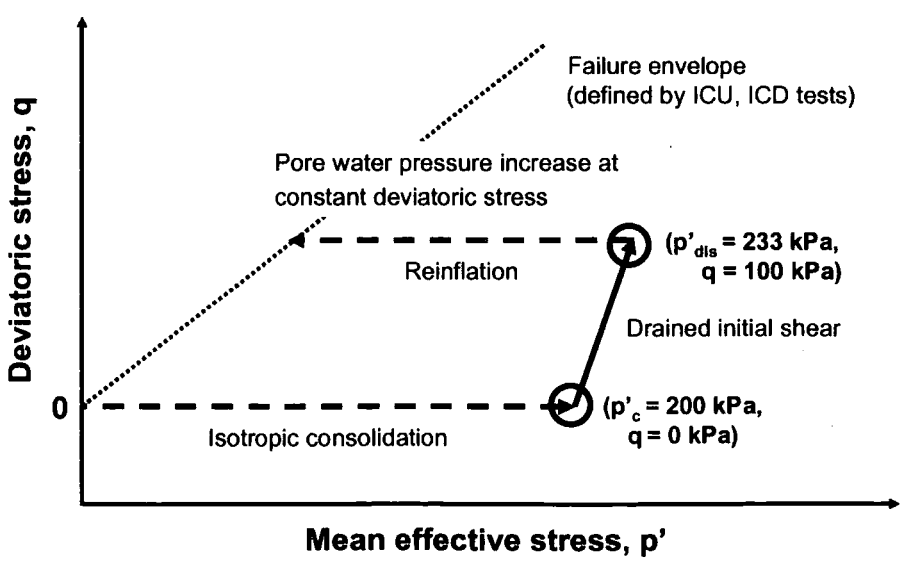

Figure 4.8 The concept of the reinflation test

4.3 Methods of analyses on deformation mechanisms

The aim was to determine the representative rates of increasing pore water pressure from the field in order to (i) closely simulate the actual processes of rainfall infiltration under rainstorms and (ii) to examine the relationship between the nature of increasing pore pressure and movement of residual soil during the reinflation testing.

4.3.1 Evaluation of field monitoring data

A previous field monitoring programme on rainfall and pore pressure that was undertaken on a natural slope at Tung Chung East between March and December, 2001 (GOL, 2002; Evans and Lam, 2003) has allowed an understanding of the actual pore pressure changes that occur on natural slopes on Lantau island. The raw data were collected from two rain gauges and ten shallow piezometers (Table 4.3, Figure 4.9). No significant slope movements occurred in the monitoring period (Evans and Lam, 2003). The analysis here of these data is particularly focused on the identification of the rates of pore water pressure increase during rainstorms, allowing better design of the reinflation tests.

Table 4.3 Geographical and site conditions of the 10 shallow piezometers, Tung Chung East, Lantau Island, Hong Kong (GOL, 2002)

	SP1	SP2	SP3	SP4	SP5	SP6	SP7	SP8	SP9	SP10
Depth (m)	2.50	3.00	2.00	2.73	1.53	3.00	2.62	1.00	3.00	1.15
Elevation (m)	49.25	33.08	32.70	66.35	66.42	48.56	91.15	91.17	74.46	74.91

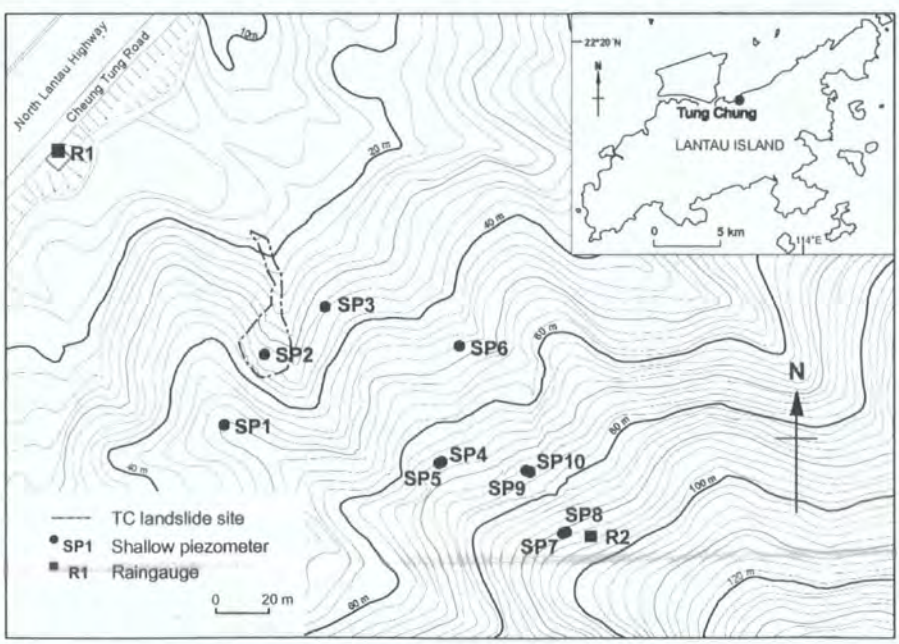

Figure 4.9 Locations of shallow piezometers (SP) and rain gauges (R) at Tung Chung East, Lantau Island (modified after Evans and Lam, 2003)

4.3.1.1 Processing of rainfall data

The rainfall records, based on tipping bucket rain gauges (threshold at 0.5 mm of rainfall), were aggregated into hourly rainfall to allow comparison with the hourly pore pressure data. Based on the processed data, a rainstorm was empirically defined as a rainfall intensity of over 30 mm/hr for at least one hour. A total of twelve rainstorms were identified. In each case, the maximum rainfall intensity, total rainfall and rainfall duration were calculated (Table 4.4). The data represent the rainfall characteristics related to the maximum pore pressure increase for eight of the piezometers. Data for piezometers SP7 and SP8 have not been included due to equipment failure (GOL, 2002).

Table 4.4 Rainstorm characteristics during the monitoring period, at Tung Chung East, Lantau Island (compiled from Evans and Lam, 2003)

No. of rainstorm	Rainstorm period (Year 2001)	Overall rainfall characteristics*					
		Max intensity (mm/hr)		Total amount (mm)		Total duration (hr)	
		R1	R2	R1	R2	R1	R2
1	Mar 25	44.5	6.5	60	8	3	2
2	May 21	39.5	11.0	51.5	16.5	4	3
3	June 8	31.5	15	50.5	21	7	3
4	June 10-11	82	88.5	209.5	198	17	13
5	June 27	31	32.5	164.5	169	14	16
6	July 6-7	49.5	43.5	253	242	20	20
7	July 13	33.5	38.5	62.5	73.5	3	3
8	July 15	75	75	182.5	181.5	10	9
9	Aug 29-30	32.5	36	105	133.5	10	19
10	Sept 1-2	51	44	212.5	200	15	14
11	Sept 5	36.5	33.5	105	104.5	13	13
12	Oct 4	30.5	28	42	39	2	2

*Data derived from rain gauges R1 and R2

4.3.1.2 Processing of pore pressure data

The rate of rainfall-induced pore pressure increase from each piezometers (in kPa/hr) was calculated and classified into three scenarios: "Scenario A": pore pressure increases from an initially positive value; "Scenario B": pore pressure increases from an initial negative pore pressure (suction) to a positive pore pressure; or "Scenario C": pore pressure increases, but remains negative. In each of the scenarios, the highest, lowest and mean rates of pore pressure increase were reported (Table 4.5).

The maximum rate of pore pressure increase in the twelve rainstorms regarding Scenarios A, B and C were 8.4 kPa/hr, 9.1 kPa/hr and 32.4 kPa/hr respectively (Table 4.5). The minimum recorded rate of pore pressure increase was 0.6 to 0.7 kPa/hr. This was related to the resolution of the piezometers, which was 0.65 kPa (GOL, 2001). It was perhaps not surprising to find that the shallow piezometers (SP5, SP8 and SP10) (less than 2 m deep) experienced the highest pore pressure increases. In contrast, the deep piezometers (SP2, SP6 and SP9) (at 3 m depth) were relatively unresponsive to rainfall.

Interesting patterns of increasing pore pressure during the rainstorms were also identified. Qualitatively, the increase rate was generalised as “rapid”, “stepped“ and “zero” / “gradual” (Figure 4.10).

Curve-fitting by the best regression line was undertaken to identify the closet function (i.e. linear, logarithmic, exponential, power) that may describe the trend of the variability of the field pore pressure increase over the rainstorm period. Both linear and non-linear trends of a total of 36 sets of Scenario A data, which recorded more than two hours of consecutive pore pressure increase, were identified as a reference for the reinflation tests. The analyses involved all the data points from each dataset that recorded the pore water pressure over time. The regression results showed that a logarithmic trend was dominant, comprising half of the data series. This was followed by the linear, exponential and power trends (Figure 4.11, Table 4.6).

Table 4.5 A summary of the rate of pore pressure increase during rainstorms based on Scenarios A, B and C

Pore pressure increase	Piezometer response at Tung Chung East, Lantau Island										Summary
	Shallow piezometers (< 2 m)			Medium-deep piezometers (2-3 m)				Deep piezometers (3 m)			
	SP5	SP8	SP10	SP1	SP3	SP4	SP7	SP2	SP6	SP9	
General pore pressure increase (kPa/hr)											
N	42	29	70	37	41	61	4	44	34	38	400
Maximum	8.4	32.4	5.2	6.5	7.8	5.9	0.7	2.6	9	1.9	32.4
Minimum	0.6	0.6	0.6	0.6	0.6	0.6	0.6	0.6	0.6	0.6	0.6
Mean	2.7	4.2	1.2	1.2	2.2	2.3	0..7	0.8	2.3	0.8	1.8
Scenario A: Positive to positive pore pressure increase (kPa/hr)											
N	35	2	41	4	2	33	0	5	13	0	135
Maximum	8.4	1.3	3.3	1.3	4.5	5.2	NA	1.3	4.6	NA	8.4
Minimum	0.6	0.6	0.6	0.6	0.6	0.6	NA	0.6	0.6	NA	0.6
Mean	2.8	1.0	0.9	0.7	2.6	2.5	NA	0.8	1.9	NA	1.6
Scenario B: Negative to positive pore pressure increase (kPa/hr)											
N	0	10	5	5	6	7	0	3	7	2	45
Maximum	NA	9.1	5.2	1.3	7.8	5.9	NA	1.3	5.2	0.7	9.1
Minimum	NA	3.2	1.3	0.7	3.2	2.6	NA	0.7	1.3	0.7	0.7
Mean	NA	7.0	3.8	0.9	4.7	4.3	NA	0.9	3.2	0.7	3.2
Scenario C: Negative to negative pore pressure increase (kPa/hr)											
N	7	17	24	28	33	21	4	36	14	36	220
Maximum	3.9	32.4	2	6.5	5.2	4.5	0.7	2.6	9	1.9	32.4
Minimum	0.6	0.6	0.6	0.6	0.6	0.6	0.6	0.6	0.6	0.6	0.6
Mean	2.1	3.0	1.1	1.3	1.7	1.1	0.7	0.8	2.2	0.8	1.5

Note: N: Number of pore pressure increase data; NA: Not applicable

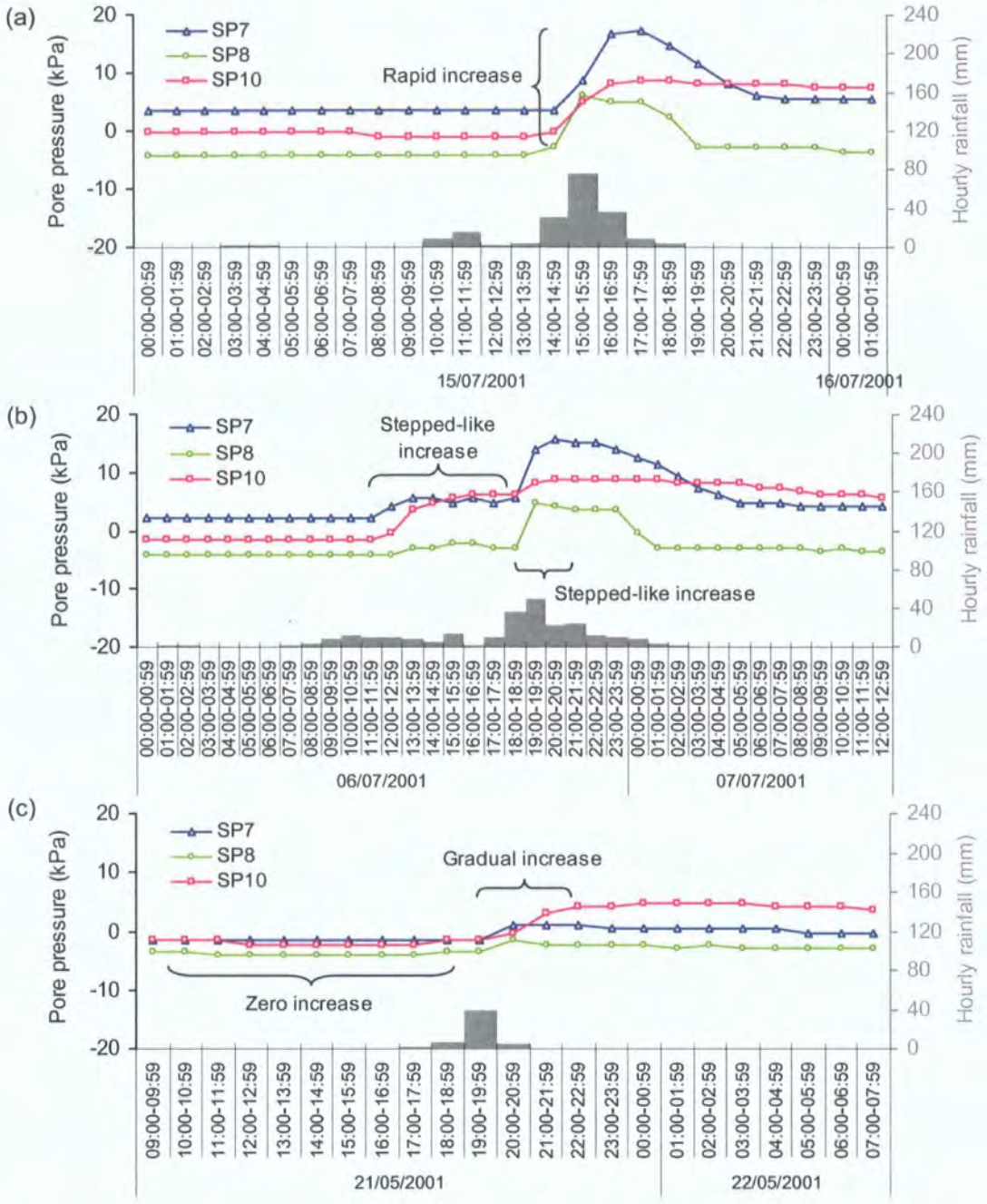

Figure 4.10 Patterns of shallow piezometer response (SP7, SP8, SP10) during rainstorms at Tung Chung East: (a) rapid; (b) stepped; and (c) zero / gradual increase of pore pressures

Figure 4.11 Patterns of increasing pore pressure (Scenario A) during rainstorms fitted by (a) logarithmic, (b) linear, (c) exponential and (d) power functions

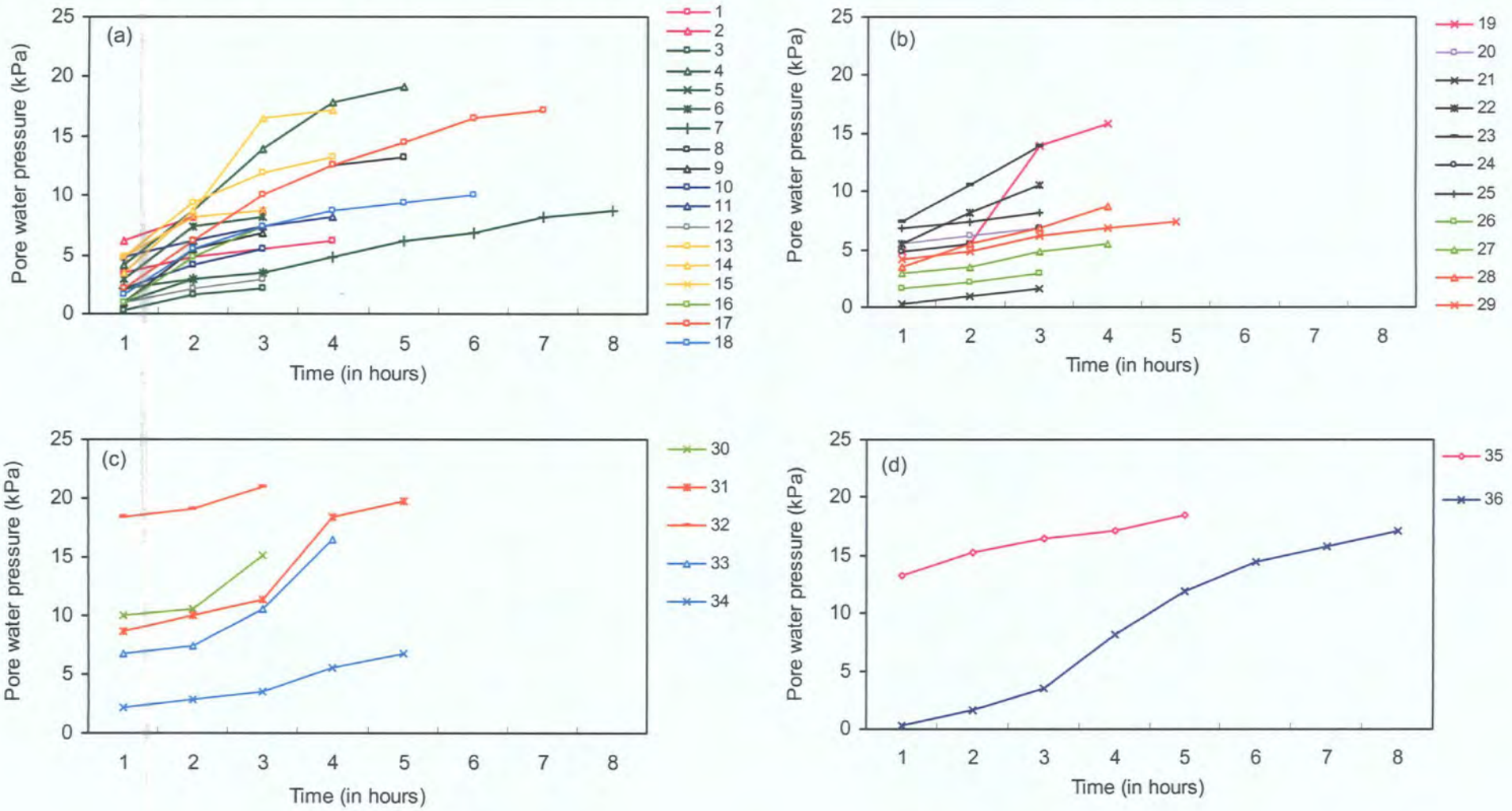

Table 4.6 Pore pressure increasing style during rainstorm periods based on 36 sets of Scenario A data, expressed by the best fit function

Function	Dataset	Rainstorm	Piezometer no. *	Best fit function	R^2 coefficient
Logarithmic	1	07/06/2001	SP10a	y = 1.8585Ln(x) + 3.4984	1.00
	2	07/06/2001	SP10b	y = 2.4225Ln(x) + 6.1865	0.98
	3	11/06/2001	SP1	y = 1.7452Ln(x) + 0.3244	1.00
	4	11/06/2001	SP4	y = 9.7337Ln(x) + 3.42	0.98
	5	11/06/2001	SP5	y = 2.4225Ln(x) + 0.9865	0.98
	6	11/06/2001	SP6	y = 4.9226Ln(x) + 3.1933	0.94
	7	11/06/2001	SP10	y = 3.243Ln(x) + 1.0886	0.89
	8	27/06/2001	SP4a	y = 7.2427Ln(x) + 1.8851	0.98
	9	27/06/2001	SP6	y = 5.5067Ln(x) + 1.1111	0.97
	10	06/07/2001	SP5a	y = 2.991Ln(x) + 2.1803	1.00
	11	06/07/2001	SP6	y = 2.4089Ln(x) + 4.6861	0.99
	12	07/07/2001	SP2	y = 1.8264Ln(x) + 0.9092	1.00
	13	15/07/2001	SP4	y = 6.1462Ln(x) + 4.9417	1.00
	14	15/07/2001	SP5	y = 10.583Ln(x) + 3.0415	0.95
	15	15/07/2001	SP10	y = 3.6803Ln(x) + 5.0019	0.95
	16	30/08/2001	SP4	y = 5.7159Ln(x) + 0.9087	1.00
	17	02/09/2001	SP4	y = 8.0477Ln(x) + 1.48	0.99
	18	05/09/2001	SP4	y = 4.708Ln(x) + 1.9374	0.99
Linear	19	07/06/2001	SP5b	y = 4.14x - 0.35	0.89
	20	08/06/2001	SP10	y = 0.65x + 4.8333	1.00
	21	27/06/2001	SP2	y = 0.65x - 0.3667	1.00
	22	27/06/2001	SP5a	y = 2.55x + 2.9667	1.00
	23	27/06/2001	SP5b	y = 3.25x + 4.1333	1.00
	24	27/06/2001	SP10a	y = x + 3.7	0.97
	25	27/06/2001	SP10b	y = 0.65x + 6.1333	1.00
	26	30/08/2001	SP10a	y = 0.65x + 0.9333	1.00
	27	30/08/2001	SP10b	y = 0.91x + 1.9	0.98
	28	01-02/09/2001	SP6	y = 1.69x + 1.9	0.99
	29	01-02/09/2001	SP10	y = 0.84x + 3.34	0.98
Exponential	30	30/08/2001	SP5	$y = 7.7127e^{0.2094x}$	0.85
	31	01/09/2001	SP5a	$y = 6.576e^{0.2244x}$	0.93
	32	01-02/09/2001	SP5b	$y = 17.059e^{0.0661x}$	0.94
	33	05/09/2001	SP5	$y = 4.5539e^{0.3019x}$	0.93
	34	05/09/2001	SP10	$y = 1.6103e^{0.2897x}$	0.98
Power	35	27/06/2001	SP4b	$y = 13.205x^{0.1991}$	0.99
	36	06-07/07/2001	SP4	$y = 0.3725x^{2.0048}$	0.98

*subscripts a and b indicate the first and second Scenario A datasets identified at the same piezometer in a particular rainstorm

4.3.2 The design of the rate of pore water pressure reinflation

The aim was to design representative rates of pore pressure reinflation at appropriate orders of magnitude, to allow realistic analyses of the relationship between the nature of pore pressure increase during rainstorm events and the deformation of the sample. This was achieved through three series of pore water pressure reinflation rates. The effects of the applied rates within the samples were assessed through comparison with three pore water pressure equalisation tests.

The first series consisted of linear rates of pore pressure reinflation ranging from 0.5 kPa/hr to 100 kPa/hr (i.e. at 0.5 kPa/hr, 1 kPa/hr, 5 kPa/hr, 10 kPa/hr, 15 kPa/hr, 50 kPa/hr and 100 kPa/hr respectively). The 0.5 kPa/hr, 1 kPa/hr and 5 kPa/hr rates represented the linear trends derived from the positive pore water pressure data (Figure 4.11b, Table 4.6, dataset 19-29). They reflect the gradual development of positive pore pressures at the site (e.g. Figure 4.10c). The designed rate of 10 kPa/hr simulated the maximum increase of field pore pressure of Scenario A (Table 4.5).

However, higher rates of linear increase (i.e. 15 kPa/hr, 50 kPa/hr and 100 kPa/hr) were also applied in this research, because there was no available documented evidence during the monitoring period indicating that the field rates had led to the initiation of landslides. This might suggest that higher rates of pore pressure increase could be relevant for simulating the field conditions during landslide-triggering rainstorms. The selected rates for the linear series of pore pressure increasing rates were well within the range used in previous studies (i.e. 0.5 kPa/hr to 240 kPa/hr) (Table 2.4). Moreover, rapid changes in pore pressure conditions in slopes as high as 70 kPa during a rainfall event have been observed in the tropics, such as in Singapore (Gasmo *et al.*, 2000; Rezaur *et al.*, 2002) (Figure 2.3).

The second series involved stepped increases of pore water pressure, which represented the sudden positive responses commonly observed during rainstorms in tropical soils (e.g. Figures 4.10a, 4.10b). The stepped rates were designed at 5 kPa, 10 kPa, 15 kPa, and 50 kPa respectively, corresponding to the linear rates to enable comparison of the deformation processes. The time lag between each step was one hour. This also permitted detailed investigation of the role played by the variability of pore water pressures on pre-failure movements by imposing an abrupt change.

The third series represented the most frequently observed non-linear trend of pore water pressure reinflation over the rainstorm periods, based on the field data (Figure 4.11a, Table 4.6, dataset 1-18). The logarithmic rates of increase used for the

reinflation tests were 54Ln, 67Ln and 77Ln, which were comparable with the linear rates at 5 kPa/hr, 10 kPa/hr and 15 kPa/hr respectively with regard to their similar test duration. For example, for the reinflation tests at 5 kPa/hr and 54Ln kPa/hr (initial back pressure = 200 kPa), the back pressure (that was used to increase pore water pressure within the sample) requires the same amount of time, that is, 40 hours, to reach the target value of 400 kPa.

The above field-referenced series of pore water pressure increasing rates were applied during reinflation testing, and the resulting soil displacements were analysed by the Saito technique to determine the underlying deformation mechanism.

4.3.3 Analysing deformation mechanism by the Saito technique

The 'Saito' technique (Saito, 1965, 1969), expressed in $\Lambda - t$ space (where Λ = 1/velocity; t = time), was applied to investigate the actual landslide processes in weathered soils for the first time. This analytical approach of landslide movements uses the displacement data which were recorded from the reinflation test. Firstly, the velocity was calculated by the change of surface displacement divided by the change of time (Figure 4.12a). Secondly, the reciprocal of velocity was plotted against time (Figure 4.12b). The time of failure might be extrapolated by extending the linear $\Lambda - t$ plot to the horizontal axis (Figure 4.12b). However, a linear trend in $\Lambda - t$ would only occur for brittle failures while an asymptotic trend suggests the dominance of plastic deformation mechanisms (Petley *et al.*, 2002; Kilburn and Petley, 2003).

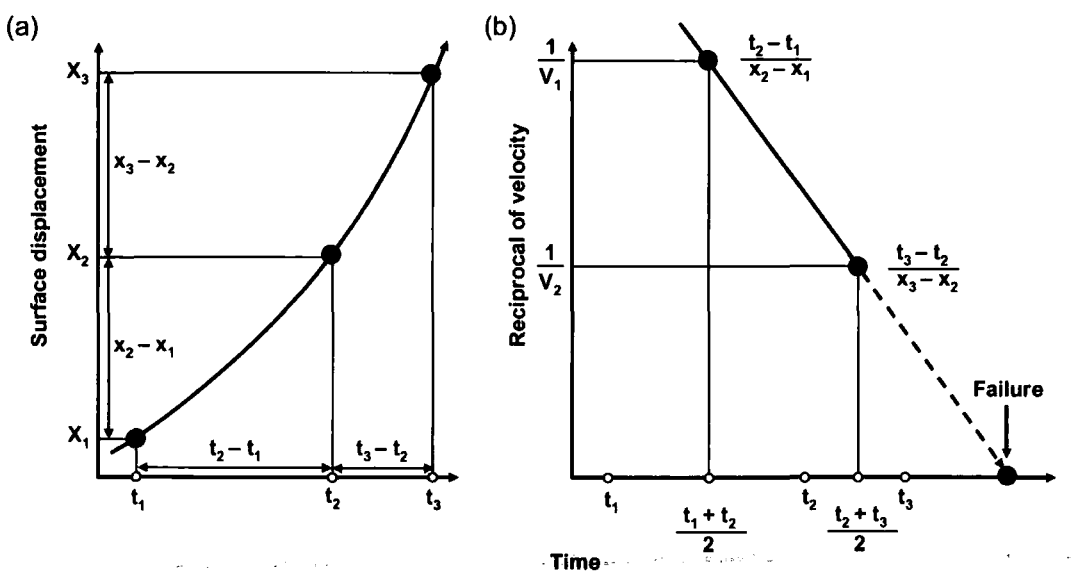

Figure 4.12 The Saito method (after Fukuzono, 1990). (a) First step: calculate velocity from surface displacement data, (b) second step: calculation for the reciprocal of velocity against time, and the extrapolation of the failure time

4.4 Chapter summary

This chapter presents a process-based approach to the investigation of the mechanisms and processes of rainfall-induced landslides on weathered tropical soil slopes. It addresses two main objectives: (1) simulation of the actual processes of rainfall-induced landslide initiation; and (2) analyses of the movement of residual soil under various rates of pore water pressures.

The first objective was addressed by undertaking representative field sampling and the design of an experimental programme. Undisturbed, weathered volcanic soil samples were collected from two landslide sites on Lantau Island, Hong Kong. Typical characteristics of the tropical soils were revealed by physical property tests. Moreover, the field conditions under rainstorms were simulated in a triaxial stress path cell by reinflation testing. The soil samples were subjected to saturation, consolidation under a low confining pressure ($\leq$ 200 kPa), and then reinflation at the field-referenced rates of pore water pressure increase. The maximum shear strength (or the failure envelope) was defined by the conventional isotropic undrained (ICU) and drained (ICD) triaxial tests.

The second objective was addressed through the design of the linear, stepped and logarithmic increase of pore water pressure at different rates, based on the patterns of rainfall-triggered pore water pressures revealed from the monitoring data at the Tung Chung site. The field rates were applied during reinflation testing. The deformation of the samples has been analysed using the Saito technique, which has allowed the determination of the nature of the deformation mechanisms of shallow rainfall-induced landslides within tropical materials.

Chapter 5 Results

5.1 Introduction

This chapter presents results obtained from the physical property tests, the conventional isotropic consolidated undrained (ICU) (Table 5.1) and drained (ICD) tests (Table 5.2), and the field-simulated pore pressure reinflation (PPR) tests under various increasing rates of pore water pressure in linear, stepped and logarithmic forms (Table 5.3). These tests carried the following objectives:

(1) to characterise the material properties of the tropical soils from the two study sites (physical property tests);
(2) to determine the soil strength parameters of the two field sites (ICU, ICD tests) as a reference for the PPR tests;
(3) to assess the influence of the rate and style of increasing pore pressure on soil behaviour towards failure (PPR tests).

Particular focus has been placed on strain development during the ICU, ICD and PPR tests, through examination of the stress-strain relationship and time-dependent soil behaviour.

Table 5.1 Isotropic consolidated undrained (ICU) testing programme

Sample number	Test type	Mean effective stress, p'_c (kPa)	Strain rate, % mm/min	Dry density, Mg/cm^3
TC11	ICU	100	0.1	1.56
TC09	ICU	200	0.1	1.61
TC10	ICU	400	0.1	1.55
PO27	ICU	100	0.1	1.50
PO34	ICU	200	0.1	1.48
PO29	ICU	400	0.1	1.49

Table 5.2 Isotropic consolidated drained (ICD) testing programme

Sample number	Test type	Mean effective stress, p'_c (kPa)	Strain rate, % mm/min	Dry density, Mg/cm^3
TC39	ICD	50	0.01	1.57
TC34	ICD	100	0.01	1.56
TC33	ICD	200	0.01	1.51
PO04	ICD	50	0.01	1.50
PO06	ICD	100	0.01	1.53
PO05	ICD	200	0.01	1.42

Table 5.3 Pore water reinflation (PPR) testing programme (p'_{dis} at 233 kPa)

(a) TC soils

Sample number	Test type	Deviatoric stress, q	PPR rate	Dry density, Mg/m^3
TC28	Linear	100	10	1.56
TC24	Linear	200	10	1.68
TC26	Linear	300	10	1.59
TC40	Linear	100	0.5	1.55
TC14	Linear	100	1	1.58
TC27	Linear	100	5	1.56
TC28	Linear	100	10	1.56
TC32	Linear	100	15	1.60
TC38	Linear	100	15	1.62
TC23	Linear	100	50	1.61
TC16	Linear	100	100	1.63
TC29	Stepped	100	5	1.52
TC21	Stepped	100	10	1.55
TC31	Stepped	100	15	1.54
TC22	Stepped	100	50	1.52
TC30	Logarithmic	100	54Ln	1.57
TC36	Logarithmic	100	67Ln	1.57
TC37	Logarithmic	100	77Ln	1.61

(b) PO soils

Sample number	Test type	Deviatoric stress, q	PPR rate	Dry density, Mg/cm^3
PO07	Linear	100	10	1.43
PO19	Linear	200	10	1.51
PO31	Linear	300	10	1.58
PO37	Linear	100	0.5	1.52
PO24	Linear	100	1	1.53
PO11	Linear	100	5	1.47
PO07	Linear	100	10	1.43
PO12	Linear	100	15	1.47
PO13	Linear	100	100	1.48
PO25	Stepped	100	5	1.51
PO23	Stepped	100	10	1.42
PO30	Stepped	100	15	1.46
PO38	Stepped (constant)	100	5	1.51
PO33	Logarithmic	100	54Ln	1.45
PO35	Logarithmic	100	67Ln	1.50
PO40	Logarithmic	100	77Ln	1.54
POD17*	Logarithmic	100	54Ln	1.45
POD14*	Logarithmic	100	67Ln	1.44
POD16*	Logarithmic	100	77Ln	1.47

* Damaged sample

5.2 Physical properties

The physical properties of Tung Chung (TC) and Pui O (PO) soil samples are summarised in Table 5.4. Both samples are intensely weathered volcanics, of which the former is derived from Mesozoic rhyolite lava and tuff while the latter is derived from Mesozoic crystalline tuff (Langford *et al.*, 1995).

Based on their particle size distribution, both soils can be classified as fine-grained, with less than 10% of particles larger than 2 mm (BSI, 1990a). They are largely composed of silt (49 - 60%), about 25% clay and less than 20% sand (Table 5.4, Figure 5.1). The samples are well-graded with a wide range of particle sizes, as indicated by high values of the uniformity coefficient (> 10) (Bell, 2000).

The specific gravity values of the samples are very similar, lying within the average range for most common soils between 2.65 to 2.75 (Aktinson and Bransby, 1978). The low values of loss on ignition demonstrate their inorganic nature.

A slightly higher moisture content was found within the PO samples. The moisture content difference at 45°C and 105°C for both the TC and PO samples was only about 0.6%, which might suggest an insignificant amount of water of crystallization within the mineral structure (Fookes, 1997). The Atterberg limits of the two fine-grained soil samples suggest that their mechanical behaviour is slightly different (Terzaghi *et al.*, 1996). Based on the plasticity chart (BS 5930: 1981), the TC material is classified as CLAY of Intermediate plasticity (denoted as CI), while the PO sample is referred as SILT of High plasticity (denoted as MH) (Figure 5.2).

The initial void ratio and dry density show that the undisturbed TC samples are denser. The initial void ratio of the undisturbed TC samples ranged between 0.60 and 0.78, with an average of 0.70, while PO samples had higher void ratios of between 0.70 and 0.89, with an average of 0.81. The denser TC samples had dry densities between 1.51 Mg/m^3 and 1.68 Mg/m^3, with an average of 1.58 Mg/m^3; whereas the PO samples were characterised by lower densities ranging from 1.42 Mg/m^3 to 1.58 Mg/m^3, with an average of 1.49 Mg/m^3.

The coefficient of permeability, k , calculated from the consolidation parameters further demonstrates that most of the TC and PO samples have values between 0.3 and 0.4 x 10^{-9} m/s (Figure 5.3, Table 5.5). The PO samples on average are more permeable than the TC samples. The average k value of the TC and PO samples are 0.22 x 10^{-9} and 0.27 x 10^{-9} m/s respectively, derived from all the undisturbed samples

under consolidation pressure at 200 kPa. Higher permeability values also tend to occur at lower effective consolidation pressures (e.g. p'_c = 50, 100 kPa) within both samples, and when the pressure was applied rapidly (e.g. TC09, TC10, TC11).

Table 5.4 Physical properties of Tung Chung (TC) and Pui O (PO) samples

Physical properties		TC (Weathered rhyolite lava and tuff)	PO (Weathered crystal tuff)
Particle size analysis			
Gravel	> 2 mm	1.3	8.9
Sand	Coarse (0.6-2 mm)	0.0	0.0
	Medium (0.2-0.6 mm)	4.8	6.9
	Fine (0.06-0.2 mm)	8.9	10.2
Silt	Coarse (0.02-0.06 mm)	14.2	9.8
	Medium (0.006-0.02 mm)	18.3	17.1
	Fine (0.002-0.006 mm)	27.8	21.7
Clay	<0.002 mm	24.7	25.5
	D_{10}, μm	0.85	0.80
	D_{30}, μm	2.52	2.54
	D_{60}, μm	8.90	14.08
Coefficient of uniformity (D_{60}/D_{10}), C_u		10.47	17.60
Specific gravity, G_s		2.683	2.684
Loss on ignition, LOI		4.686	2.598
Moisture content, % (at 45°C/ 105°C) #		17.3 / 17.9	18.9 / 19.5
Liquid limit, W_L % (at 45°C/ 105°C)		46.96 / 47.54	54.31 / 55.10
Plastic limit, W_P % (at 45°C/ 105°C)		23.82 / 24.32	29.25 / 29.97
Plasticity Index, I_P		23.14 / 23.22	25.06 / 25.13
Void ratio, e #		0.70	0.81
Bulk density, γ_{wet}, Mg/m^3 #		1.85	1.76
Dry density, γ_d, Mg/m^3 #		1.58	1.49

Results were derived from all of the undisturbed samples. The other physical properties were tested on loose samples

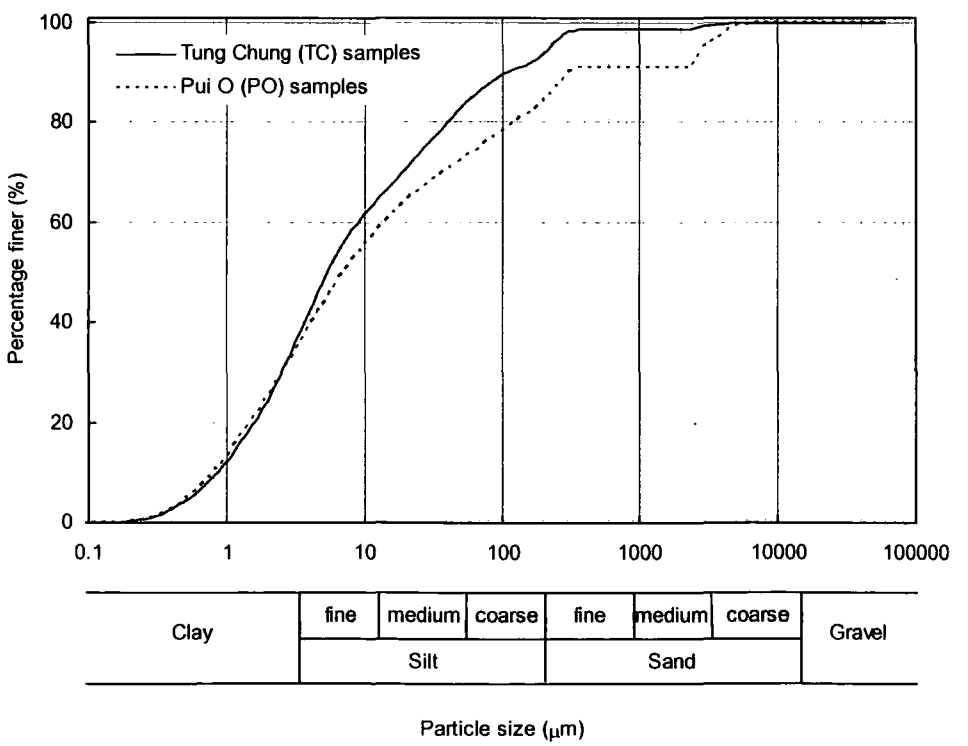

Figure 5.1 Particle size distribution chart for TC and PO soil samples

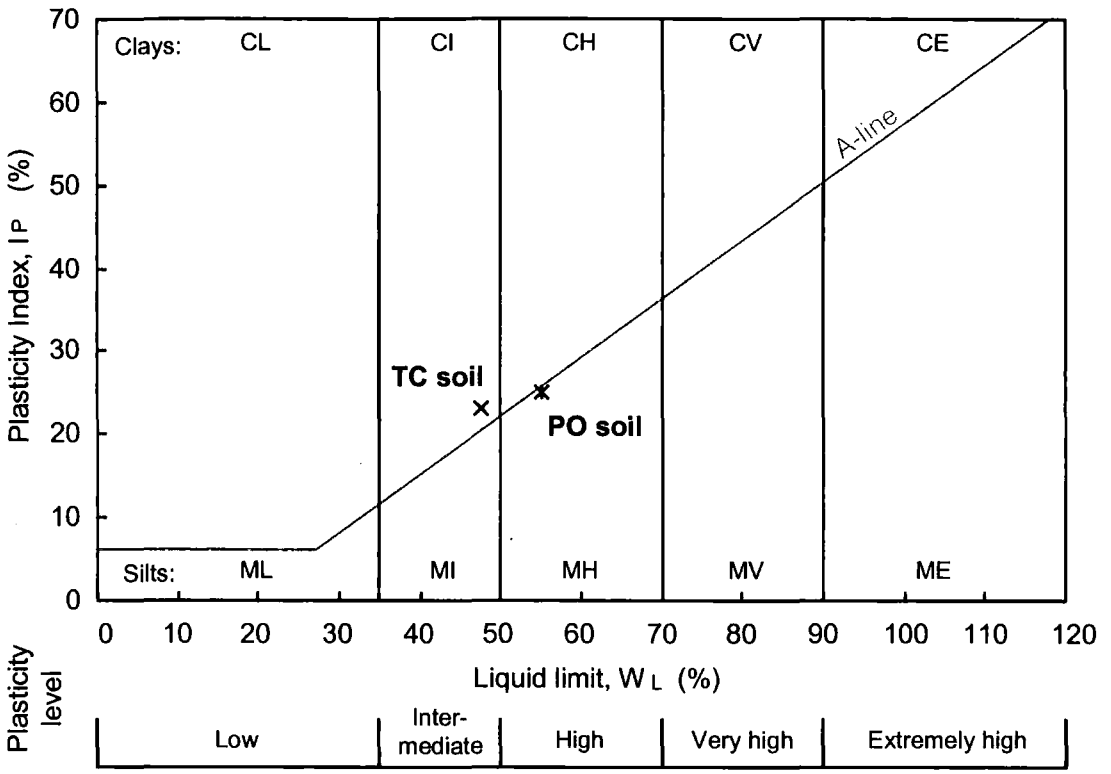

Figure 5.2 Classification of TC and PO soils in the plasticity chart (after BSI, 1981)

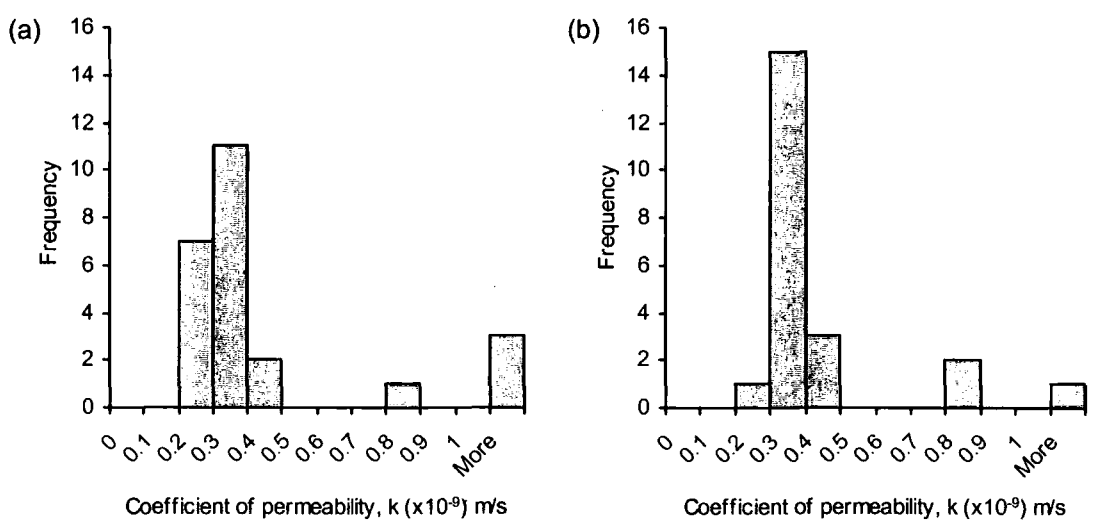

Figure 5.3 Histogram showing the frequency distribution of the coefficient of permeability of undisturbed samples under consolidation pressures 50-400 kPa:
(a) undisturbed TC samples; (b) undisturbed PO samples

Table 5.5 The coefficient of permeability derived from all samples at consolidation stage

(a) TC samples

	Sample number	Consolidation pressure (p'_c, in kPa)	Permeability coefficient (k, x10^{-9} m/s)
ICU	TC11*	100	0.19
	TC09*	200	1.9
	TC10*	400	3.3
ICD	TC39	50	1.5
	TC34	100	0.78
	TC33	200	0.29
PPR	TC28	200	0.22
	TC24	200	0.19
	TC26	200	0.21
(Linear)	TC40	200	0.22
	TC14	200	0.19
	TC27	200	0.15
	TC28	200	0.22
	TC32	200	0.18
	TC38	200	0.14
(Step)	TC23	200	0.21
	TC16	200	0.22
	TC29	200	0.23
	TC21	200	0.33
	TC31	200	0.20
(Log)	TC22	200	0.32
	TC30	200	0.25
	TC36	200	0.27
	TC37	200	0.14

*Opening valves after target consolidation pressure was achieved, instead of ramping

(b) PO samples

	Sample number	Consolidation pressure (p'_c, in kPa)	Permeability coefficient (k, x10^{-9} m/s)
ICU	PO27	100	0.71
	PO34	200	0.25
	PO29	400	0.11
ICD	PO04	50	1.5
	PO06	100	0.76
	PO05	200	0.26
PPR	PO07	200	0.30
	PO19	200	0.24
	PO31	200	0.23
(Linear)	PO37	200	0.26
	PO24	200	0.22
	PO11	200	0.29
	PO07	200	0.30
	PO12	200	0.27
(Step)	PO13	200	0.31
	PO25	200	0.27
	PO23	200	0.32
	PO30	200	0.26
	PO38	200	0.30
(Log)	PO33	200	0.24
	PO35	200	0.24
	PO40	200	0.23
	POD17	200	0.36
	POD14	200	0.29
	POD16	200	0.29

5.3 Saturation

The saturation stage was applied to all soil samples before the ICU, ICD and PPR testing. All samples were fully saturated with B-values equal to 0.98 or higher (Table 5.6). The axial length, volume and void ratio of the samples changed little during saturation stage as most samples showed only a slight increase in length and volume change of less than 1% (Table 5.6). The void ratios were essentially unchanged. The effect of the saturation stage on the sample dimensions, therefore, was not significant.

Overall, the TC samples swelled to a larger degree during saturation (0.08-0.88% swelling), while the PO samples were much less responsive (0.01-0.24% swelling) (Table 5.6).

Table 5.6 Sample dimensions in axial length (L), volume (V) and void ratio (e) before and after saturation, with the degree of change expressed in strain (ε)

	Sample number	Before saturation L_0 (mm)	V_0 (mm^3)	e_0	After saturation L_{sat} (mm)	$\varepsilon_{L,sat}$ (%)	V_{sat} (mm^3)	$\varepsilon_{v,sat}$ (%)	e_{sat}	B-value
ICU PPR (Linear)	TC11	77.32	87828	0.72	77.87	0.71*	88453	0.71*	0.73	1.00
	TC09	76.09	88489	0.67	75.82	0.35	88175	0.35	0.66	1.00
	TC10	75.89	85570	0.74	75.28	0.80	84883	0.80	0.72	0.98
ICD PPR (Linear)	TC39	76.44	83304	0.72	76.38	0.08	83238	0.08	0.71	0.99
	TC34	75.82	83206	0.72	76.38	0.74*	83820	0.74*	0.73	1.00
	TC33	76.64	81871	0.78	76.70	0.08*	81935	0.08*	0.78	0.99
ICU PPR (Linear)	TC28	76.38	83372	0.72	76.85	0.62*	83885	0.62*	0.72	1.00
	TC24	75.32	80330	0.60	75.88	0.74*	80927	0.74*	0.60	1.00
	TC26	76.30	84541	0.69	76.39	0.12*	84641	0.12*	0.69	0.99
ICD PPR (Linear)	TC40	76.53	86383	0.74	76.98	0.58*	86887	0.58*	0.75	1.00
	TC14	75.59	85728	0.70	75.26	0.44	85354	0.44	0.70	1.00
	TC27	75.56	82035	0.72	75.74	0.24*	82231	0.24*	0.72	0.99
ICU PPR (Step)	TC28	76.38	83372	0.72	76.85	0.62*	83885	0.62*	0.73	1.00
	TC32	76.45	84482	0.68	76.76	0.41*	84824	0.41*	0.68	1.00
	TC38	76.23	83835	0.66	76.51	0.37*	84143	0.37*	0.66	0.98
ICD PPR (Step)	TC23	76.07	84241	0.66	76.69	0.82*	84928	0.82*	0.66	0.99
	TC16	75.11	81021	0.64	74.46	0.87	80320	0.87	0.64	0.98
	TC29	76.58	80042	0.77	77.08	0.65*	80564	0.65*	0.77	1.00
ICU PPR (Step)	TC21	75.46	82147	0.74	75.84	0.50*	82561	0.50*	0.74	0.99
	TC31	76.04	84163	0.75	76.16	0.16*	84296	0.16*	0.75	0.99
	TC22	75.79	84603	0.77	76.13	0.45*	84982	0.45*	0.77	0.99
ICD PPR (Step)	TC30	76.64	82271	0.71	77.01	0.48*	82668	0.48*	0.71	1.01
	TC36	76.15	80555	0.71	76.82	0.88*	81264	0.88*	0.71	0.99
	TC37	76.38	82926	0.66	76.58	0.26*	83143	0.26*	0.66	0.99
ICU PPR (Log)	PO27	74.98	83211	0.80	75.11	0.17*	83355	0.17*	0.80	0.98
	PO34	75.71	87772	0.82	75.78	0.09*	87854	0.09*	0.82	0.98
	PO29	74.75	82251	0.80	74.84	0.12*	82350	0.12*	0.80	0.98
ICD PPR (Log)	PO04	76.84	85730	0.79	76.85	0.01*	85741	0.01*	0.79	1.00
	PO06	77.00	84863	0.76	77.04	0.05*	84907	0.05*	0.76	0.99
	PO05	78.14	86718	0.89	78.15	0.01*	86729	0.01*	0.89	1.00
ICU PPR (Log)	PO07	78.09	90862	0.88	78.08	0.01	90850	0.01	0.88	1.01
	PO19	74.88	86991	0.77	74.90	0.03*	87014	0.03*	0.77	0.99
	PO31	75.70	84547	0.70	75.60	0.13	84436	0.13	0.70	0.98
ICD PPR (Log)	PO37	77.10	86111	0.76	77.22	0.16*	86245	0.16*	0.77	1.00
	PO24	74.63	87832	0.75	74.73	0.13*	87949	0.13*	0.75	0.99
	PO11	76.54	86440	0.83	76.49	0.07	86384	0.07	0.83	1.00
ICU PPR (Linear)	PO07	78.09	90862	0.88	78.08	0.01	90850	0.01	0.88	1.01
	PO12	76.18	86761	0.83	76.18	0.00	86761	0.00	0.83	1.00
	PO13	74.62	82900	0.82	74.58	0.05	82855	0.05	0.82	1.00
ICD PPR (Linear)	PO25	76.20	84520	0.78	76.37	0.22*	84709	0.22*	0.78	0.98
	PO23	74.69	85870	0.89	74.60	0.12	85767	0.12	0.89	1.00
	PO30	75.24	88230	0.84	74.93	0.41	87866	0.41	0.83	0.98
ICU PPR (Linear)	PO38	77.85	85342	0.77	78.04	0.24*	85550	0.24*	0.78	1.00
	PO33	76.73	89605	0.85	76.81	0.10*	89698	0.10*	0.85	1.00
	PO35	78.17	88095	0.79	78.20	0.04*	88129	0.04*	0.79	0.98
ICD PPR (Step)	PO40	78.36	88309	0.74	78.43	0.09*	88388	0.09*	0.74	1.00
	POD17	75.70	86713	0.85	75.68	0.03	86690	0.03	0.85	0.98
	POD14	76.23	88975	0.86	76.18	0.07	88916	0.07	0.86	0.98
ICU PPR (Step)	POD16	75.93	85571	0.83	75.88	0.07	85514	0.07	0.83	0.99

*Sample swelled

5.4 Consolidation

The isotropic consolidation properties in terms of the coefficient of consolidation (c_{vi}) and coefficient of volume compressibility (m_{vi}) are presented in Table 5.7. These were used to determine the coefficient of permeability (k).

A decrease in axial length, volume and void ratio was clearly shown during consolidation at various effective stresses (cf. Tables 5.6, 5.8). The axial strains after consolidation ranged from 0.70 to 2.80% (average: 1.40%) within the TC samples, and from 0.48 to 3.05% (average 1.78%) within the PO samples. The maximum, minimum and average volumetric strains were 8.45%, 2.17%, 5.03% for the TC samples, and 10.42%, 2.15% and 5.99% for the PO samples, respectively. The void ratio after consolidation was between 0.54 and 0.68 (average: 0.62) for the TC samples and between 0.61 and 0.78 (average: 0.70) for the PO samples. Therefore, the looser PO samples were subjected to larger axial and volumetric strains but still had higher void ratios during the consolidation process.

The form of the consolidation curves appeared largely similar between the TC (except TC09, TC10, TC11) and PO samples (Figure 5.4). Also, less time was required to complete consolidation at lower effective stresses, as shown by the position of the flat lines showing zero volume change. The consistent behaviour was related to the same gradual rate of increase in the consolidation pressure being applied. In contrast, the sudden increase of volumetric strain in samples TC09, TC10 and TC11 were due to a different consolidation procedure which involved the opening of valves immediately after the target consolidation pressure was reached.

The consolidation curves further demonstrated that the volumetric strain was positively related to the amount of effective stress applied (Figure 5.5). Samples subjected to higher effective stresses generally resulted in the larger amount of volumetric strain and vice versa. The unexpectedly lower volumetric strain of sample TC09 after consolidation appeared to be associated with its much lower initial void ratio (Figure 5.6) (Table 5.6).

However, complexities in the consolidation behaviour were also observed which could not simply be explained by the effective stress level or the initial void ratio. This was illustrated by the subtle variability in volumetric strain within some of the TC and PO samples of the same void ratio tested under the same effective stress (Figure 5.7). This interesting result suggests the heterogeneous nature of the weathered samples.

Table 5.7 Isotropic consolidation properties in terms of coefficient of consolidation (c_{vi}) and coefficient of volume compressibility (m_{vi})

	Sample number	Coefficient of consolidation			Coefficient of volume compressibility			
		D_c (mm)	t_{100} (min)	c_{vi} (m^2/year)	ΔV_c (cm^3)	V_0 (cm^3)	$\Delta\sigma'$ (kPa)	m_{vi} (m^2/MN)
ICU	TC11	37.73	300	2.0	2.71	88.5	100	0.31
ICD	TC09	37.80	21	28	3.80	88.2	200	0.22
PPR	TC10	36.59	11	50	7.17	84.9	400	0.21
(Linear)	TC39	37.00	50	11	1.81	83.2	50	0.43
	TC34	36.64	100	5.5	3.82	83.8	100	0.46
	TC33	35.83	200	2.6	5.82	81.9	200	0.36
	TC28	36.57	200	2.8	4.35	83.9	200	0.26
	TC24	36.27	200	2.7	3.62	80.9	200	0.22
	TC26	36.89	200	2.8	4.00	84.6	200	0.24
	TC40	37.21	200	2.9	4.31	86.9	200	0.25
(Step)	TC14	37.30	200	2.9	3.70	85.4	200	0.22
	TC27	36.84	200	2.8	2.80	82.2	200	0.17
	TC28	36.57	200	2.8	4.35	83.9	200	0.26
	TC32	36.92	200	2.8	3.46	84.8	200	0.20
	TC38	36.98	200	2.8	2.78	84.1	200	0.17
	TC23	36.95	200	2.8	4.00	84.9	200	0.24
	TC16	36.43	200	2.7	4.08	80.3	200	0.25
	TC29	35.63	200	2.6	4.58	80.6	200	0.28
	TC21	36.05	200	2.7	6.56	82.6	200	0.40
	TC31	36.85	200	2.8	3.89	84.3	200	0.23
	TC22	36.59	200	2.8	6.35	85.0	200	0.37
(Log)	TC30	36.10	200	2.7	5.00	82.7	200	0.30
	TC36	36.02	200	2.7	5.20	81.3	200	0.32
	TC37	36.72	200	2.8	2.78	83.1	200	0.17
ICU	PO27	36.95	100	5.6	3.39	83.4	100	0.41
ICD	PO34	37.54	200	2.9	4.93	87.9	200	0.28
PPR	PO29	35.92	400	1.3	8.58	82.4	400	0.26
(Linear)	PO04	37.37	50	12	1.85	85.7	50	0.43
	PO06	36.80	100	5.6	3.75	84.9	100	0.44
	PO05	36.91	200	2.8	5.15	86.7	200	0.30
	PO07	37.68	200	2.9	5.95	90.9	200	0.33
	PO19	37.71	200	2.9	4.67	87.0	200	0.27
	PO31	36.99	200	2.8	4.36	84.4	200	0.26
	PO37	36.83	200	2.8	5.07	86.2	200	0.29
	PO24	38.14	200	3.0	4.09	87.9	200	0.23
(Step)	PO11	36.99	200	2.8	5.72	86.4	200	0.33
	PO07	37.68	200	2.9	5.95	90.9	200	0.33
	PO12	37.19	200	2.9	5.25	86.8	200	0.30
	PO13	36.63	200	2.8	6.00	82.9	200	0.36
	PO25	36.73	200	2.8	5.39	84.7	200	0.32
	PO23	37.29	200	2.9	6.19	85.8	200	0.36
	PO30	37.87	200	3.0	5.00	87.9	200	0.28
	PO38	36.46	200	2.7	6.11	85.6	200	0.36
(Log)	PO33	37.80	200	2.9	4.74	89.7	200	0.26
	PO35	37.08	200	2.8	4.75	88.1	200	0.27
	PO40	37.16	200	2.8	4.58	88.4	200	0.26
	POD17	37.17	200	2.8	7.06	86.7	200	0.41
	POD14	37.69	200	2.9	5.58	88.9	200	0.31
	POD16	36.94	200	2.8	5.63	85.5	200	0.33

Table 5.8 Axial length (L), volume (V), strains (ε) and void ratio (e) after consolidation

	Sample number	Consolidation pressure (kPa)	After consolidation				
			L_c (mm)	V_c (mm^3)	$\varepsilon_{L,c}$ (%)	$\varepsilon_{v,c}$ (%)	e_c
ICU	TC11	100	76.67	85739	1.54	3.07	0.68
ICD	TC09	200	75.17	84378	0.86	4.31	0.59
PPR	TC10	400	73.89	77714	1.85	8.45	0.58
(Linear)	TC39	50	75.72	81428	0.86	2.17	0.68
	TC34	100	75.38	80002	1.31	4.56	0.65
	TC33	200	75.49	76113	1.58	7.11	0.65
	TC28	200	75.72	79540	1.47	5.18	0.64
	TC24	200	74.83	77304	1.38	4.48	0.54
	TC26	200	75.44	80637	1.24	4.73	0.61
	TC40	200	75.95	82582	1.34	4.95	0.66
	TC14	200	74.73	81654	0.70	4.33	0.62
	TC27	200	74.52	79429	1.61	3.41	0.63
	TC28	200	75.72	79540	1.47	5.18	0.64
	TC32	200	76.00	81368	0.99	4.07	0.61
	TC38	200	75.76	81360	0.98	3.31	0.61
	TC23	200	75.45	80924	1.62	4.71	0.60
	TC16	200	73.15	76237	1.76	5.08	0.55
(Step)	TC29	200	76.21	75981	1.13	5.69	0.68
	TC21	200	74.47	75998	1.81	7.95	0.61
	TC31	200	75.38	80402	1.02	4.62	0.67
	TC22	200	74.77	78636	1.79	7.47	0.64
(Log)	TC30	200	75.87	77664	1.48	6.05	0.61
	TC36	200	74.67	76069	2.80	6.39	0.61
	TC37	200	75.87	80366	0.93	3.34	0.61
ICU	PO27	100	74.57	79967	0.72	4.06	0.73
ICD	PO34	200	74.94	82929	1.11	5.61	0.72
PPR	PO29	400	72.80	73769	2.73	10.42	0.61
(Linear)	PO04	50	76.48	83893	0.48	2.15	0.75
	PO06	100	76.32	81158	0.93	4.42	0.68
	PO05	200	76.23	81576	2.46	5.94	0.78
	PO07	200	76.14	84896	2.48	6.55	0.75
	PO19	200	73.73	82343	1.56	5.37	0.68
	PO31	200	74.51	80073	1.44	5.17	0.61
	PO37	200	76.18	81171	1.35	5.88	0.66
	PO24	200	73.39	83864	1.79	4.65	0.67
	PO11	200	75.05	80668	1.88	6.62	0.71
	PO07	200	76.14	84896	2.48	6.55	0.75
	PO12	200	75.02	81514	1.52	6.05	0.72
	PO13	200	72.92	76854	2.23	7.24	0.68
(Step)	PO25	200	74.87	79323	1.96	6.36	0.67
	PO23	200	72.88	79577	2.31	7.22	0.75
	PO30	200	73.57	82871	1.82	5.68	0.73
	PO38	200	76.08	79440	2.51	7.14	0.65
(Log)	PO33	200	75.7	84962	1.45	5.28	0.76
	PO35	200	77.19	83377	1.29	5.39	0.70
	PO40	200	77.28	83812	1.47	5.18	0.65
	POD17	200	73.37	79633	3.05	8.14	0.70
	POD14	200	74.71	83335	1.93	6.28	0.75
	POD16	200	74.55	79889	1.75	6.58	0.71

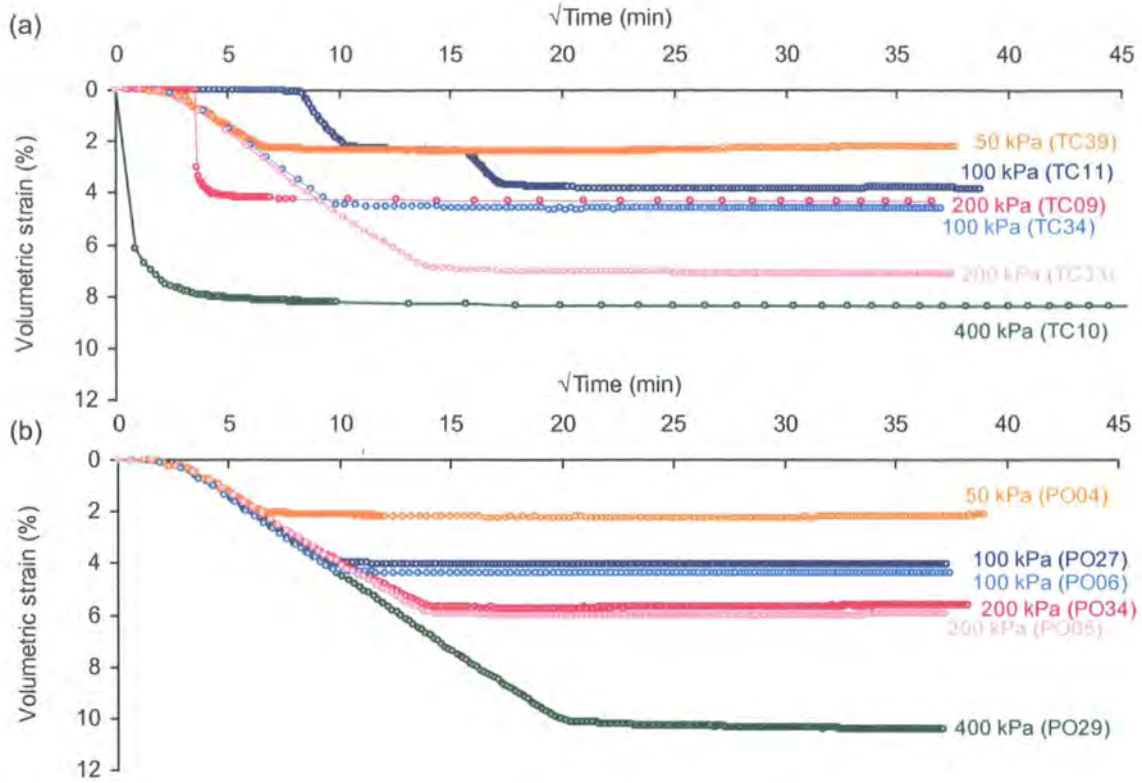

Figure 5.4 Consolidation curves at effective stresses 50, 100, 200 and 400 kPa on samples prepared for the ICU and ICD tests: (a) TC samples; (b) PO samples

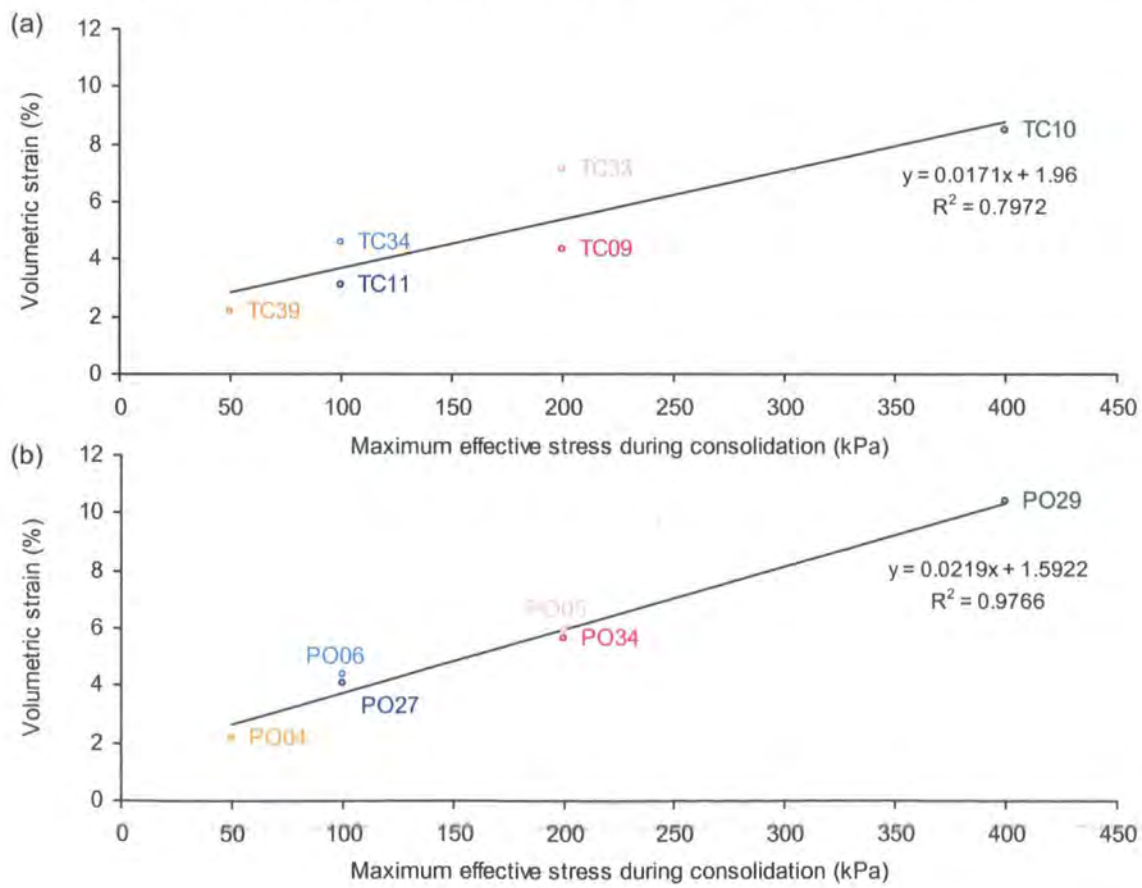

Figure 5.5 Plots of maximum effective stress against volumetric strain during consolidation: (a) TC samples; (b) PO samples

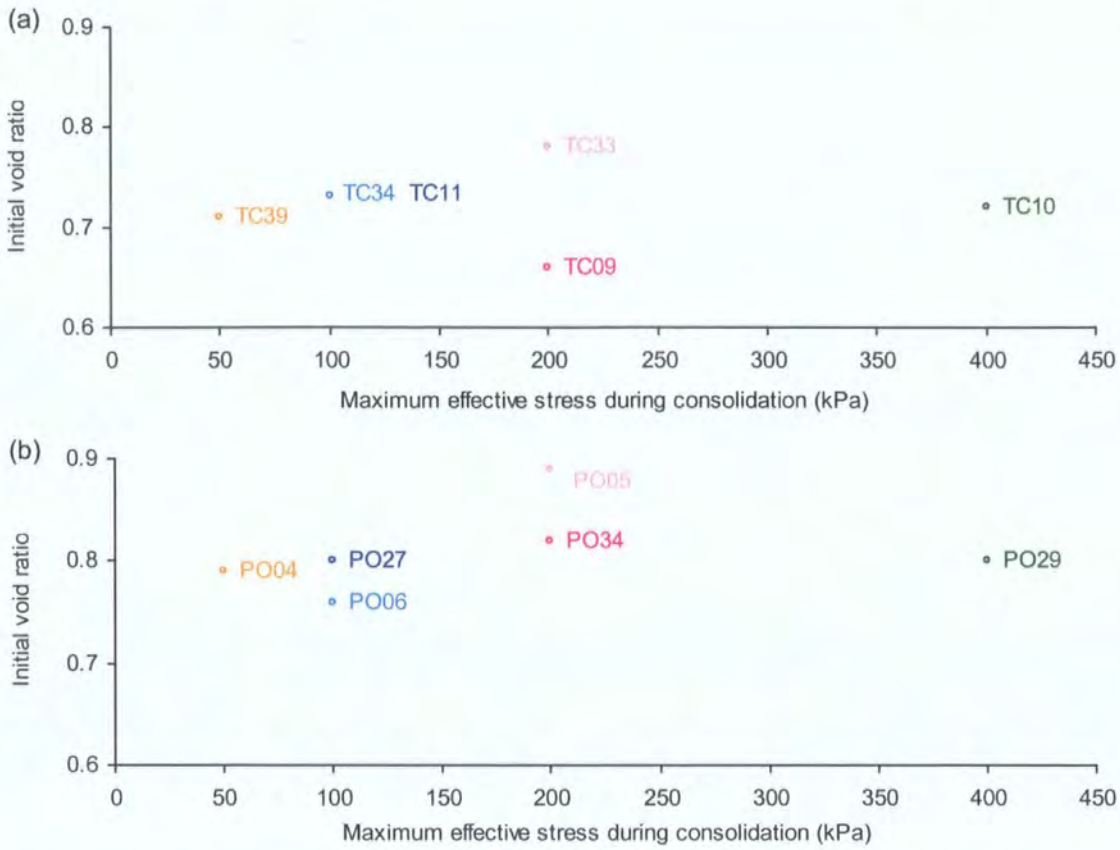

Figure 5.6 Plots of maximum effective stress during consolidation against initial void ratio: (a) TC samples; (b) PO samples

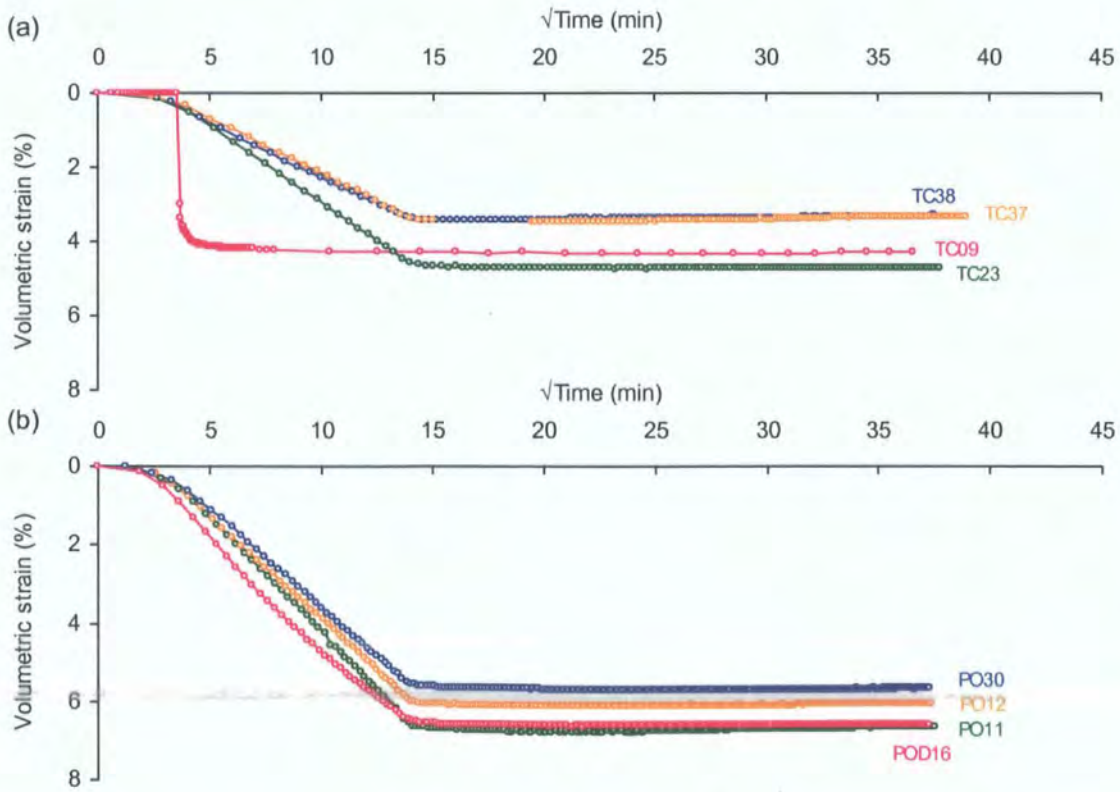

Figure 5.7 Consolidation curves at effective stress 200 kPa on samples having the same initial void ratio: (a) TC samples (e = 0.66); (b) PO samples (e = 0.83)

5.5 Isotropic consolidated undrained (ICU) shear tests

This section presents the shearing stage of the ICU tests including (1) an exploration of strain development prior to failure; (2) determination of the failure envelope and the related shear strength parameters; and (3) the stress-strain relationship under these strain-rate controlled triaxial tests.

5.5.1 Strain development prior to failure

Failure analyses seldom consider strain development towards failure. However, plotting axial strain contours in terms of the effective cohesion (c') and angle of internal friction (ϕ') allow the strain development process during the strain-controlled ICU (and ICD) test results (Table 5.9, Figure 5.8) to be compared with the stress-controlled PPR tests. The shear strength parameters were derived from the Mohr circles (Figure 5.9).

During the undrained shear, both samples rapidly mobilised frictional strength while there was a slight increase of cohesion at 1% strain, followed by a sharp decrease at small strains (Figure 5.8). This was also reflected by the steepness of the axial strain contours which increased rapidly below 5% axial strain (Figure 5.9), implying a disproportionate increase of shear stress mobilisation. At larger strains, however, the derived effective cohesion and friction angles were similar towards failure. This was indicated by the largely constant slopes of $\tau_{max} - \sigma'$ at 5-20% strains (Figure 5.9).

Changes of the shear strength parameters (c', ϕ') were more pronounced within the PO samples. They generated a higher frictional angle and lower cohesion than the TC samples during undrained testing.

Table 5.9 Strain development in terms of failure parameters derived from ICU tests

(a) TC soils (TC09, TC10, TC11)

Failure criteria	Effective frictional angle, ϕ' (°)	Effective cohesion, c' (kPa)	Correlation coefficient, R^2
τ_{max}	27.0	7.4	1.00
ε_a = 0.5 %	11.0	15.0	0.99
ε_a = 1 %	14.7	16.0	1.00
ε_a = 2 %	19.7	14.9	1.00
ε_a = 3 %	22.7	12.9	1.00
ε_a = 4 %	24.0	12.2	1.00
ε_a = 5 %	25.9	9.8	1.00
ε_a = 6 %	27.5	7.9	1.00
ε_a = 7 %	27.7	8.2	1.00
ε_a = 8 %	27.3	9.9	1.00
ε_a = 9 %	28.2	8.6	1.00
ε_a = 10 %	28.7	7.4	1.00
ε_a = 11 %	28.5	7.5	1.00
ε_a = 12 %	29.0	6.5	1.00
ε_a = 13 %	29.0	10.2	1.00
ε_a = 14 %	28.3	8.4	1.00
ε_a = 15 %	28.1	8.9	1.00
ε_a = 16 %	27.5	10.8	1.00
ε_a = 17 %	28.3	8.4	1.00
ε_a = 18 %	27.3	10.6	1.00
ε_a = 19 %	27.0	11.1	1.00
ε_a = 20 %	26.9	11.5	1.00
ε_a = 25 %	26.0	11.7	1.00
ε_a = 30 %	25.6	10.5	1.00

(b) PO soils (PO27, PO29, PO34)

Failure criteria	Effective frictional angle, ϕ' (°)	Effective cohesion, c' (kPa)	Correlation coefficient, R^2
τ_{max}	33.8	0	1.00
ε_a = 0.5 %	15.0	11.2	1.00
ε_a = 1 %	19.1	14.0	1.00
ε_a = 2 %	25.8	8.7	1.00
ε_a = 3 %	30.0	4.6	1.00
ε_a = 4 %	31.1	4.1	1.00
ε_a = 5 %	32.8	1.8	1.00
ε_a = 6 %	33.4	1.4	1.00
ε_a = 7 %	33.5	2.4	1.00
ε_a = 8 %	34.3	0.8	1.00
ε_a = 9 %	35.2	0.3	1.00
ε_a = 10 %	34.1	1.0	1.00
ε_a = 11 %	34.8	0.7	1.00
ε_a = 12 %	34.9	0.5	1.00
ε_a = 13 %	34.4	1.1	1.00
ε_a = 14 %	34.8	0.1	1.00
ε_a = 15 %	34.0	1.7	1.00
ε_a = 16 %	33.2	2.6	1.00
ε_a = 17 %	33.2	2.5	1.00
ε_a = 18 %	33.3	1.6	1.00
ε_a = 19 %	33.4	1.2	1.00
ε_a = 20 %	33.3	1.4	1.00
ε_a = 25 %	32.2	1.9	1.00
ε_a = 30 %	32.7	1.0	1.00

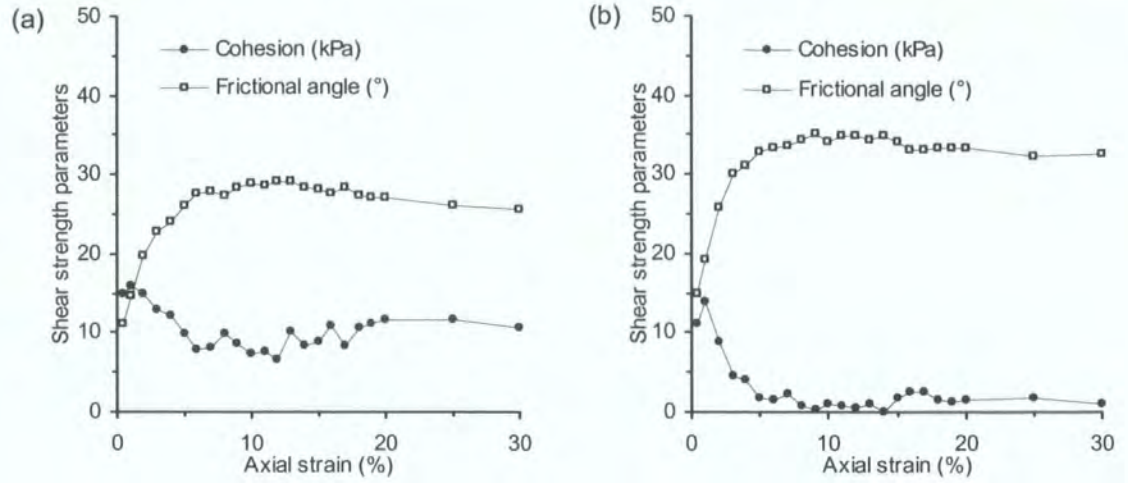

Figure 5.8 Strain development during ICU tests in terms of effective cohesion and frictional angle: (a) TC samples (TC09, TC10, TC11); (b) PO samples (PO27, PO29, PO34)

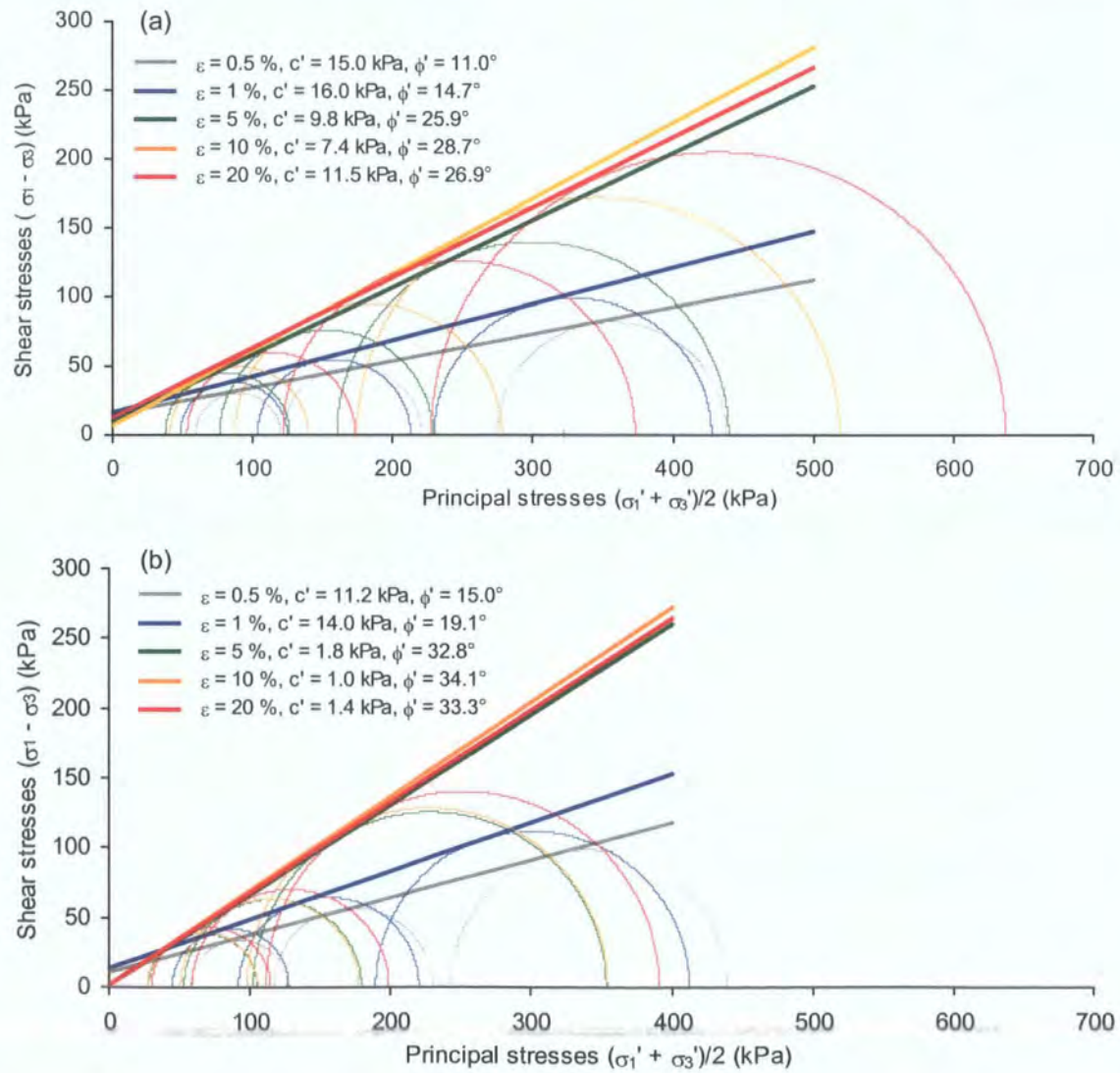

Figure 5.9 Strain development during ICU tests revealed from the Mohr circles at equal strains: (a) TC samples (TC09, TC10, TC11); (b) PO samples (PO27, PO29, PO34)

5.5.2 The ICU failure envelope

The failure envelope is commonly defined either by the maximum shear stress (τ_{max}) or for plastic materials where the deviatoric stress reaches 20% axial strain (Selby, 1993). Mohr circles show that the respective failure envelopes developed at τ_{max} (Figure 5.10) and 20% axial strain (Figure 5.11) within each group of samples are almost the same (Table 5.9). They are characterised by a nearly perfect linear correlation ($R^2 \geq 0.99$) with similar derived effective frictional angle (ϕ') and effective cohesion (c') (Table 5.9). The highest effective frictional angle and cohesion for the samples were mobilised at 13% axial strain (TC) and 7% axial strain (PO) respectively (Table 5.9). They appear to be the best-defined ICU failure envelope, among the commonly accepted criteria.

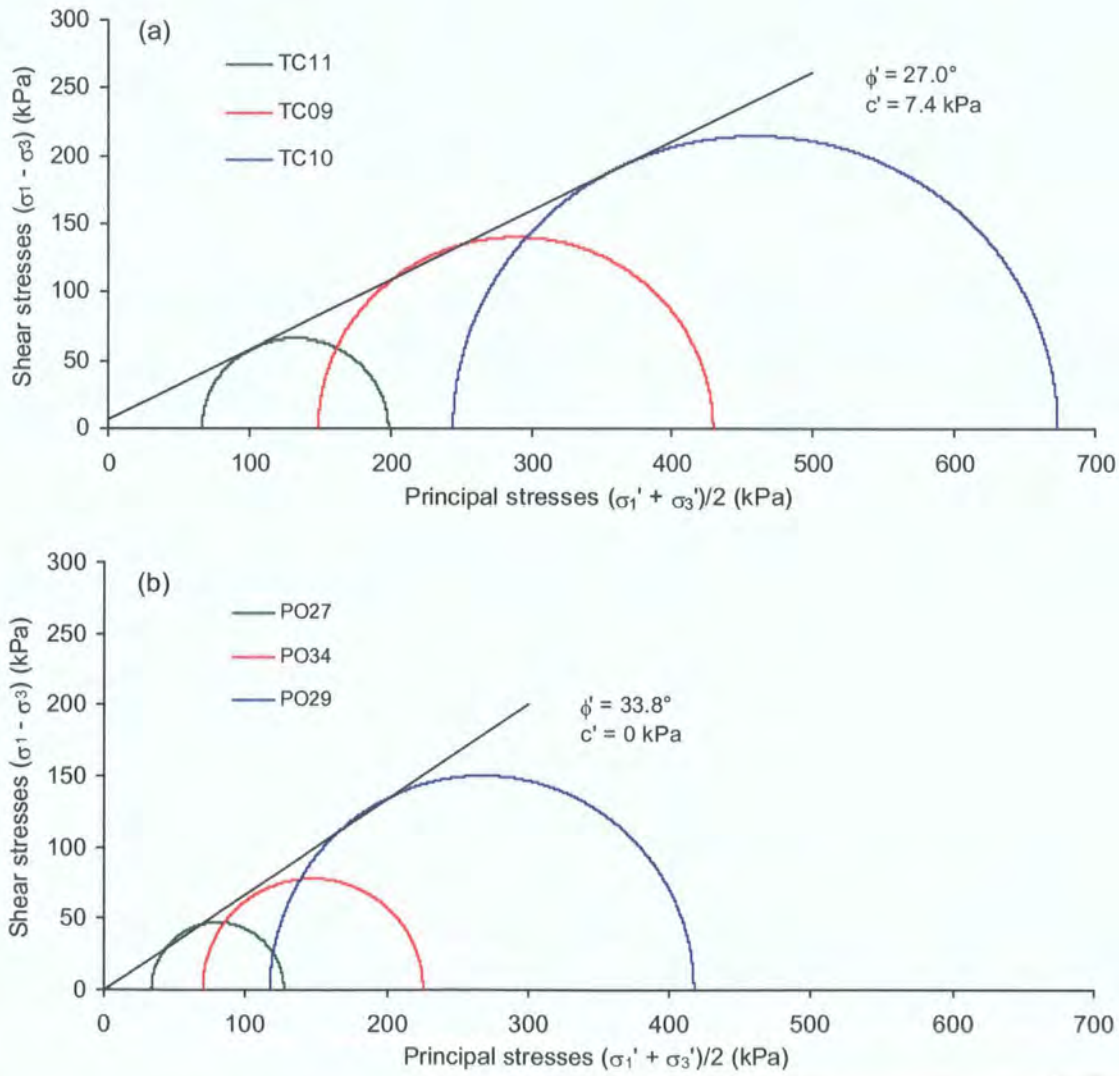

Figure 5.10 Best-fit failure envelopes defined by the stress conditions at maximum shear stress, derived from three ICU tests at effective stresses 100, 200 and 400 kPa:
(a) TC samples; (b) PO samples

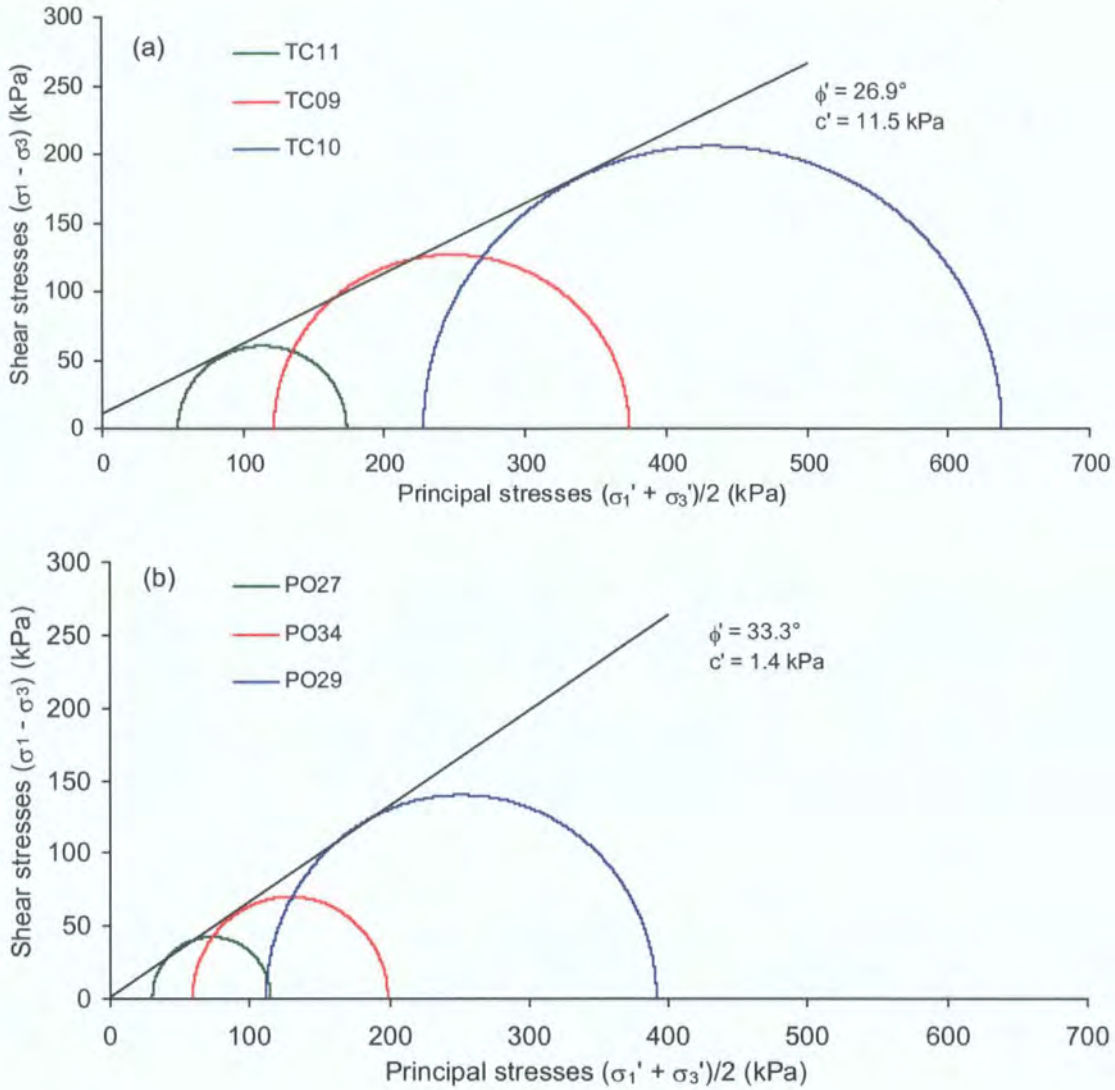

Figure 5.11 Best-fit failure envelopes defined by the stress conditions at 20 % axial strain, derived from three ICU tests at effective stresses 100, 200 and 400 kPa:
(a) TC samples; (b) PO samples

The undrained stress paths in Figure 5.12 also indicate that both samples behaved like a typical normally consolidated clay. Pore water pressures increased during shear. Other evidence, as previously shown, includes the linear failure envelope, very low cohesion value and the effective frictional angles lying between 20° and 35° (Craig, 1997) (Figures 5.10, 5.11).

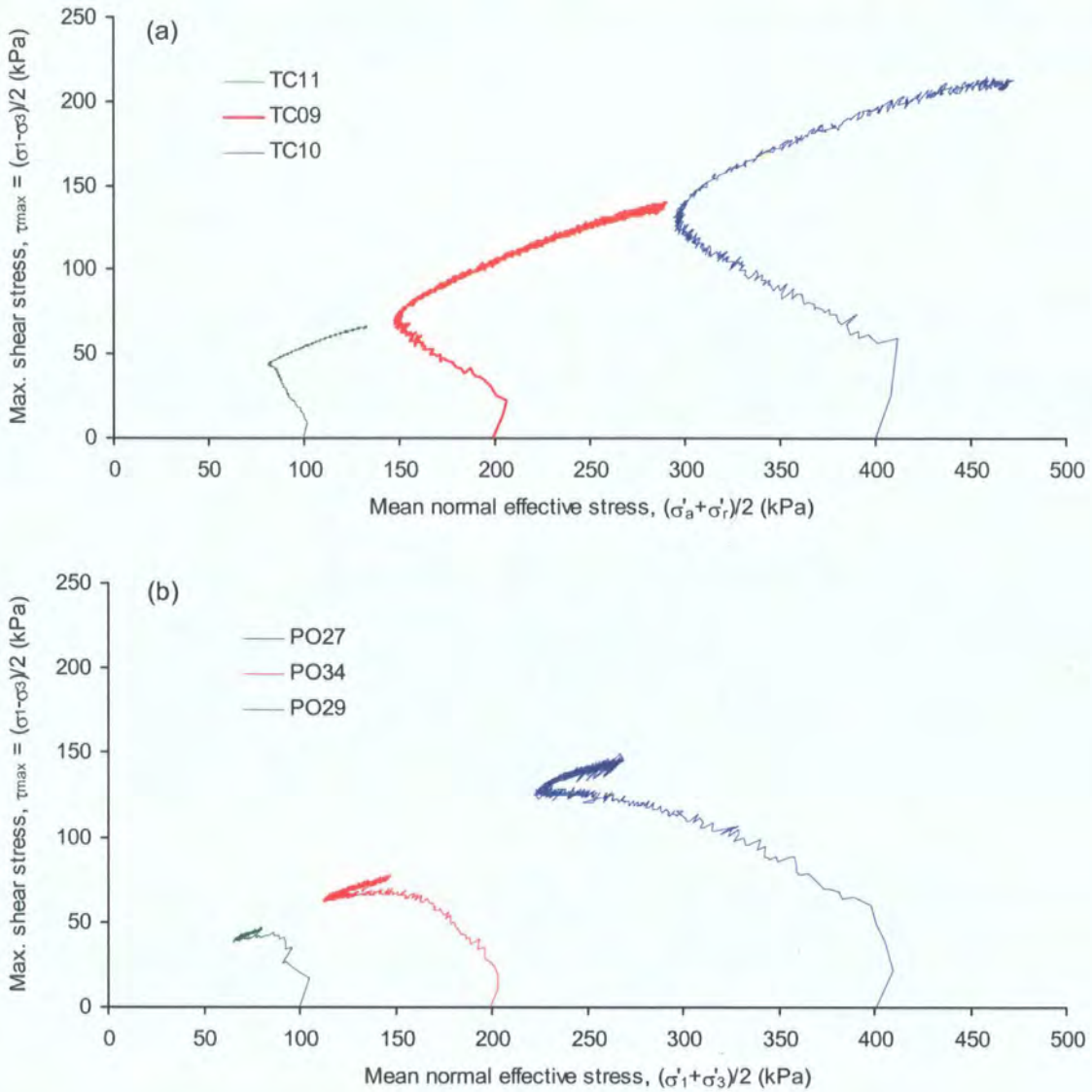

Figure 5.12 Stress paths derived from three ICU tests at effective stresses 100, 200 and 400 kPa: (a) TC samples; (b) PO samples

5.5.3 Stress-strain soil behaviour

The nature of deformation processes of the weathered TC and PO soils has been revealed by plotting the stress-strain curves. Plastic behaviour was predominant during the undrained tests (Figure 5.13), which was also indicated by the formation of typical barrel-like shapes with no evidence of shear surfaces on the tested samples (Appendix 1a).

A high resistance to deformation was shown by the stiff stress-strain curve at small strains until reaching about 2% axial strain (Figure 5.13). Afterwards, the TC

samples displayed slight strain hardening with a more gentle continual increase of deviatoric stress (Figure 5.13a); while the PO samples maintained the deviatoric stress at a more or less constant level at larger strains, showing typical ductile deformation (Figure 5.13b). Strain hardening behaviour was also observed in undisturbed samples of argillaceous rocks in Taiwan and Barbados (Fan *et al.*, 1996).

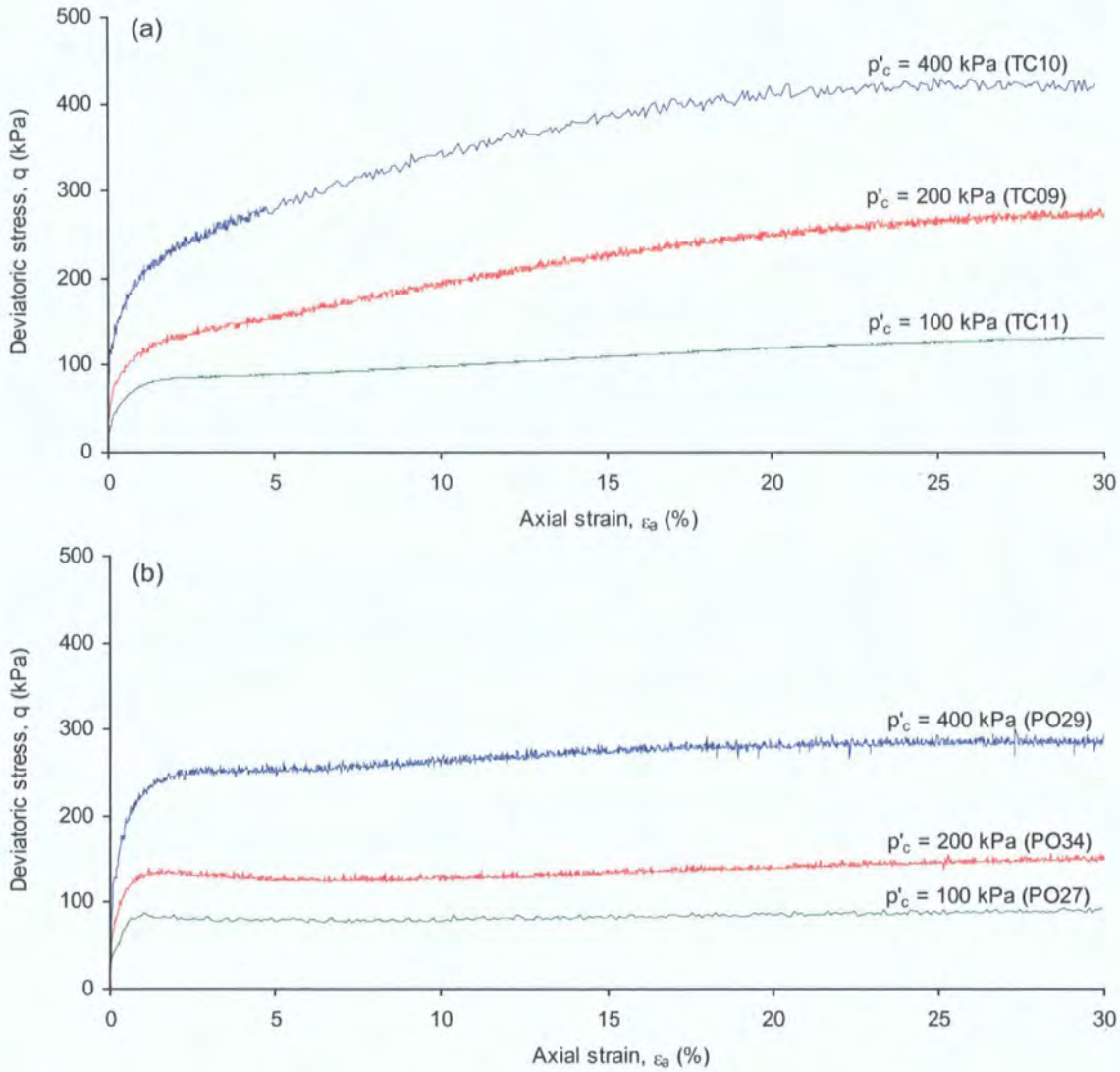

Figure 5.13 Stress-strain soil behaviour during the ICU tests at effective stresses 100, 200 and 400 kPa: (a) TC samples; (b) PO samples

5.6 Isotropic consolidated drained (ICD) shear tests

This section focuses on the sample behaviour under the drained shearing process, including the (1) pre-failure strain development, (2) the failure envelope and (3) the overall stress-strain behaviour.

5.6.1 Strain development prior to failure

The linear envelopes derived at various axial strains ($R^2 \geq 0.95$) reveal the pre-failure strain development under drained stress conditions (Table 5.10).

Similar to the undrained tests, the drained shear rapidly mobilised friction and caused a slight increase in cohesion at small strains within both samples (Figure 5.14). The rapid increase of frictional angle was up to about 10% strain and continued to increase slightly until reaching around 15% strain (Table 5.10, Figure 5.14). Such strain development was clearly revealed by the sharp increase of the slope in $\tau_{max} - \sigma'$ (Figure 5.15). Maximum cohesion was mobilised at 4-5 % within TC samples and 2 % within PO samples (Table 5.10). As the strain developed, cohesion dropped and became stable. The friction values remained similar towards failure (Figure 5.14), as indicated by the overlapping of the strain contours (Figure 5.15).

However, unlike the undrained tests, the behaviour during drained shear was less stiff, with the maximum cohesion and friction occurring at a larger strain during the drained process (Figure 5.14). This key difference might be related to the slower shearing strain rate applied for the drained tests.

Table 5.10 Strain development in terms of failure parameters derived from ICD tests

(a) TC soils (TC33, TC34, TC39)

Failure criteria	Effective frictional angle, ϕ' (°)	Effective cohesion, c' (kPa)	Correlation coefficient, R^2
τ_{max}	29.0	8.3	1.00
ε_a = 0.5 %	6.9	6.5	0.95
ε_a = 1%	10.2	8.6	0.96
ε_a = 2 %	15.0	9.5	0.99
ε_a = 3 %	18.4	9.6	1.00
ε_a = 4 %	20.7	10.5	1.00
ε_a = 5 %	22.5	10.5	1.00
ε_a = 6 %	24.4	9.4	1.00
ε_a = 7 %	25.6	8.9	1.00
ε_a = 8 %	26.6	8.4	1.00
ε_a = 9 %	27.5	7.9	1.00
ε_a = 10 %	28.2	7.2	1.00
ε_a = 11 %	28.4	7.6	1.00
ε_a = 12 %	28.8	7.6	1.00
ε_a = 13 %	28.8	8.2	1.00
ε_a = 14 %	28.9	8.0	1.00
ε_a = 15 %	28.8	8.3	1.00
ε_a = 16 %	29.0	7.4	1.00
ε_a = 17 %	28.8	7.9	1.00
ε_a = 18 %	28.6	8.5	1.00
ε_a = 19 %	28.6	8.0	1.00
ε_a = 20 %	28.5	8.1	1.00
ε_a = 25 %	27.8	8.4	1.00
ε_a = 30 %	27.2	8.2	1.00

(b) PO soils (PO04, PO05, PO06)

Failure criteria	Effective frictional angle, ϕ' (°)	Effective cohesion, c' (kPa)	Correlation coefficient, R^2
τ_{max}	30.4	10.0	1.00
ε_a = 0.5 %	3.5	15.8	1.00
ε_a = 1 %	5.6	21.8	0.99
ε_a = 2 %	23.8	10.6	0.99
ε_a = 3 %	15.1	20.7	1.00
ε_a = 4 %	18.8	17.6	1.00
ε_a = 5 %	21.6	14.5	1.00
ε_a = 6 %	23.7	13.1	1.00
ε_a = 7 %	25.4	11.7	1.00
ε_a = 8 %	26.6	11.2	1.00
ε_a = 9 %	27.9	9.5	1.00
ε_a = 10 %	28.6	9.7	1.00
ε_a = 11 %	29.2	9.2	1.00
ε_a = 12 %	29.7	8.6	1.00
ε_a = 13 %	29.8	9.6	1.00
ε_a = 14 %	30.3	8.5	1.00
ε_a = 15 %	30.4	8.9	1.00
ε_a = 16 %	30.4	9.0	1.00
ε_a = 17 %	30.2	10.1	1.00
ε_a = 18 %	30.3	10.0	1.00
ε_a = 19 %	30.2	10.0	1.00
ε_a = 20 %	30.1	10.6	1.00
ε_a = 25 %	29.3	11.7	1.00
ε_a = 30 %	28.5	12.2	1.00

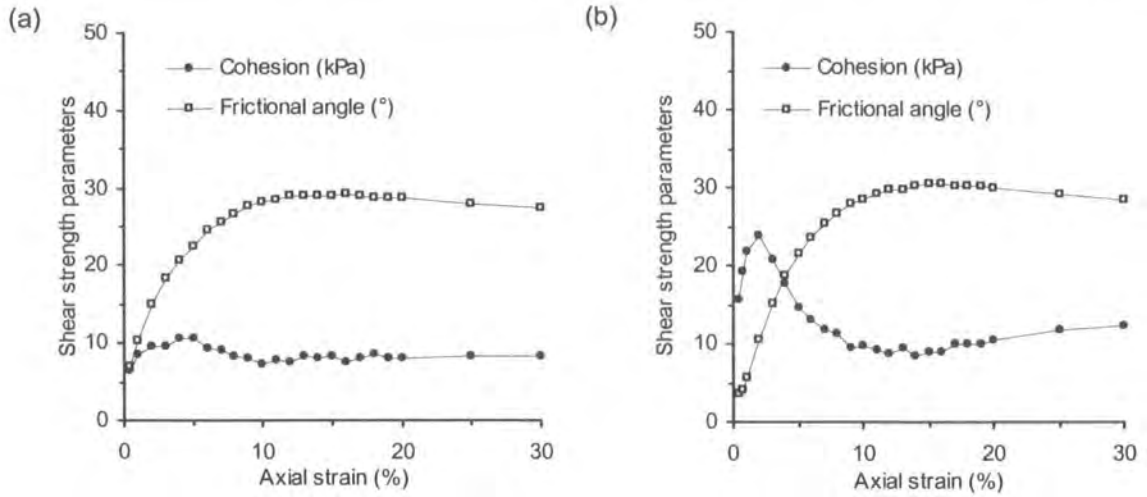

Figure 5.14 Strain development during ICD tests in terms of effective cohesion and frictional angle: (a) TC samples (TC33, TC34, TC39); (b) PO samples (PO04, PO05, PO06)

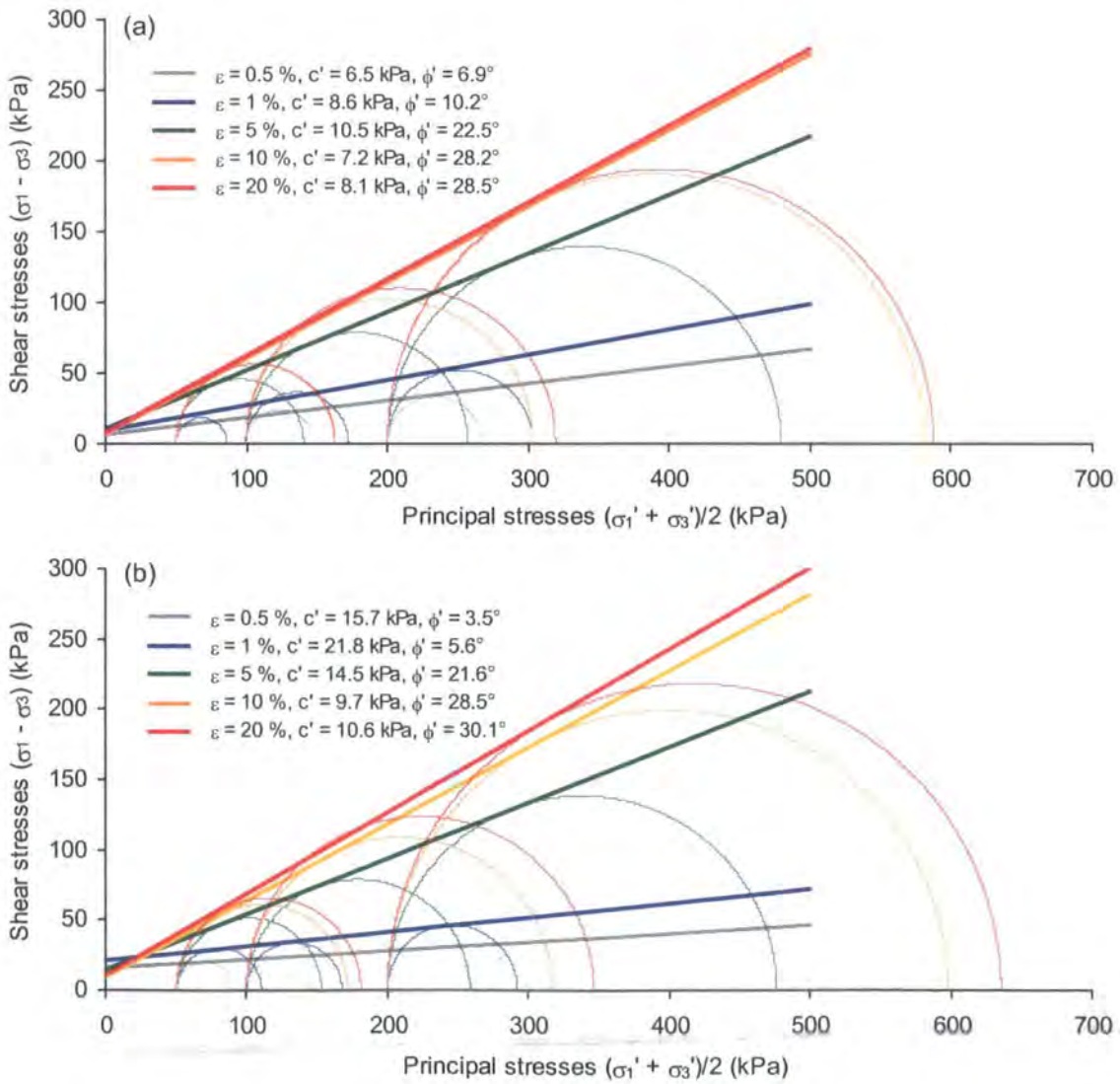

Figure 5.15 Strain development revealed from the Mohr circles at equal strains during ICD tests: (a) TC samples (TC33, TC34, TC39); (b) PO samples (PO04, PO05, PO06)

5.6.2 The ICD failure envelope

The ICD failure envelope could be well-defined at the maximum shear stress, where both samples obtained the highest effective frictional angle (Figure 5.16, Table 5.10). However, the highest frictional angle was also mobilised at 16% strain within TC samples and at 15-16% strain within PO samples respectively.

The failure envelope was linear (R^2 = 1.0). The mobilised soil strength parameters (ϕ', c') were 29.0°, 8.3 kPa for TC samples and 30.4°, 10.0 kPa for PO samples (Table 5.10). Hence, the PO samples had slightly higher strength, given their higher effective frictional angle and cohesion during shear.

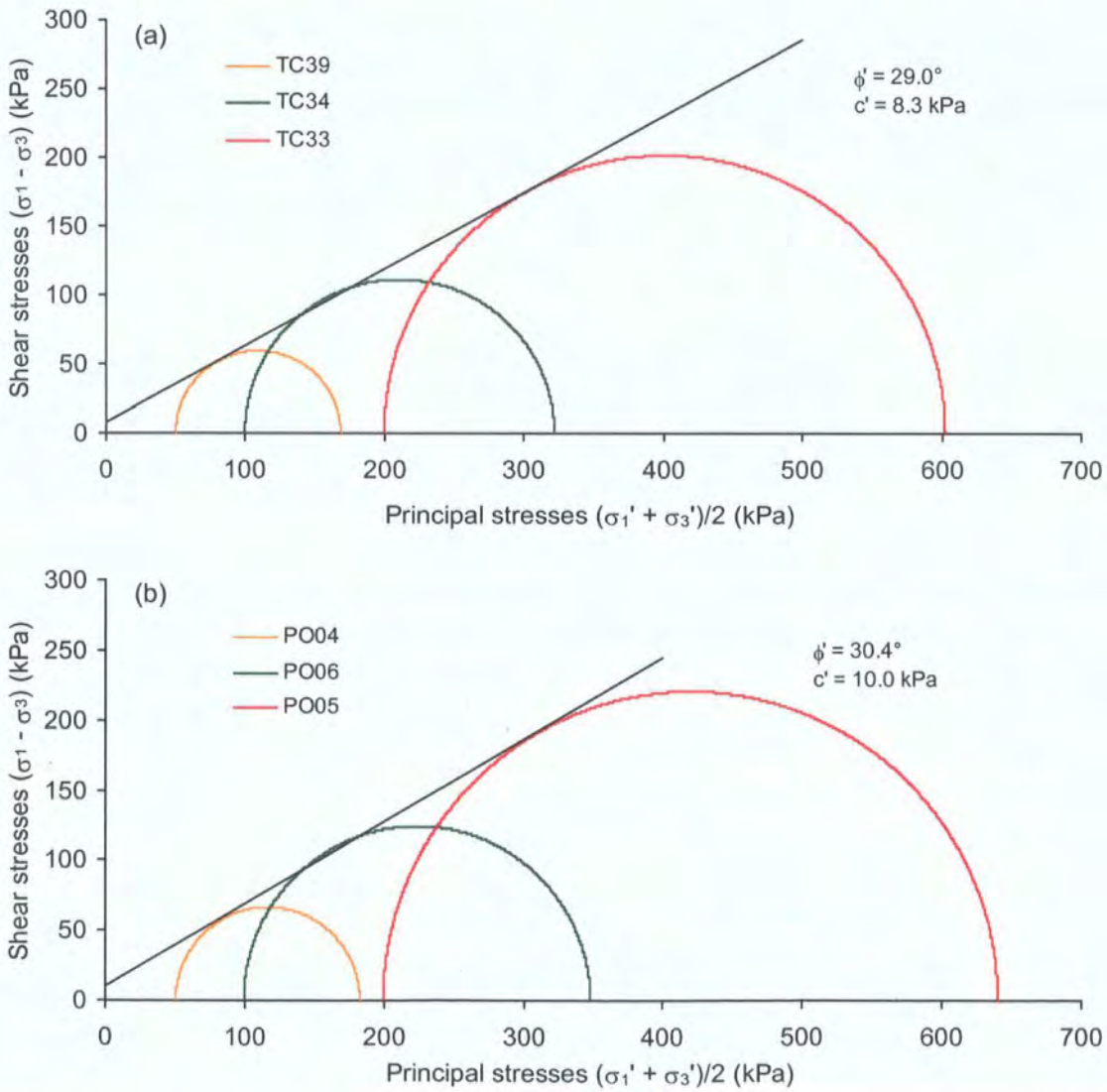

Figure 5.16 Best-fit failure envelopes defined by the stress conditions at maximum shear stress, derived from three ICD tests at effective stresses 50, 100 and 200 kPa:
(a) TC samples; (b) PO samples

5.6.3 Stress-strain soil behaviour

Both TC and PO samples exhibited ductility during the ICD tests (Figure 5.17). The form of the stress-strain curves was very similar. They involved a substantial increase in deviatoric stress of up to about 15% axial strain followed by a slight decrease (especially at p'_c = 200 kPa), but the deviatoric stress remained generally constant over large strains. Comparing with the undrained tests, the drained tests mobilised higher deviatoric stress under the same mean effective stress, although their behaviour was less stiff at small strains (cf. Figures 5.13, 5.17). Plastic deformation was dominant (Appendix 1b), which involved contractive behaviour with volumetric strains of up to 3.4% (TC samples) and 5.1% (PO samples) respectively (Figure 5.18).

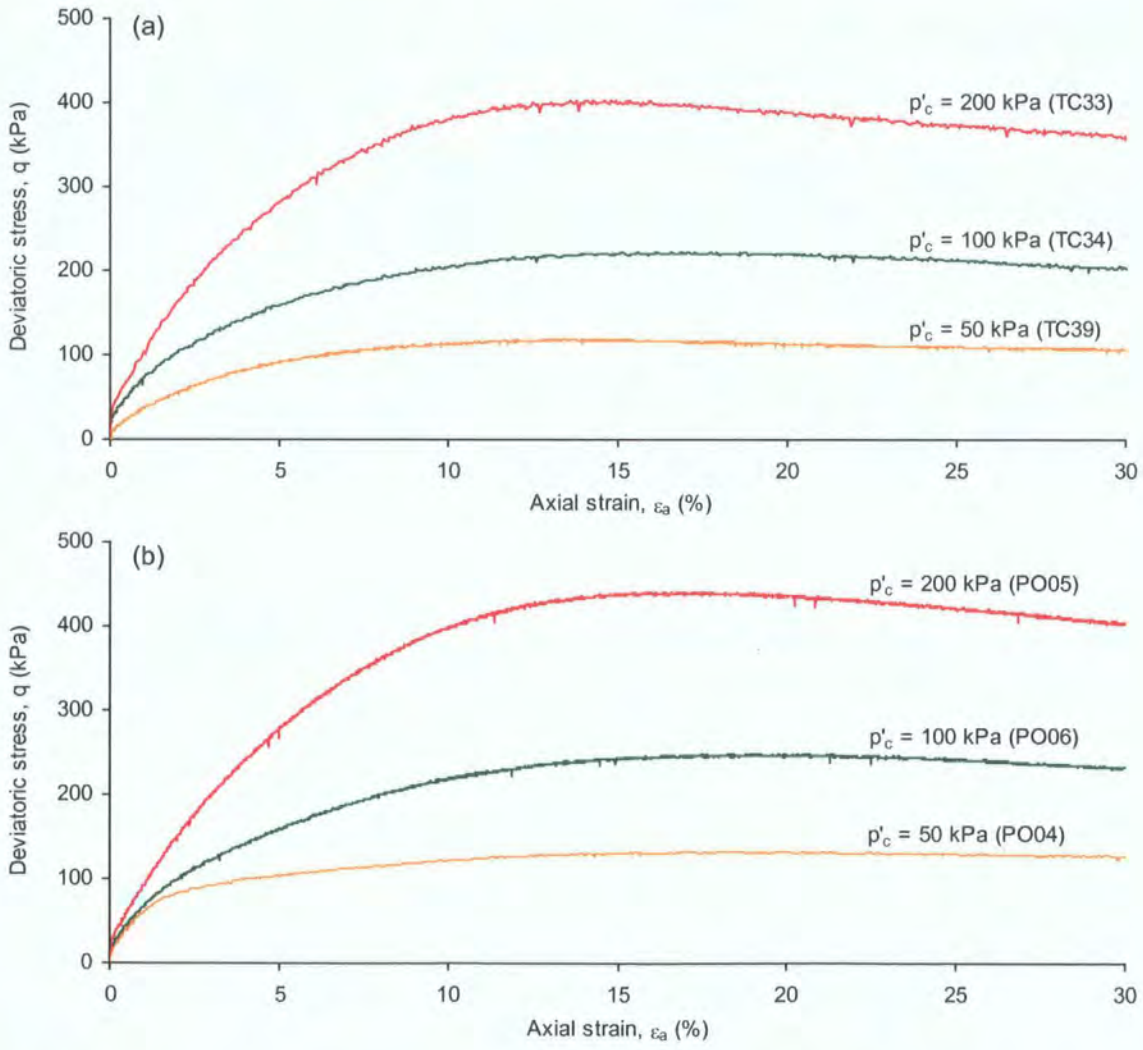

Figure 5.17 Stress-strain soil behaviour during the ICD tests at effective stresses 50, 100 and 200 kPa: (a) TC samples; (b) PO samples

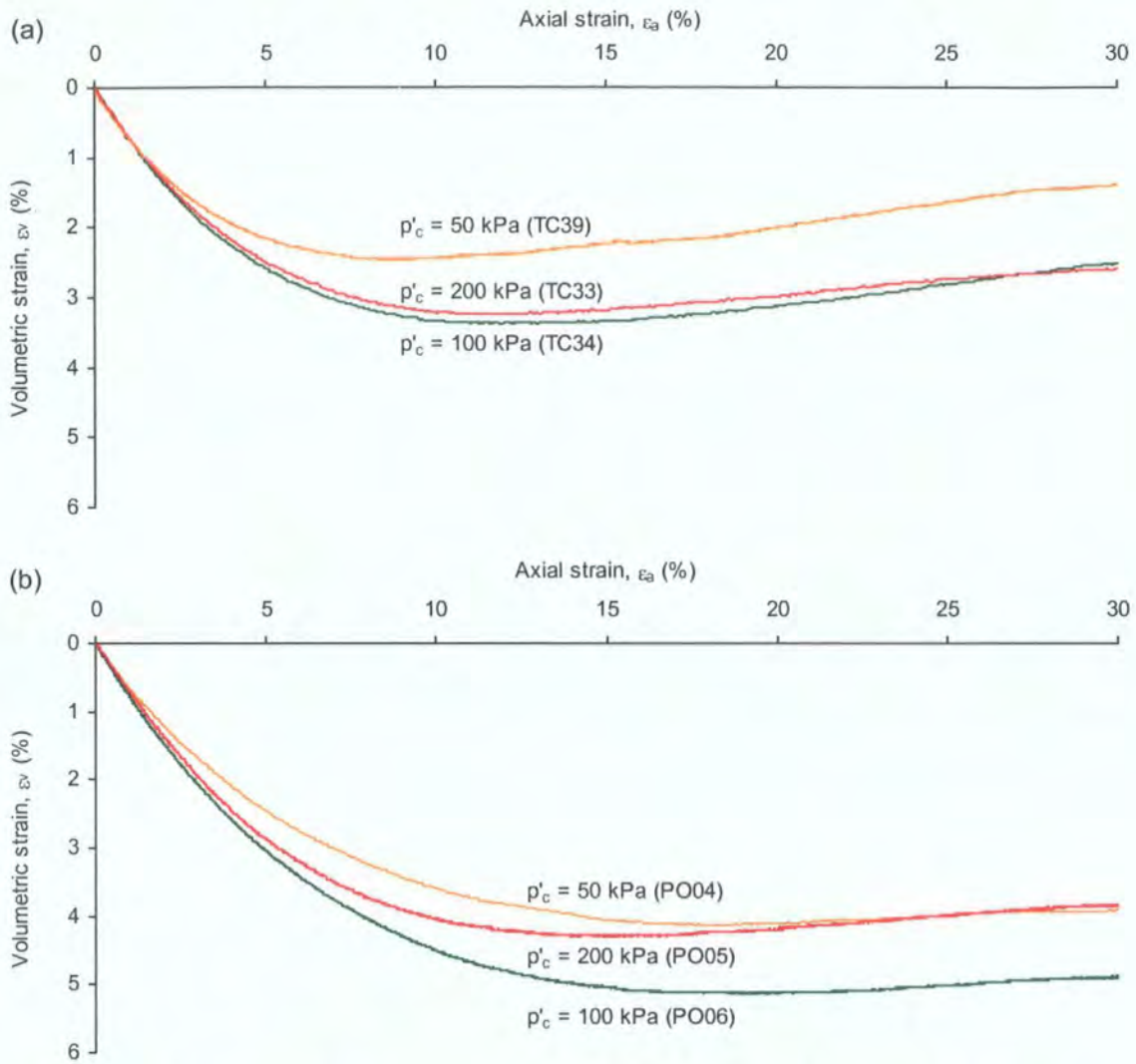

Figure 5.18 Contractive behaviour during the ICD tests at effective stresses 50, 100 and 200 kPa: (a) TC samples; (b) PO samples

5.7 Pore water pressure reinflation (PPR) tests

The pore water pressure reinflation (PPR) tests were undertaken to investigate the soil deformation processes under actual shallow-seated slope conditions during rainstorm events (Table 5.3). This section presents the stress path information for the initial (drained) shear phase, which brought the samples to a pre-failure stress state below their maximum strength for the reinflation testing. The stress development towards failure has been examined through a series of reinflation experiments conducted at three different deviatoric stress levels (q = 100, 200 and 300 kPa) under a linear reinflation rate of 10 kPa/hr. This allowed the establishment of the reinflation test failure envelope. The associated stress-strain behaviour was also analysed. Finally, the deformation behaviour of the tropical weathered soils under the field-referenced linear, stepped and logarithmic reinflation rates were explored.

5.7.1 Drained initial shear

With reference to the failure envelope derived from the ICD tests, the TC and PO samples reached 24.8% and 22.7% of their maximum strength respectively after being subjected to the initial drained shear until reaching a deviatoric stress level of 100 kPa (Figure 5.19). The corresponding stress conditions were at p'_{dis} = 233 kPa, q = 100 kPa. Two additional reinflation tests were undertaken from each site at q = 200 kPa and q = 300 kPa to construct the failure envelope for comparison with the ICU and ICD tests. All of them represented the pre-failure conditions as the initial stress state for the reinflation tests.

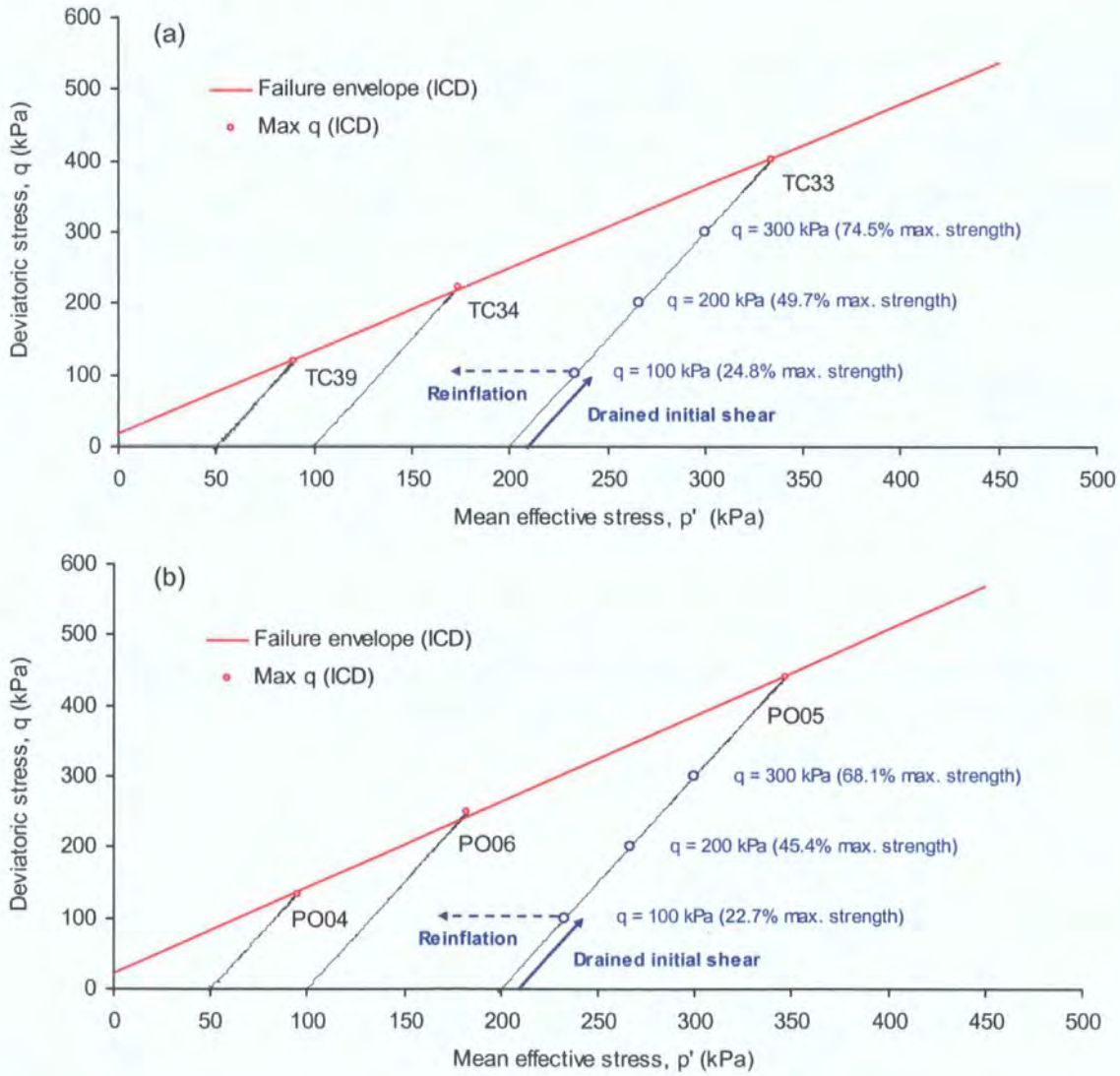

Figure 5.19 Stress conditions in relation to the maximum soil strength after drained initial shear: (a) TC samples; (b) PO samples

During the stress-controlled drained initial shear phase, the axial and volumetric strains increased with a decrease in the void ratio (cf. Tables 5.8, 5.11). The typical stress paths, plastic stress-strain relationship and contractive behaviour are presented in Figures 5.20 (TC samples) and 5.21 (PO samples). The amount of the increasing strains appeared to be directly proportional to the applied deviatoric stress levels (i.e. at 100 kPa, 200 kPa and 300 kPa). Moreover, the stiffness of the stress-strain behaviour within the TC and PO samples was similar, probably because of the application of the same stress rate (Figures 5.20, 5.21).

Table 5.11 Axial length (L), volume (V), strains (ε) and void ratio (e) after drained initial shear

	Sample number	Drained initial shear pressure (kPa)	After drained initial shear				
			L_{dis} (mm)	V_{dis} (mm^3)	$\varepsilon_{L,\,dis}$ (%)	$\varepsilon_{v,\,dis}$ (%)	e_{dis}
PPR	TC28	100	75.04	78983	2.36	5.84	0.63
	TC24	200	73.16	76176	3.58	5.87	0.51
	TC26	300	71.75	78942	6.07	6.73	0.57
(Linear)	TC40	100	75.20	82011	2.33	5.62	0.65
	TC14	100	74.26	81277	1.33	4.78	0.61
	TC27	100	73.66	78770	2.75	4.21	0.62
	TC28	100	75.04	78983	2.36	5.84	0.63
	TC32	100	75.43	80982	1.73	4.53	0.61
	TC38	100	75.35	81105	1.52	3.61	0.60
(Step)	TC23	100	74.66	80274	2.65	5.48	0.58
	TC16	100	72.34	75752	2.85	5.69	0.54
	TC29	100	75.50	75470	2.05	6.32	0.67
	TC21	100	73.47	75199	3.13	8.92	0.59
	TC31	100	74.79	79914	1.80	5.20	0.66
	TC22	100	73.83	77916	3.02	8.32	0.63
(Log)	TC30	100	75.04	77023	2.56	6.83	0.60
	TC36	100	73.59	75242	4.20	7.41	0.59
	TC37	100	75.35	79971	1.61	3.81	0.60
PPR	PO07	100	75.03	84004	3.91	7.54	0.74
	PO19	200	71.14	80230	5.02	7.80	0.63
	PO31	300	70.78	77626	6.38	8.06	0.56
(Linear)	PO37	100	75.33	80419	2.45	6.76	0.65
	PO24	100	72.38	83042	3.14	5.58	0.65
	PO11	100	74.00	79730	3.26	7.70	0.69
	PO07	100	75.03	84004	3.91	7.54	0.74
	PO12	100	74.03	80687	2.82	7.00	0.70
(Step)	PO13	100	71.98	76157	3.49	8.08	0.67
	PO25	100	73.77	78464	3.40	7.37	0.65
	PO23	100	71.60	78402	4.02	8.59	0.73
	PO30	100	72.60	82021	3.11	6.65	0.71
	PO38	100	74.78	78316	4.18	8.46	0.63
	PO33	100	74.66	84242	2.80	6.08	0.74
(Log)	PO35	100	76.53	82820	2.14	6.02	0.69
	PO40	100	76.45	83232	2.52	5.83	0.64
	POD17	100	72.06	78597	4.78	9.34	0.68
	POD14	100	73.78	82592	3.15	7.11	0.73
	POD16	100	73.71	79211	2.86	7.37	0.69

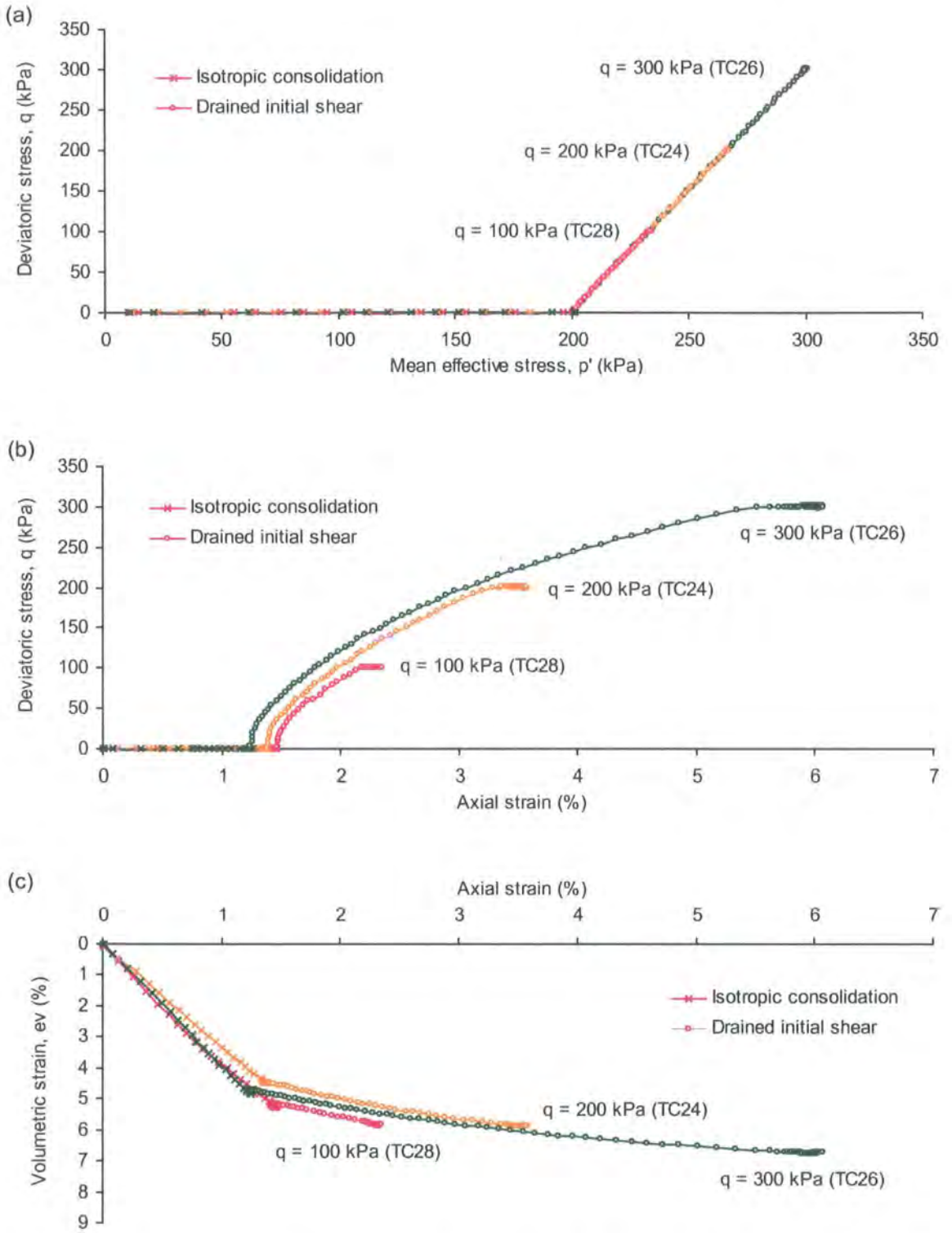

Figure 5.20 Soil behaviour during isotropic consolidation (p'_c = 200 kPa) and drained initial shear (q = 100, 200, 300 kPa) within TC samples: (a) stress paths; (b) stress-strain relationship; and (c) volumetric change

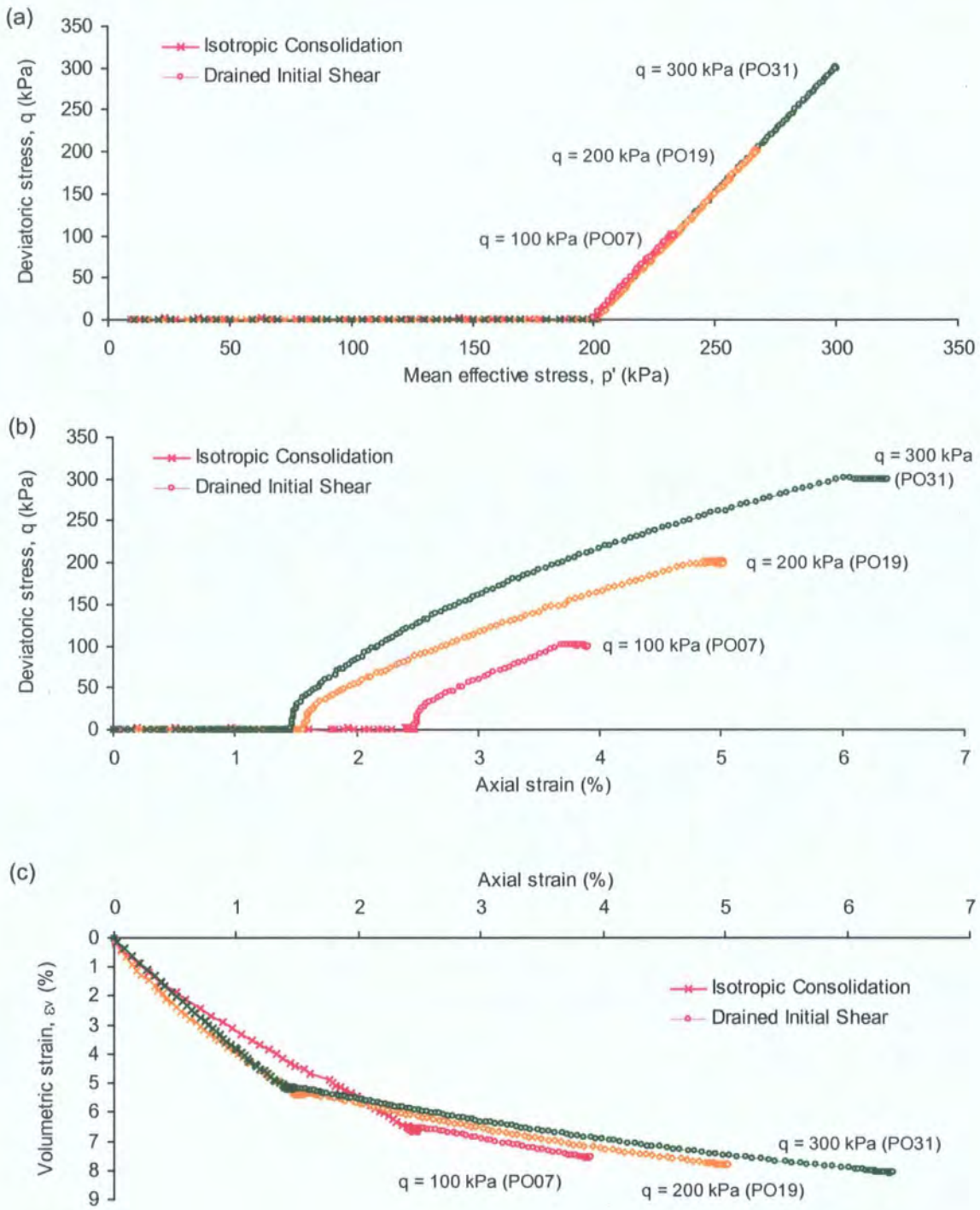

Figure 5.21 Soil behaviour during isotropic consolidation (p'_c = 200 kPa) and drained initial shear (q = 100, 200, 300 kPa) within PO samples: (a) stress paths; (b) stress-strain relationship; and (c) volumetric change

For the majority of tests which were consolidated (p'_c) at 200 kPa and then initially sheared to q = 100 kPa, the maximum, minimum and the average axial strains were generally lower within the undisturbed TC samples, at 4.20%, 1.33% and 2.39% respectively. Corresponding values for the undisturbed PO samples were 4.18%, 2.14% and 3.20% (Table 5.11).

Lower mean volumetric strains were also found in the undisturbed TC samples at 5.78%, with the maximum at 8.92% and 3.61% at minimum. The undisturbed PO samples developed greater strains (7.07% on average), with a maximum of 8.59% and a minimum of 5.58%. This was also reflected by the lower void ratio after drained initial shear ranging from 0.54 to 0.67 within the TC samples, with the PO samples yielding values between 0.63 and 0.74 (Table 5.11).

The strain values exhibited by the three damaged PO samples (POD14, POD16, POD17) were not significantly different from the undisturbed PO samples, although they mobilised higher volumetric strains above the average (Table 5.11). Hence, the disturbances caused by trimming appeared to have only a minor influence on the soil behaviour.

In overview, the net amount of axial and volumetric strains generated as a result of the drained initial shear was smaller than the strains exhibited during the isotropic consolidation stage (Figures 5.22, 5.23). This was probably due to the low level of deviatoric stress, q = 100 kPa, being applied.

The form of the stress-strain curves was very similar within each group of samples, indicating that their behaviour was unaffected by the strain values after isotropic consolidation (Figures 5.22, 5.23). However, sample variability might explain the stiffer behaviour in the TC samples and the more abrupt but consistent change in the stiffness in the PO samples at deviatoric stress around 30 kPa.

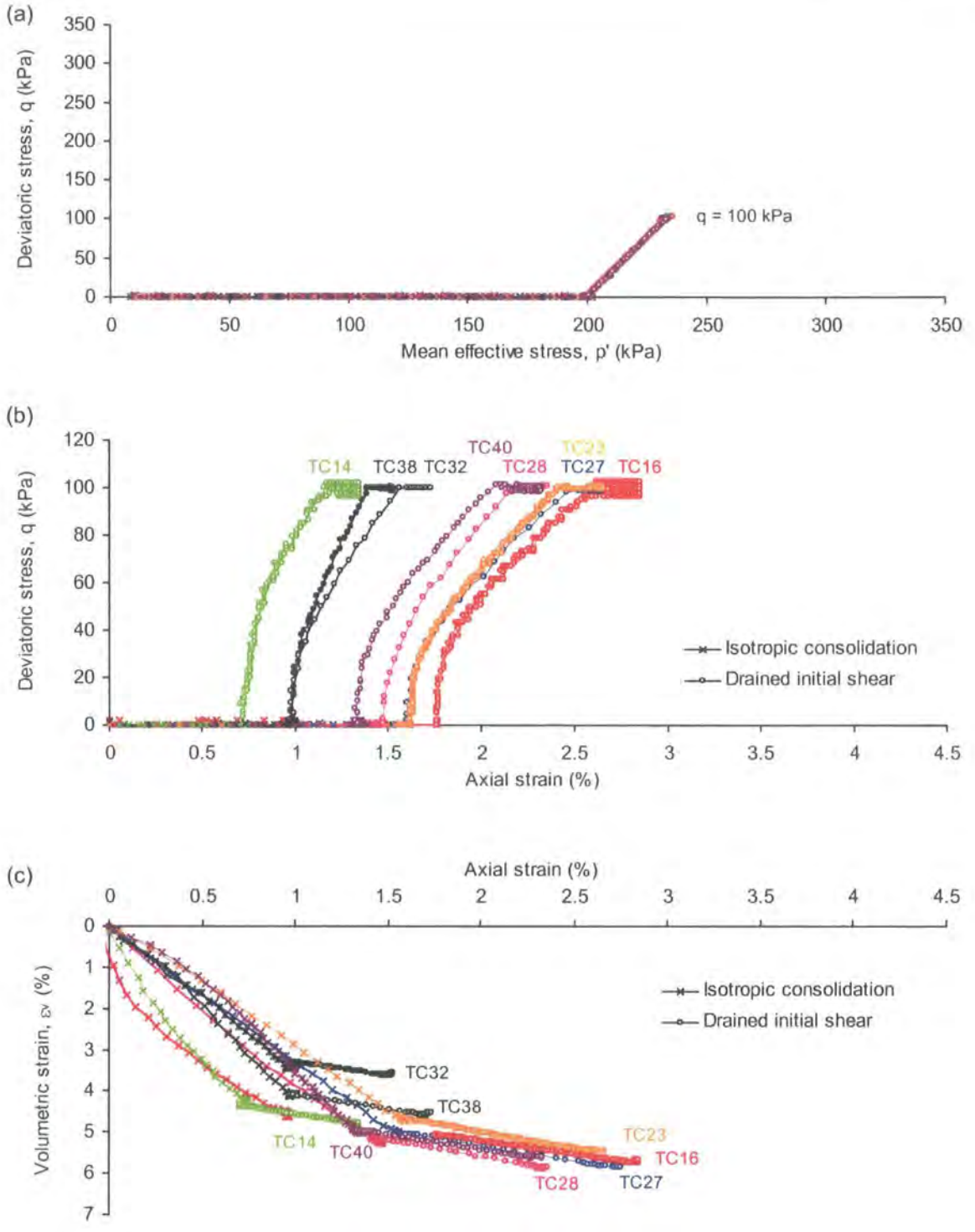

Figure 5.22 Soil behaviour during isotropic consolidation (p'_c = 200 kPa) and drained initial shear (q = 100 kPa) within TC samples: (a) stress paths; (b) stress-strain relationship; and (c) volumetric change

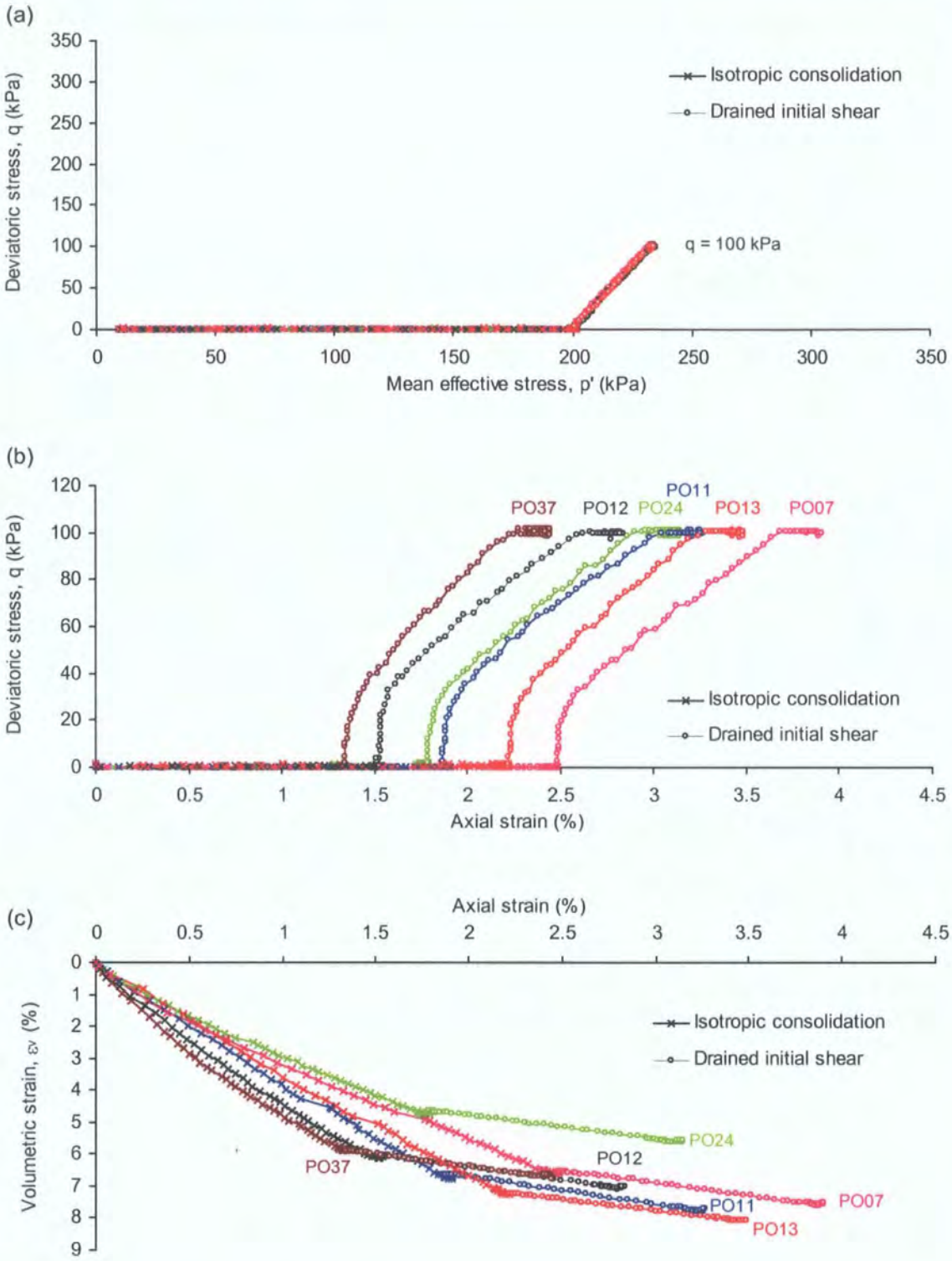

Figure 5.23 Soil behaviour during isotropic consolidation (p'_c = 200 kPa) and drained initial shear (q = 100 kPa) within PO samples: (a) stress paths; (b) stress-strain relationship; and (c) volumetric change

Interestingly, all of the TC and PO samples demonstrated creep after the target drained shear value was attained, where strains were accumulating at the same deviatoric stress level under constant mean effective stress (i.e. constant stress conditions at p'_{dis} = 233 kPa, q = 100 kPa) (Figures 5.22b, 5.23b). Plots of axial strain against time further revealed both a primary and a secondary creep phase (Figure 5.24). Strains increased at a decreasing strain rate after the target stresses were reached after 200 minutes (i.e. primary creep). The transition of primary creep to secondary creep appeared to occur at 400 min, when the strains began to increase at a constant rate (Figure 5.24).

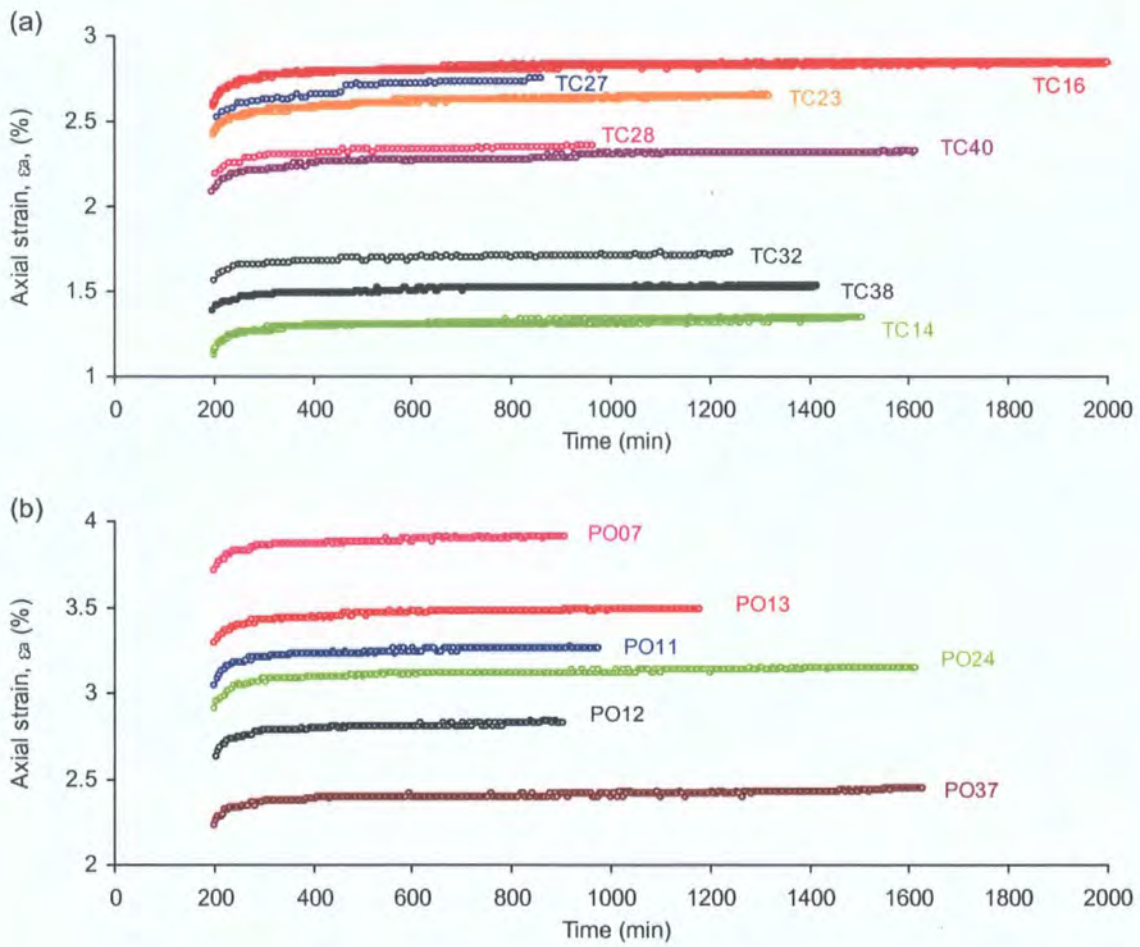

Figure 5.24 Plots of axial strain against time showing the primary and secondary creep phase at constant stress conditions (p'_{dis} = 233 kPa, q = 100 kPa) at the final stage of initial drained shear: (a) TC samples; (b) PO samples

The creep behaviour is more clearly revealed in plots of normalised initial axial strain against time (Figure 5.25). The TC samples showed a wider range of changes in strain rate (Figure 5.25a) than the PO samples (Figure 5.25b). The density of the TC samples, however, did not seem to explain the differences of the creep curves as their initial void ratios were largely similar (except TC16) (Table 5.8). In contrast, the PO samples, which exhibited similar gradients of the creep curves, had a greater range of initial void ratios (Table 5.8). The variations appear to reflect the heterogeneity within the undisturbed TC and PO samples.

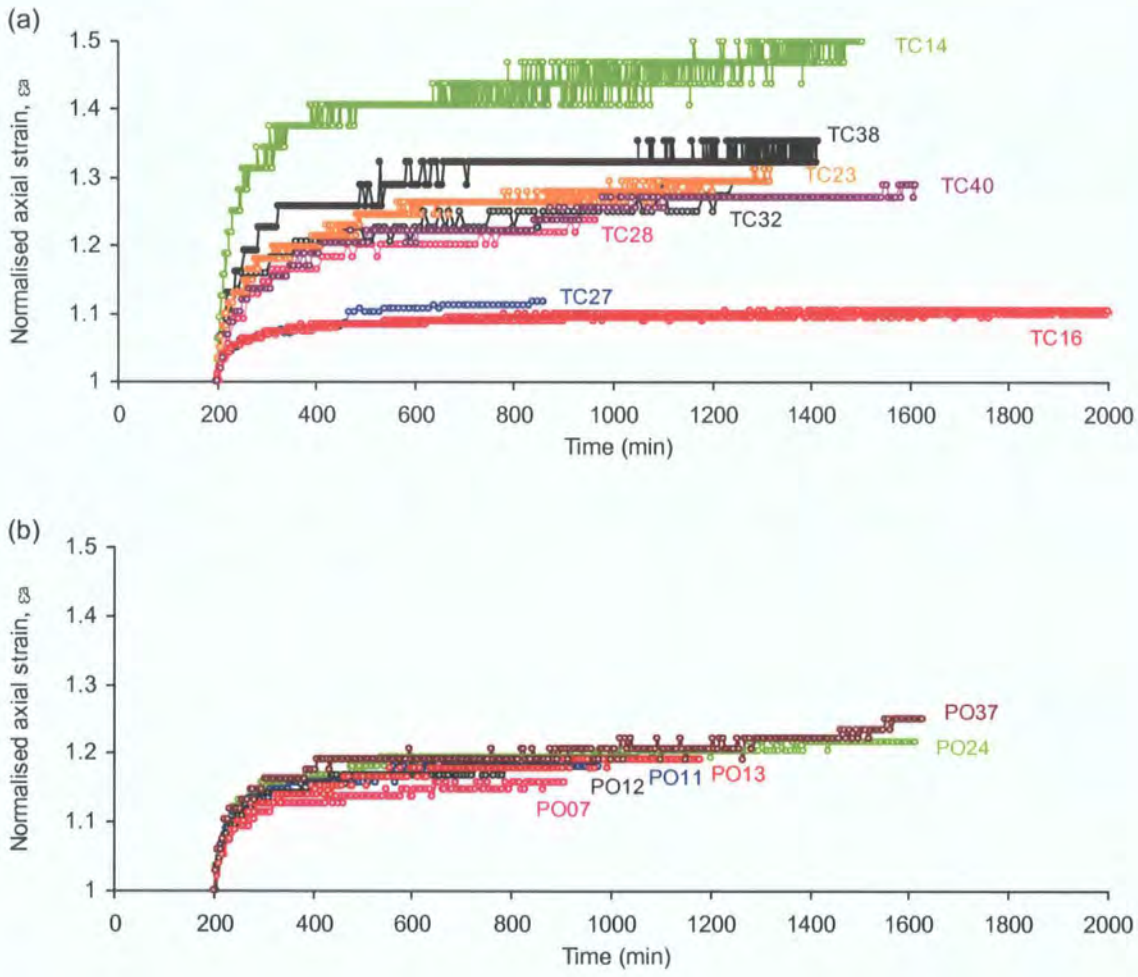

Figure 5.25 Plots of normalised axial strain against time showing the primary and secondary creep phase at constant stress conditions (p'_{dis} = 233 kPa, q = 100 kPa) at the final stage of initial drained shear: (a) TC samples; (b) PO samples

5.7.2 Strain development prior to failure

An overview of the pre-failure strain development during the reinflation process in terms of effective cohesion and frictional angle is presented in Table 5.12 and Figure 5.26, which were derived from the Mohr circles (Figure 5.27).

Table 5.12 Strain development in terms of failure parameters derived from PPR tests

(a) TC soils (TC24, TC26, TC28)

	Axial strain	Effective frictional angle, ϕ' (°)	Effective cohesion, c' (kPa)	Correlation coefficient, R^2
DIS	ε_a = 2 %	14.1	29.7	1.00
	ε_a = 3 %	18.4	29.4	0.96
	ε_a = 4 %	21.1	26.0	0.98
	ε_a = 5 %	25.4	18.9	0.99
PPR	ε_a = 6 %	27.2	16.3	1.00
	ε_a = 7 %	28.0	15.5	1.00
	ε_a = 8 %	29.0	14.2	1.00
	ε_a = 9 %	29.2	14.1	1.00
	ε_a = 10 %	29.5	14.5	1.00
	ε_a = 11 %	30.1	13.2	1.00
	ε_a = 12 %	30.1	13.8	1.00
	ε_a = 13 %	30.2	12.2	1.00
	ε_a = 14 %	30.5	13.5	1.00
	ε_a = 15 %	30.5	13.9	1.00
	ε_a = 16 %	30.5	14.1	1.00
	ε_a = 17 %	30.7	13.7	1.00
	ε_a = 18 %	30.7	13.7	1.00
	ε_a = 19 %	30.6	14.4	1.00
	ε_a = 20 %	30.6	14.3	1.00
	ε_a = 25 %	30.7	14.1	1.00
	ε_a = 30 %	30.1	15.3	1.00

(b) PO soils (PO07, PO19, PO31)

	Axial strain	Effective frictional angle, ϕ' (°)	Effective cohesion, c' (kPa)	Correlation coefficient, R^2
DIS	ε_a = 2 %	10.5	32.5	0.85
	ε_a = 3 %	15.5	26.0	0.94
	ε_a = 4 %	20.6	23.7	0.99
	ε_a = 5 %	22.1	22.7	0.99
PPR	ε_a = 6 %	29.1	9.9	1.00
	ε_a = 7 %	30.7	7.9	1.00
	ε_a = 8 %	31.5	7.3	1.00
	ε_a = 9 %	32.4	4.8	1.00
	ε_a = 10 %	33.1	5.1	1.00
	ε_a = 11 %	33.5	4.3	1.00
	ε_a = 12 %	33.6	3.7	1.00
	ε_a = 13 %	N.A	N.A	N.A
	ε_a = 14 %	34.0	3.9	1.00
	ε_a = 15 %	34.1	4.0	1.00
	ε_a = 16 %	N.A	N.A	N.A
	ε_a = 17 %	34.0	4.5	1.00
	ε_a = 18 %	N.A	N.A	N.A
	ε_a = 19 %	N.A	N.A	N.A
	ε_a = 20 %	34.2	4.1	1.00
	ε_a = 25 %	34.4	3.6	1.00
	ε_a = 30 %	N.A	N.A	N.A

ε_a = 2-5 %: drained initial shear (DIS); N.A.: No data has been recorded

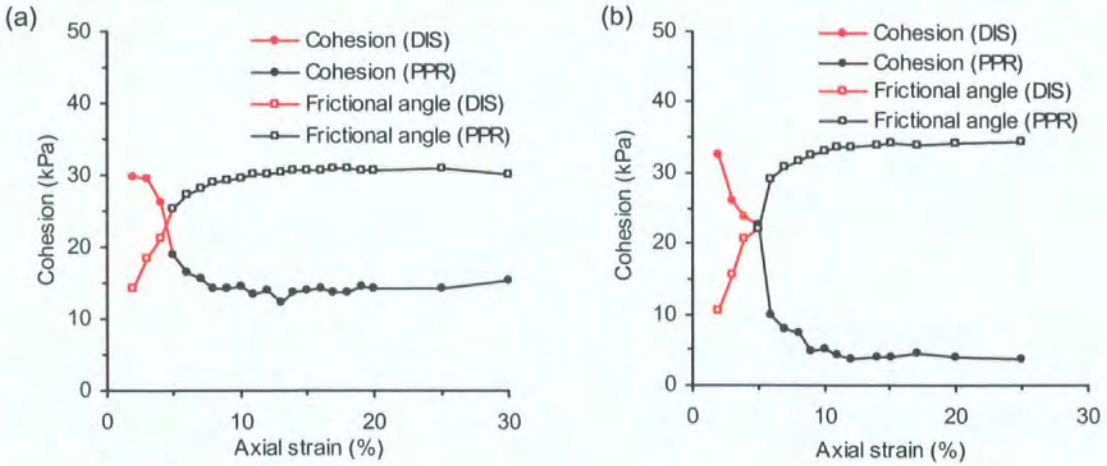

Figure 5.26 Strain development during PPR tests (including the drained initial shear phase) in terms of effective cohesion and frictional angle: (a) TC samples (TC24, TC26, TC28); (b) PO samples (PO07, PO19, PO31)

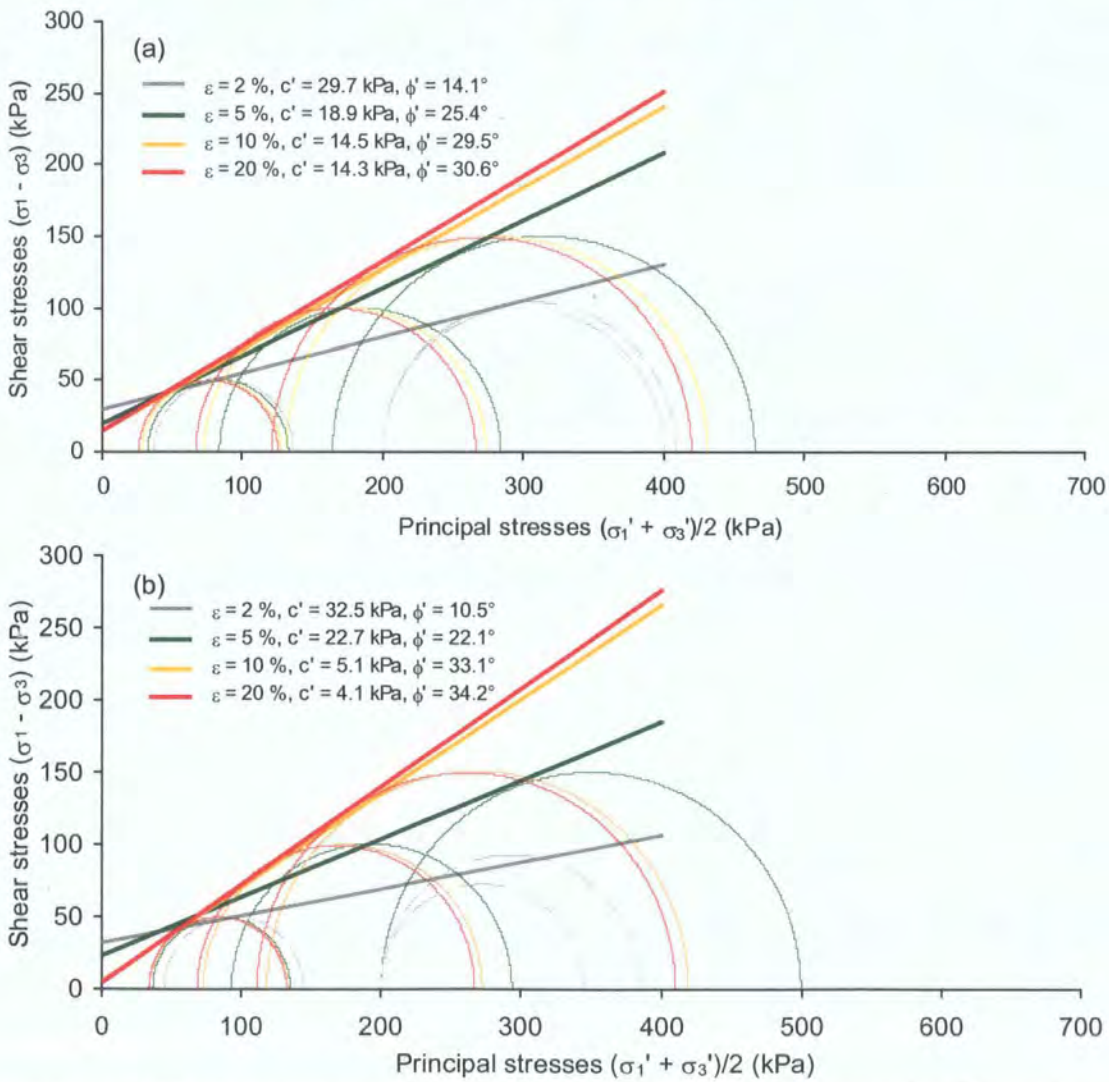

Figure 5.27 Strain development during the PPR tests, undertaken at constant deviatoric stresses 100, 200 and 300 kPa with 10 kPa/hr pore pressure increase, revealed from Mohr circles at equal strains: (a) TC samples (TC24, TC26, TC28); (b) PO samples (PO07, PO19, PO31)

The mobilisation of cohesion during the stress-controlled initial drained shear and the reinflation (PPR) process (transition at 5% strain) was different from the strain rate controlled ICU and ICD compression, as shown within the TC and PO samples (cf. Figures 5.8, 5.14, 5.26). The pore pressure reinflation involved a sharp drop in cohesion at small strains, followed by lower but relatively constant values at the larger strains (Figure 5.26). This did not occur during the compression tests which generated an initial increase in cohesion instead (Figures 5.8, 5.14). However, the development of friction during reinflation was similar to the standard triaxial tests, with a rapid increase to relatively constant values at larger strains, as the soil particles were resisting against the shear force under both conditions.

The changes of the cohesion and frictional strength parameters were also indicated by the intercepts and the steepness of the strain contours in $\tau_{max} - \sigma'$ (Figure 5.27). In general, the stress-controlled strain contours derived from the reinflation had steeper slopes and higher cohesion intercepts giving higher c' and ϕ' values (Figure 5.27).

An alternative and more precise way to assess strain development towards failure as a result of pore water pressure increase is to plot strain rate contours (Figure 5.28). Strain rates of 0.1, 1-4, 6-7, 9-11, 13 and 15 microstrains per second (μs/sec) were recorded within both the TC and PO samples and the respective strain rate contours were determined. At the start of the reinflation tests, where effective stress levels were highest, the samples showed little movement, with strain rates less than 0.1 μs/sec. This "zero movement" zone became larger at lower deviatoric stress levels. The contours were widely spread until strain rates reached 1 μs/sec. Afterwards, steeper gradients were exhibited as the mean effective stress decreased towards final failure. The acceleration appeared the most abrupt at lower deviatoric stress levels, as shown by the closely-spaced contours. These implied that, given the same soil depth (represented by p'), slopes with a lower angle (indicated by lower q) would sustain a higher pore water pressure level without significant movements (e.g. less than 1 μs/sec). However, the acceleration towards final failure would be more sudden (Figure 5.28).

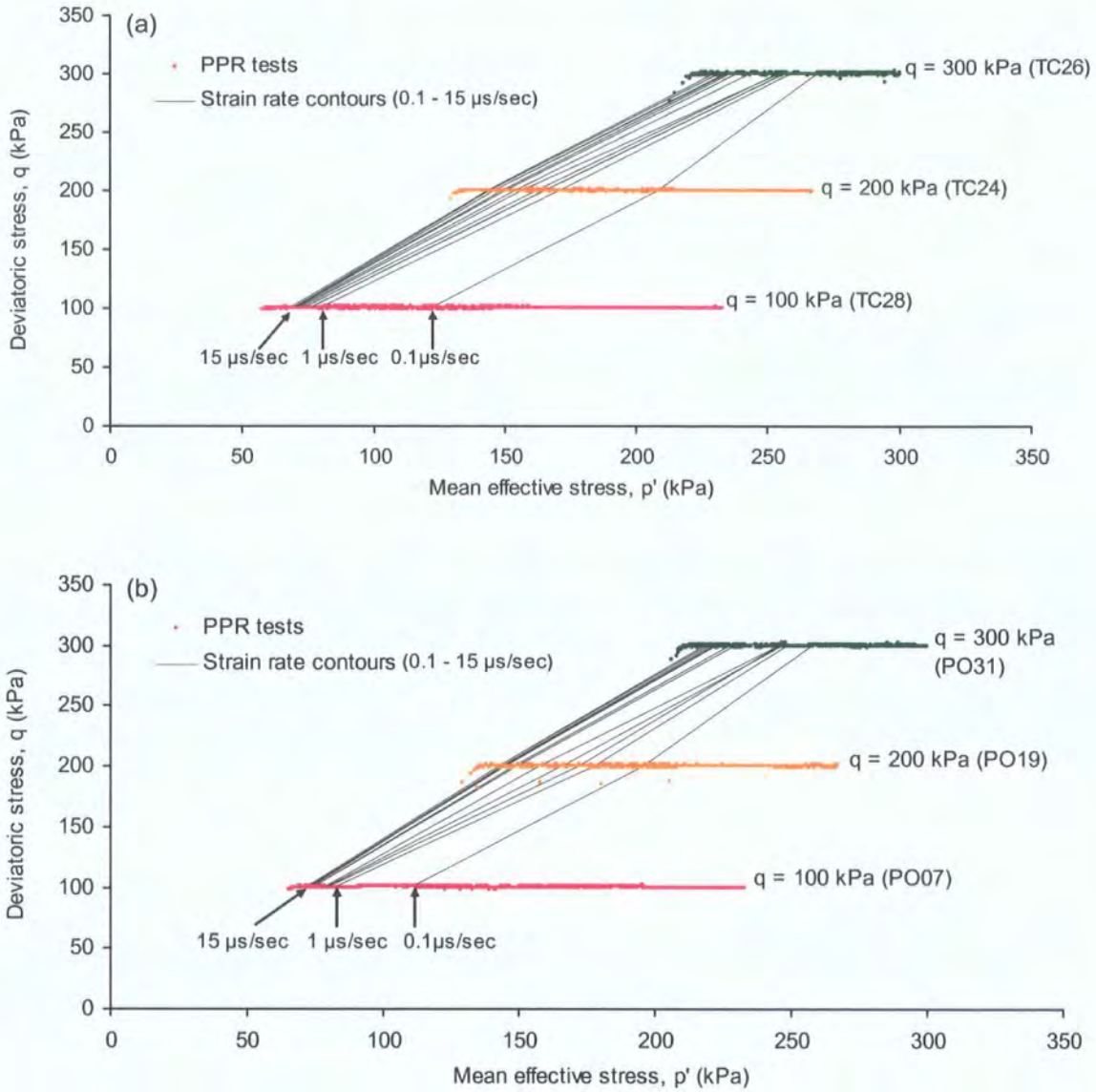

Figure 5.28 Strain development expressed in velocity contours during 10 kPa/hr pore pressure increase at different deviatoric stress levels: (a) TC samples; (b) PO samples

The accelerating movements towards failure in relation to pore water pressure increase can be presented in plots of inverse axial strain rate (Λ) against mean effective stress (p') (Figure 5.29) or against time (t) (Figure 5.30). The distinctive asymptotic trend demonstrated by both the TC and PO samples indicates plastic deformation (Petley *et al.*, 2002, 2005c). Statistical analyses further showed that they were best described by the exponential function (Table 5.13).

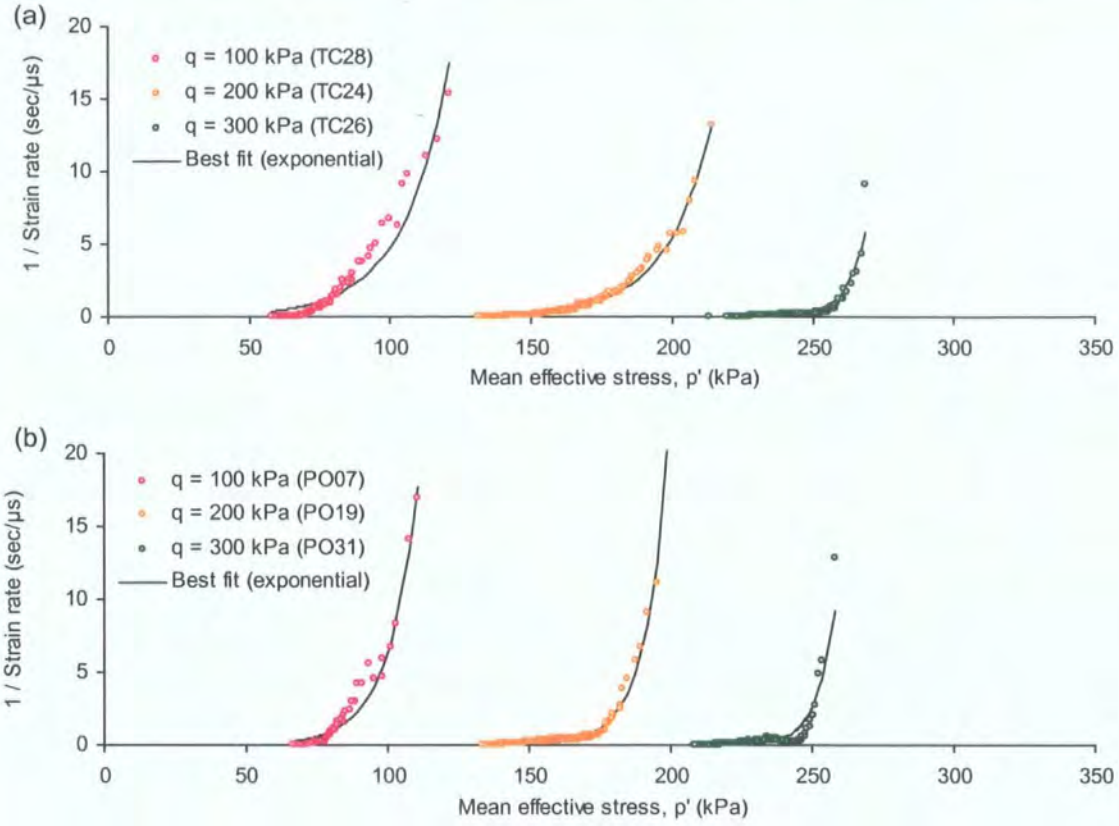

Figure 5.29 Plots of $\Lambda - p'$ during 10 kPa/hr linear pore pressure increase at deviatoric stress levels 100, 200 and 300 kPa: (a) TC samples; (b) PO samples

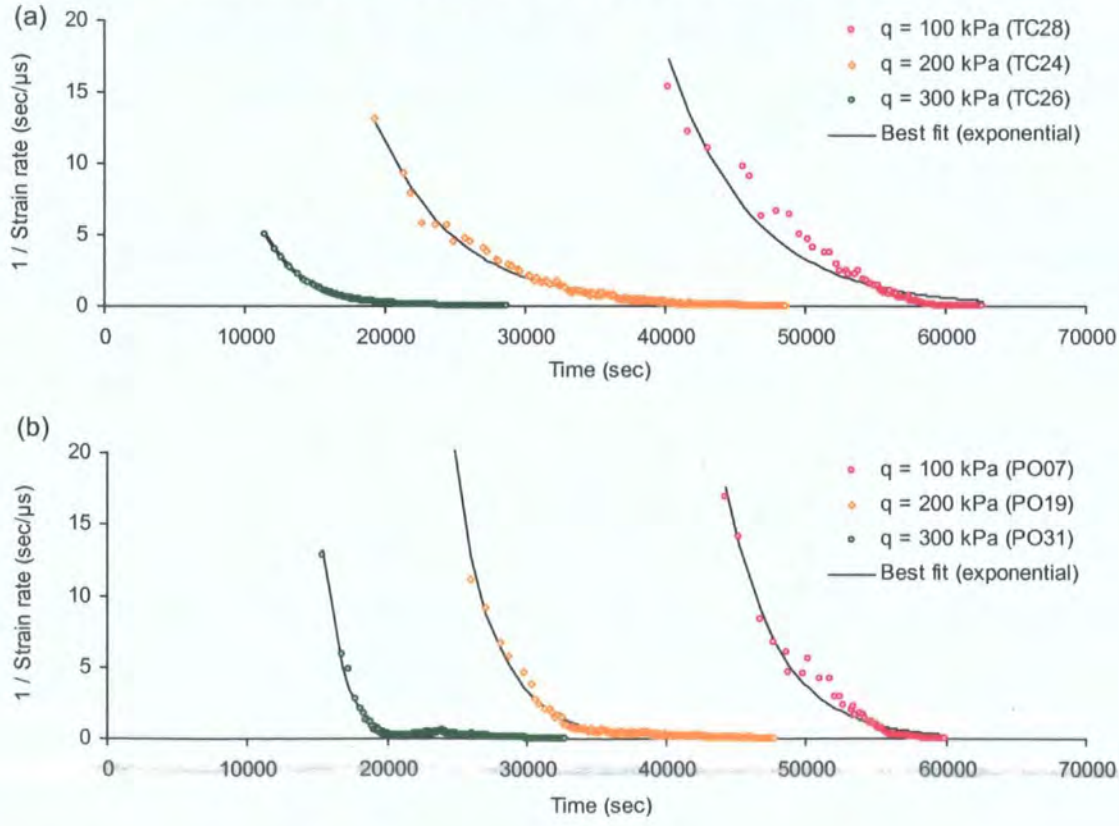

Figure 5.30 Plots of $\Lambda - t$ during 10 kPa/hr linear pore pressure increase at deviatoric stress levels 100, 200 and 300 kPa: (a) TC samples; (b) PO samples

Table 5.13 Best fit coefficients for plots in $\Lambda - p'$ and $\Lambda - t$ under 10 kPa/hr pore water pressure increase at deviatoric stress levels 100, 200 and 300 kPa

(a) TC soils

Sample number	PPR rate (10 kPa/hr)	Number of data	$\Lambda - p'$		$\Lambda - t$	
			R^2 (linear)	R^2 (exponential)	R^2 (linear)	R^2 (exponential)
TC28	q = 100	130	0.84	0.93	0.84	0.93
TC24	q = 200	255	0.61	0.99	0.61	0.99
TC26	q = 300	225	0.25	0.86	0.26	1.00

(b) PO soils

Sample number	PPR rate (10 kPa/hr)	Number of data	$\Lambda - p'$		$\Lambda - t$	
			R^2 (linear)	R^2 (exponential)	R^2 (linear)	R^2 (exponential)
PO07	q = 100	100	0.77	0.97	0.77	0.97
PO19	q = 200	240	0.25	0.99	0.25	0.99
PO31	q = 300	328	0.17	0.80	0.17	0.96

5.7.3 The PPR failure envelope

The commonly accepted failure criterion regarding the maximum deviatoric stress does not apply to the stress-controlled reinflation tests, as the shear stress has been held constant below the maximum level until reaching failure. The failure criteria for PPR tests, however, could be more appropriately assessed using the axial strain development as expressed by the strain contours (Table 5.12, Figure 5.27). These strain envelopes derived from the reinflation process were strongly linear (R^2 = 1.00) (Table 5.12).

Another common failure definition for plastic materials at 20% strain (Selby, 1993) was not found to be the best criterion for the TC and PO samples, where the maximum effective frictional angle and cohesion were not mobilised (Table 5.12) (Figure 5.31). Instead, the failure envelope appeared to be more appropriately defined during the drained initial shear stage at 3% axial strain for the TC samples and at 5% axial strain for the PO samples. The corresponding ϕ' and c' were 18.4°, 29.4 kPa respectively for the TC samples and 22.1°, 22.7 kPa respectively for the PO samples (Table 5.12).

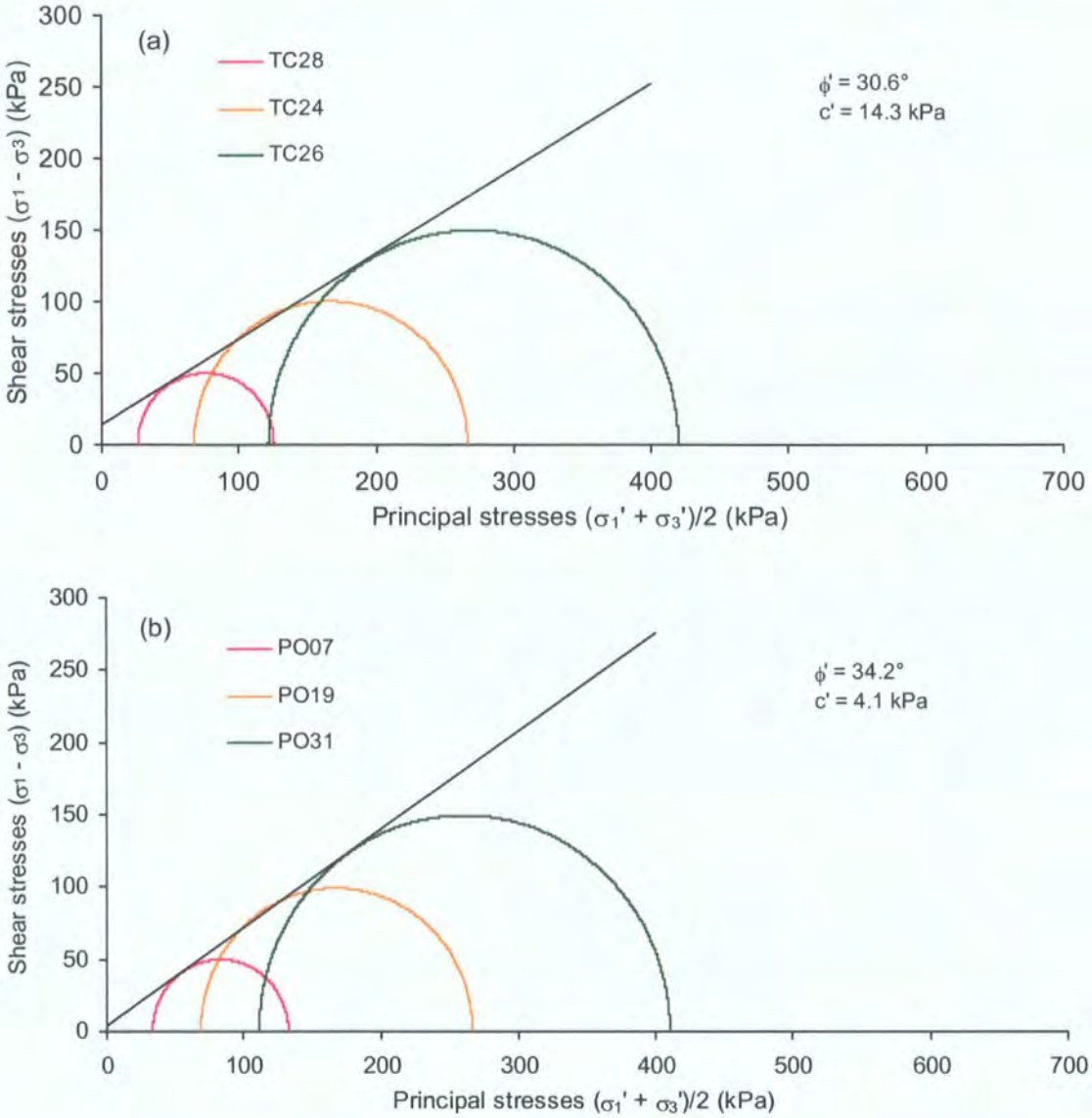

Figure 5.31 Best-fit failure envelopes defined by the stress conditions at 20% axial strain, derived from three PPR tests initiated at deviatoric stresses 100, 200 and 300 kPa: (a) TC samples; (b) PO samples

5.7.4 Stress-strain soil behaviour

Stress-strain behaviour under pore water pressure reinflation (PPR) test can be expressed in plots of axial strain against deviatoric stress (Figure 5.32) to compare with the ICU (Figure 5.13) and the ICD (Figure 5.17) tests. The stress-strain curves, as shown in Figure 5.32, represent the stress-controlled soil behaviour during the drained initial shear and the subsequent reinflation. Unsurprisingly, the TC and PO samples showed a stiff stress-strain behaviour during the initial drained shear, similar to the conventional tests. However, during the subsequent reinflation, the deviatoric stress

was held constant (Figure 5.32). This involved plastic deformation, as evident by the barrel-like lateral expansion (Appendix 1c).

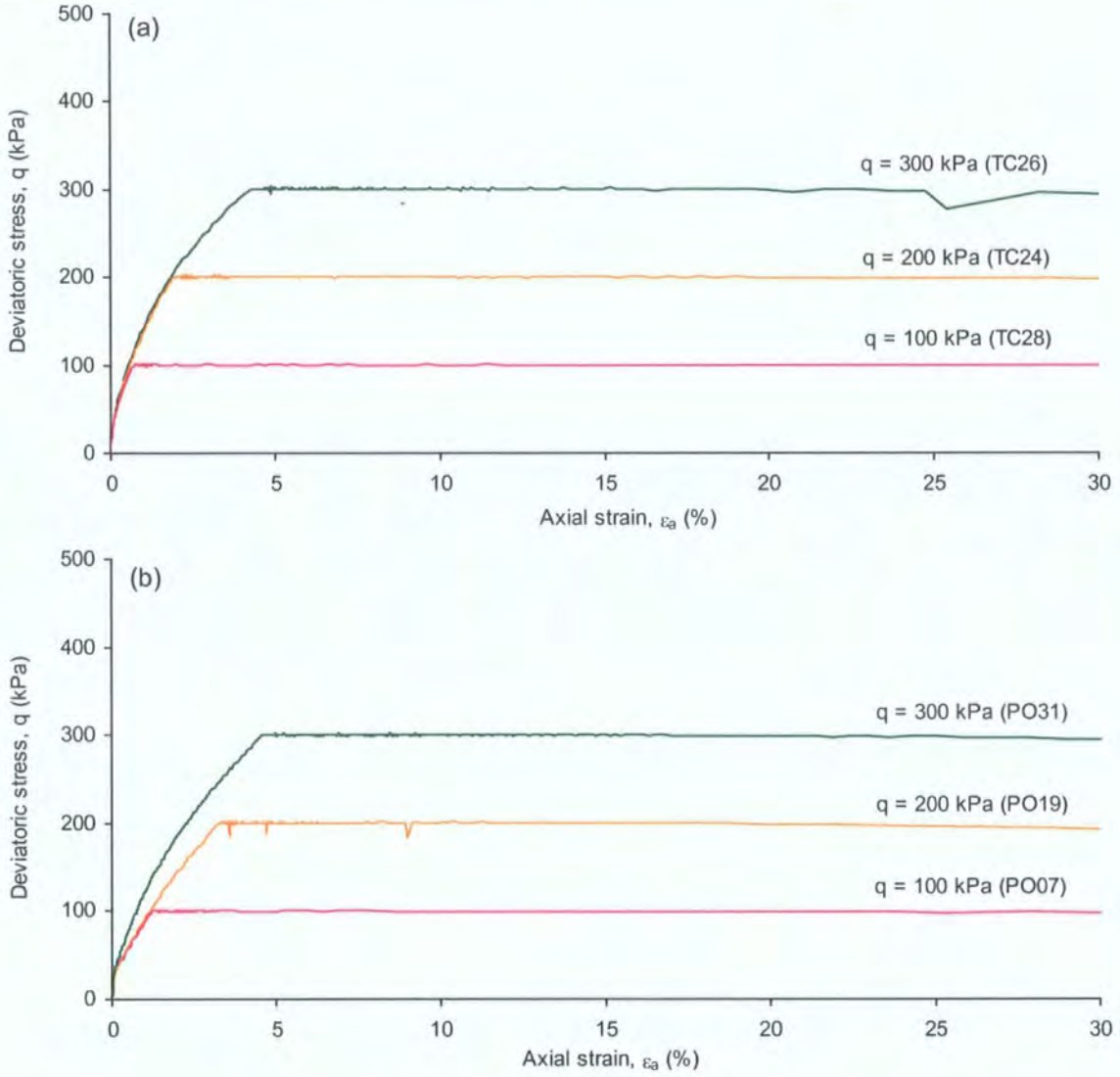

Figure 5.32 Stress-strain behaviour at p'_c = 200 kPa under 10 kPa/hr linear pore water pressure increase at deviatoric stress levels 100, 200 and 300 kPa:
(a) TC samples; (b) PO samples

Regarding the volumetric strains, contractive behaviour (shown by the positive volumetric strain values) was demonstrated throughout the drained initial shear (Figure 5.33), similar to the behaviour exhibited under the ICD conditions (Figure 5.18). The larger volumetric strains were associated with the higher deviatoric stress levels being applied (Figure 5.33).

In contrast, volumetric expansion within the samples was noted during the reinflation process, as indicated by the negative change in the volumetric strains (Figure 5.33). The dilation might be related to the application of a higher effective stress during the consolidation stage (section 4.2.3) that overconsolidated the samples (i.e. the samples became denser than they were in the field) (Dixon, 2007).

The expansion was particularly significant at the beginning of the reinflation process, followed by a more gradual increase towards the end of the test. The largest increase in sample volume (i.e. TC28, PO07) was generated at the lowest deviatoric stress level (i.e. q = 100 kPa) under the same rate of reinflation (i.e. 10 kPa/hr). This might be related to the relatively higher void ratio after the lower level of initial drained shear applied (Table 5.11), which facilitated greater deformation by the subsequent reinflation. Moreover, the form of the strain curves is different between the TC and PO samples (Figure 5.33), which reflects sample variability.

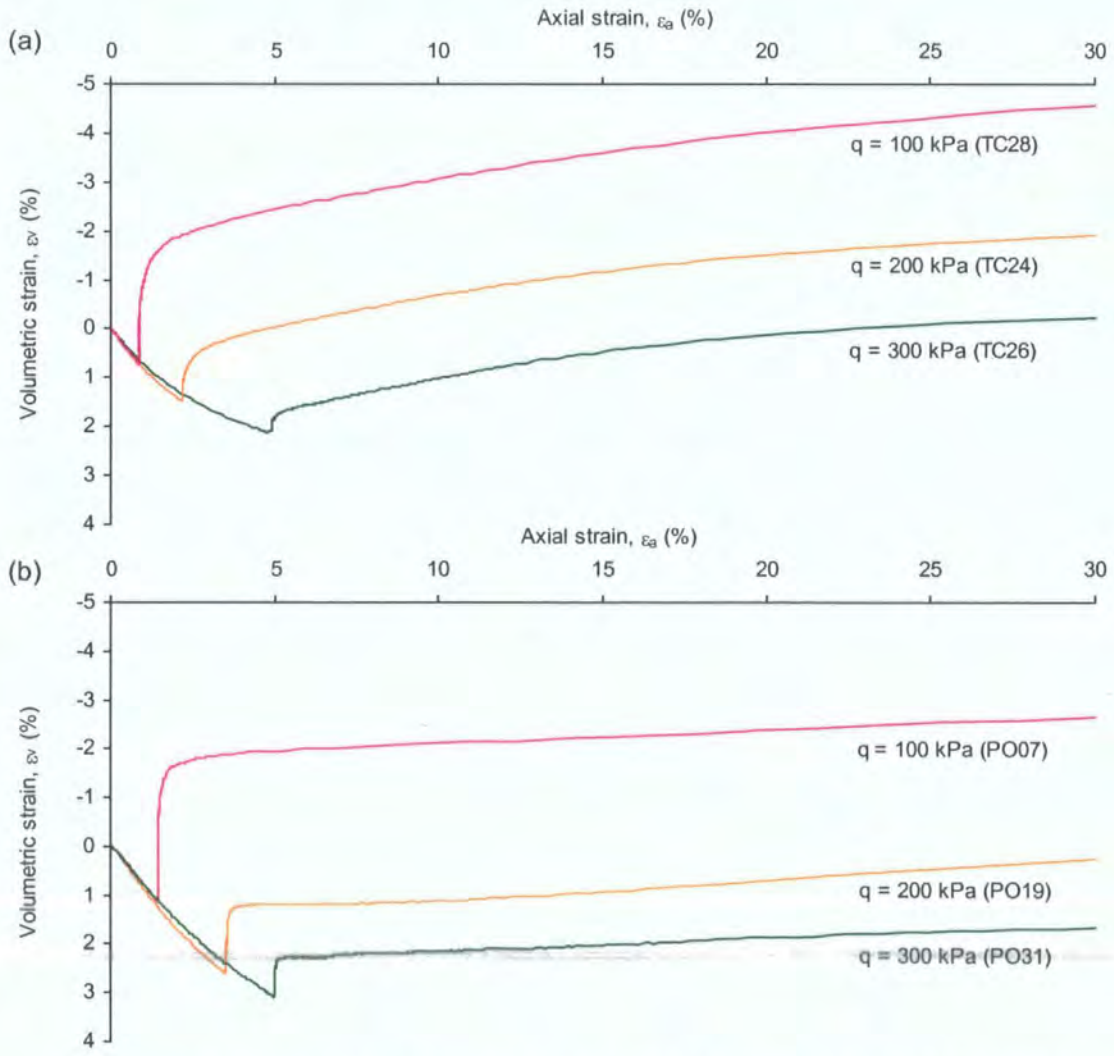

Figure 5.33 Volumetric behaviour during the drained initial shear and reinflation tests at deviatoric stress levels 100, 200 and 300 kPa: (a) TC samples; (b) PO samples

5.7.5 Deformation behaviour under reinflation

5.7.5.1 Linear rates of pore water pressure increase

During the reinflation testing at various linear rates (Table 5.3), both TC and PO samples showed no movement or very low strain rates initially as p' decreased from 233 kPa to about 110 kPa, irrespective of the different pore water pressure rates applied (Figure 5.34).

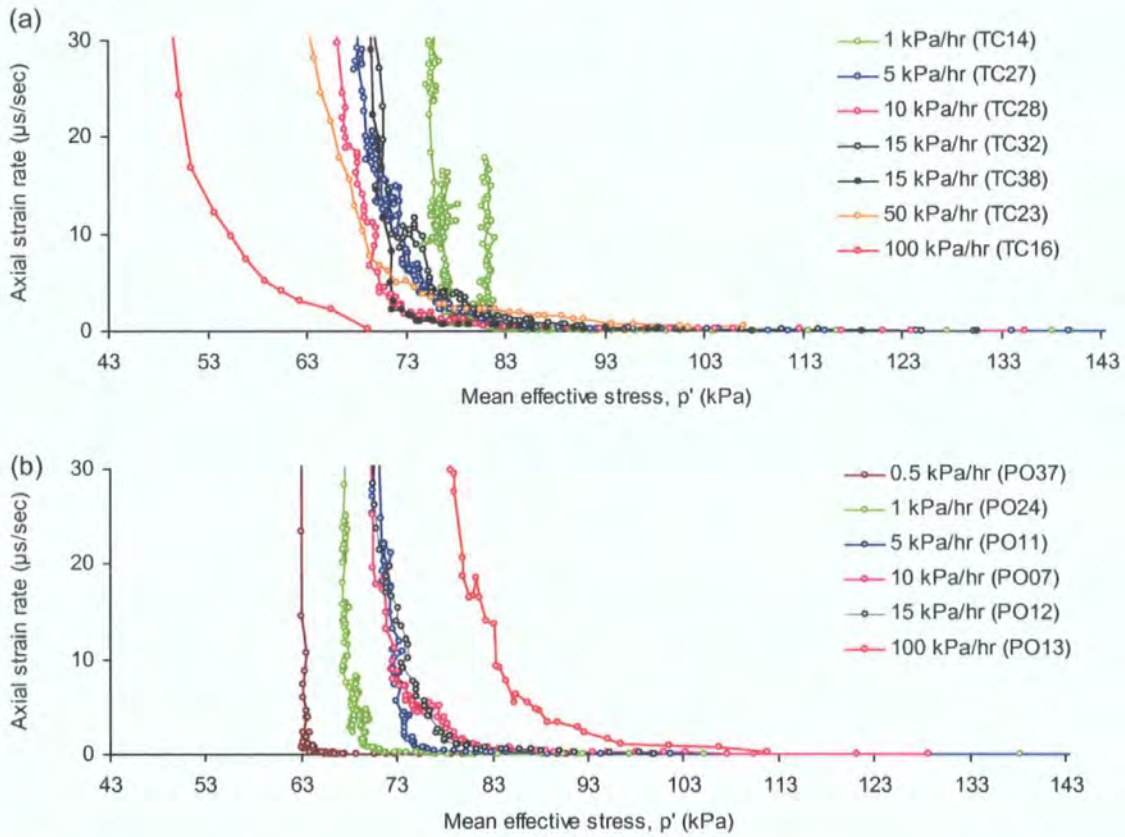

Figure 5.34 Plots of $\dot{\varepsilon} - p'$ under linear pore water pressure increase at 0.5 kPa/hr to 100 kPa/hr: (a) TC samples; (b) PO samples

This phase of little movement was followed by a rapid acceleration at p' of less than 113 kPa towards failure (Figure 5.34). The timing of the acceleration under the same reinflation rates appeared similar between the TC and the PO samples (Figure 5.35). It was surprising to note that the acceleration did not start at the same mean effective stress within either the TC or the PO soils of similar void ratios (Figure 5.34, Table 5.11), contrasting with the critical state theory. Interestingly, for the reinflation tests undertaken at 1 kPa/hr, the acceleration behaviour was obviously disturbed by occasional periods of deceleration (Figure 5.34a).

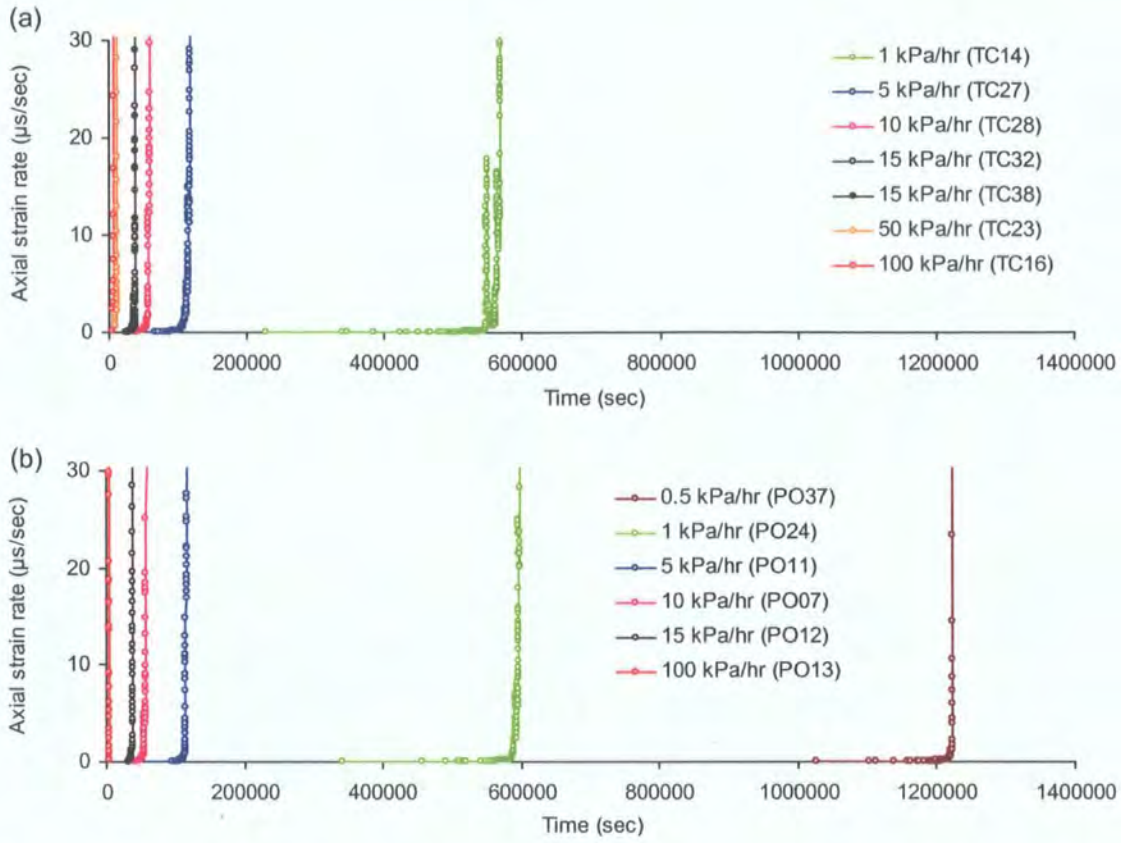

Figure 5.35 Plots of $\dot{\varepsilon} - t$ under linear pore water pressure increase at 0.5 kPa/hr to 100 kPa/hr: (a) TC samples; (b) PO samples

The accelerating behaviour of the TC and PO samples can be best described with the exponential function in $\Lambda - p'$ and in $\Lambda - t$ space (Table 5.14, Figures 5.36, 5.37). The best fit coefficients were statistically significant ($R^2 \geq 0.90$), except for the tests at lowest rates: 0.5 kPa/hr (PO37) ($R^2 \geq 0.70$) and 1 kPa/hr tests (TC14) ($R^2 \geq 0.88$). The asymptotic trend in $\Lambda - t$ space indicates plastic deformation (Figure 5.37) (Petley *et al.*, 2002, 2005c), as also evident by the barrel-like lateral expansion of the tested samples (Appendix 2a).

Table 5.14 Best fit coefficients for plots in $\Lambda - p'$ and $\Lambda - t$ under linear pore water pressure increase at 0.5 kPa/hr to 100 kPa/hr

(a) TC soils

Sample number	PPR rate (linear)	Number of data	$\Lambda - p'$		$\Lambda - t$	
			R^2 (linear)	R^2 (exponential)	R^2 (linear)	R^2 (exponential)
TC14	1 kPa/hr	345	0.73	0.88	0.73	0.88
TC27	5 kPa/hr	227	0.58	0.98	0.58	0.98
TC28	10 kPa/hr	130	0.84	0.93	0.84	0.93
TC32	15 kPa/hr	94	0.72	0.96	0.73	0.96
TC38	15 kPa/hr	67	0.79	0.96	0.80	0.96
TC23	50 kPa/hr	62	0.69	0.94	0.69	0.94
TC16	100 kPa/hr	24	0.63	1.00	0.62	0.93

(b) PO soils

Sample number	PPR rate (linear)	Number of data	$\Lambda - p'$		$\Lambda - t$	
			R^2 (linear)	R^2 (exponential)	R^2 (linear)	R^2 (exponential)
PO37	0.5 kPa/hr	68	0.87	0.93	0.89	0.70
PO24	1 kPa/hr	222	0.61	0.89	0.61	0.90
PO11	5 kPa/hr	101	0.43	0.98	0.43	0.98
PO07	10 kPa/hr	100	0.77	0.97	0.77	0.97
PO12	15 kPa/hr	76	0.72	0.92	0.73	0.91
PO13	100 kPa/hr	71	0.55	0.97	0.55	0.97

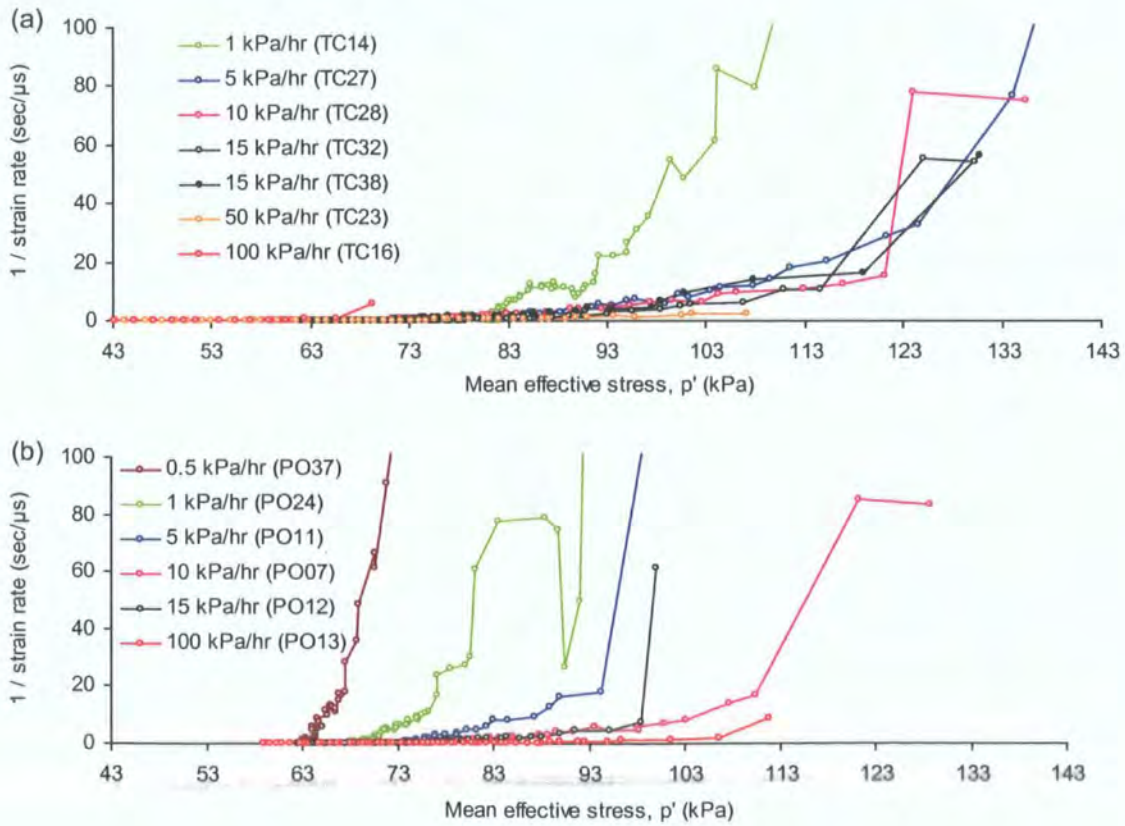

Figure 5.36 Plots of $\Lambda - p'$ during linear rates of pore water pressure increase from 0.5 kPa/hr to 100 kPa/hr: (a) TC samples; (b) PO samples

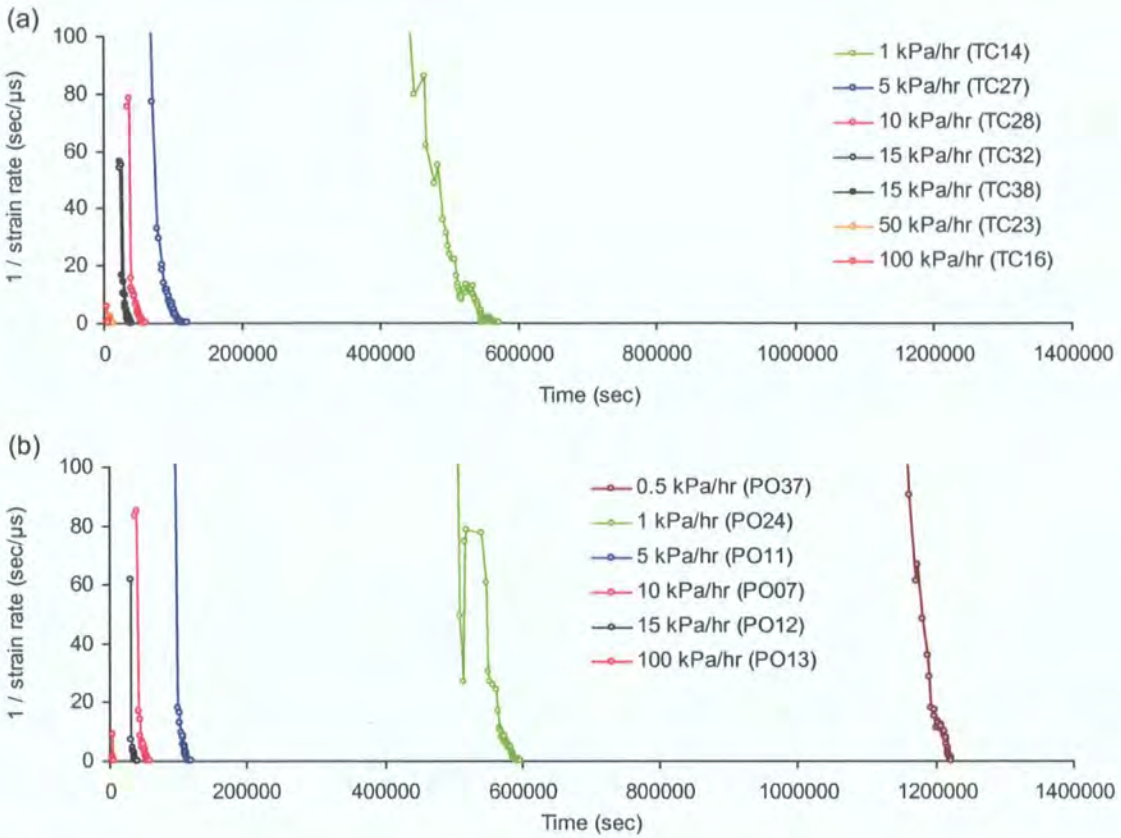

Figure 5.37 Plots of $\Lambda - t$ during linear rates of pore water pressure increase from 0.5 kPa/hr to 100 kPa/hr: (a) TC samples; (b) PO samples

In general, there was a negative relationship between increasing rates of pore water pressure and the gradient of the curve in $\Lambda - p'$ or $\Lambda - t$ (Figures 5.36, 5.37). Higher pore water pressure rates appeared to lead to lower gradients in $\Lambda - p'$ and $\Lambda - t$ space, as clearly demonstrated by the PO samples (Figures 5.36b, 5.37b).

However, the acceleration behaviour of the TC samples has proven difficult to characterise, especially in plots of $\Lambda - p'$ (Figure 5.36a). The results were further analysed by isolating the effect of sample density (Figures 5.38, 5.39). It is interesting to note that the systematic negative relationship between the reinflation rates and the slope of $\Lambda - p'$ and $\Lambda - t$ space in the PO samples also held true for the TC samples. The acceleration behaviour under the different rates of reinflation was consistent between the TC and the PO samples.

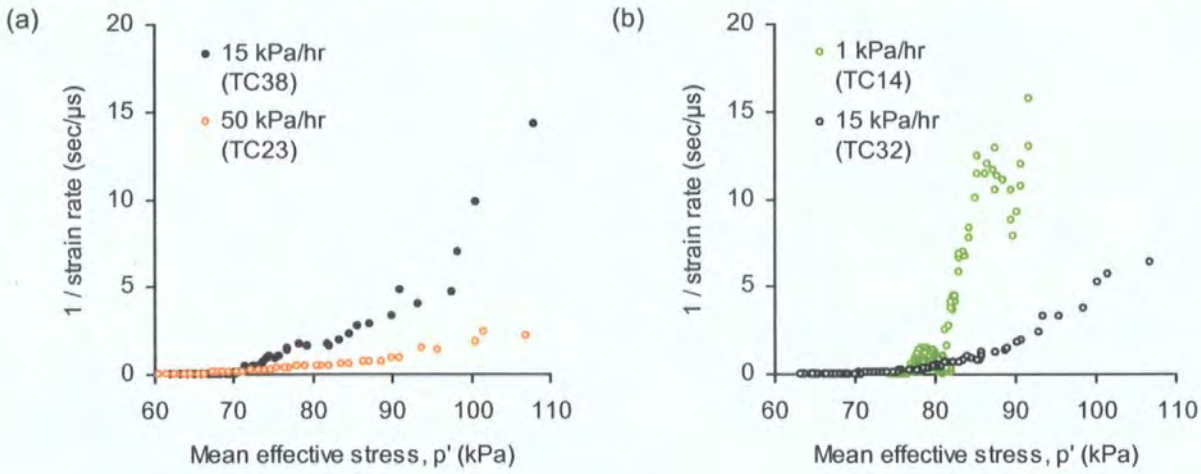

Figure 5.38 Acceleration movements in $\Lambda - p'$ during reinflation test on TC samples: (a) 15 kPa/hr vs 50 kPa/hr (initial void ratio before saturation: 0.66); (b) 1 kPa/hr vs 15 kPa/hr (initial void ratio after drained initial shear: 0.61)

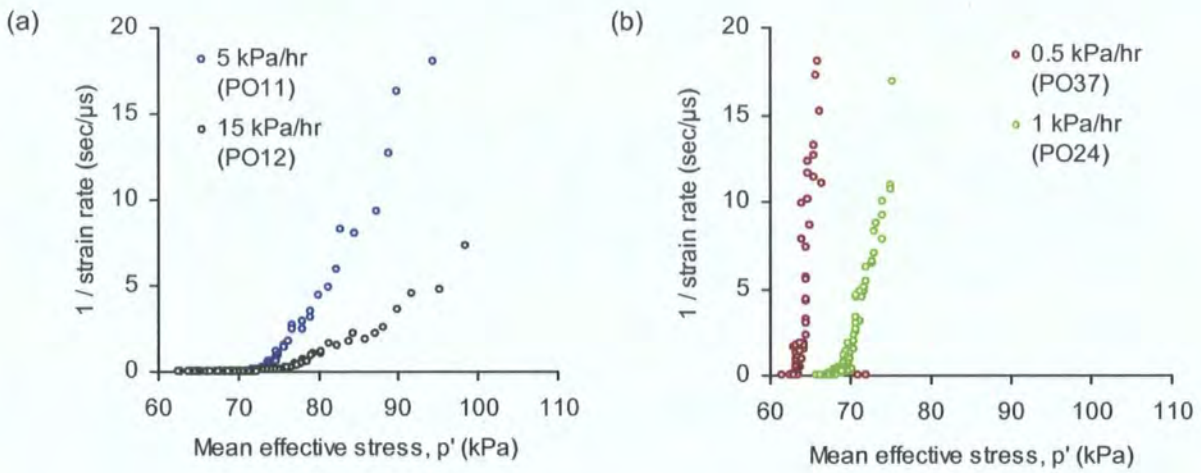

Figure 5.39 Acceleration movements in $\Lambda - p'$ during reinflation test on PO samples: (a) 5 kPa/hr vs 15 kPa/hr (initial void ratio before saturation: 0.83); (b) 0.5 kPa/hr vs 1 kPa/hr (initial void ratio after drained initial shear: 0.65)

5.7.5.2 Stepped rates of pore water pressure increase

This series of reinflation tests also started at mean effective stress of 233 kPa under a constant deviatoric stress of 100 kPa, but using stepped rates of increase of pore pressure. The time interval between each stepped reinflation was one hour (Table 5.3). An additional stepped test (PO38) was undertaken to examine the soil movements under constant stress (i.e. p', q) conditions. This test replicated the 5 kPa stepped test up to 350 kPa when the first sign of acceleration was shown. At this point, the pore water pressure was held constant over time until the strain rate stabilised before another stepped increase at 5 kPa was applied.

The strain development under the stepped rates in $\dot{\varepsilon} - p'$ (Figure 5.40) and $\dot{\varepsilon} - t$ (Figure 5.41) were initially very similar to those subjected to the linear rates of increasing pore water pressure (cf. Figures 5.34, 5.35), in that they demonstrated very little movement after the start of reinflation. The strain rate under the stepped reinflation remained more or less at zero until p' was at about 83 kPa for the TC and PO samples.

However, the subsequent changing rates of strain development (alternate acceleration and deceleration) formed the most distinctive and intriguing feature from these stepped tests (Figures 5.40, 5.41). The changing strain rates occurred at the same effective stress, as shown by the clustering of points in $\dot{\varepsilon} - p'$ (Figure 5.40). The process was further illustrated, in real time, by the plots of $\dot{\varepsilon} - t$ (Figure 5.41). After the pore water pressure was increased stepwise to a new level, the strain rate increased immediately reaching a maximum but then decelerated back towards the initial strain rate (the "minimum") until the next step. Moreover, the change of strain rate between the maxima and minima was increasingly large as the effective stress decreased stepwise towards failure (Figures 5.40, 5.41). The strain rate values at the maxima and minima were not random, but showed a very significant exponential relationship, especially in relation to the mean effective stress ($R^2 > 0.99$) (Table 5.15).

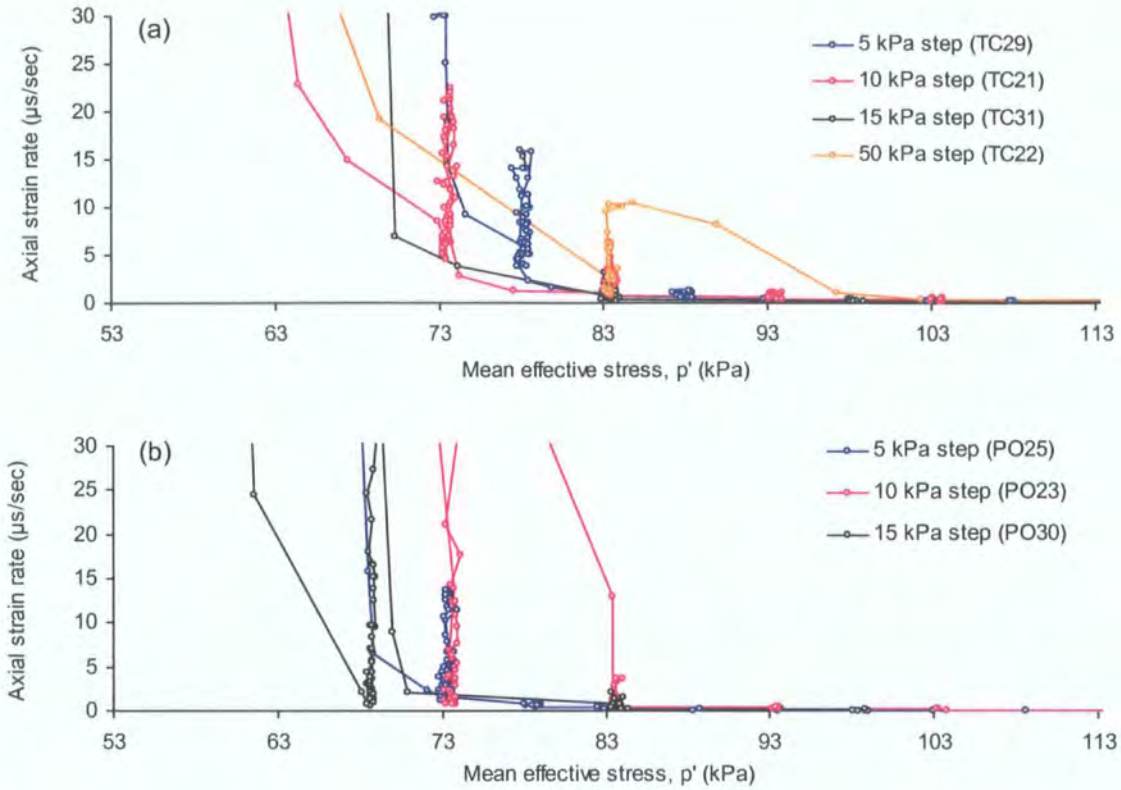

Figure 5.40 Plots of $\dot{\varepsilon} - p'$ under stepped pore water pressure increase at 5, 10, 15 and 50 kPa/hr: (a) TC samples; (b) PO samples

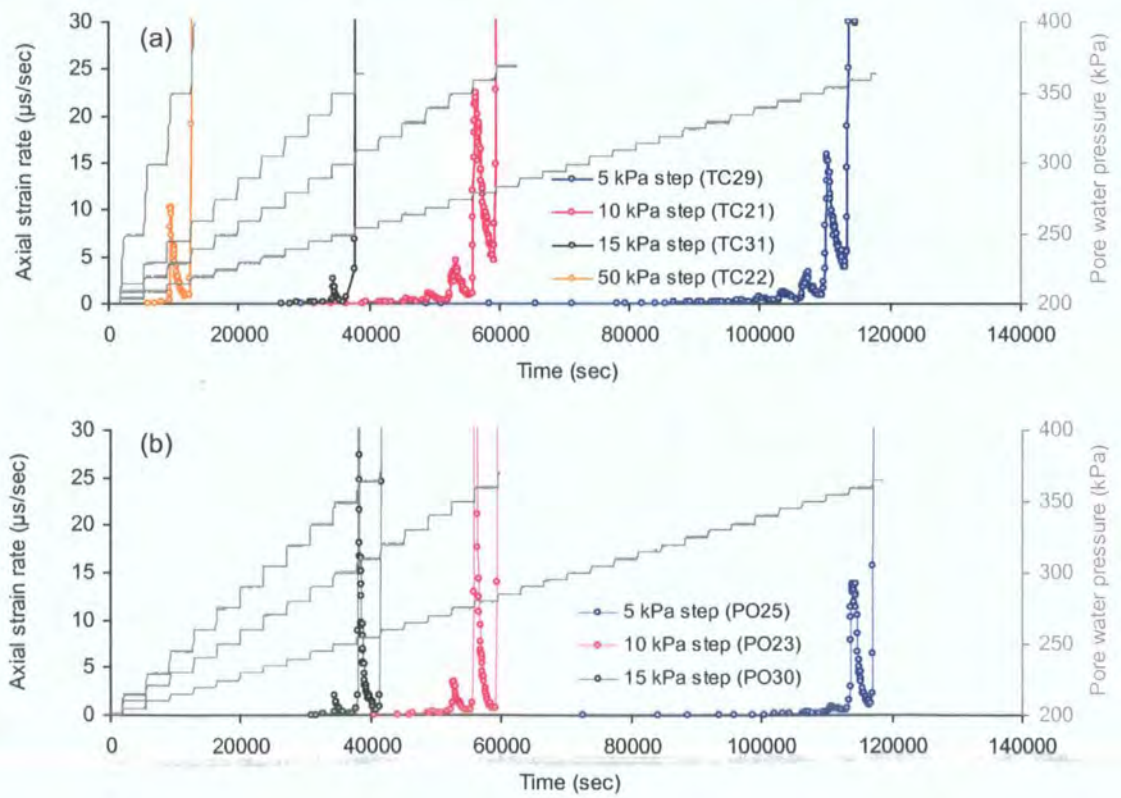

Figure 5.41 Plots of $\dot{\varepsilon} - t$ under stepped pore water pressure increase at 5, 10, 15 and 50 kPa/hr: (a) TC samples; (b) PO samples

Table 5.15 The $\dot{\varepsilon} - p'$ and $\dot{\varepsilon} - t$ relationship at the strain rate maxima and minima during stepped pore water pressure increase*

Sample number	PPR rate (stepped)	Number of data points	$\dot{\varepsilon} - p'$ R^2 (exponential)	$\dot{\varepsilon} - t$ R^2 (exponential)
TC29	5 kPa	6 maxima	1.00	0.99
TC21	10 kPa	5 maxima	0.99	0.98
PO25	5 kPa	4 maxima	1.00	Not applicable
TC29	5 kPa	5 minima	1.00	0.81
TC21	10 kPa	4 minima	1.00	1.00

*Statistical test were applicable only to stepped tests having more than four maxima / minima

In overview, the strain rates became increasingly large as the mean effective stress decreased in steps. Their relationship is best described by the exponential function in $\Lambda - p'$ and $\Lambda - t$ space (Table 5.16), although unsurprisingly the R^2 coefficients were not as significant compared with the tests under the linear pore water pressure rates. The exponential relationship was weakened as higher stepped rates were applied.

Table 5.16 Best fit coefficients for plots in $\Lambda - p'$ and $\Lambda - t$, under stepped pore water pressure increase at 5, 10, 15 and 50 kPa/hr

(a) TC soils

Sample number	PPR rate (stepped)	Number of data	$\Lambda - p'$ R^2 (linear)	$\Lambda - p'$ R^2 (exponential)	$\Lambda - t$ R^2 (linear)	$\Lambda - t$ R^2 (exponential)
TC29	5 kPa step	216	0.75	0.90	0.74	0.90
TC21	10 kPa step	185	0.66	0.91	0.63	0.93
TC31	15 kPa step	39	0.80	0.76	0.77	0.79
TC22	50 kPa step	48	0.39	0.80	0.11	0.63

(b) PO soils

Sample number	PPR rate (stepped)	Number of data	$\Lambda - p'$ R^2 (linear)	$\Lambda - p'$ R^2 (exponential)	$\Lambda - t$ R^2 (linear)	$\Lambda - t$ R^2 (exponential)
PO25	5 kPa step	105	0.77	0.96	0.80	0.96
PO23	10 kPa step	81	0.59	0.85	0.50	0.88
PO30	15 kPa step	90	0.53	0.62	0.31	0.49

The associated exponential $\Lambda - p'$ and the asymptotic trend in $\Lambda - t$ space for the TC and the PO samples were not largely affected by the fluctuating strain rates during the stepped reinflation process (Figures 5.42, 5.43). This implies plastic deformation, which was further supported by the barrel-like expansion within the tested samples (Appendix 2b).

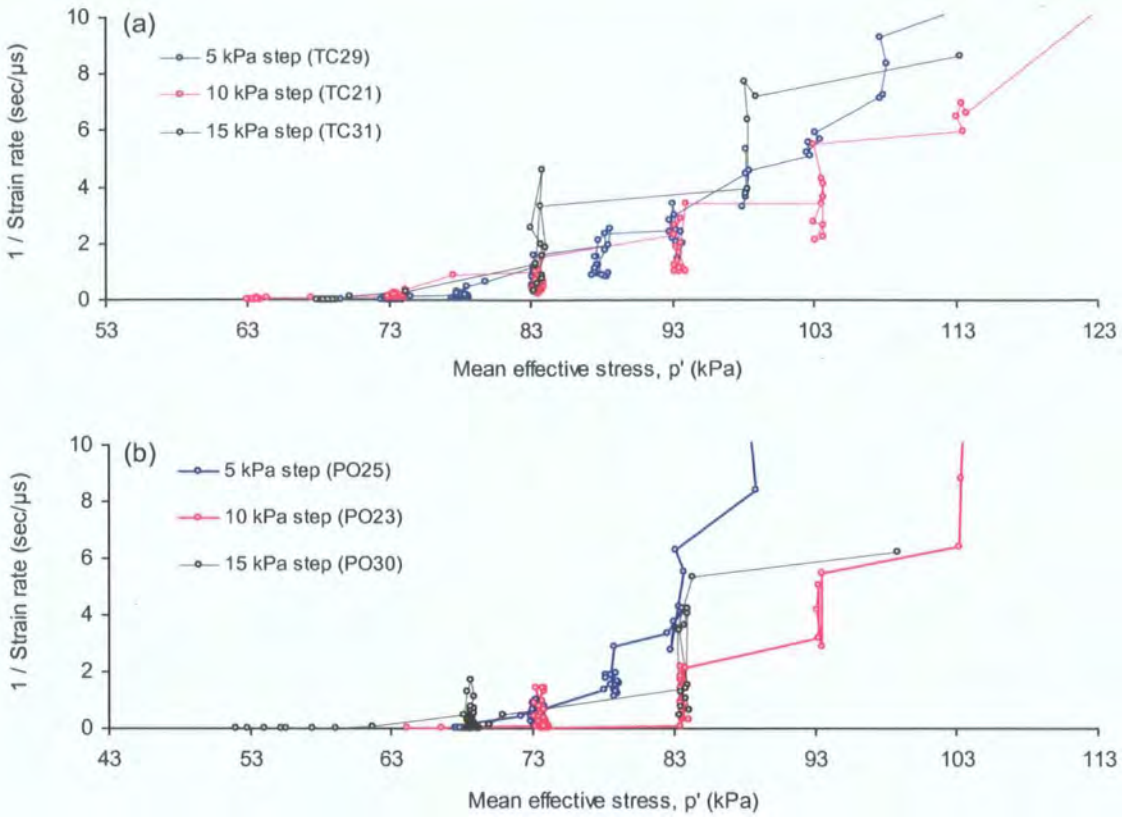

Figure 5.42 Plots of $\Lambda - p'$ during stepped rates of pore water pressure increase at 5, 10, 15 and 50 kPa/hr: (a) TC samples; (b) PO samples

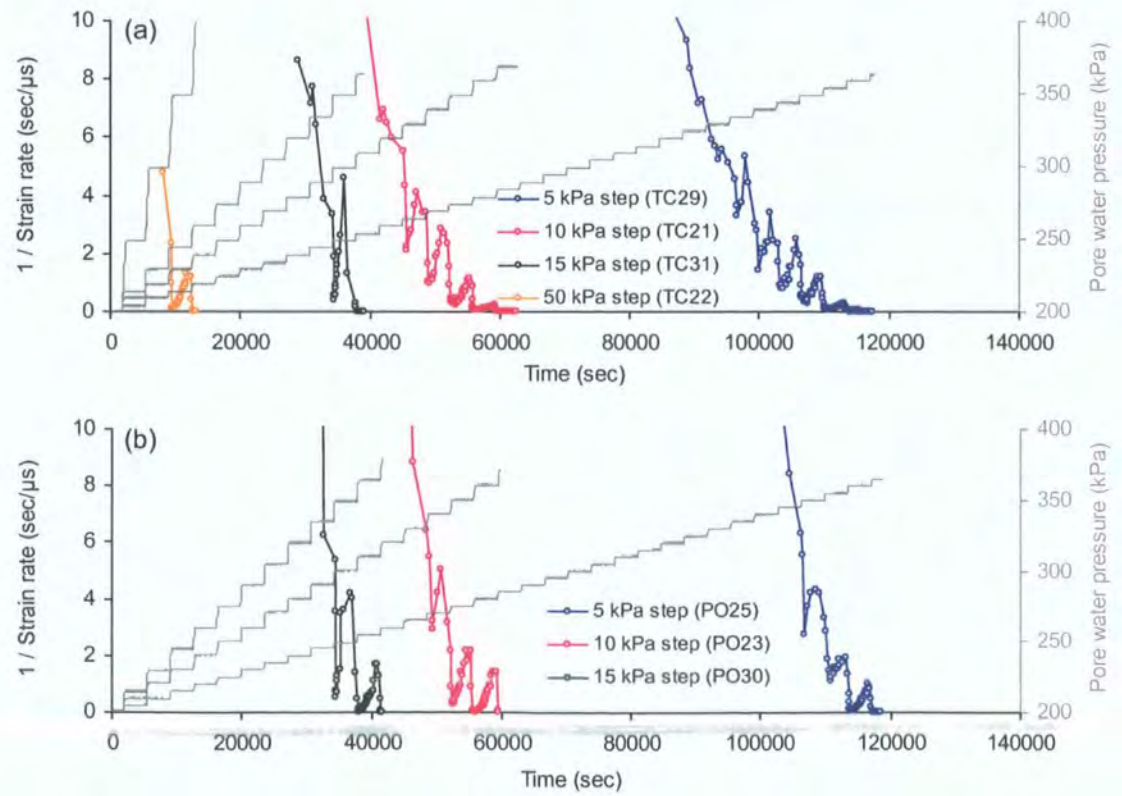

Figure 5.43 Plots of $\Lambda - t$ during stepped rates of pore water pressure increase at 5, 10, 15 and 50 kPa/hr: (a) TC samples; (b) PO samples

The strain rates developed under the stepped rates were further compared with the linear rates. It was interesting to note that the strain rate minima of the stepped tests were similar to the strain rates derived from the linear reinflation, especially within the TC samples subjected to low stepped rates (Figures 5.44-5.47). However, this coincidence was not clearly seen at higher reinflation rates, or within the PO samples (Figures 5.45-5.49). The observed movements appeared to fall within the margin of error as shown by the two identical 15 kPa/hr tests (Figure 5.49a).

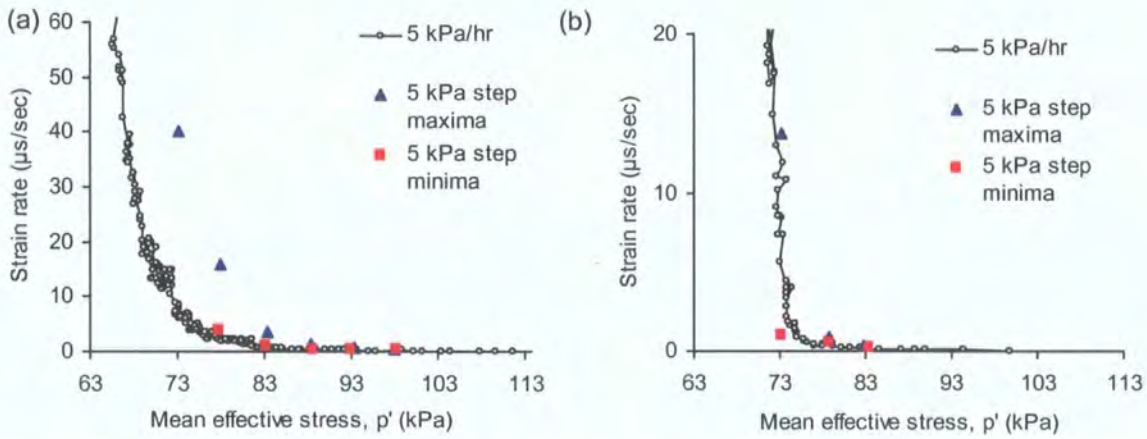

Figure 5.44 Comparison of strain development under linear and stepped pore water pressure rates at 5 kPa/hr in plots of $\dot{\varepsilon} - p'$: (a) TC samples; (b) PO samples

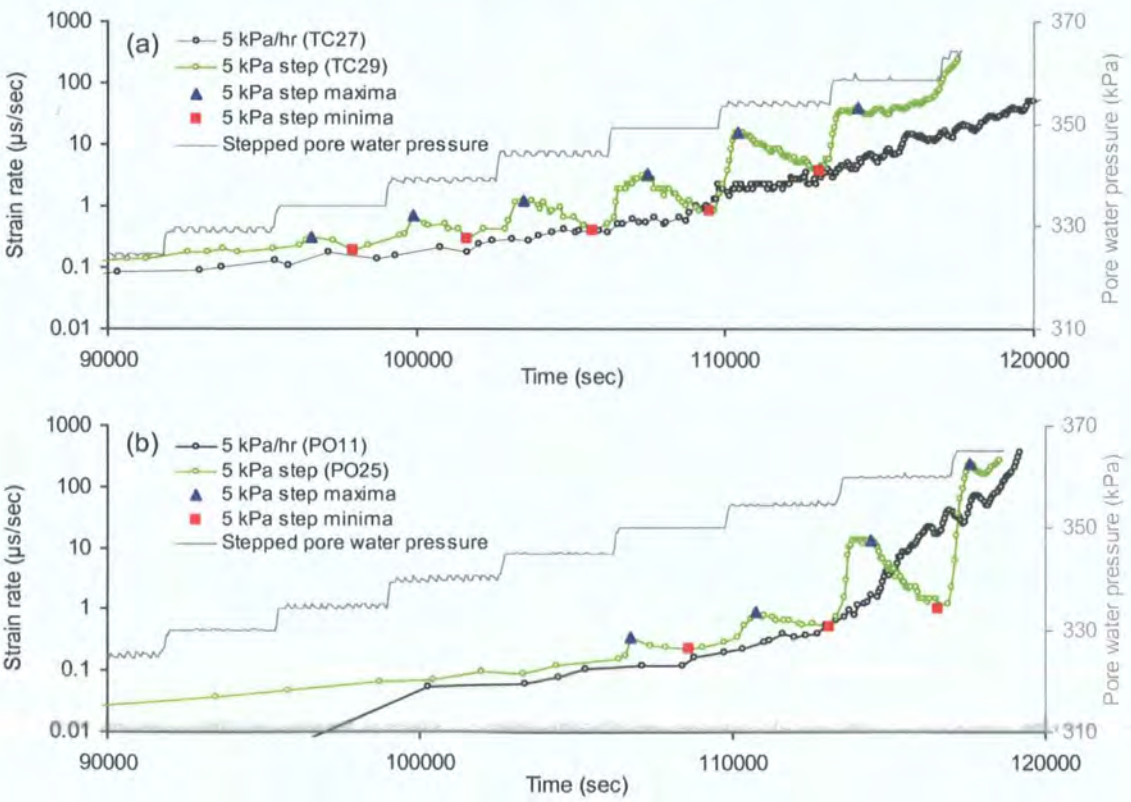

Figure 5.45 Comparison of strain rate development under the linear and stepped reinflation tests at 5 kPa/hr in plots of $\dot{\varepsilon} - t$ space: (a) TC samples; (b) PO samples

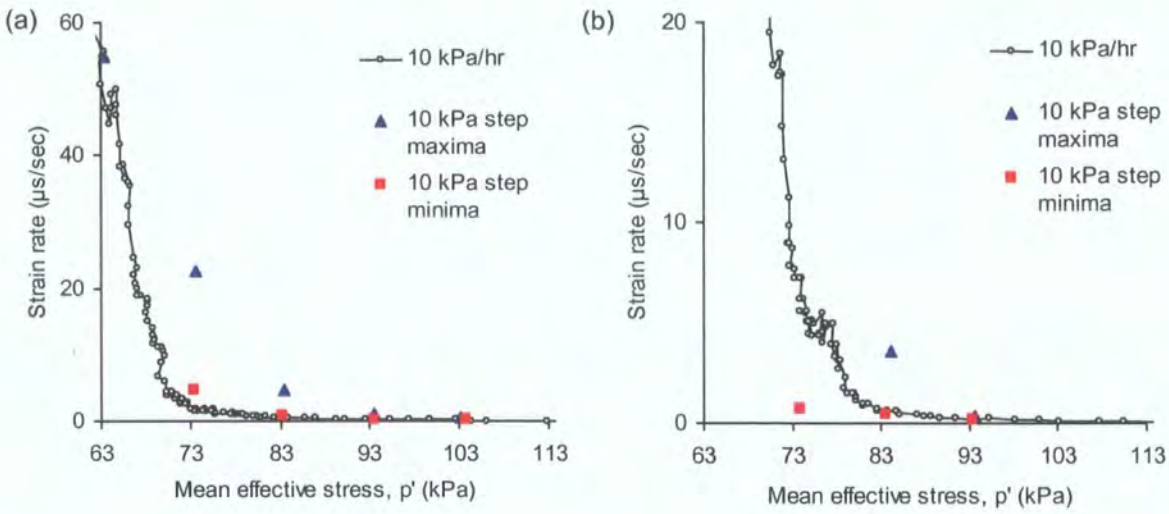

Figure 5.46 Comparison of strain development under linear and stepped pore water pressure rates at 10 kPa/hr in plots of $\dot{\varepsilon} - p'$: (a) TC samples; (b) PO samples

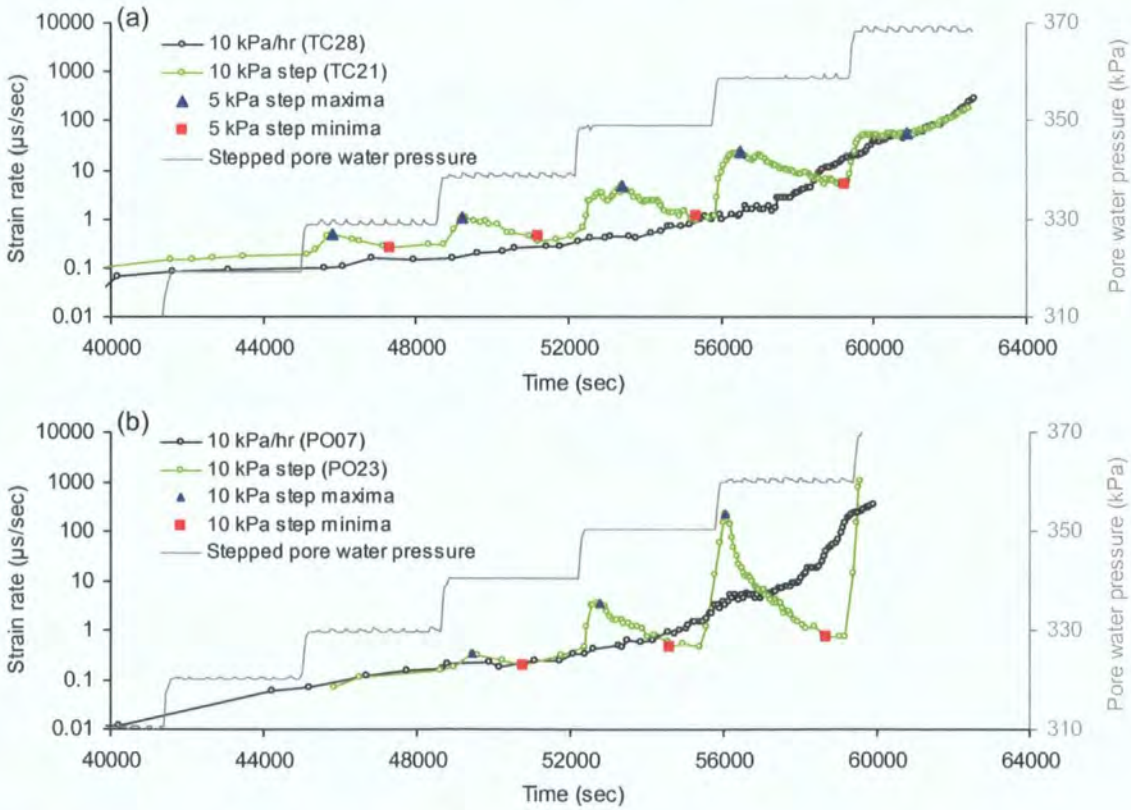

Figure 5.47 Comparison of strain rate development under the linear and stepped reinflation tests at 10 kPa/hr in plots of $\dot{\varepsilon} - t$ space: (a) TC samples; (b) PO samples

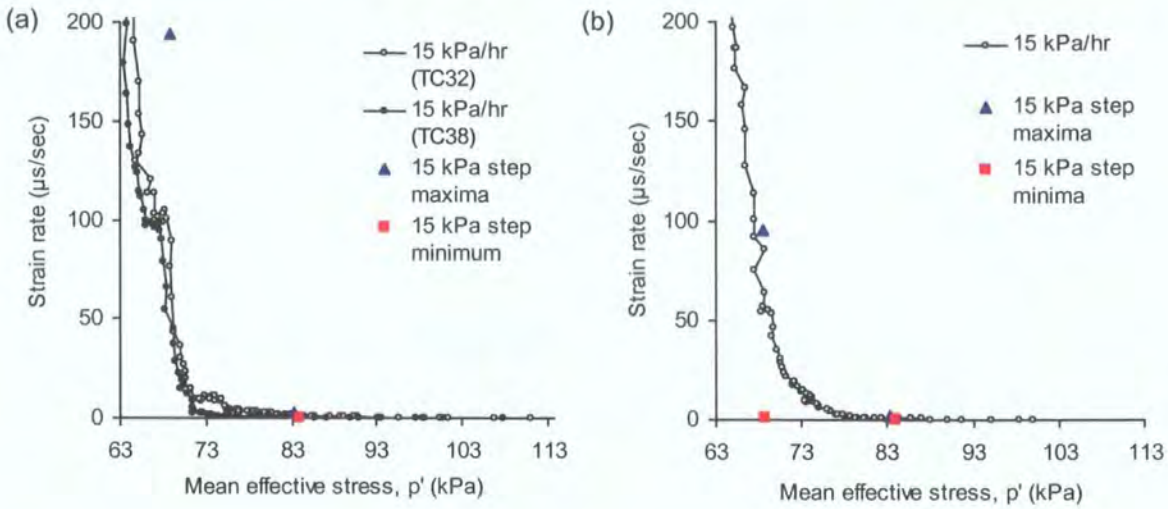

Figure 5.48 Comparison of strain development under linear and stepped pore water pressure rates at 15 kPa/hr in plots of $\dot{\varepsilon} - p'$: (a) TC samples; (b) PO samples

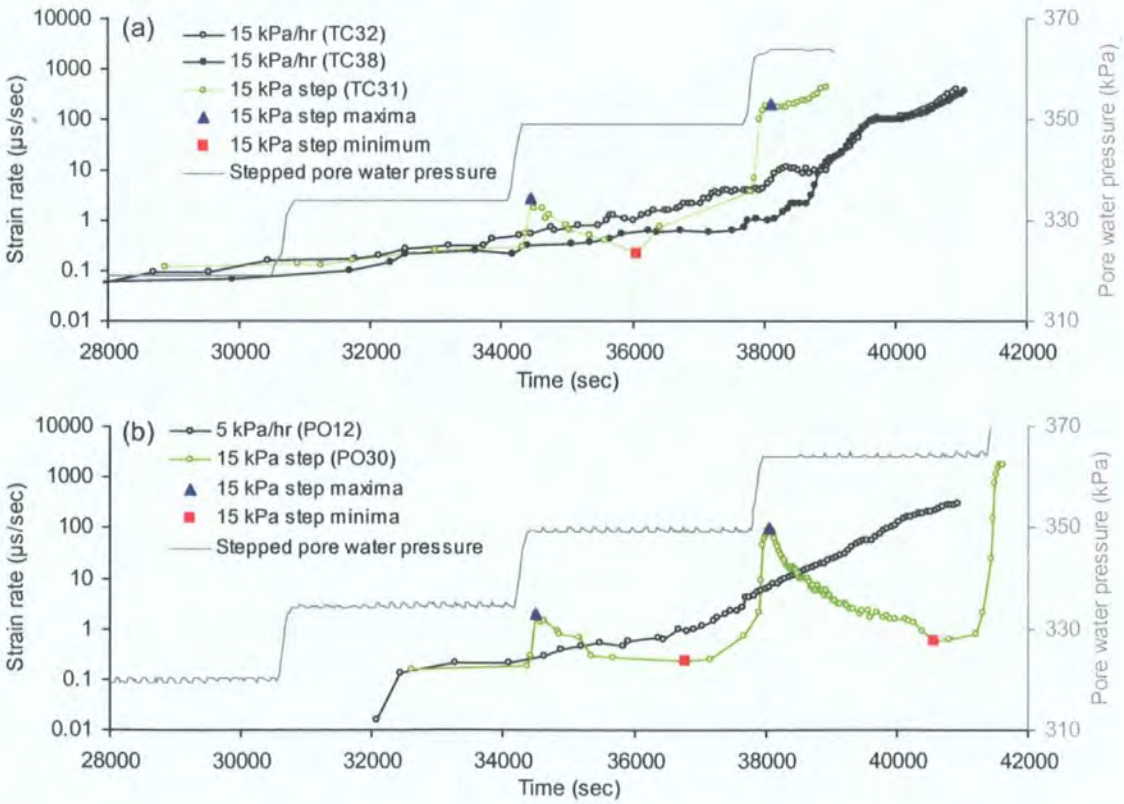

Figure 5.49 Comparison of strain rate development under the linear and stepped reinflation tests at 15 kPa/hr in plots of $\dot{\varepsilon} - t$ space: (a) TC samples; (b) PO samples

The plots in $\dot{\varepsilon} - t$ space plots (Figures 5.45, 5.47, 5.49) also revealed some complexities of strain development at time periods when the stress state was held constant (i.e. constant p', q). Several intriguing movements were identified towards the final failure:

Firstly, in sample TC29 (5 kPa stepped test) and TC21 (10 kPa stepped test), the strain rate was found to be constant (instead of decreasing) with slight accelerations and decelerations (Figure 5.50). The behaviour of sample TC21 was even more interesting as the strain rate changed from being constant to a rapid increase towards failure under the same level of pore water pressure (Figure 5.50b). Acceleration was also observed in TC29 shortly before the last step of reinflation (Figure 5.50a).

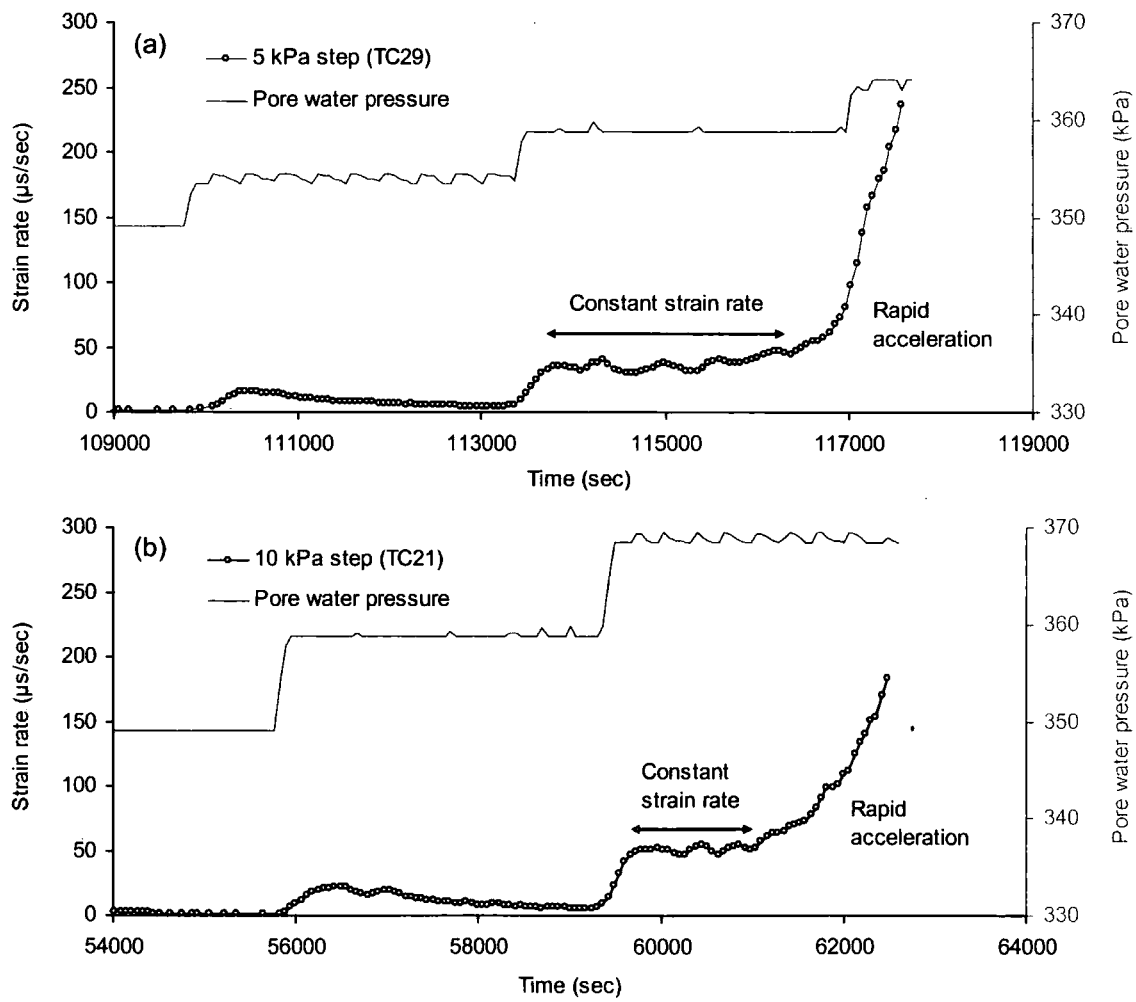

Figure 5.50 Examples showing strain rate fluctuating around a constant level of constant stress state followed by rapid acceleration to failure: (a) TC29 (5 kPa step); (b) TC21 (10 kPa step)

The second type of interesting movement at constant stress state was characterised by an initial decrease of strain rate, followed by rapid increase to failure in a short period of time (Figure 5.51). This was shown by sample TC31 (15 kPa step) (Figure 5.51a) and PO25 (5 kPa step) (Figure 5.51b).

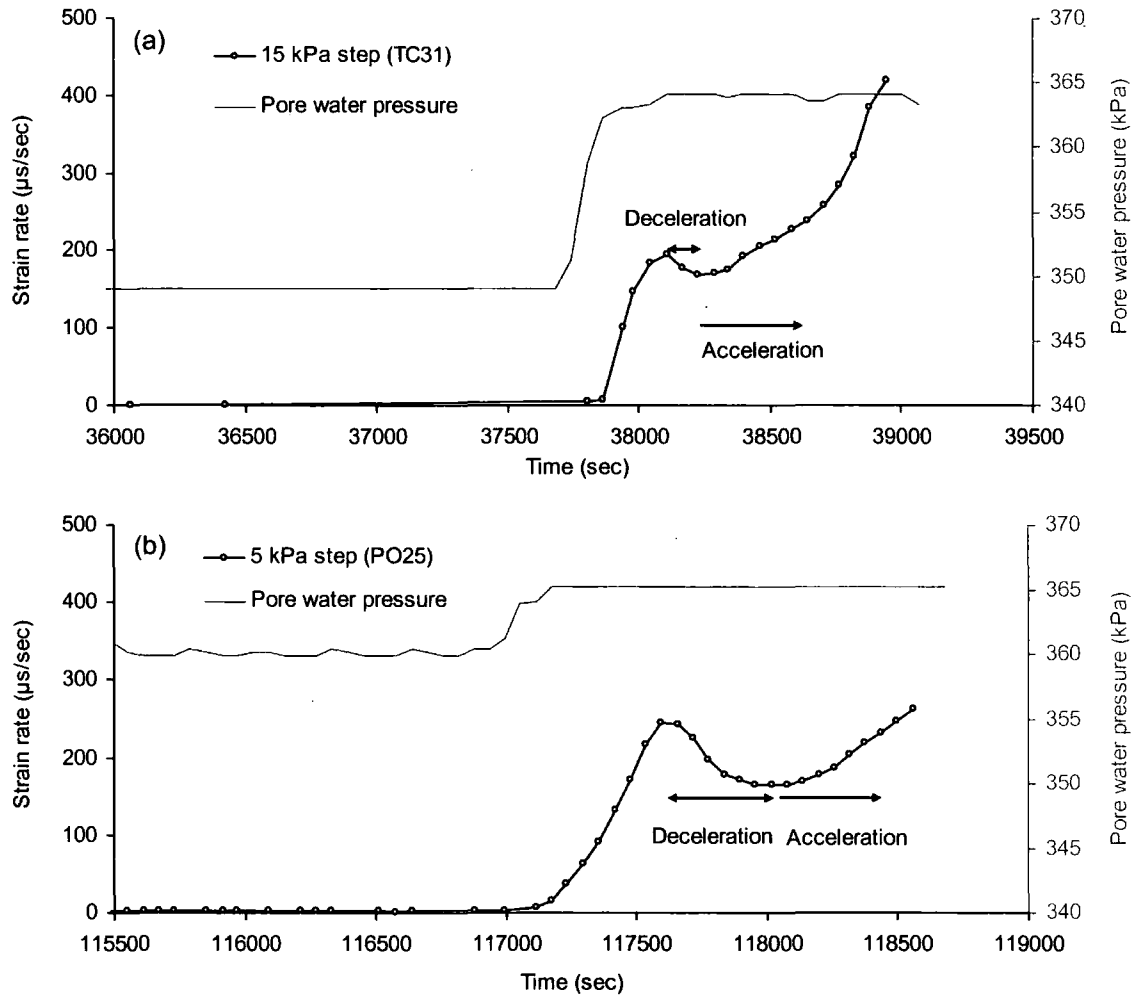

Figure 5.51 Examples showing strain rate decelerated initially but followed by rapid acceleration to failure: (a) PO sample (5 kPa step); (b) TC sample (15 kPa step)

An additional stepped test (PO38) was undertaken to examine further the strain development at constant stress conditions, by holding the pore water pressure and deviatoric stress over time (Figure 5.52). The increases of strain rate at pore water pressure levels 350 kPa, 355 kPa, 360 kPa and 365 kPa were not relevant as they were directly associated with the stepped increase of pore water pressure. Most importantly, at the time periods between each step under constant stresses, the results showed that strain developed at a decreasing strain rate and dropped to a near-constant, very low rate on the order of 0.001 µs/sec and 0.01 µs/sec (Figure 5.52).

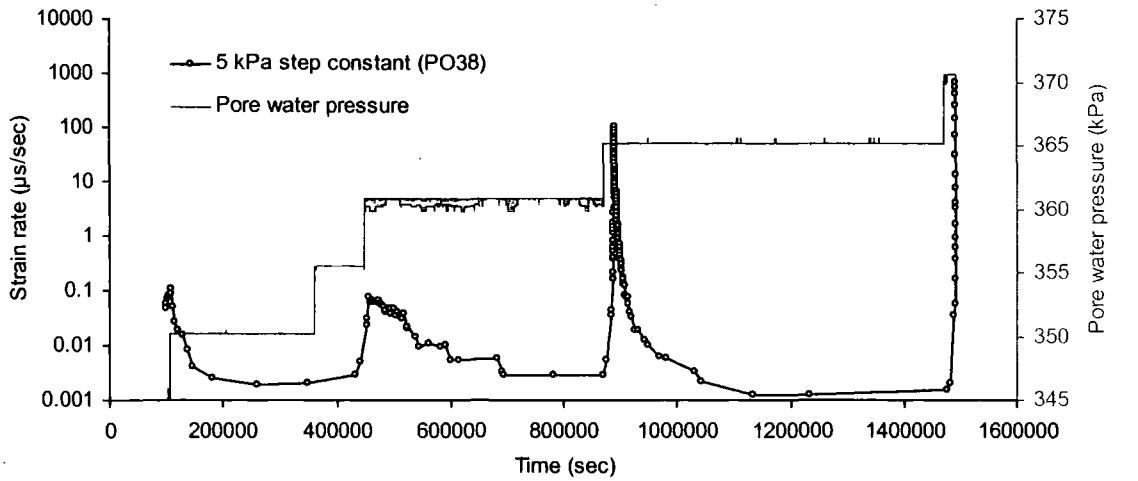

Figure 5.52 Strain rate dropped to near-constant values (on the order of 0.01 to 0.001µs/sec) when pore water pressure was held constant over time

It was even more surprising, in the same test, to find that the strain rate did not change but remained very low even after reaching the critical pore water pressure level (370 kPa) at 10:15 a.m. (Figure 5.53). The first sign of strain rate increase only came after 1 hour 35 mins. This was followed by slowly increasing strain rates below 0.1 µs/sec for 4 hours. Very surprisingly, a sudden acceleration occurred afterwards reaching up to 663 µs/sec at failure, under constant stress state. This change of strain rates may suggest the contribution of creep processes in the initiation of a failure.

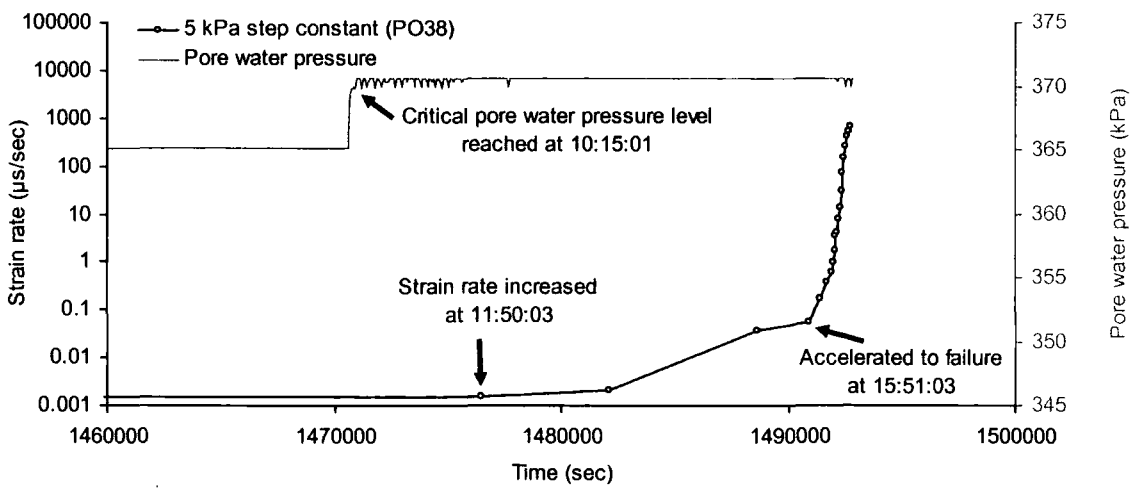

Figure 5.53 Strain rate development under constant stress state at the critical pore water pressure level

5.7.5.3 Logarithmic rates of pore water pressure increase

The reinflation tests with logarithmic rates of pore water pressure increase represented the most frequently observed pattern in the field (Figure 4.11). This series was designed at 54, 67 and 77Ln kPa/hr which were comparable to the linear and the stepped rates, undertaken at initial mean effective stress of 233 kPa and a constant deviatoric stress of 100 kPa (Table 5.3). In addition, three damaged PO samples (POD14, POD16, POD17) that were slightly cracked during the trimming process were also tested at the same rates to investigate the effect of the disturbance on the strain rate behaviour.

Similar to the results shown under the linear and the stepped rates of pore water pressure increase, the logarithmic series also demonstrated very low initial strain rates in terms of mean effective stress (Figure 5.54) and in real time (Figure 5.55). No significant movements were shown until p' decreased to about 85-88 kPa for TC samples and 73 kPa for PO samples (Figure 5.54), after 20000 seconds (Figure 5.55).

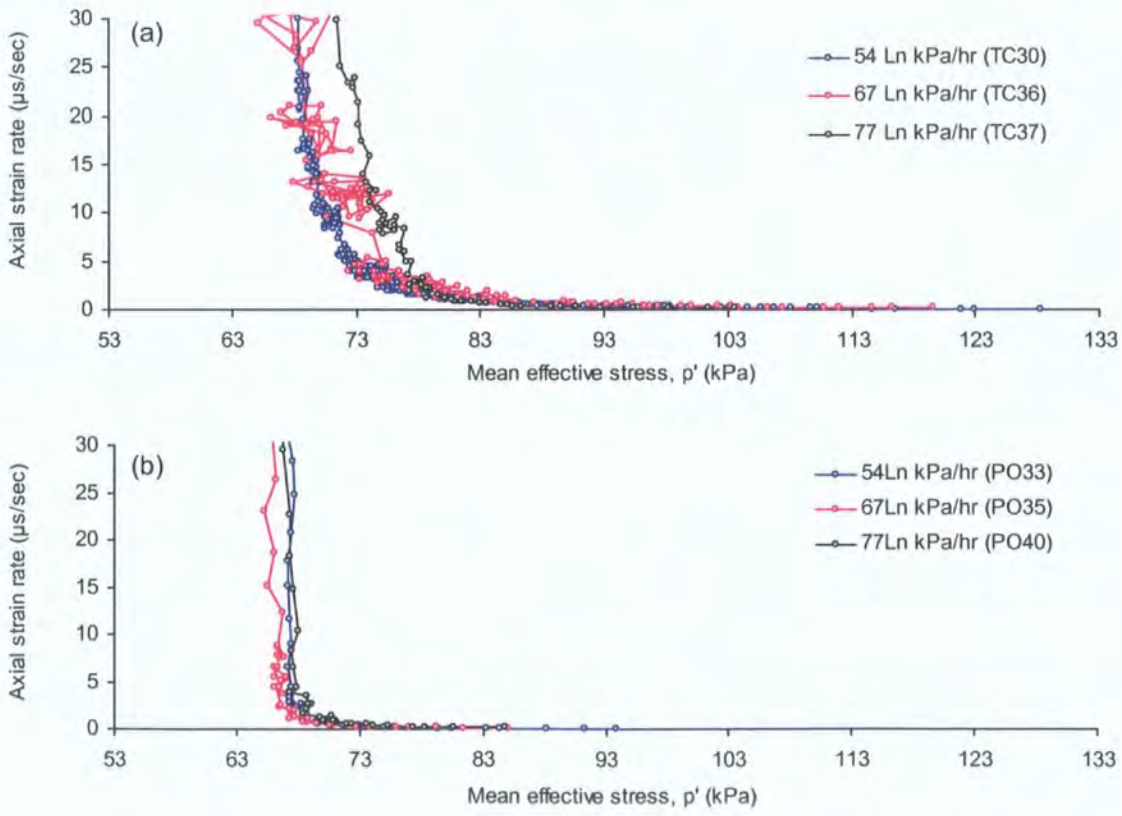

Figure 5.54 Plots of $\dot{\varepsilon} - p'$ under logarithmic pore water pressure increase at 54, 76 and 77Ln kPa/hr: (a) TC samples; (b) PO samples

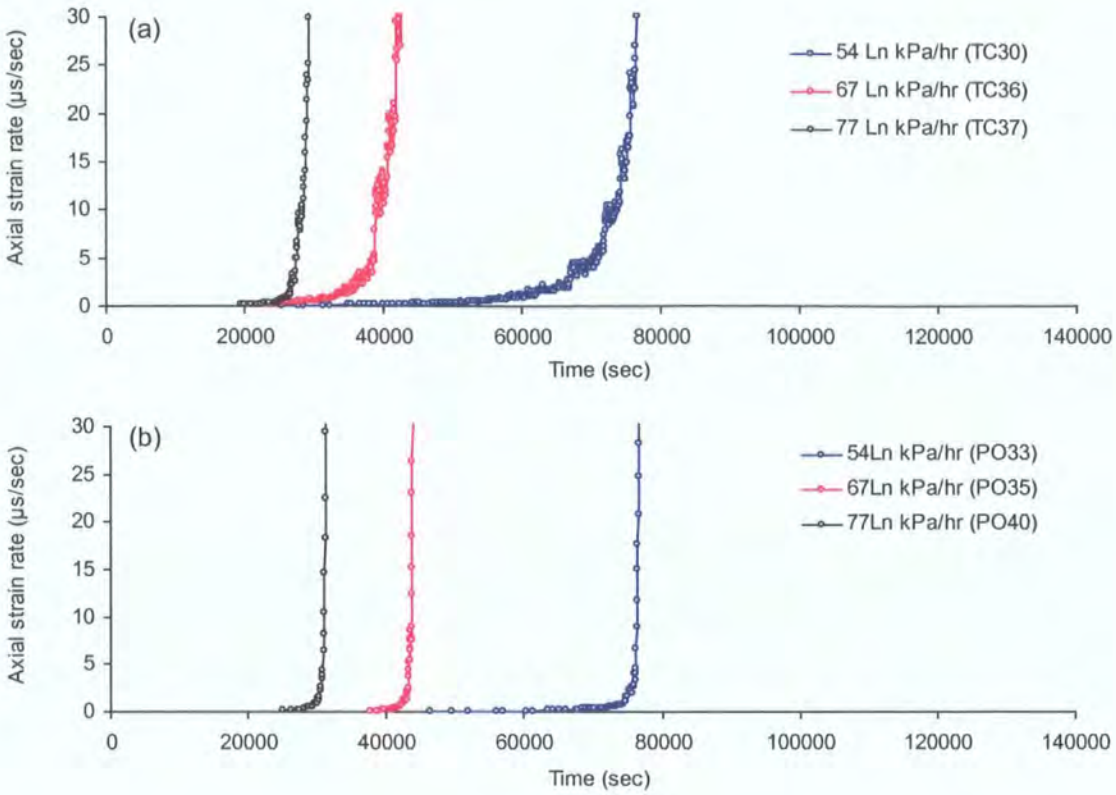

Figure 5.55 Plots of $\dot{\varepsilon} - t$ under logarithmic pore water pressure increase at 54, 67 and 77Ln kPa/hr: (a) TC samples; (b) PO samples

During the acceleration period, strain rate development in $\dot{\varepsilon} - p'$ and $\dot{\varepsilon} - t$ space for both samples under different logarithmic rates appeared very similar (Figures 5.54, 5.55), although it was noted that the PO samples generally displayed more sudden acceleration to failure. The subtle differences are more clearly shown by the plots in $\Lambda - p'$ (Figure 5.56) and in $\Lambda - t$ space (Figure 5.57).

These subtle differences are also reflected by statistical analyses (Table 5.17). The relationship in $\Lambda - p'$ and the $\Lambda - t$ space for the TC samples was significantly exponential ($R^2 \geq 0.91$). On the other hand, the movement behaviour of the two PO samples was better described by the linear trend ($R^2 \geq 0.92$) (Figure 5.58) than the exponential function ($R^2 \geq 0.88$). This suggests that the two PO samples may have experienced more sudden brittle failure (Petley *et al.*, 2002; Kilburn and Petley, 2003). Indeed, a mixed failure mode was observed where both shear plane formation and bulging were demonstrated (Figure 5.59).

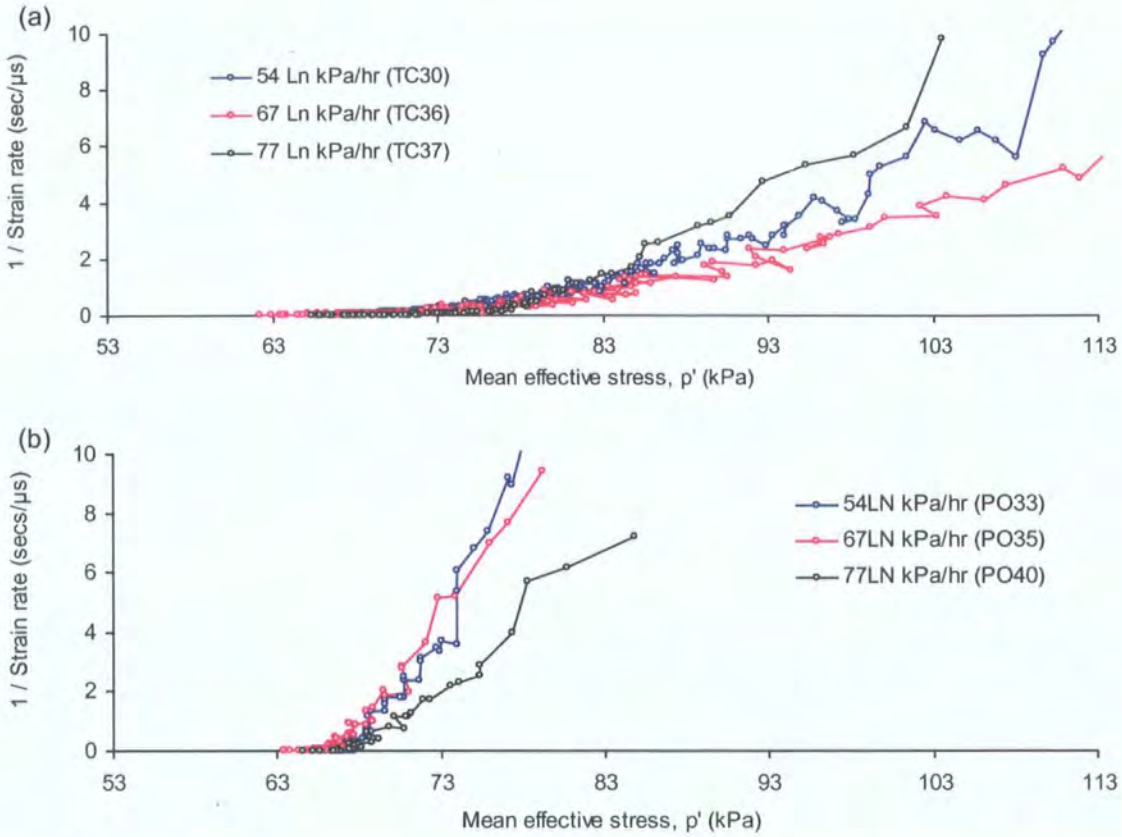

Figure 5.56 Plots of $\Lambda - p'$ under logarithmic pore water pressure increase at 54, 67 and 77Ln kPa/hr: (a) TC samples; (b) PO samples

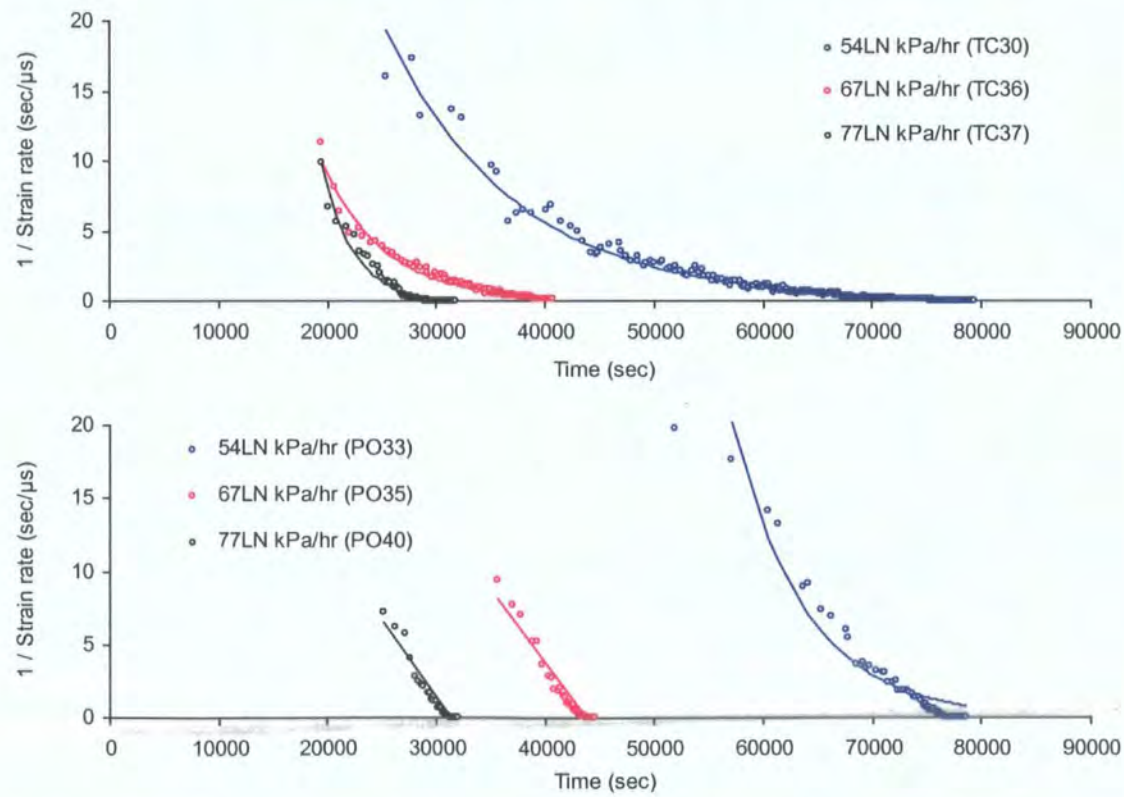

Figure 5.57 Plots of $\Lambda - t$ under logarithmic pore water pressure increase at 54, 67 and 77Ln kPa/hr: (a) TC samples; (b) PO samples

Table 5.17 Best fit coefficients for plots in $\Lambda - p'$ and $\Lambda - t$ under logarithmic pore water pressure increase at 54, 76, 77Ln kPa/hr

(a) TC soils

Sample number	PPR rate (linear)	Number of data	$\Lambda - p'$		$\Lambda - t$	
			R^2 (linear)	R^2 (exponential)	R^2 (linear)	R^2 (exponential)
TC30	54Ln kPa/hr	356	0.80	0.91	0.68	0.97
TC36	67Ln kPa/hr	200	0.79	0.96	0.73	0.97
TC37	77Ln kPa/hr	103	0.77	0.93	0.72	0.98

(b) PO soils

Sample number	PPR rate (linear)	Number of data	$\Lambda - p'$		$\Lambda - t$	
			R^2 (linear)	R^2 (exponential)	R^2 (linear)	R^2 (exponential)
PO33	54Ln kPa/hr	91	0.62	0.89	0.62	0.89
PO35	67Ln kPa/hr	73	0.92	0.88	0.93	0.88
PO40	77Ln kPa/hr	41	0.94	0.89	0.94	0.89

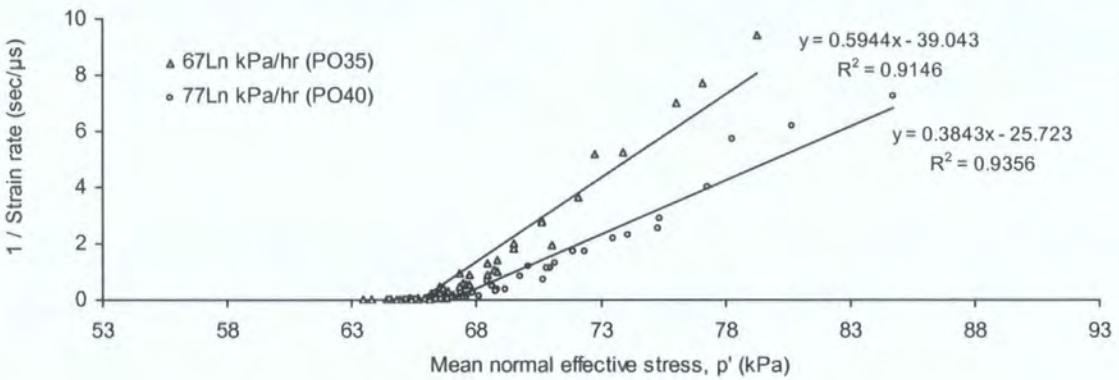

Figure 5.58 Linear trend in $\Lambda - p'$ was significant in PO samples under logarithmic rates 67Ln and 77Ln kPa/hr

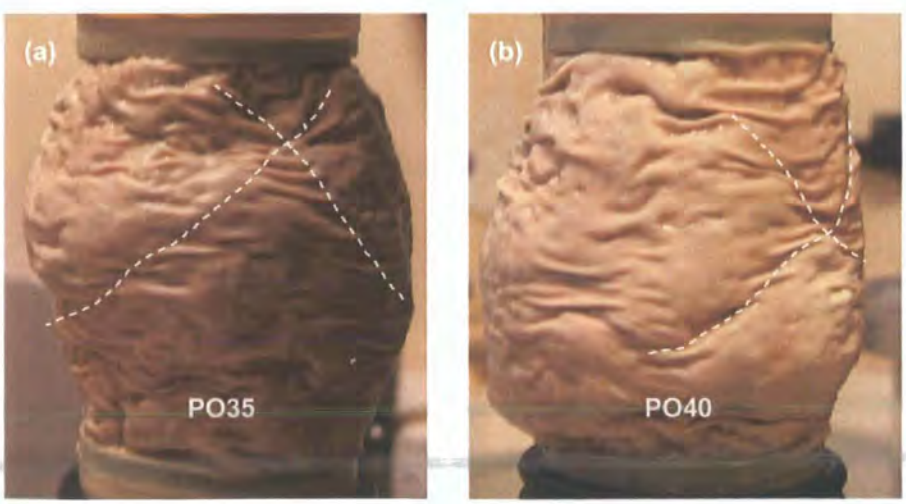

Figure 5.59 Mixed ductile-brittle failure mode showing shear surfaces (dotted white lines) and bulged form: (a) PO35 (67Ln kPa/hr); (b) PO40 (77Ln kPa/hr)

Comparative results were also obtained from three damaged PO samples (POD14, POD16, POD17) which were tested under the same logarithmic rates as the undisturbed samples. The comparison of the acceleration behaviour is presented in $\Lambda - p'$ (Figure 5.60) and $\Lambda - t$ space (Figure 5.61). Interestingly, the strain rate development of all the damaged PO samples initiated earlier at higher p' and showed a more significant exponential trend ($R^2 \geq 0.92$) (Table 5.18) than that of the linear trend exhibited by the undisturbed PO samples (cf. Table 5.17) (Figures 5.60, 5.61). Ductile deformation was dominant as shown by their barrelled shape (Appendix 2c).

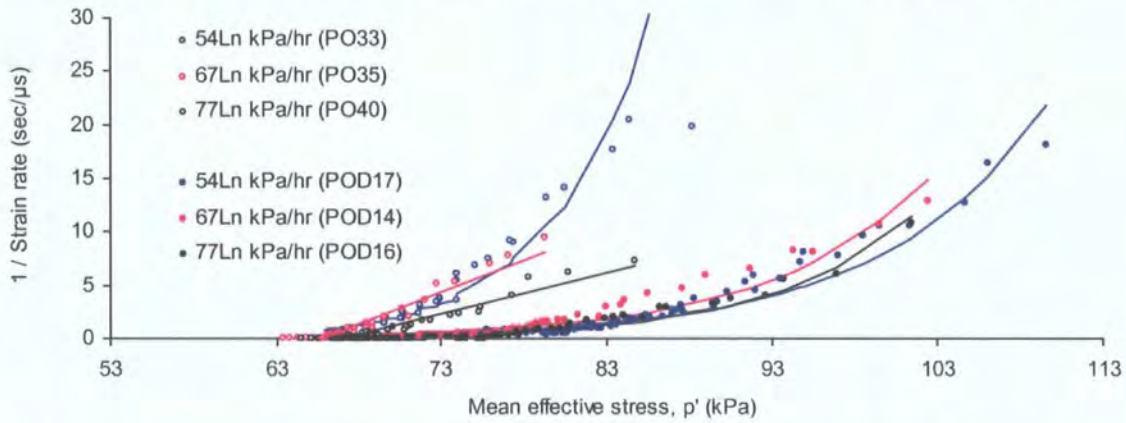

Figure 5.60 Comparison of acceleration patterns between undisturbed and damaged PO samples in $\Lambda - p'$ space

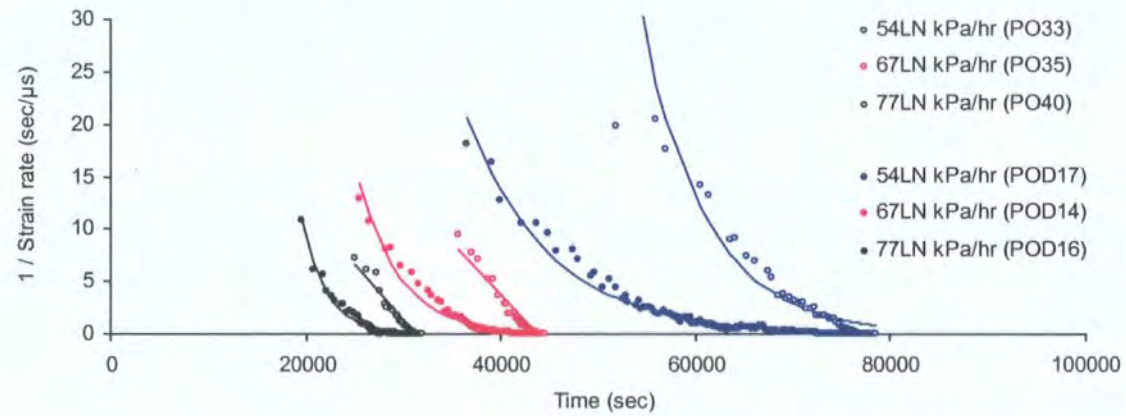

Figure 5.61 Comparison of acceleration patterns between undisturbed and damaged PO samples in $\Lambda - t$ space

Table 5.18 Best fit coefficients for plots in $\Lambda - p'$ and $\Lambda - t$ of damaged PO samples, under logarithmic pore water pressure increase at 54, 76, 77Ln kPa/hr

Sample number	PPR rate (linear)	Number of data	$\Lambda - p'$		$\Lambda - t$	
			R^2 (linear)	R^2 (exponential)	R^2 (linear)	R^2 (exponential)
POD17	54Ln kPa/hr	286	0.71	0.94	0.62	0.97
POD14	67Ln kPa/hr	129	0.81	0.92	0.76	0.95
POD16	77Ln kPa/hr	94	0.75	0.96	0.70	0.97

5.8 Chapter summary

5.8.1 Physical characteristics of the tropical soils

The material properties of two tropical soil samples collected from the Tung Chung (TC) and the Pui O (PO) sites were characterised through the physical property tests (section 5.2). The tests have revealed that both of them were intensely weathered Mesozoic volcanic tuff which were fine-grained and well-graded, composed of high silt (50-60%) and clay (25%) contents with less than 10% gravel. They were low in organic content. The plastic nature of the samples was further shown by the Atterberg limits which further classified the TC samples as CLAY of intermediate plasticity and PO samples as SILT of high plasticity. The undisturbed TC samples were denser than the undisturbed PO samples, having a higher dry density (or a lower void ratio).

5.8.2 The ICU, ICD and PPR failure parameters

All the undisturbed TC and PO samples prepared for the ICU, ICD and PPR tests were fully saturated (B-value $\geq$ 0.98). Swelling was not significant (section 5.3). The saturated samples were then consolidated at low confining stresses 50-400 kPa, which expectedly resulted in a decrease in axial length, volume and void ratio. The looser PO samples had higher consolidated strains (section 5.4).

The soil strength parameters mobilised during the ICU, ICD and PPR tests, in terms of the effective frictional angle (ϕ') (Figure 5.62) and cohesion (c') (Figure 5.63), were determined by the Mohr circles constructed at different axial strains (0.5-30%). As strains developed towards failure, all samples showed a rapid mobilisation of friction followed by a stabilisation. However, the most distinctive difference between the strain-controlled compression (ICU, ICD) and the stress-controlled reinflation (PPR) tests was found in the development of cohesion at small strains. Cohesion increased initially under compression, whereas the reinflation process generated a decrease in cohesion throughout the test.

The failure envelope was defined for the plastic TC and PO samples where the highest effective frictional angle and cohesion were mobilised with reference to the strain development. For the ICU tests, this occurred at 13% and 7% axial strain within the TC and the PO samples respectively rather than the commonly adopted criteria: (1) 20% strain or (2) maximum shear stress. The mobilised effective frictional angle (ϕ') and cohesion (c') were 29.0°, 10.2 kPa (TC samples) and 33.5°, 2.4 kPa (PO samples) respectively (Table 5.9). For the ICD tests, the failure could be well-defined at the maximum shear stress, where ϕ' and c' were 29.0°, 8.3 kPa (TC samples) and 30.4°,

10.0 kPa (PO samples) respectively (Table 5.10). For the stress-controlled PPR tests, the criterion of maximum shear stress could not apply. The maximum effective frictional angle and cohesion were not found at 20% strain, but at $\leq 5\%$ strain instead for both the TC and PO samples during the drained initial shear stage (Table 5.12). The mobilised ϕ' and c' were 18.4°, 29.4 kPa (TC samples) and 22.1°, 22.7 kPa (PO samples) respectively.

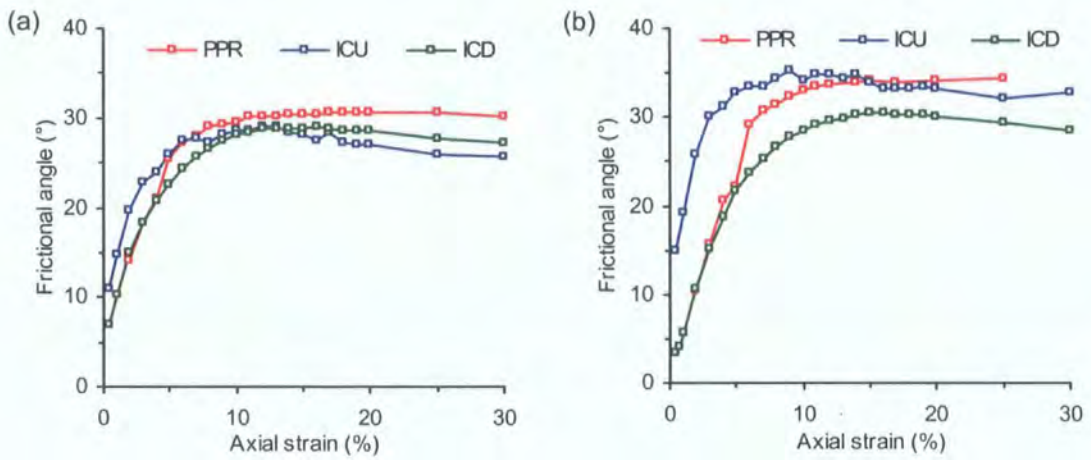

Figure 5.62 Mobilisation of effective frictional angle (ϕ') derived from the ICU, ICD and PPR tests up to 30% axial strain: (a) TC samples; (b) PO samples

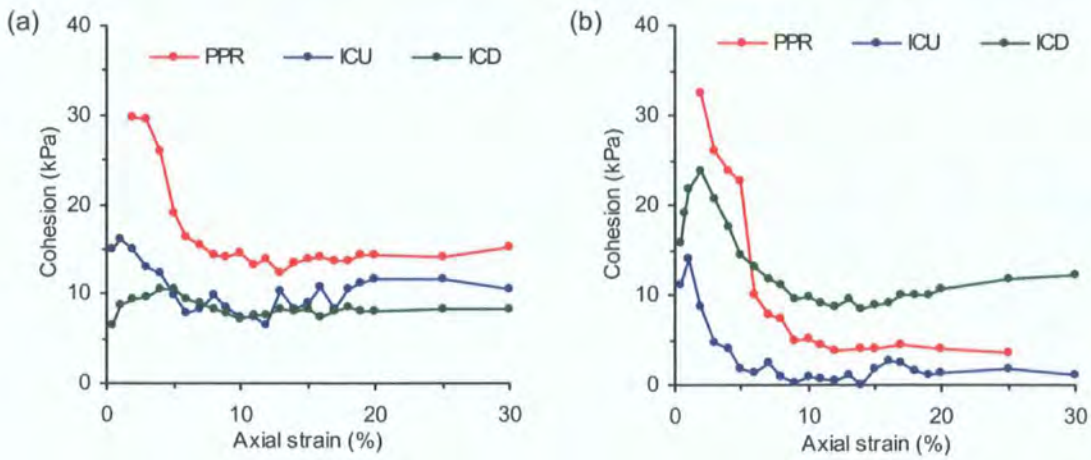

Figure 5.63 Mobilisation of effective cohesion (c') derived from the ICU, ICD and PPR tests up to 30% axial strain: (a) TC samples; (b) PO samples

Plastic deformation within the weathered TC and PO samples was evident by the stress-strain curves derived from the ICU and ICU tests, the asymptotic trend in $\Lambda - t$ space from the PPR tests, and the barrel-like lateral expansion exhibited by the samples in all of the ICU, ICD and PPR tests. However, the samples under the ICD test exhibited contractive volumetric behaviour, but dilated under the PPR test.

Chapter 6 Discussion

This chapter first examines the nature of the weathered volcanic soils collected from Tung Chung (TC) and Pui O (PO) on Lantau Island. This is followed by discussion of the patterns of volumetric behaviour during pore pressure reinflation. The associated accelerating strain development is evaluated against fundamental components of soil behaviour: elasticity, plasticity and creep, to reveal the underlying deformation mechanisms. Three key landslide movement stages are proposed that provide important implications for the processes of shallow rainfall-induced landslides in the weathered materials that typically occur in tropical environments.

6.1 The nature of weathered volcanics

6.1.1 Degree of weathering

The high degree of decomposition by weathering under the hot, humid tropical climate of Lantau Island is indicated by the mature grading curves (Figure 5.1) (Terzaghi *et al.*, 1996). In comparison, the TC samples appear to be more deeply weathered than the PO samples, as shown by the higher proportion of fines and lower amounts of gravel (Table 5.4). This is supported by the widely established view that the degree of weathering affects the grading of residual soils (Lumb, 1962, 1965; Thomas, 1994; Rahardjo *et al.*, 2004).

However, as the TC and the PO samples are from the Mesozoic (Langford *et al.*, 1995), the weathering degree might have been expected to be similar. The higher sand and gravel content of the PO samples is more likely to be attributed to the coarser nature of the parent rock (i.e. coarse-grained crystal tuff) (GCO, 1988b) rather than the degree of weathering.

The silty-clayey fines are probably the products of intense chemical weathering derived from the decomposition of ferromagnesian and feldspathic minerals, while the larger sand and gravel-sized grains are mostly the remains of highly resistant quartz inherited from the parent rock (Lumb, 1962, 1965; Mitchell and Sitar, 1982; Vaughan, 1988; McFeat-Smith *et al.*, 1989; Irfan, 1994; Langford *et al.*, 1995). In fact, kaolinite may account for the large proportion of silt in both the TC and PO samples, as its lateral dimension lies in the range of fine to medium silt (Wen and Aydin, 2003). The TC and PO samples, therefore, may both represent their most intensely weathered

state (residual soil), and be recognised as Grade VI of fine ash tuff and coarse ash tuff respectively (GCO, 1988a ,1988b).

The particle size distributions of the TC and PO samples (Figure 5.1, Table 5.4) conform to previous findings in deeply-weathered volcanics, which show the dominance of silty and clay particles with minor sand (Lumb, 1962, 1965, 1975; GCO, 1998a, 1998b; GEO, 1994a; Irfan, 1998b, 1999; Ng and Pang, 2000). In particular, they are also consistent with the findings of other studies on residual soil undertaken at the TC site (clayey SILT; clay content: 25-40%, mean 34%) (Evans and Lam, 2003) and North Lantau (slightly clayey sandy silt) (Franks and Woods, 1993). The tested samples reflect the well-graded nature of residual soils (Kenney, 1984).

6.1.2 Mineralogy

Kaolinite and halloysite are the most common clay minerals found in tropical residual soils (Vaughan, 1988; Terzaghi *et al.*, 1996; Fookes, 1997; Queiroz de Carvalho and Simmons, 1997; Maail *et al.*, 2004). Kaolinite appears to be the dominant clay mineral for the fine-grained TC and PO samples. This is supported by (1) the Atterberg limits, (2) the moisture content data, (3) the volumetric behaviour during the saturation stage and (4) the degree of weathering.

The Atterberg limits obtained from both samples (Table 5.4) fall within the typical liquid and plastic limits for kaolinite, which lie typically between 30 and 110%, and 25 to 40% respectively (Selby, 1993). The insignificant difference between the sample moisture content derived at 45-50°C and 105°C suggests that the clay minerals are inactive, without large quantities of drying-sensitive clay minerals such as halloysite in weathered volcanics (Irfan, 1996). Moreover, the negligible amount of swelling upon saturation (Table 5.6) further confirms that the soil specimens are rich in kaolin of low swelling capacity (Queiroz de Carvalho and Simmons, 1997). Finally, kaolinite is dominant in soils at their most advanced stage of weathering (Lumb and Lee, 1975), consistent with the weathering grade (Grade VI) of the TC and PO samples (Figure 6.1).

The above observations are consistent with other clay mineralogy studies on weathered volcanic soil, which report the dominance of inactive kaolinite (Irfan, 1996, 1998b, 1999; Campbell and Koor, 1999; Franks *et al.*, 1999; Duzgoren-Aydin *et al.*, 2002). For example, a kaolinite composition of up to 56% of the soil total weight has been found in volcanic residual soils in Hong Kong (Irfan, 1998b).

(a) TC31 (b) PO31

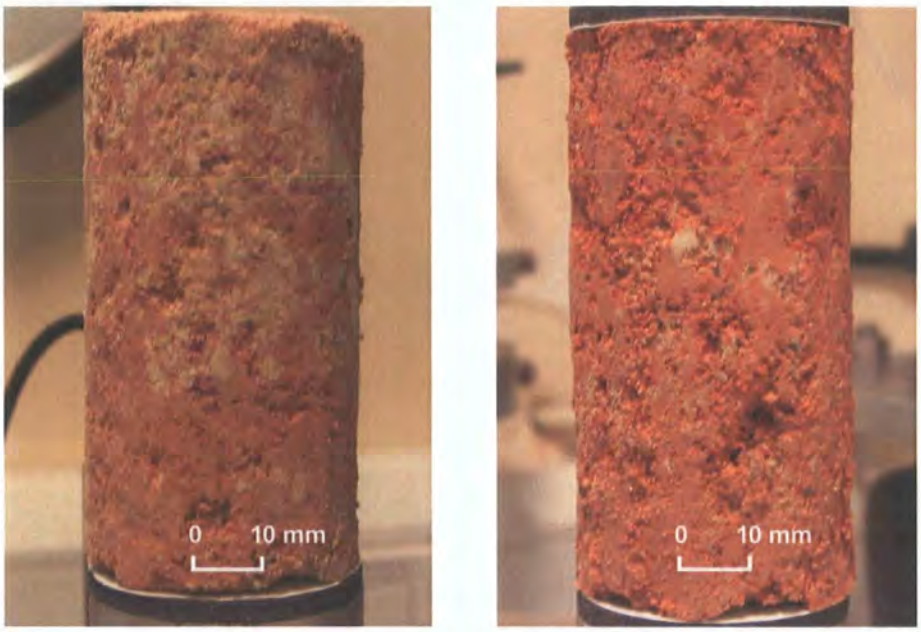

Figure 6.1 The deep reddish-brown colour indicates a high degree of chemical weathering: (a) TC31; (b) PO31

6.1.3 Plasticity

The plastic nature of the deeply-weathered TC and PO samples is shown by the medium to high Atterberg limits (Table 5.4, Figure 5.2), which are largely consistent with previous residual soil studies conducted in Hong Kong (typical LL: 25-65%; PI: 0-30%) (Lumb, 1962), in North Lantau (LL: 35-60%; PI: 10-30%; intermediate to high plasticity) (Franks and Woods, 1993) and particularly at Tung Chung (LL: 35-50%) (Evans and Lam, 2003).

Plastic behaviour is further revealed from the standard undrained (Figure 5.13) and drained tests (Figure 5.17), which displayed a barrelling effect during compression testing (Appendices 1a, 1b), and yielded stress-strain curves which do not have a peak and residual pattern. The behaviour is similar to the weathered argillaceous rocks reported in Fan *et al.* (1994) at confining pressures between 100 and 400 kPa. Plastic deformation has also been regarded as representative soil behaviour for Hong Kong slopes (Lumb, 1975).

6.1.4 Soil structure

Structure refers to the particle arrangements (fabric) and interparticle bonding generally possessed by natural, undisturbed soil (Mitchell and Soga, 2005). The structure of the undisturbed TC and PO soil samples appears to be weakly-bonded, as a result of relict bonding from the weathered parent rock as well as secondary bonding due to cementation by sesquioxides, which is typical for intensely weathered soils (Mitchell and Sitar, 1982; Irfan, 1996, 1999). Evidence for the weakly-bonded structure has been revealed by the soil behaviour in the testing programme, as follows:

The non-zero cohesion intercept exhibited by both samples during the conventional and reinflation tests suggests the presence of a bonded structure (Figures 5.9, 5.15, 5.27) (Vaughan, 1988). However, the value of cohesion is low, which indicates that the samples are weakly bonded in association with the secondary bonding. The limited true cohesion is probably related to the high degree of decomposition (Au, 1998). For these intensely-weathered soils, the cohesive strength could be contributed to by mineral crystallisation and precipitation of cementing material during weathering (Leroueil and Vaughan, 1990). The cementation by iron minerals is pre-dominant in the tested samples, as suggested by their lack of relict structure (structureless clayey silt to silty clay matrix with some sand-size quartz grains) and the deep reddish-brown colour (Figure 6.1). Such 'laterization' is however weaker within the tested samples than those developed in other tropical areas (Irfan, 1998b, 1999), due to the low iron content of the Hong Kong soils (Lumb, 1962). Nevertheless, the void ratios, which indicate the impact of leaching and loss of mineral matter, are similar to residual soils from Brazil (0.8-1.5) and India (0.5-1.1) (Rao and Revanasiddappa, 2002).

The direct effects of bonded structure on soil behaviour, such as yield stress and peak strength (Fookes, 1997), are not clearly shown in the stress-strain curves derived from the drained and undrained tests (Figures 5.13, 5.17). However, the effect can be more readily seen in plots of $\varepsilon - p'$ (Figure 6.2). The undisturbed samples exhibited a more sudden development of strains within a small range of mean effective stresses, compared with the disturbed samples. The distinctive soil behaviour suggests the presence of a weak bonded structure (Boonsinsuk and Yong, 1982; Fookes, 1997). This can be attributed to the high degree of weathering (Grade V or above), application of high confining pressure or bond breakage during the saturation stage (Ebuk, 1991; Brenner *et al.*, 1997).

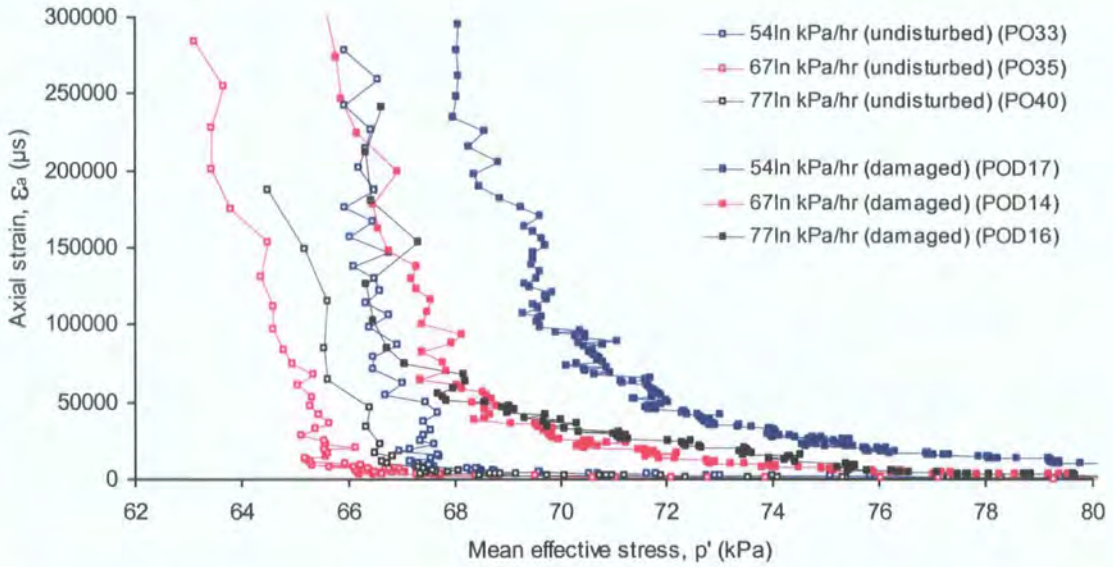

Figure 6.2 Comparison of soil behaviour in plots of $\varepsilon - p'$ exhibited by undisturbed and damaged PO samples

This study appears to confirm that the natural soil structure that arises from cementation or secondary inter-particle bonding probably has significant effects on the engineering behaviour (Leroueil and Vaughan, 1990). Examples include undisturbed, weathered, argillaceous sediments from Taiwan and Barbados (Fan *et al.*, 1996), undisturbed weathered volcanic Hawaiian soils (Zhu and Anderson, 1998), undisturbed Tessina landslide samples that are composed of the matrix of highly fractured, permeable molasse deposits associated with tectonic activity (Petley *et al.*, 2002; Petley *et al.*, 2005b, 2005c), and undisturbed fine ash to lapilli tuff saprolitic soil in Hong Kong (Wen and Aydin, 2005). These studies suggest that plastic failure could also have been observed in undisturbed materials that are naturally "destructured" by the weathering processes. Thus the plastic failure within the undisturbed Hong Kong residual samples tested at low confining pressures can be explained.

6.1.5 Heterogeneity

The heterogeneous nature of the soil samples, which has been revealed during various stages of the testing programme, is associated with the natural characteristics of tropical residual soil (Vaughan, 1988; Fookes, 1997, Zhu and Anderson, 1998). This was first shown by the subtle differences in volumetric strain under the same consolidation pressure (200 kPa) within each group of the TC and PO samples (Figure 6.3). Sample variability is also indicated by the range of stiffness in stress-strain behaviour during initial drained shear stage (Figure 6.4), under the same stress state

(initial state: p'_c = 200 kPa, q = 0 kPa; final state: p'_{dis} = 233 kPa, q = 100 kPa, sheared at 0.5 kPa/min). However, the variations in volumetric and axial deformation cannot be effectively explained by dry density alone, as indicated by their statistically insignificant relationship (Figures 6.5, 6.6). These are more likely to be attributed to structure-related features within the samples that have not been quantified in this study, such as soil microstructure, fabric and mineral composition (Fookes, 1997), and the occasional presence of fine roots within the samples.

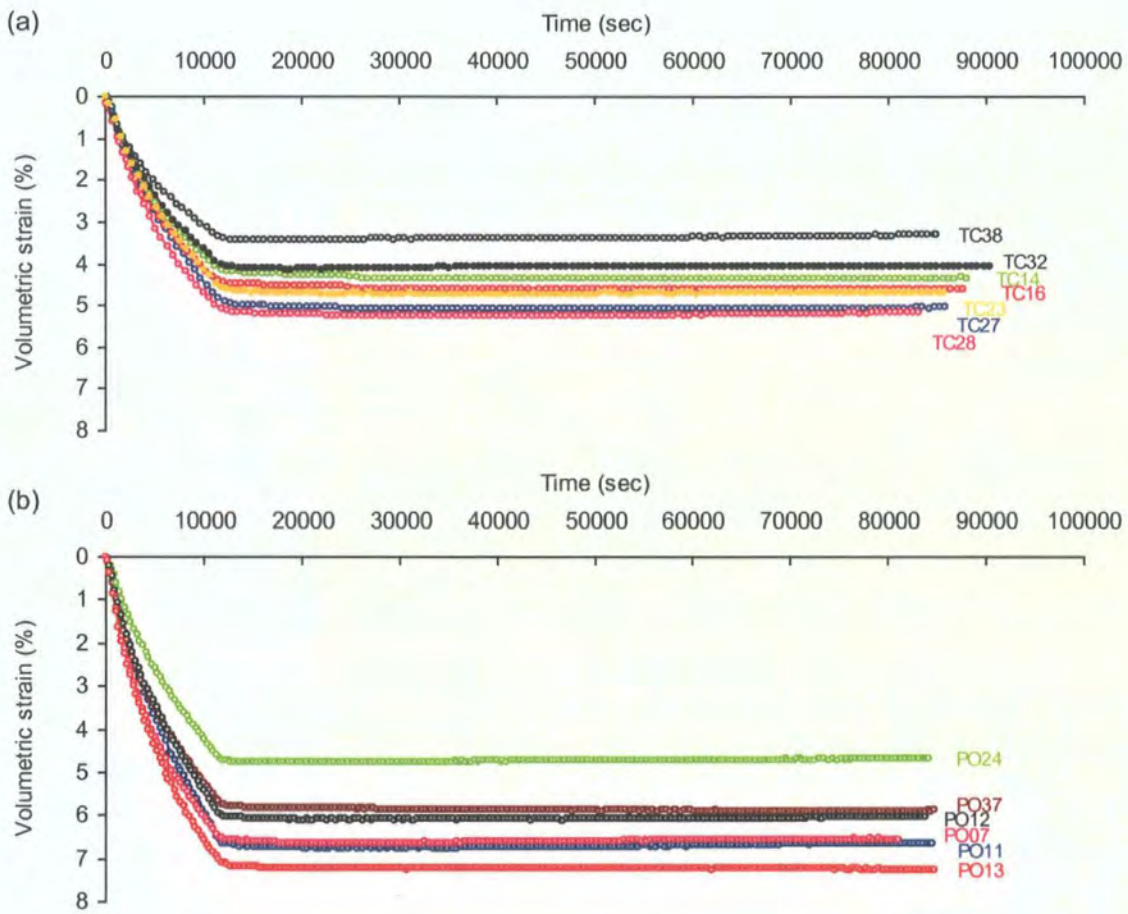

Figure 6.3 Consolidation curves at effective stress 200 kPa for samples prepared for the linear reinflation tests: (a) TC samples; (b) PO samples

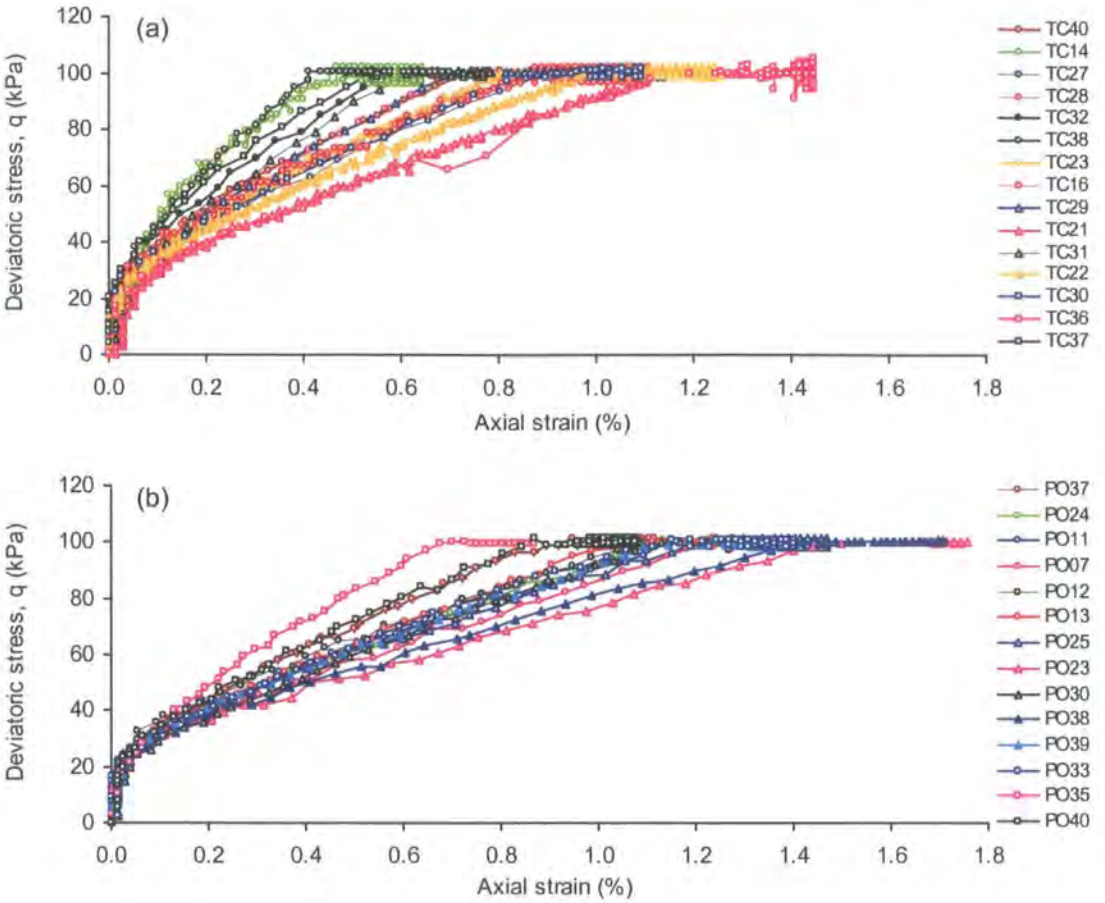

Figure 6.4 Stress-strain behaviour during drained initial shear (initial p'_c = 200 kPa) exhibited by samples prepared for the reinflation test: (a) TC samples; (b) PO samples

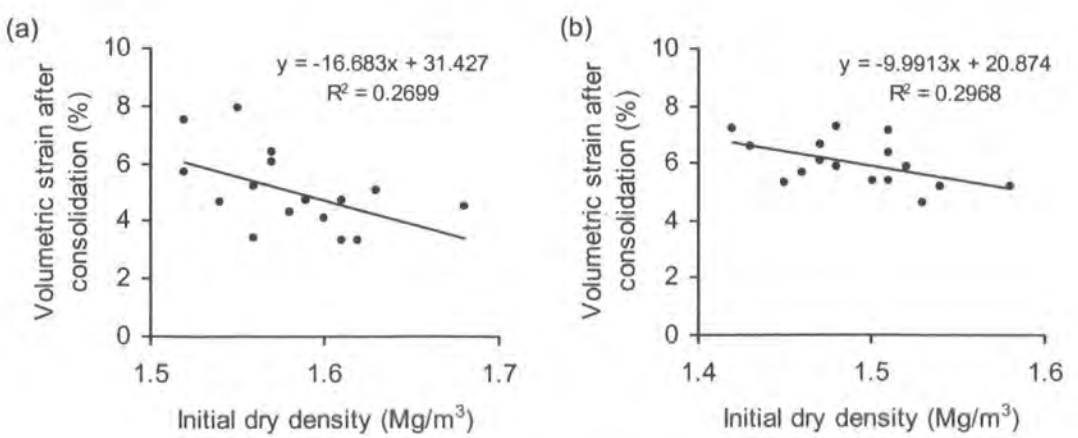

Figure 6.5 The sample variability as shown by volumetric strain against the initial dry density during the consolidation stage at effective stress 200 kPa: (a) TC samples; (b) PO samples

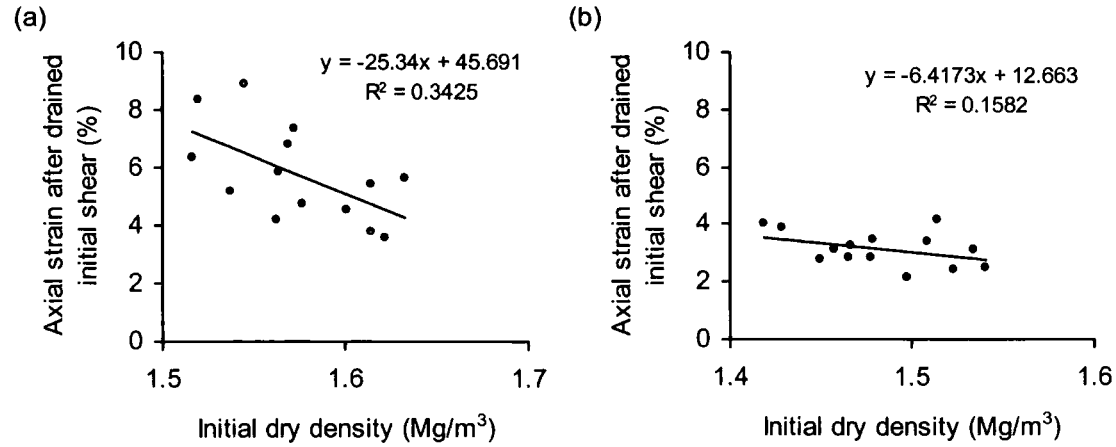

Figure 6.6 Relationship between initial dry density and axial strain after drained initial shear: (a) TC samples; (b) PO samples

6.1.6 Permeability

The standard permeability test (Head, 1998) was not used in this research. However, the coefficient of permeability, k, derived from the consolidation process suggests that the PO samples are more permeable than the TC samples. This could be related to their higher gravel and sand contents (Table 5.4), and their lower density (Figure 6.7). However, there is no direct correlation between the sample density and permeability (Figure 6.7). The poor relationship may be related to other factors such as particle arrangement or heterogeneity of the samples.

The permeability coefficient is useful to identify two different groups of samples for comparison purpose (Figure 6.7). However, caution should be taken as it may not necessarily reflect the true degree of permeability for the samples. The hydraulic conductivity of weathered volcanics around the TC site was found to range from 1-7.6 x 10^{-6} m/s (Lan *et al.*, 2005). Table 5.5 shows lower permeability coefficients and has indicated that the coefficient is highly affected by the consolidation procedure. The values of the permeability coefficient derived from consolidation at a controlled rate of increasing effective stress (except TC09, TC10, TC11 which were subjected to a sudden increase of effective stress) were much lower on average. The resulted lower permeability values were not surprising as a longer time would be required to reach the theoretical state of consolidation (i.e. higher values of t_{100}) under the controlled rate of increasing effective stress. Similarly, under the same consolidation rate, samples consolidated at a higher effective stress would have a higher value of t_{100} that gave a lower value of c_{vi} and hence a lower k value (cf. TC33, TC34, TC39 or cf. PO04, PO05, PO06).

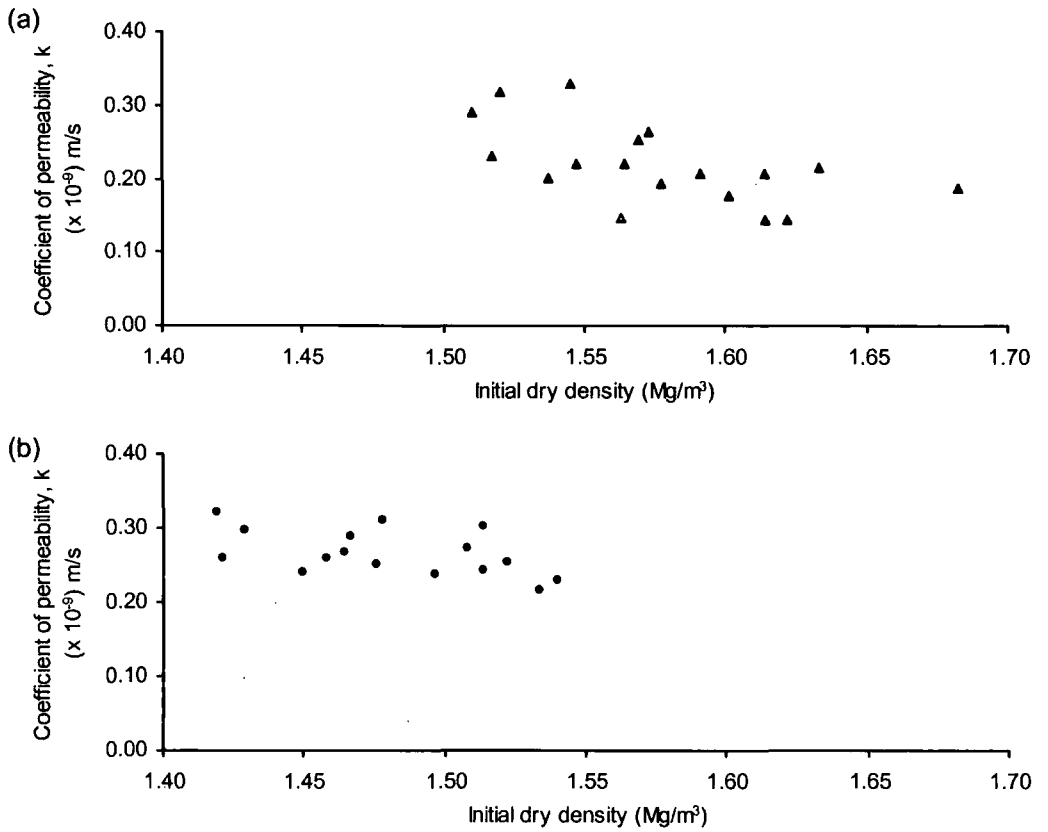

Figure 6.7 Relationship between initial dry density and the coefficient of permeability derived under the same consolidation pressure and procedure: (a) TC samples; (b) PO samples

6.1.7 Soil strength

6.1.7.1 Effective strength parameters

The effective cohesion and frictional angle from the ICU, ICD and PPR tests have first been evaluated against the standard failure criteria for plastic materials, that is at 20 % axial strain (Selby, 1993). Under this criterion, the PPR tests mobilised the highest values of effective frictional angle with relatively high cohesion (Figure 6.8). Similarly, a higher strength envelope has been derived under the field stress path than from conventional tests in other undisturbed soils (GCO, 1982; GEO, 1994a; Anderson and Sitar, 1995; Zhu and Anderson, 1998).

The higher angle of internal friction derived from the PO samples under the same effective stress state can be attributed to (1) the higher proportion of the more-resistant gravel (> 2 mm) and sand-sized quartz grains within weathered crystal tuff (Table 5.4) (Kenney, 1984) and (2) the presence of some hardened, iron-cemented aggregates (Mitchell and Sitar, 1982; Irfan, 1998b). The presence of iron materials is indicated by their reddish-brown colour (Figure 6.1).

The effective cohesion values of both the TC and PO samples are unsurprisingly low. The results conform to previous studies which note that the apparent cohesive strength could drop to low values or even zero due to the release of soil suction upon full saturation (Lumb, 1965, 1975; Brand *et al.*, 1983) (Figure 2.4). The small value of the cohesion intercept indicates that the saturated TC and PO samples behave as frictional materials during shear.

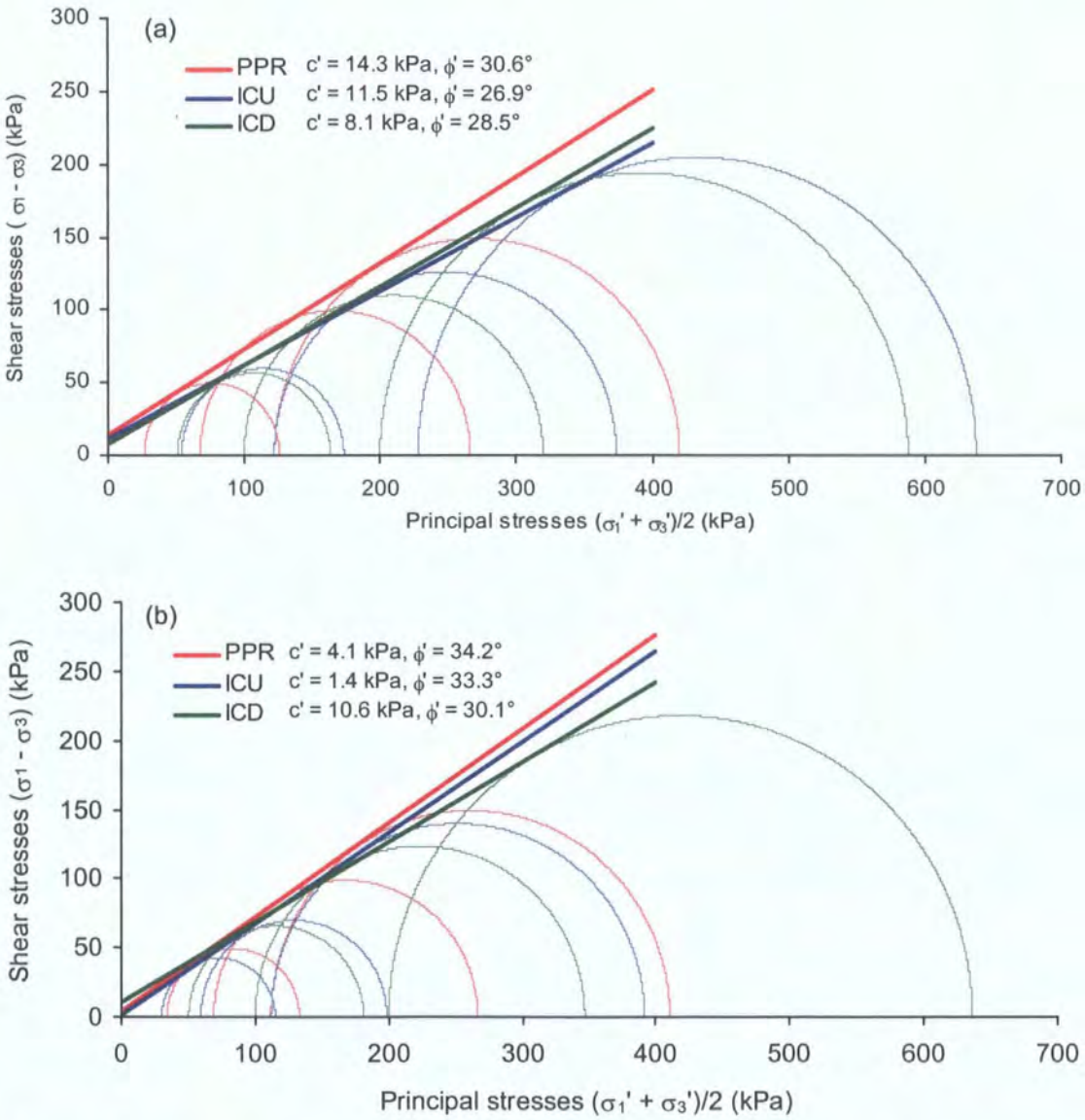

Figure 6.8 Comparison of failure envelopes, effective fictional angle (ϕ') and cohesion (c') values derived from ICU, ICD and PPR tests at 20 % axial strain: (a) TC; (b) PO samples

However, very few studies have reported the actual values of effective frictional angle and cohesion or used the same criteria to compare the two types of tests (except Anderson and Sitar, 1995; Zhu and Anderson, 1998) (Table 6.1). This highlights the fact that there is no standard criteria to define the sample failure or strength for field stress path tests. Some studies have not defined the strength parameters (GEO, 1994a; Anderson and Riemer, 1995; Gabet and Mudd, 2006), whilst others adopt two main criteria for the analysis of rainfall-induced landslide initiation: (1) the maximum stress ratio (σ_1'/σ_3') which is defined as the point of maximum stress obliquity (GCO, 1982; GEO, 1994a); and (2) the "yield" strength which is the turning point of the horizontal field stress path, identified by the onset of rapid increases in axial strain (Anderson and Sitar, 1995; Zhu and Anderson, 1998).

Table 6.1 Effective frictional angle and cohesion reported on undisturbed soils under conventional and field stress path tests

Soil material	Anisotropic consolidated undrained (ACU) test	Constant shear drained (CSD) test	Reference
Residual / colluvial	ϕ'_{pk} = 30.8°, c'_{pk} = 1.7 kPa ϕ'_{ss} = 31.9°, c'_{ss} = 2.3 kPa	ϕ'_y = 36.7°, c'_y = 0.7 kPa ϕ'_f = 35.3°, c'_f = 1.0 kPa	Anderson and Sitar (1995)
Residual	ϕ'_y = 39.6°, c'_y = 3.0 kPa ϕ'_{ls} = 31.7°, c'_{ls} = 3.0 kPa	ϕ'_y = 32.1°, c'_y = 6.9 kPa ϕ'_{ls} = 35.3°, c'_{ls} = 4.2 kPa	Zhu and Anderson (1998)

Strength description (subscript): *pk* = peak; *y* = yield; *ss* = steady state; *ls* = large strain

The first criterion has the advantage of allowing a comparison with conventional tests in terms of stress state, whereas the second criterion does not make any reference to the conventional tests, and hence may not be comparable. The second criterion also does not consider strain accumulation, but defines the strength parameters at the drop in shear stress (Anderson and Riemer, 1995), which is opposite to the compression tests. Moreover, the "yield" point can be difficult to identify, as shown in GEO (1994a) and the present study, for those samples which do not exhibit marked decrease in deviatoric stress during the test. Most importantly, based on the strain rate contours (Figure 5.28), the "yield" criterion appears unrelated to the initiation of landslides, as the acceleration of strain occurs well before the decrease of deviatoric stress.

Therefore, a third criterion is proposed here which derives the strength envelope using the stress conditions at a common value of axial strain. The main advantage is that the strength parameters (c' , ϕ') derived from the strain-rate controlled conventional drained (ICD), undrained (ICU) tests and the stress-controlled pore water pressure reinflation (PPR) test can be compared, through common axial strain values. An example has been shown in Figure 6.8, in which the cohesion and the effective frictional angle have been determined at 20 % axial strain (Selby, 1993). Based on this cross-referenced criterion, it can be confirmed with confidence that the strength parameters derived from the reinflation test, at 20% strain, are indeed the highest (cf. Tables 5.9, 5.10, 5.12).

Interestingly, Figures 5.62 and 5.63 further demonstrate that the strength parameters vary at different strains. In other words, the pore pressure reinflation process does not necessarily mobilise the highest strength compared with those derived from the conventional tests throughout the shearing process. For example, Figure 5.62 shows that the ICU test mobilised a higher frictional angle than the PPR tests at small strains for the TC ($\leq$ 6 % strain) and PO ($\leq$ 14 % strain) samples. This may explain why there have been very few attempts to compare the strength parameters between the conventional and the reinflation tests. A comparison among the strength parameters commonly defined by the Mohr circles at different strain values during PPR, ICU and ICD tests (Figures 5.62, 5.63) provides an alternative way to examine the processes leading to failure for the first time.

In addition, all of the ICU, ICD and PPR tests reveal that the key failure processes of landslides involve an increase of effective frictional angle (Figure 5.62) and a loss of effective cohesion (Figure 5.63). Similar behaviour has been observed during uniaxial compression testing of granitic rocks, which has been attributed to increasing brittle damage (Eberhardt *et al.*, 2004) (Figure 6.9). The increase in frictional strength was due to the shearing of interlocking asperities along a discontinuous shear surface whilst the loss of cohesion was associated with the destruction of remnant intact rock bridges (Eberhardt *et al.*, 2004). The distinctive difference for TC and PO soils, as plastic materials, was the less dramatic process of decreasing cohesive strength and mobilisation of frictional strength that lasted over higher strains. The drop in cohesion of the TC and PO samples was less sudden and did not approach zero; and the generation of frictional strength was smaller (Figures 5.62, 5.63).

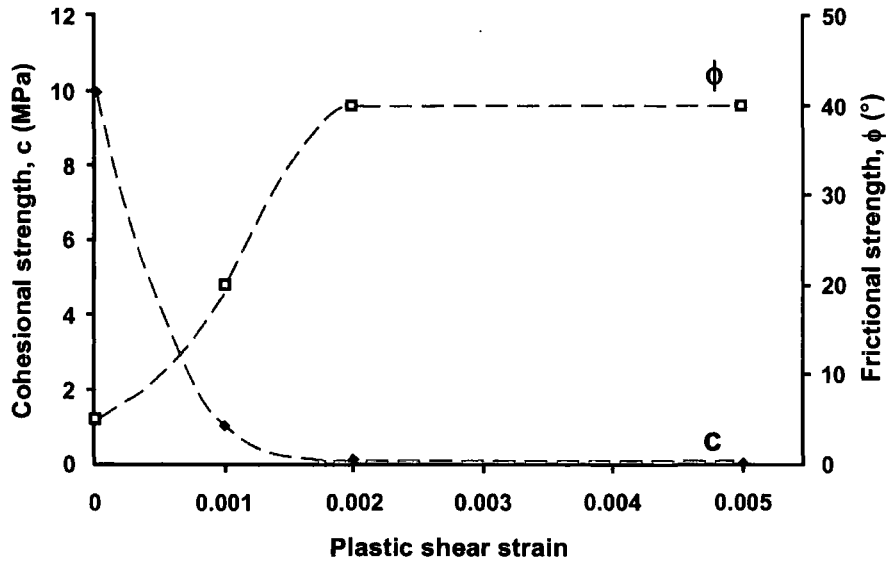

Figure 6.9 Decreasing cohesion and mobilisation of frictional strength during uniaxial compression damage testing of granitic rocks (after Eberhardt *et al.*, 2004)

The less dramatic, initial loss of cohesion of the TC and PO samples during the reinflation tests was not surprising as they were intensely weathered materials. The weak bonds between the soil particles were damaged due to the increase of pore fluid pressure. This was followed by a relatively constant cohesion value in which movements were possibly taking place at the residual strength of the material. In contrast, the conventional drained and undrained tests showed an increase of cohesion at small strains (Figure 5.63) which indicates a slightly different failure mechanism. The exceptional initial increase of cohesion appears to be mobilised from the rapid increase of shear stress within the samples under the strain-controlled compression, rather than reflecting the stress-controlled soil behaviour in the field condition which the soil particles are pushed apart by increasing pore water pressure.

As for the development of friction, the PPR, ICU and ICD tests exhibited similar processes with rapid mobilisation of friction at small strains up to around 10 % axial strain, which becomes constant thereafter. This is probably because higher levels of friction have to be mobilised to resist the initiation of movement between soil particles due to the increasing shear stress. The highest frictional strength was mobilised by the ICU tests at small strains, but was exceeded by the PPR tests in the large strain range. These similar values of friction angle derived at large strains ($\geq$ 10 %) could be related to the balance between the shear stress and the resistance force once movement has fully developed.

6.1.7.2 The effective strength envelope

The linear form of the effective strength envelopes derived from the TC and PO samples in the conventional triaxial tests (Figures 5.9, 5.15) and reinflation tests (Figure 5.27) has also been observed in other studies on undisturbed samples, including decomposed volcanics (DV) (GCO, 1982), completely to highly decomposed volcanics (C/HDV) (GEO, 1994a), volcanic saprolite, residual transitional volcanic soil, creeping saprolite, and completely decomposed tuff specimens tested along pre-existing shear planes (Irfan, 1994; Zhu and Anderson, 1998).

The stress paths derived from the undrained compression tests on TC and PO samples further indicate their normally consolidated soil behaviour (Figure 5.12), which is typical for residual soils (Leroueil and Vaughan, 1990). This implies that the samples have not been subjected to higher effective confining pressures than those applied during the triaxial tests (Head, 1998). The result is consistent and reflects the shallow depth of the sampling site and the loose and weak nature of the weathered soil samples in the field. This is in agreement with an observation in completely decomposed fine ash tuff by Gan and Fredlund (1996) of the transition of the curvilinear to linear segment of the strength envelope at a normal stress of about 105 kPa, due to the destruction of cementation bonds. Therefore, a curved strength envelope for the residual soil samples might appear if tested at a lower mean effective stress levels.

Based on field stress simulation tests, Zhu and Anderson (1998) attributed the linearity of the Hawaiian residual soil strength envelopes to the large proportion of fine particles (25 - 40% clay; 55 - 50% silt), which ultimately determine the shear strength of the soil after bonding is broken. Similarly, the predominant proportion of clay-sized (25%) and silty particles (50 - 60%) of the TC and PO samples may be responsible for the linear envelopes. This suggests that the strength envelope of volcanic residual soil can be well-defined, even allowing for the natural variability of the samples.

6.2 Volumetric behaviour during pore water reinflation testing

Dilative behaviour has been observed within the TC and PO samples during the reinflation tests (Figure 5.33). The result is consistent with previous experimental studies on undisturbed samples that simulate the field conditions for rainfall-induced landslides (GCO, 1982; GEO, 1994a; Anderson and Riemer, 1995; Anderson and Sitar, 1995; Zhu and Anderson, 1998; Dai *et al.*, 1999a; Gabet and Mudd, 2006). The behaviour has been commonly attributed to the increase of pore water pressure (e.g. Anderson and Riemer, 1995; Dai *et al.*, 1999a). However, the different patterns of volumetric expansion observed from the reinflation experiments further reveal that the volumetric increase may also involve "true dilation" due to various interparticle movements within the samples driven by constant shear.

6.2.1 Patterns of dilative behaviour

In this research, analysis of the void ratio (e) against mean effective stress (p') graphs suggests that the identified dilative soil behaviour generally undergoes three phases leading to failure, characterised by Type 1 to Type 3.

Type 1 displays a distinctive linear $e - p'$ relationship. It dominates the initial part of the reinflation test starting from p' = 233 kPa to around p' = 120 kPa, undertaken at various reinflation rates (Figure 6.10) and styles (Figure 6.11). This also generally describes the dilative soil behaviour during pore water pressure increase at the lowest rate: the 0.5 kPa/hr tests in both samples (Figure 6.12).

However, at the low reinflation rates, dilation can be further characterised by "cycles" of irregular gradual volume increase and sample contraction (Figure 6.12). These irregularities gradually disappear at higher reinflation rates as shown by the 5 kPa/hr tests (Figure 6.13).

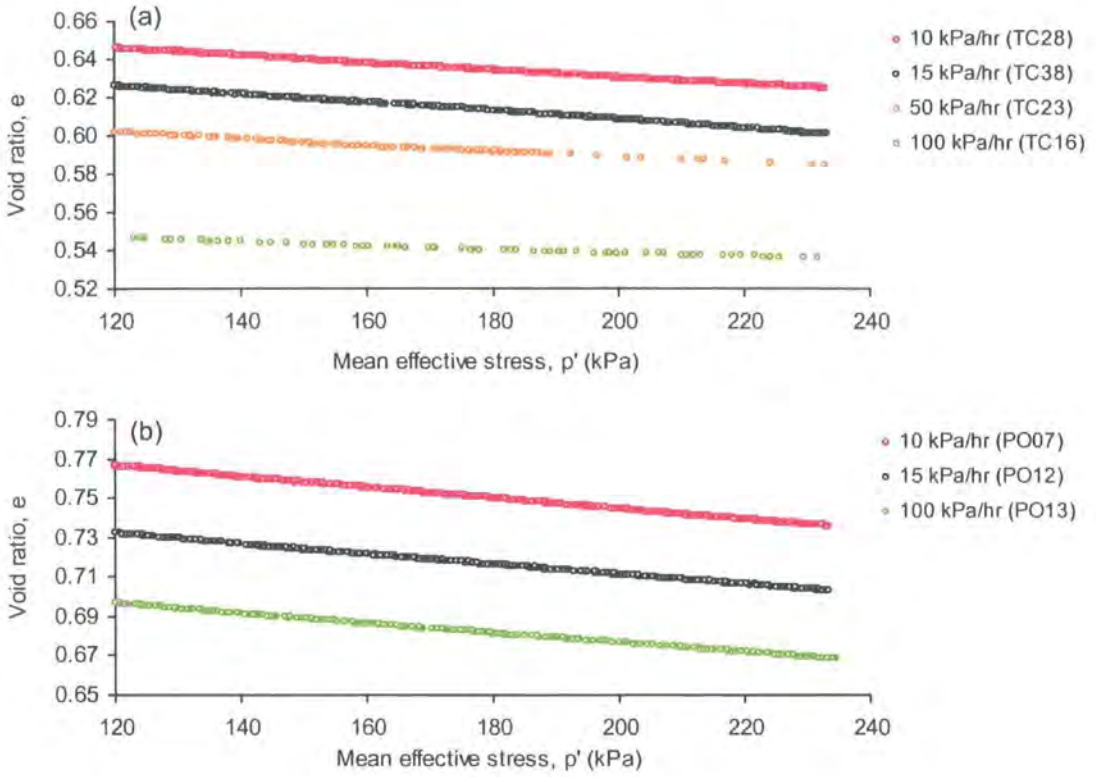

Figure 6.10 Linear $e-p'$ relationship during the initial stage of the reinflation test at various rates: (a) TC samples; (b) PO samples

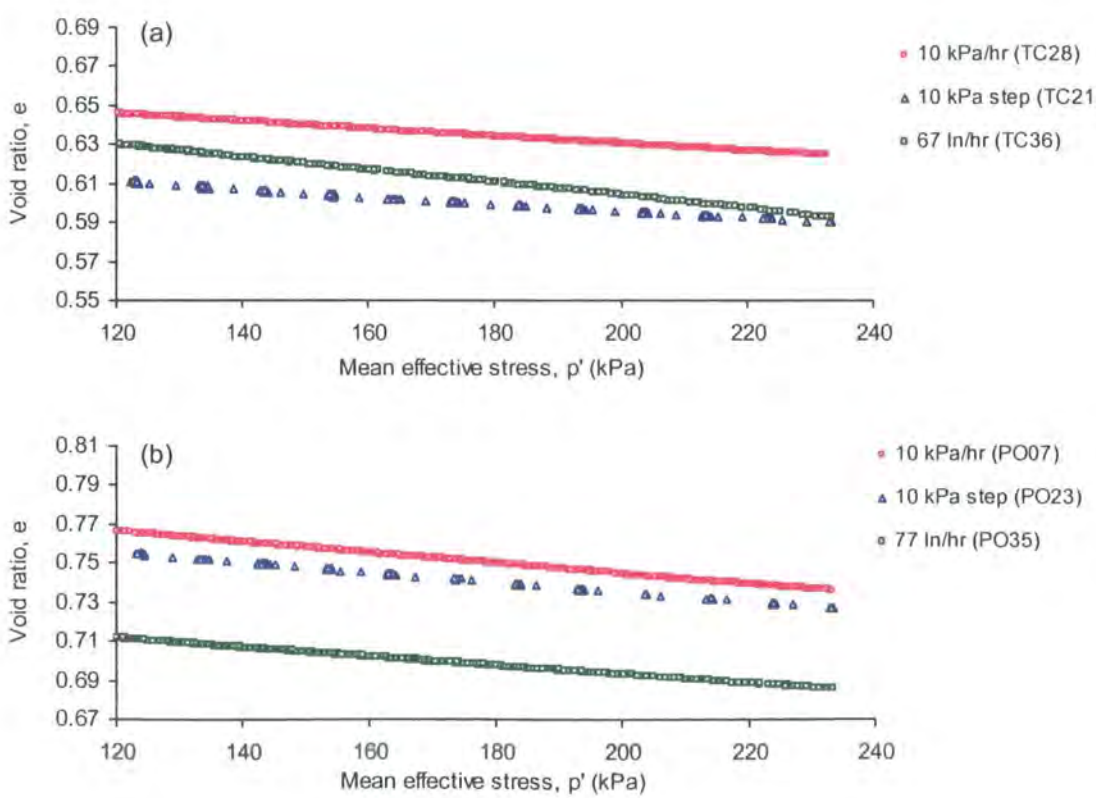

Figure 6.11 Linear $e-p'$ relationship during the initial stage of the reinflation test at comparable linear, stepped and logarithmic rates: (a) TC samples; (b) PO samples

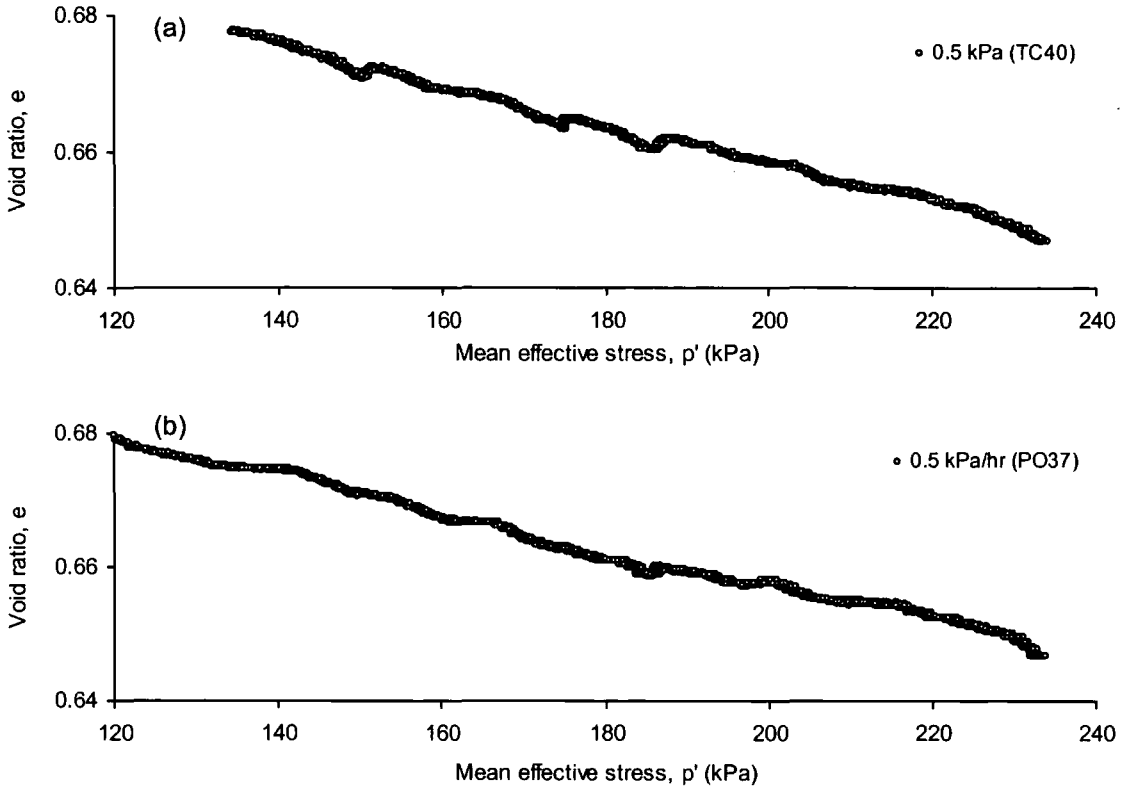

Figure 6.12 Plots of $e - p'$ showing uneven patterns during the 0.5 kPa/hr reinflation test: (a) TC40; (b) PO37

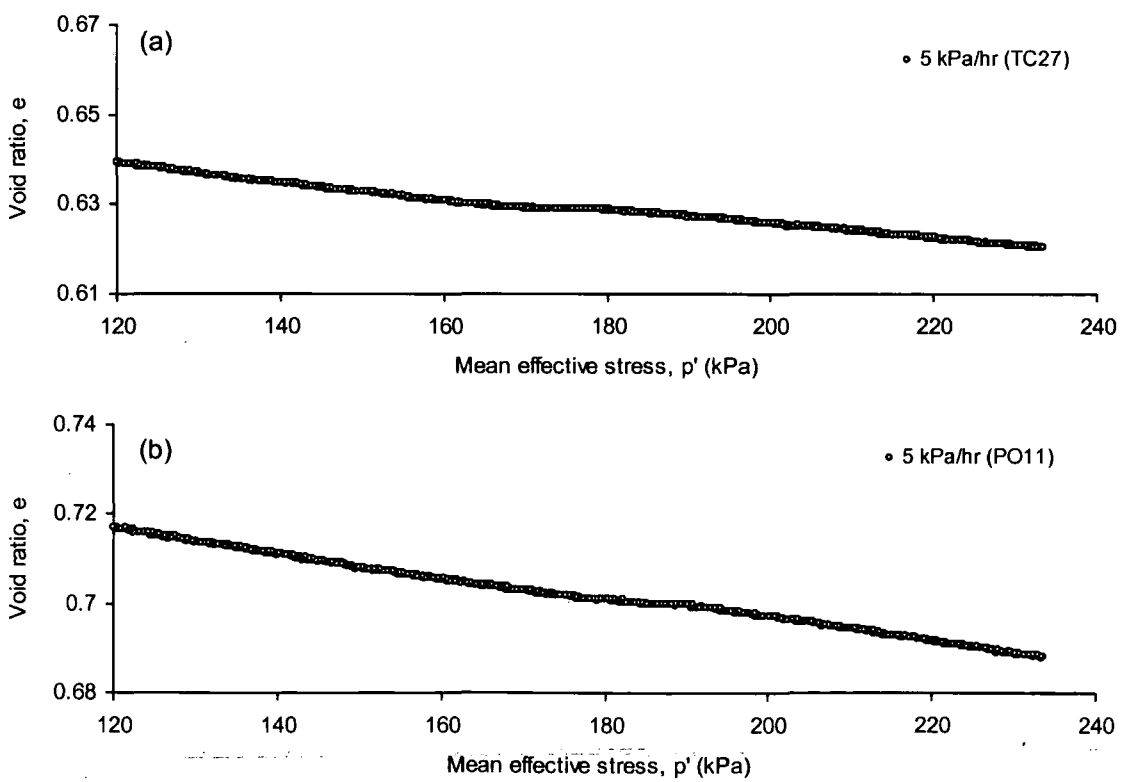

Figure 6.13 Plots of $e - p'$ showing disappearance of the uneven patterns during the 5 kPa/hr reinflation test: (a) TC27; (b) PO11

The Type 2 pattern exhibits a short-term, sudden increase in the sample volume during a small change in stress state, indicated by a stepped-like pattern in $e-p'$ plots (Figure 6.14). Interestingly, this pattern was not limited to the stepped rate reinflation tests but was also found during the linear patterns of pore water pressure increase.

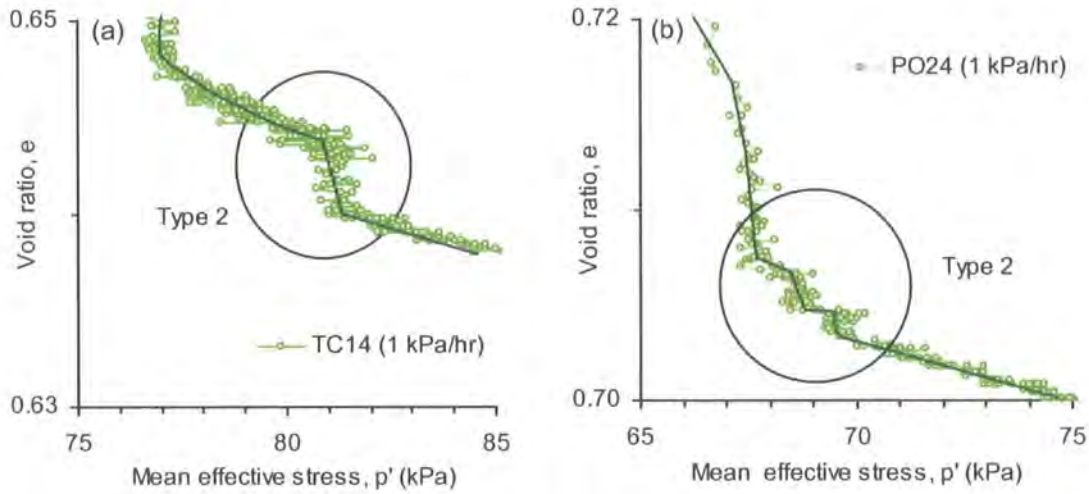

Figure 6.14 The presence of "kicks" along $e-p'$ curve during linear reinflation tests at 1 kPa/hr: (a) TC14; (b) PO24

The Type 3 pattern involves rapid, continuous increases in the void ratio, associated with final failure (Figure 6.15). This phenomenon commonly occurs at p' around 70 kPa (q = 100 kPa) for the TC and PO samples.

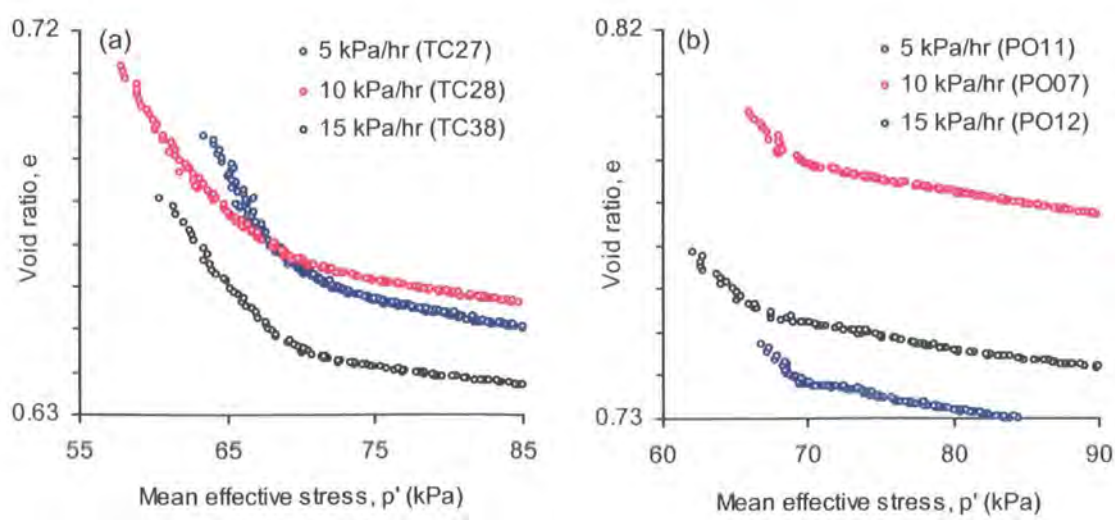

Figure 6.15 Rapid continuous dilation towards final failure during linear reinflation tests: (a) TC samples; (b) PO samples

The Type 1 to Type 3 patterns of dilative behaviour during the increasing pore water pressure suggest three different inter-particle movements occurring within the soil samples, characterised as "push and climb", "localised slide" and "generalised slide" respectively (Figure 6.16). The transition from Type 1 to Type 3 is likely to have associated with the increasing volume of pore fluid, thus reducing the contacts between soil particles facilitated by the constant shear. The process is further illustrated in Figures 6.16, 6.17.

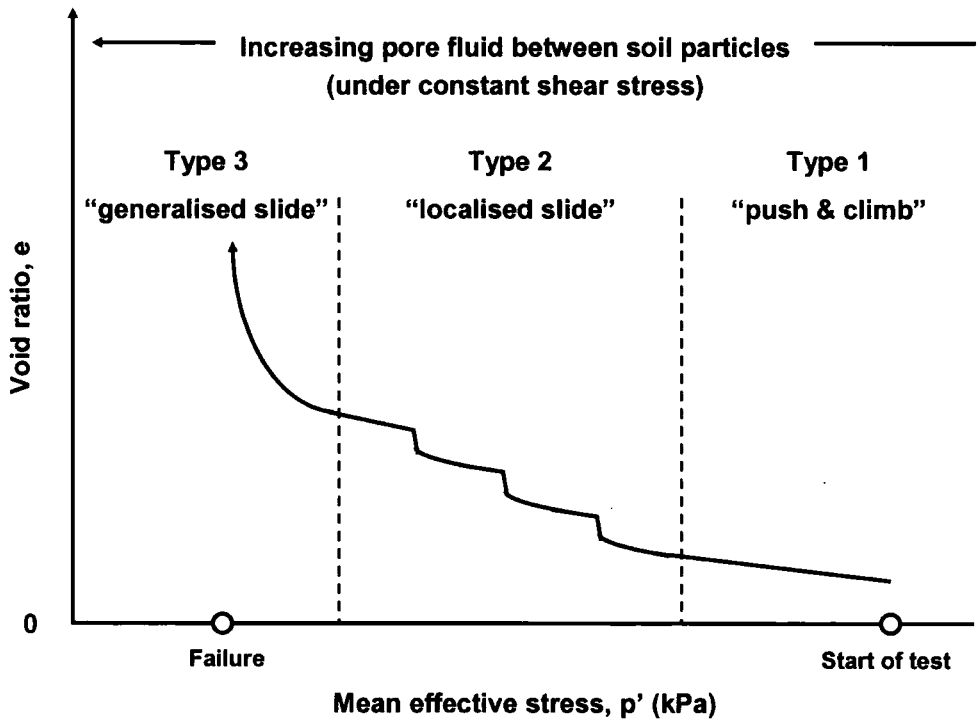

Figure 6.16 Explanation of dilative $e-p'$ relationship in terms of interparticle movement within the soil samples during reinflation test: Type 1 (push and climb), Type 2 (localised slide) and Type 3 (generalised slide)

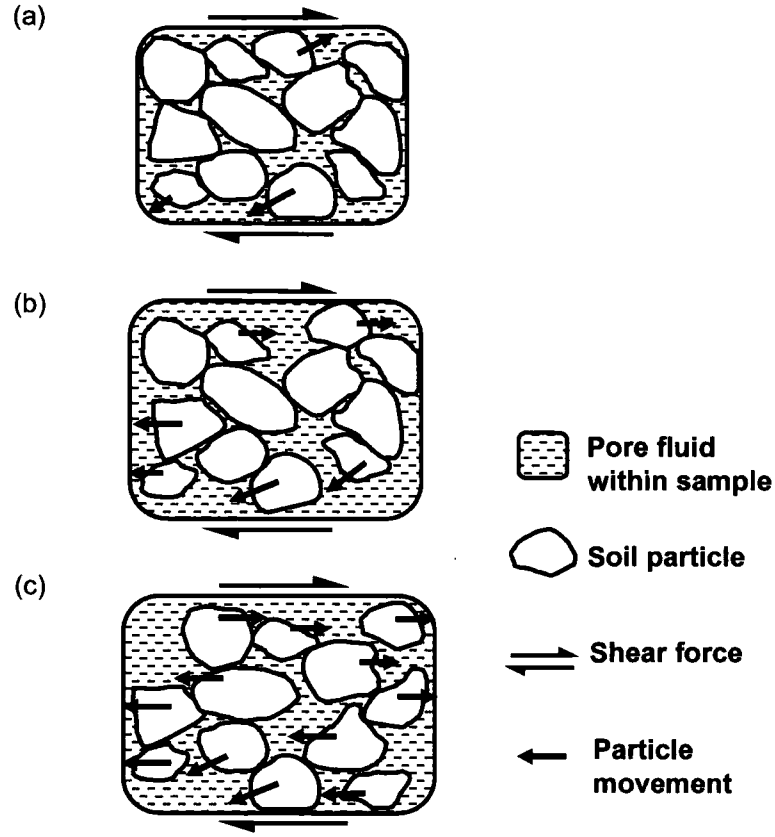

Figure 6.17 Interparticle movements within the sample during reinflation test: (a) Type 1 (push and climb); (b) Type 2 (localised slide) and (c) Type 3 (generalised slide)

At the start of the reinflation test, the linear $e - p'$ relationship (Type 1) (Figures 6.16, 6.17a) appears to have mainly contributed by the increase of pore fluid getting into the sample rather than shear deformation (Figures 6.10, 6.11). Expansion or swelling caused by a decrease in effective stress is recognised (Selby, 1993; Terzaghi *et al.*, 1996; Mitchell and Soga, 2005), which is also found in previous field simulation experiments (Anderson and Riemer, 1995; Zhu and Anderson, 1998; Dai *et al.*, 1999a; Chen and Yang, 2000; Ohtsuka and Miyata, 2001). However, the irregularities exhibited by the reinflation tests at low rates (Figures 6.12, 6.13) further suggest that the soil particles are also being pushed apart under shear. As effective stress decreases, the increasing water volume moves the particles further apart and enables them to push and climb over the adjacent particles under shear force. Such movement is also reported in some recent field simulation experiments (Gabet and Mudd, 2006). However, relative interparticle movements are limited due to strong interlocking with the other particles under high mean effective stress. This is reflected by little axial strain development (Figure 6.18).

In addition, some particles may fill up the void space that has been previously occupied by another particle under shear. The process is indicated by the irregular $e-p'$ pattern of which the push-and-climb related dilation is disturbed by some slight contractions (Figure 6.12). The contractions driven by shear appear to result in a small increase of axial strain of less than 0.1% within the TC and PO samples (Figure 6.18). Unfortunately, the pattern is less clearly observed during reinflation at higher rates (Figure 6.13), probably because the more rapid volumetric increase masks the contribution of shear deformation.

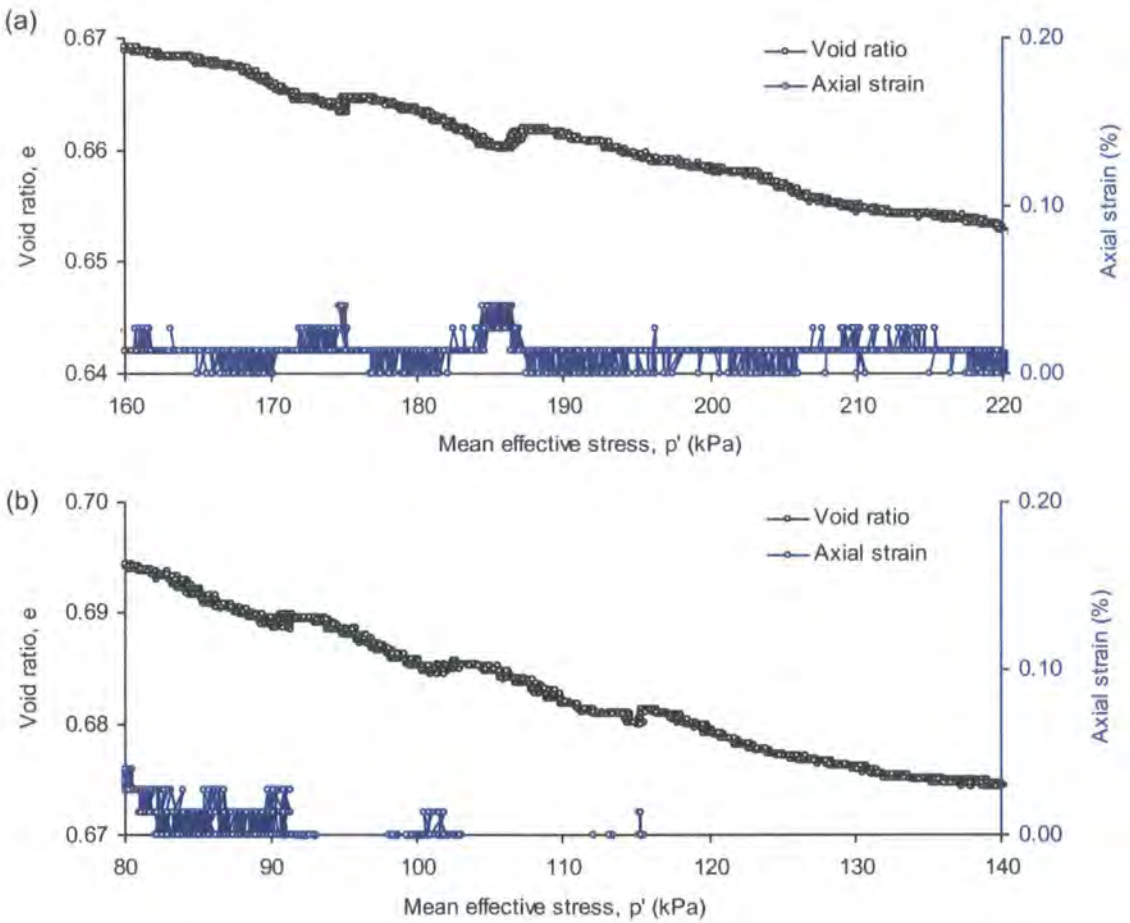

Figure 6.18 The dilative-contractive $e-p'$ pattern and the corresponding axial strain during 0.5 kPa/hr reinflation test: (a) TC40; (b) PO37

The Type 2 dilative behaviour appears to be attributed to localised sliding (Figures 6.16, 6.17b). The slip movements are aided by the increasing amount of pore fluid that reduces the inter-particle contacts as effective stress decreases further. Some particles within the sample begin to slide past each other in the direction of shear. This is evident from the sudden increase of axial strain following an increase of the void ratio within the TC and PO samples (Figure 6.19). However, the movements are still being restricted and blocked by the interlocked particles. In this stage, dilatancy contributed by shear deformation becomes increasingly dominant over volumetric deformation, as indicated by the more irregular $e - p'$ curves (Figure 6.14).

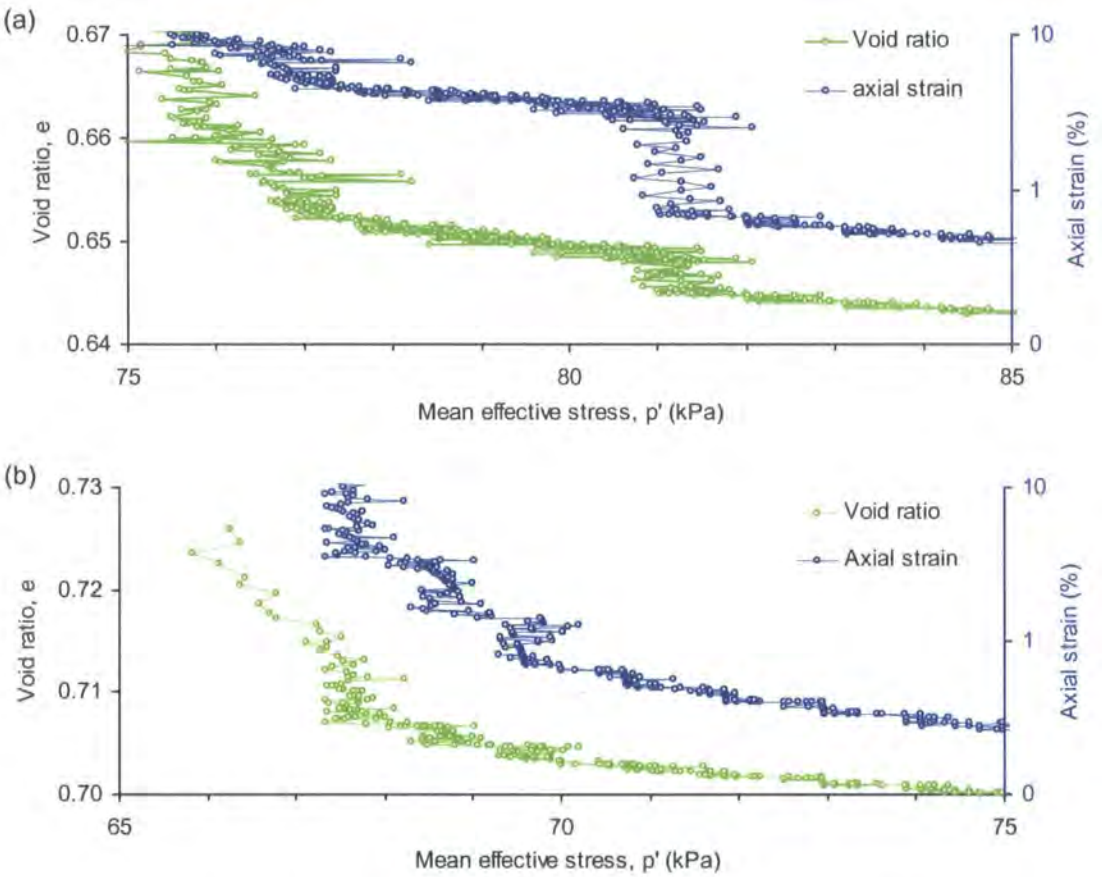

Figure 6.19 Sudden change of void ratio and axial strain against mean effective stress: (a) TC14; (b) PO24

Type 3 represents failure as a result of the generalised slip movements between particles (Figure 6.16, Figure 6.17c). The sample is largely restructured due to particle rearrangement under shear. Most particles are aligned and more free to slide pass each other. The sliding may also propagate due to stress transfer between particles. The dilatant behaviour is mainly controlled by shear deformation. The highly non-linear $e - p'$ pattern (Figure 6.15) is possibly related to plastic strain.

6.2.2 Changes of void ratio under stepped reinflation

The contribution of the shear deformation due to interparticle movement and the pore water pressure increase on the volumetric behaviour of the samples can be further analysed with reference to the stepped reinflation tests.

Consistent stepped-like patterns in $e-p'$ are distinctive during the stepped reinflation tests (e.g. Figure 6.20), comprising two main characteristics: The sample volume increased (1) slightly during the stepped increases of pore water pressure (e.g. from 108 kPa to 103 kPa, from 103 kPa to 98 kPa etc.), and (2) to a relatively larger degree when pore water pressure was held constant (e.g. at 108 kPa, at 103 kPa etc.). The former was related to the increasing pore fluid pushing into the sample to decrease the mean effective stress, controlled by the test apparatus. The latter, however, was more likely to be associated with the "true dilation" due to internal remoulding within the sample under constant stress conditions, facilitated by one of the interparticle movements driven by constant shear (Figures 6.16, 6.17). The non-linear increase in void ratio further indicates that the role of shear deformation becomes more important as the effective stress level gets lower (towards failure) (Figure 6.20).

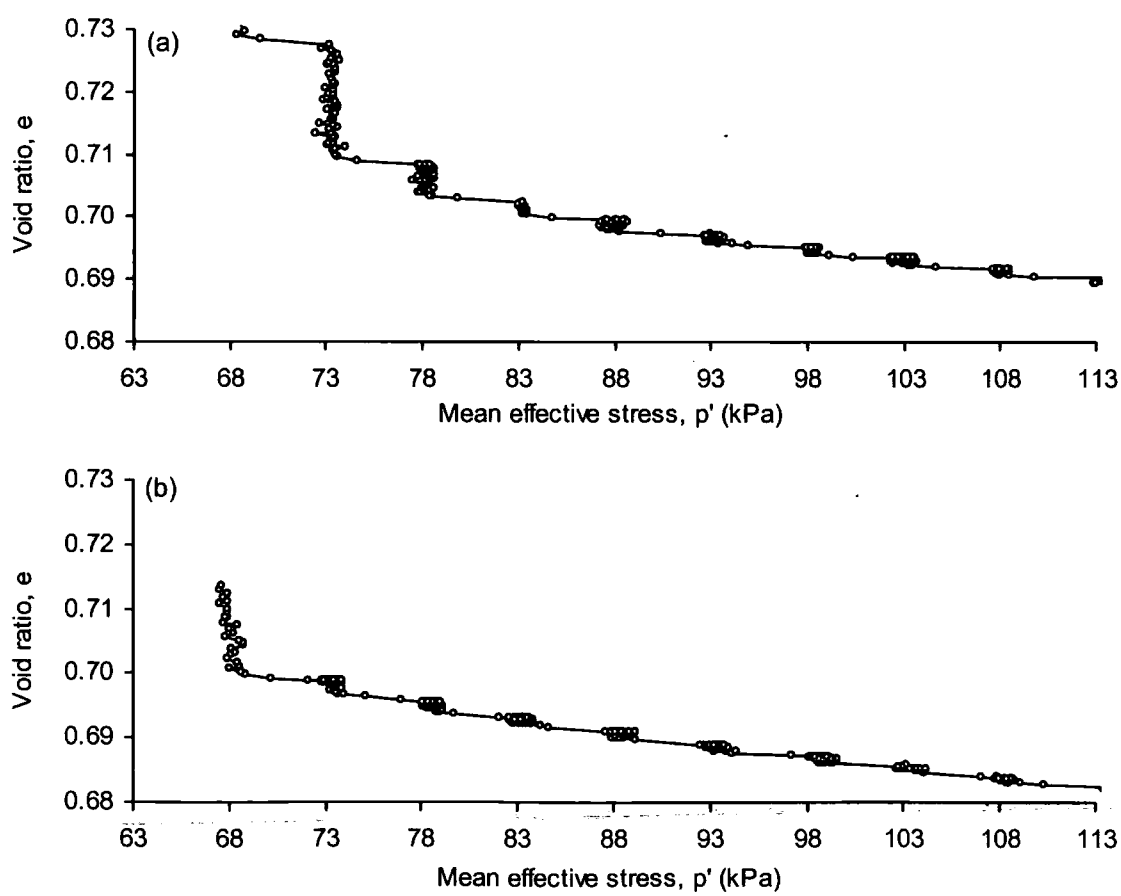

Figure 6.20 Typical stepped-like pattern in $e-p'$ stepped reinflation tests demonstrated by the 5 kPa stepped test: (a) TC29; (b) PO25

An interesting pattern emerged when the process was examined against time. It was clear that the void ratio increased following the stepped reinflation, but increased at a decreasing rate soon after the new pore pressure level was attained (Figure 6.21). The slowing down of volumetric expansion could be related to the rate of pore water pressure distribution throughout the sample, which is controlled by the soil permeability. The effect of equalisation is indicated by the shape of the $e-time$ curves (Figure 6.21).

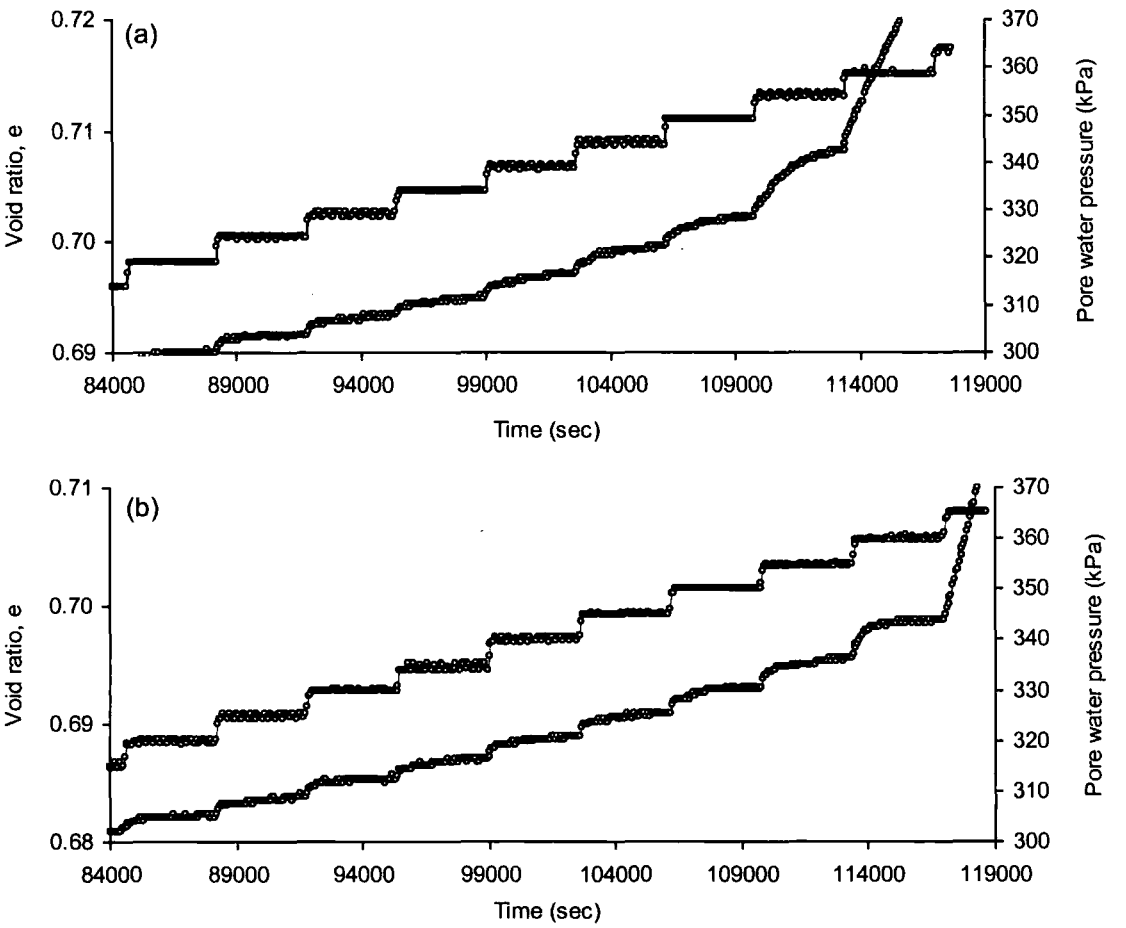

Figure 6.21 Typical patterns of slope changes in $e-time$ under stepped reinflation tests for (a) TC and (b) PO samples, demonstrated by the 5 kPa stepped test

During a stepped rate of reinflation, say 5 kPa, the pore water pressure distribution within the less permeable TC samples tends to be more uneven. The rate of increase of pore water pressure applied at both ends of the samples would be equal to 5 kPa immediately but not likely to reach 5 kPa in the middle of the sample at the same time due to lower permeability. When the pore water pressure is held constant, the dilation is slowed because the increased pressure (i.e. 5 kPa) must be distributed to the middle of the sample to equalise with the new pressure level. The effect is revealed by the more generalised and gentle $e-time$ curves (Figure 6.21a). However,

this pore pressure distribution process is more efficient within the more permeable PO samples, meaning that the increased pore water pressure can be quickly equalised throughout the sample. Therefore, the PO samples have sharper $e-time$ curves which follow closely with the stepped pore pressure increase (Figure 6.21b).

Plots of axial strain against void ratio further indicate that the decreasing rate of the volumetric expansion may be associated with the increasing plastic strains as the pore water pressure level becomes higher (Figure 6.22). The increasing void ratio and the accumulation of axial strain under constant stress conditions (when pore water pressure was held constant) (Figure 6.22) also suggest the presence of true dilation due to interparticle movements within the TC and the PO samples.

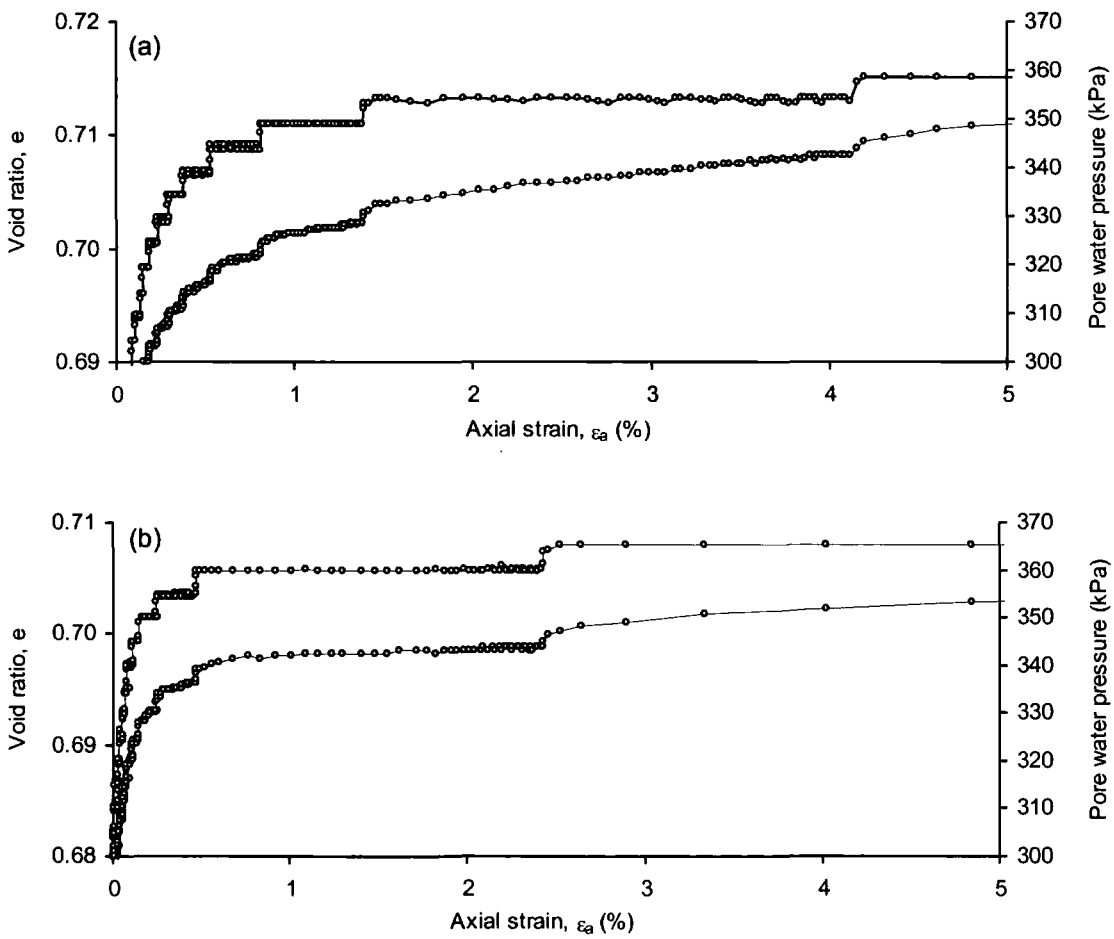

Figure 6.22 Typical $e-\varepsilon_a$ plots under stepped reinflation tests showing the increasing plastic strains: (a) TC samples; (b) PO samples

6.3 Deformation mechanism

Another important aspect of soil movement behaviour lies in the stress-deformation and stress-deformation-time relationship (Mitchell and Soga, 2005). The associated fundamental soil behaviour involves elastic deformation, plastic deformation and creep phenomena (section 2.5). These deformation mechanisms are well-observed in deep-seated landslide systems, leading to catastrophic movement (brittle failure); steady, constant, creep-like movement (ductile failure); and a sudden failure preceded by long periods of creep (ductile-brittle failure) respectively (Petley, 1996; Petley and Allison, 1997).

6.3.1 Is it elastic deformation?

Elastic behaviour refers to recoverable deformation which involves a linear relationship between stress and strain (Carson, 1971; Craig, 1997). It is a common phase for both brittle and ductile deformation in most geological materials (Petley and Allison, 1997). Such behaviour can be normally examined through the linear section of the stress-strain curve in plots of $\varepsilon_a - q$ (where ε_a is axial strain; q is deviatoric stress) (Figure 2.2), derived from conventional drained and undrained triaxial tests (Wood, 1990). However, this evaluation method is not directly applicable for the reinflation tests as the deviatoric stress has been kept constant. Alternatively, elastic behaviour under reinflation process is assessed through plots of (a) axial strain against effective stress, $\varepsilon_a - p'$ and (b) the change of axial strain against effective stress, $\Delta\varepsilon_a - p'$ in this research. The results from the linear and the stepped reinflation tests have been used to evaluate if the TC and PO samples exhibit the elastic behaviour.

6.3.1.1 Evaluation of stress-strain relationship

The highly non-linear stress-strain relationship derived from the linear reinflation tests indicates no sign of elasticity even at small strains ($\leq$ 1 %) (Figure 6.23). This is perhaps not very surprising as most natural soils are not elastic materials (Wood, 1990; Selby, 1993; Smith and Smith, 1998; Parry, 2004; Yu, 2006). The highly non-linear behaviour of geomaterials has also been observed in other experimental studies (Burland, 1989). For the weathered TC and PO soils, the non-linearity could be related to their heterogeneous nature (Craig, 1997) (section 6.1.5). The inelastic strains may also be associated with the presence of very hard soil particles (Nemat-Nasser, 2004), such as quartz indicated by the sand and gravel contents of the weathered samples (Table 5.4).

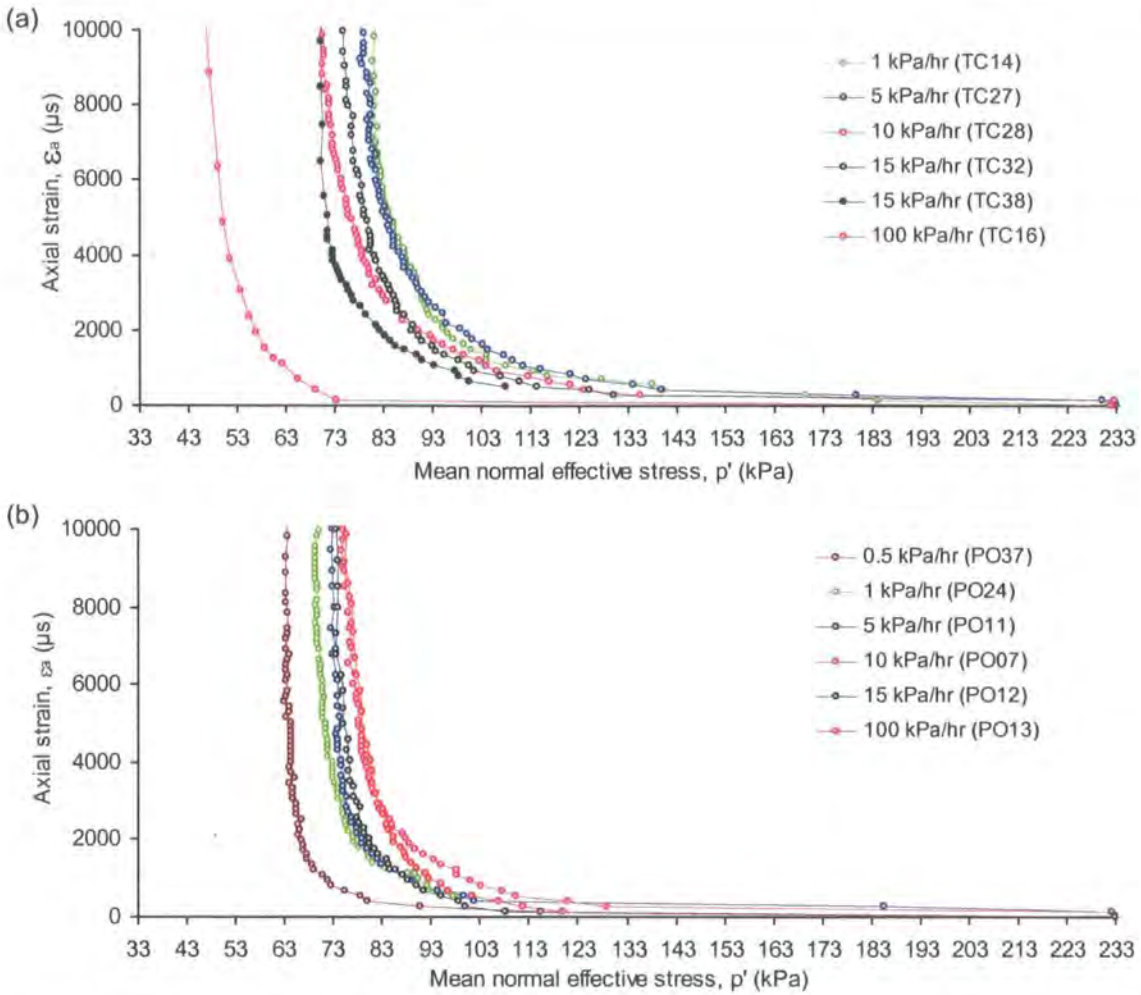

Figure 6.23 Non-linear stress-strain relationship begins at the early stage of the linear reinflation tests (equivalent to axial strain up to 1%): (a) TC samples; (b) PO samples

6.3.1.2 Evaluation of stress-strain relationship under stepped reinflation

The stepped reinflation tests allow examination of the contribution of the elastic component in explaining the strain patterns (Figure 6.24). If the soil samples were perfectly elastic and perfectly permeable, the resulted strain pattern would have been stepped-like in proportional to the applied pore water pressure (Figure 6.24b). The accumulation of strain ($\Delta\varepsilon$) at each equal stepped reinflation would be constant (Figure 6.24c). For an elastic but finitely permeable material, the strain would probably increase at a slower rate during the increase in stepped pore water pressure. When pore water pressure is held constant, strain would still be increasing but at a decreasing rate (Figure 6.25b). However, the change in elastic strain would be the same against the mean effective stress (Figure 6.25c).

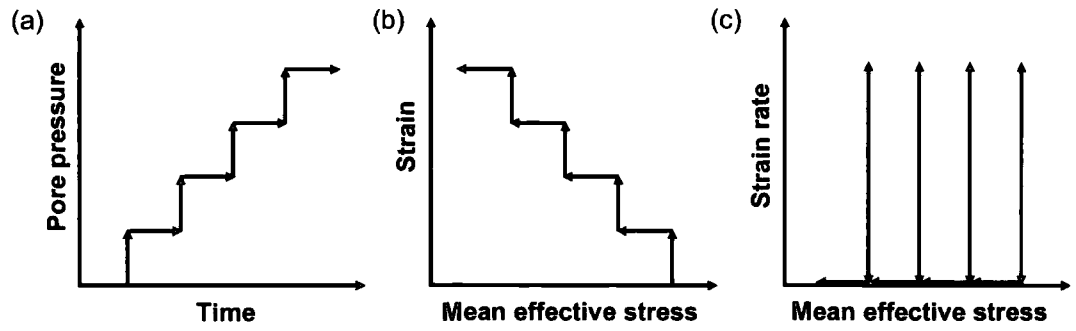

Figure 6.24 Expected elastic behaviour during the reinflation tests under instantaneous pore pressure increase for a perfectly permeable material, expressed in plots of:
(a) pore pressure - time; (b) $\varepsilon - p'$; (c) $\Delta\varepsilon - p'$

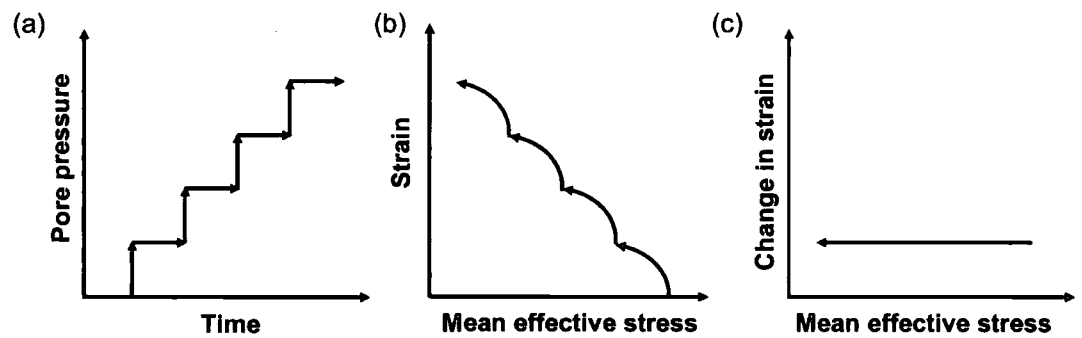

Figure 6.25 Expected elastic behaviour during the reinflation tests under instantaneous pore pressure increase for a finitely permeable material, expressed in plots of:
(a) pore pressure - time; (b) $\varepsilon - p'$; (c) $\Delta\varepsilon - p'$

However, evidence from the stepped reinflation dataset suggests the tested samples do not possess the elastic element. The most direct evidence lies in the non-linear $\Delta\varepsilon_a - p'$ relationship derived from stepped reinflation tests for the TC and PO samples (Figure 6.26). It is evident that the accumulated axial strains (i.e. $\Delta\varepsilon_a$) increase more than proportionately at each step of increase in pore water pressure (i.e. decreasing p'), indicating the absence of elastic properties.

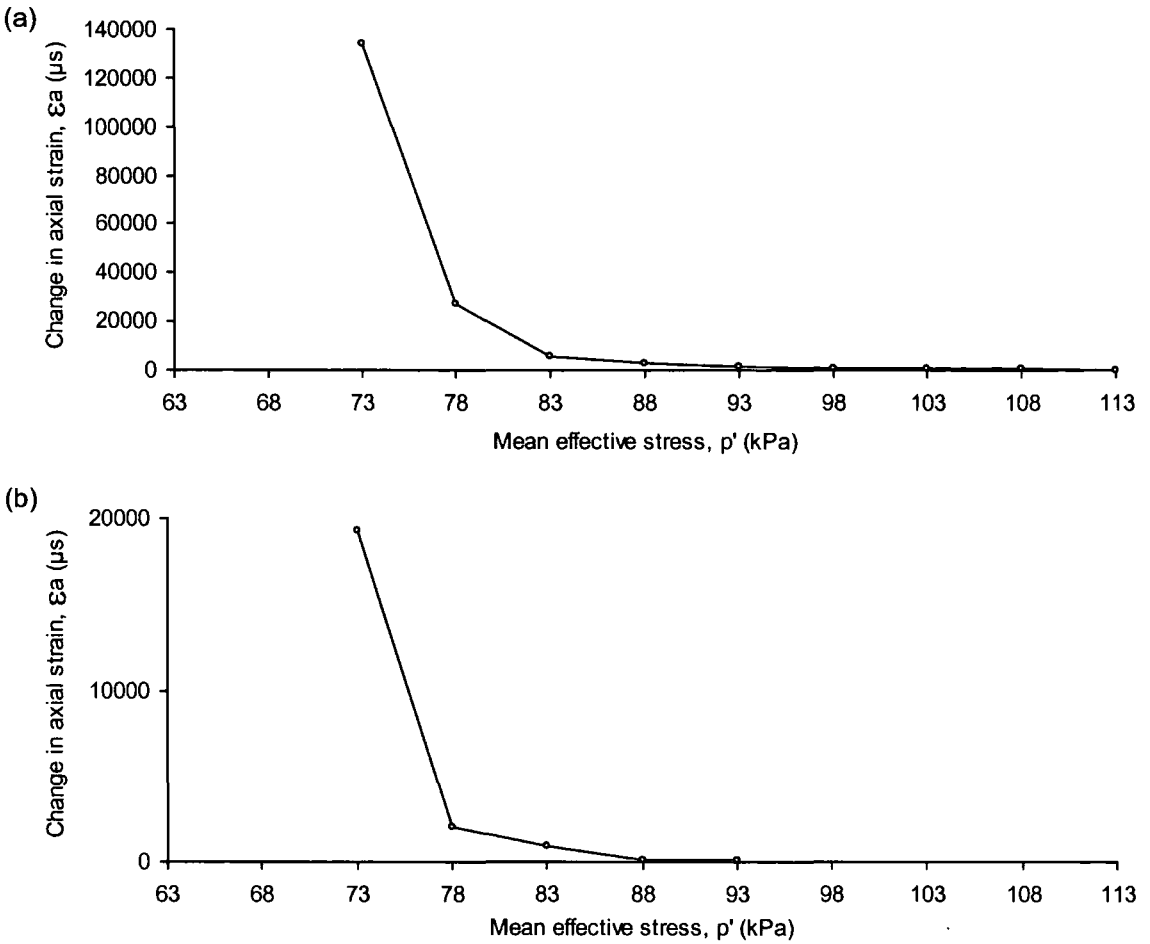

Figure 6.26 Typical examples of non-linear $\Delta\varepsilon_a - p'$ relationship during the reinflation tests: (a) TC29 and (b) PO25

Based on the findings from the reinflation tests, it is evident that the stress-strain relations of the weathered TC and PO samples cannot be explained by classic elastic behaviour. The other fundamental soil components such as plasticity and creep need to be examined.

6.3.2 The role of plastic deformation

6.3.2.1 Initial zero movement below yield stress state

In the initial phases of the reinflation, there was little or no strain development (Figures 6.23, 6.27). This might be interpreted as the classic behaviour of perfectly plastic materials. The lack of initial strain development has also been noted in previous experimental studies (Anderson and Riemer, 1995; Anderson and Sitar, 1995; Zhu and Anderson, 1998; Dai *et al.*, 1999a). No deformation occurs probably because the magnitude of the initial shear stresses is smaller than the yield stress/strength associated with the friction within a perfectly plastic material (Selby, 1993). This could be explained with reference to the Type 1 volumetric behaviour (Figures 6.16, 6.17a), where the soil particles are largely interlocked. The magnitude of the initial applied stress is insufficient to loosen the interparticle contacts, resulting in little strain. Therefore, in this research, plastic yield can be determined by the initiation of movement (strain or strain rate) in terms of mean effective stress. Based on the experiments, the plastic yield stress at q = 100 kPa appears to lie around p' = 143 kPa and p' = 133 kPa for the TC and PO samples respectively.

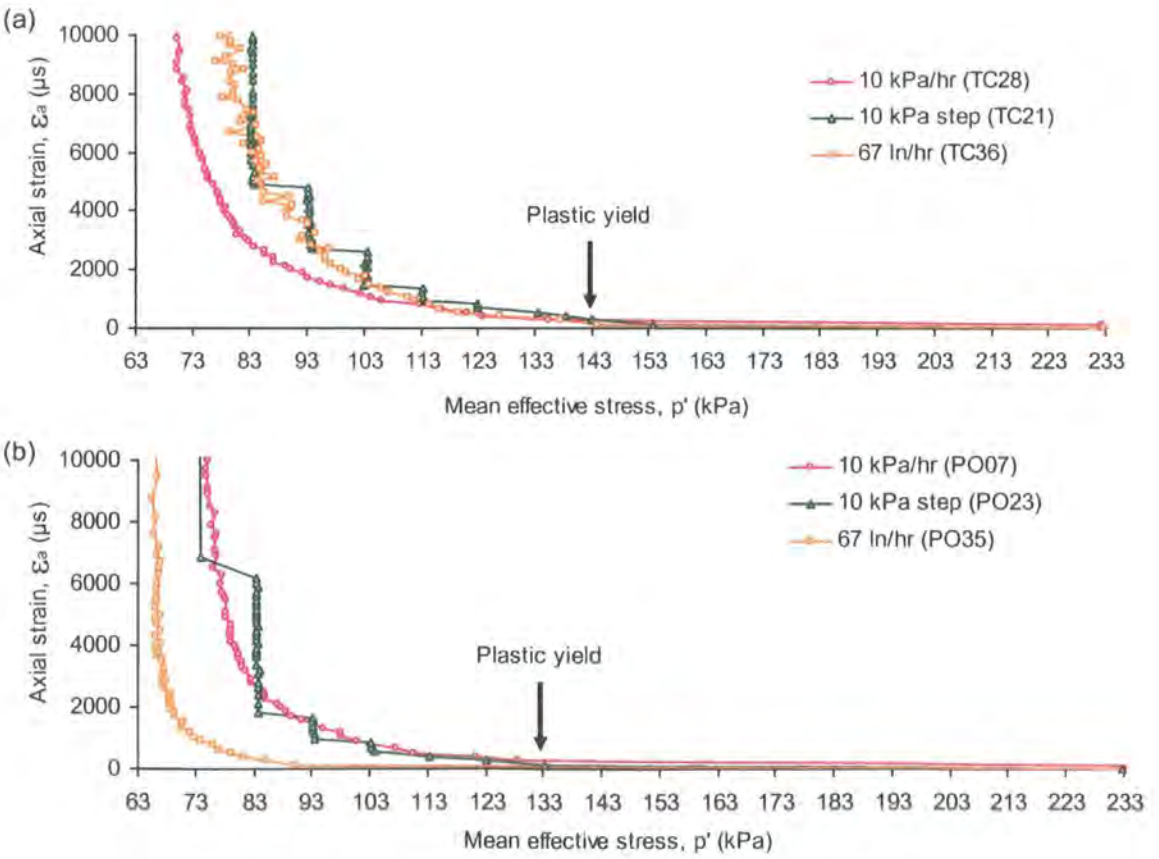

Figure 6.27 Little movement at the initial stage of reinflation suggests the presence of a yield state: (a) TC samples; (b) PO samples

6.3.2.2 Asymptotic trend in $\Lambda - t$ space

Once the yield stress is exceeded, plastic deformation occurs, as demonstrated by the asymptotic trend in the Saito analysis in plots of $\Lambda - t$ (Petley *et al.*, 2002), which is especially obvious for the linear (Figure 6.28) reinflation tests. The asymptotic trend in fact reflects the key property of plastic behaviour, that a decrease in stress (p') leads to a non-linear increase in strain rate ($\dot{\varepsilon}$) (Figure 6.29). The relationship is best described by the exponential function (Tables 5.14, 5.16, 5.17) that has not been addressed by previous observations (Fukozono, 1985, 1996; Voight, 1988a, 1989b) (Figure 2.15). The dominance of plastic failure for all of the applied pore water pressure rates is probably because the samples are in a very intensely decomposed state, meaning that the strains could be easily distributed within the weakly structured soils (Fookes, 1997). Wang *et al.* (2007) noted that the high degree of weathering changed the deformation style of the Jinnosuke-dani landslide in Japan to a homogenous plastic sliding style (Figure 6.30). More conventional evidence of plastic behaviour include the stress-strain curves without sharp peak in plots of axial strain (ε) against deviatoric stress (q) (Figures 5.13, 5.17) and the barrel-like sample form (Appendices 1c, 2) (e.g. Zhu and Anderson, 1998).

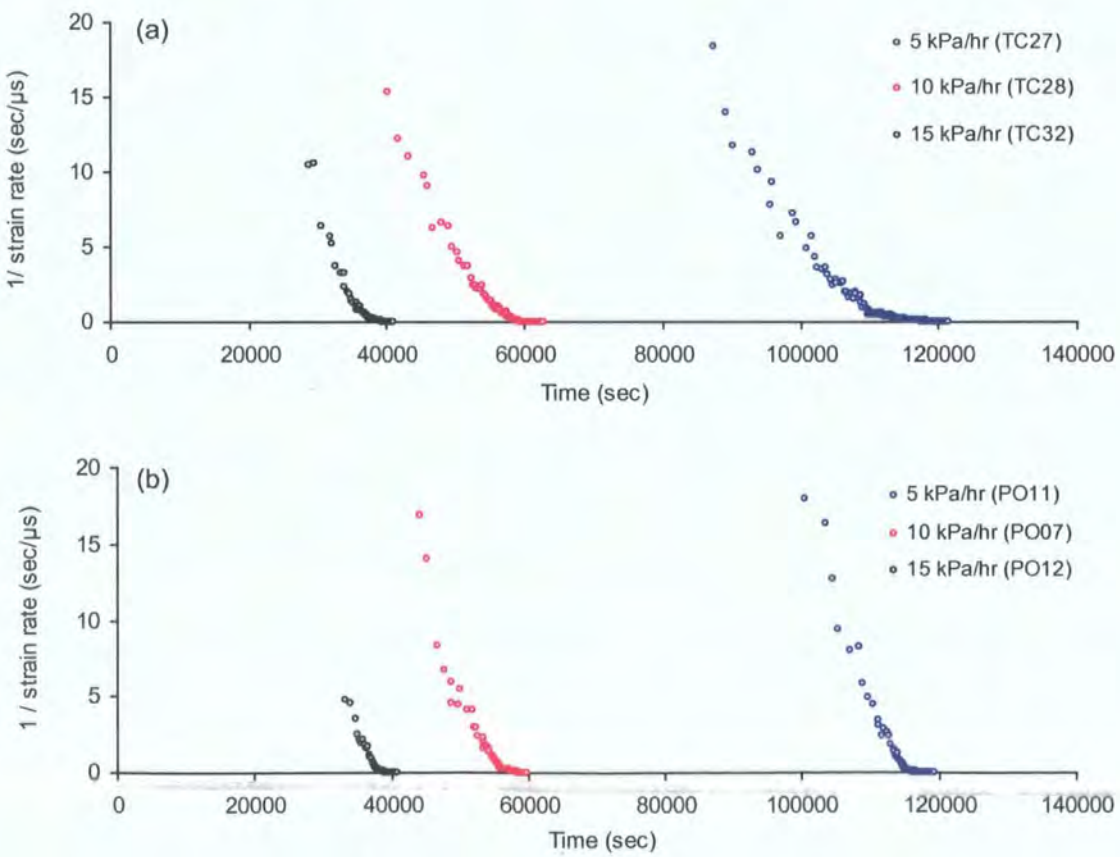

Figure 6.28 Plastic deformation revealed by asymptotic trend in $\Lambda - t$ during linear reinflation tests: (a) TC; (b) PO samples

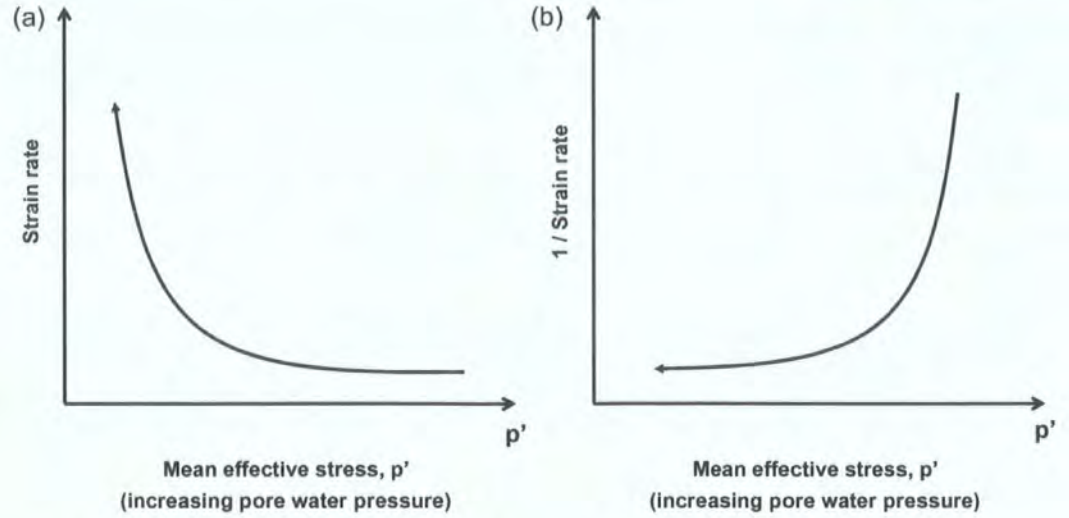

Figure 6.29 Plastic behaviour expressed in plots of (a) $\dot{\varepsilon} - p'$ and (b) $\Lambda - p'$

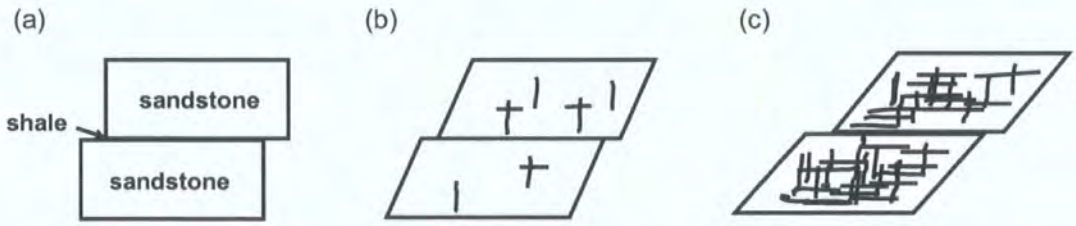

Figure 6.30 The influence of weathering on the deformation style of the Jinnosuke-dani landslide, Japan: (a) Fresh; (b) moderately weathered; (c) strongly weathered (after Wang *et al.*, 2007)

6.3.2.3 The relationship between reinflation rate and the slope in $\Lambda - p'$

Through Saito analyses, the results also show how the rate of pore water pressure increase controls the deformation behaviour, as observed from the systematic change of the gradient of the asymptotic curves in $\Lambda - p'$ exhibited by samples with the same density (Figures 5.38, 5.39, 6.31). The association with the rates of pore water pressure increase appears to be consistent with the findings reported in undisturbed Tessina mudslide matrix (Petley *et al.*, 2005a) (Figure 2.12b). The impact of the reinflation rate is also revealed from the change of slopes in $\varepsilon - p'$ within the TC (Figure 6.32) and the PO samples (Figure 6.33), suggesting that there was no unique failure stress state.

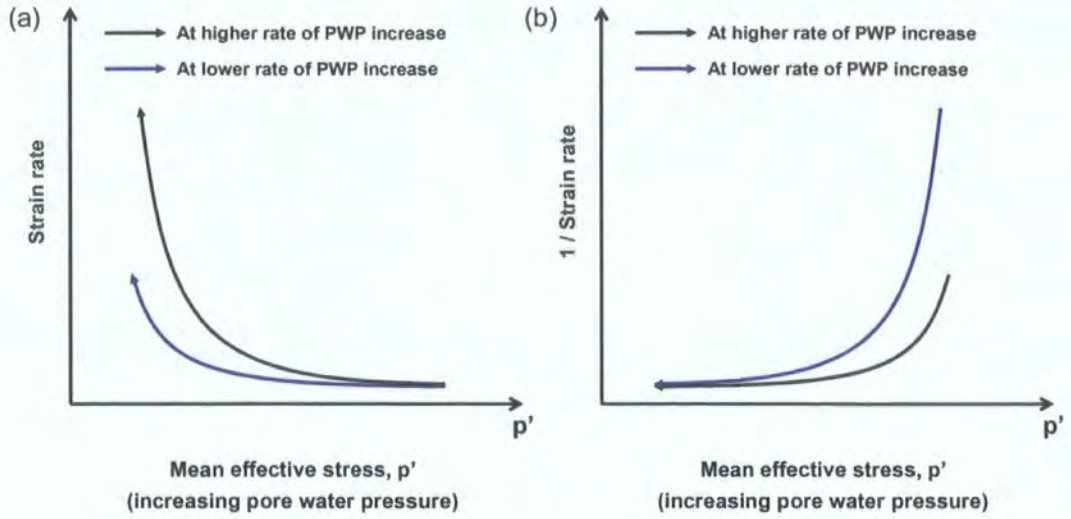

Figure 6.31 The influence of the rate of pore water pressure increase on the slope of the line in (a) $\dot{\varepsilon} - p'$; (b) $\Lambda - p'$

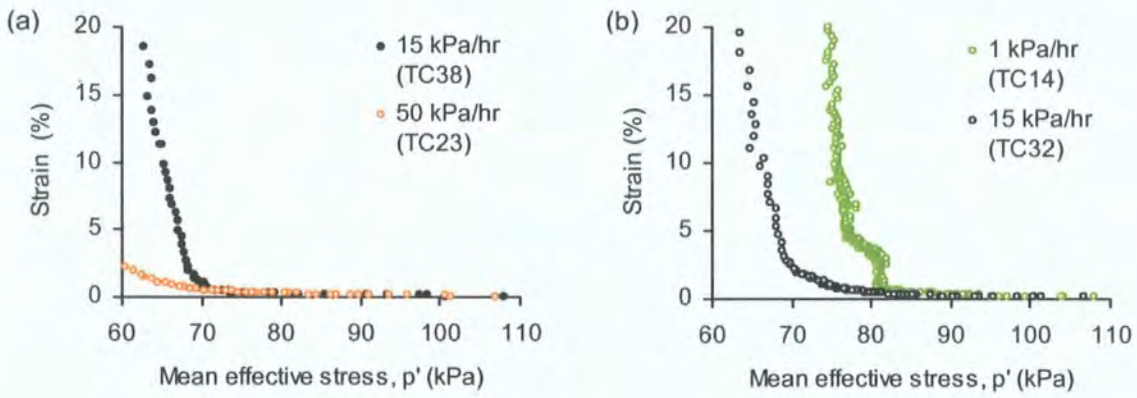

Figure 6.32 Acceleration movements in $\varepsilon - p'$ during reinflation test on TC samples: (a) 15 kPa/hr vs 50 kPa/hr (initial void ratio before saturation: 0.66); (b) 1 kPa/hr vs 15 kPa/hr (initial void ratio after initial drained shear: 0.61)

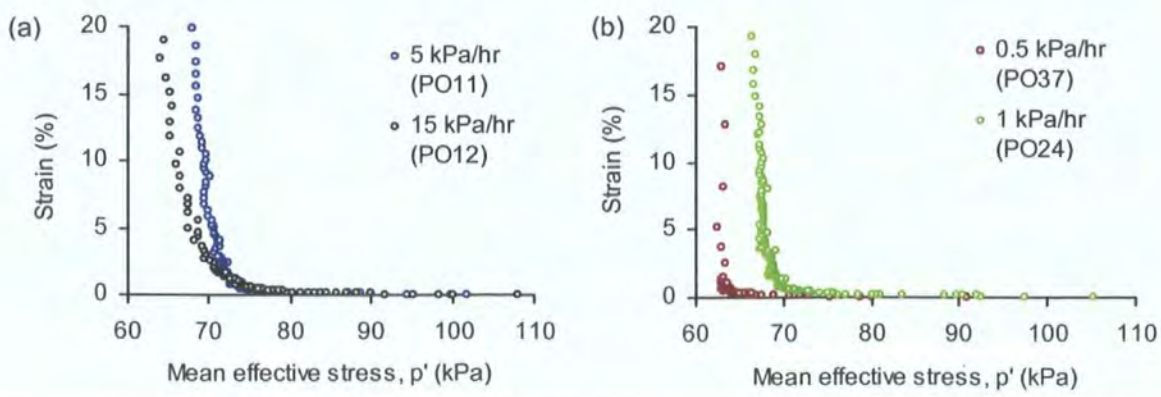

Figure 6.33 Acceleration movements in $\varepsilon - p'$ during reinflation test on PO samples: (a) 5 kPa/hr vs 15 kPa/hr (initial void ratio before saturation: 0.83); (b) 0.5 kPa/hr vs 1 kPa/hr (initial void ratio after drained initial shear: 0.65)

The results are not likely to be affected by pore pressure equalisation processes, especially for the PO samples given their higher permeability (section 6.1.6). The pore pressure equalisation tests further indicate that the pore water pressures within PO samples are equalised, as there is little difference between the back pressure and pore pressure up to 100 kPa stepped rate measured from the top and the bottom of sample respectively (Figure 6.34).

Hence, the relationship between the reinflation rates and the slopes in $\Lambda - p'$ and $\varepsilon - p'$ shown by the undisturbed samples could not be fully explained by the critical state theory, which implies that implied an ultimate and unique failure stress state regardless of the rate of pore water pressure or initial sample density (Atkinson and Bransby, 1978; Atkinson, 1993). This might be due to the fact that the critical state theory was developed from remoulded natural or reconstituted soils which did not take into account the impact of micro- and macrostructure of undisturbed soils on their behaviour (Burland, 1990).

Higher pore water pressure rates possibly cause higher degrees of destructuring, in which the stresses within the sample could not be localised in the quickly destructured state, leading to more plastic behaviour (Figures 5.38, 5.39, 6.31). Transition of soil behaviour (plastic to brittle or vice versa) in relation to the rates of pore water pressure, however, was not identified in this study.

However, Figure 6.31 does not include the intriguing decreasing strain rate observed from the stepped rate tests during the time periods when pore water pressure was held constant. The observed deceleration cannot be explained by the notable time-dependent "strength regain" mechanism proposed by Angeli *et al.* (1996, 1999, 2004), as their theory has not considered shear strength under constant pore water pressure conditions. Moreover, for the residual soils tested in this study, it is doubtful if the structure destroyed during the reinflation tests could be recovered, such as through the precipitation of cementing agents, within the short time scale of the experiment (Leroueil and Vaughan, 1990). This suggests that other factors in addition to plasticity, such as permeability, may be more relevant to explain the soil behaviour.

6.3.2.4 The role of permeability on strain development

The pore pressure equalisation tests on the TC and PO samples indicate that the soil behaviour is affected by permeability. This effect is particularly apparent on the less permeable TC samples, as indicated by the higher degree of deficiency between

the applied back pressure and the soil pore pressure response (differences are up to 20 kPa for TC sample and 2 kPa for PO samples during tests up to the highest stepped reinflation rate at 100 kPa) (Figure 6.34). The direct impact of permeability has been indicated by the systematic changes of void ratio under stepped pore water pressure increases (Figure 6.21).

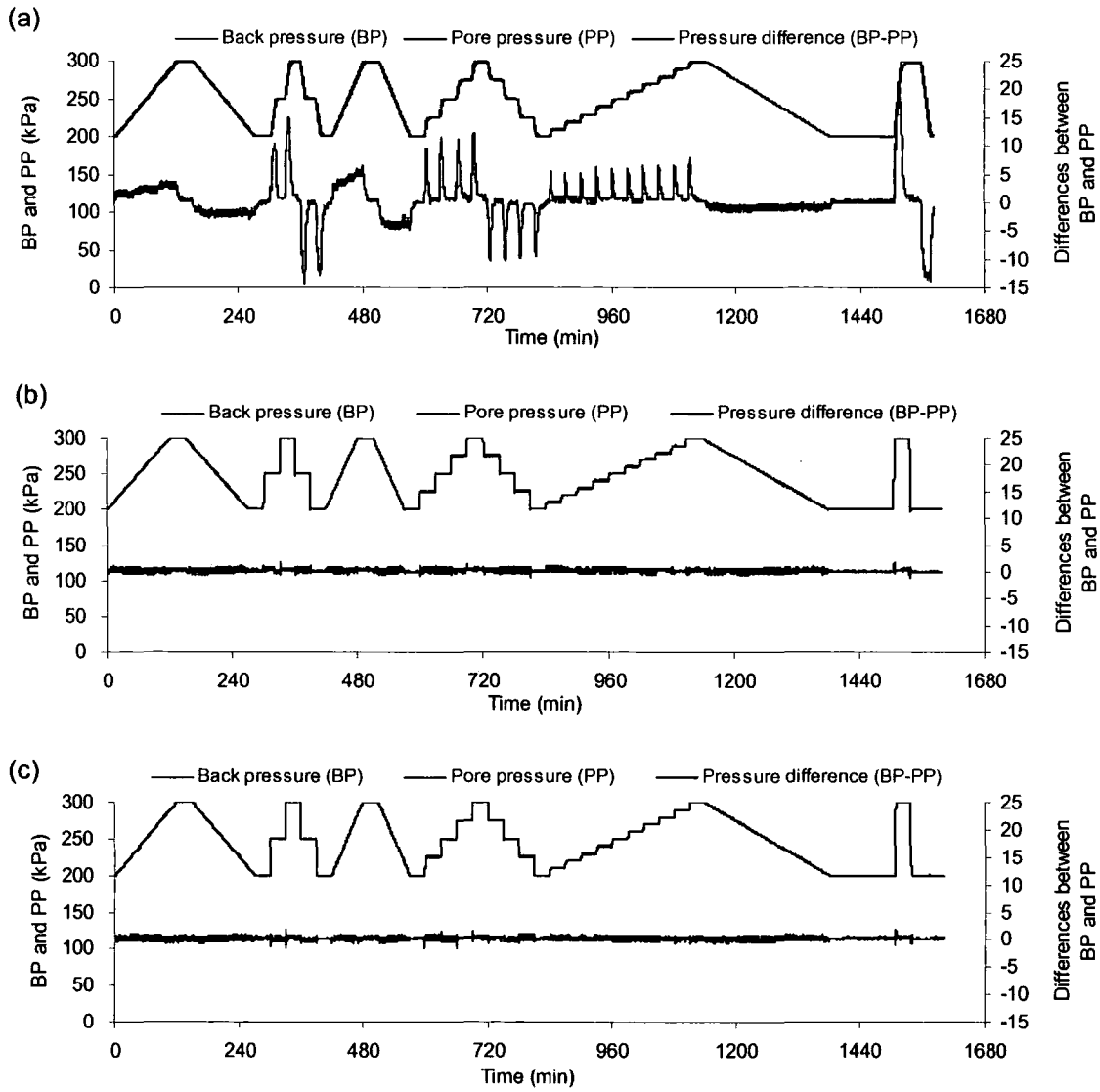

Figure 6.34 Pore pressure equalisation test on samples: (a) TC25; (b) PO18; and (c) PO32

The influence of permeability on plastic behaviour is clearly reflected during the stepped reinflation tests in two key patterns (Figure 6.35). For the relatively less permeable soils (the TC samples), the difference between the pore pressure increase experienced within the sample and the applied back pressure increase is larger at higher rate of pore water pressure (Figure 6.34). This probably affects the strain in two ways: (1) a more gentle $\varepsilon - time$ slope during the stepped increase of pore water pressure, and (2) the rate of strain will decrease rather than being constant when the

new pore pressure level is held over time (i.e. represented by the solid line in Figure 6.35). The effects can be illustrated with reference to the results from a 10 kPa stepped reinflation test (Figures 6.36a, 6.37a). During the 10 kPa stepped reinflation, the sample volume increased as the pore fluid was pushing through the sample and resulted in a corresponding axial strain (section 6.2.2). However, the increase of strain for the less permeable TC samples would be less immediate than the applied stepped rate as the 10 kPa reinflation had not yet reached the middle of the sample. When pore water pressure level was held constant, the pressure distribution process continued but the increase of strain was slower as the increased pore water pressure (i.e. 10 kPa) was distributing to the middle of the sample. The process of pore water equalisation within the less permeable TC samples is suggested by $\varepsilon - time$ curves composed of a series of gentle slopes (Figure 6.36a) and the "smoother" peak-trough pattern in plots of $\dot{\varepsilon} - time$ (Figure 6.37a).

For the relatively more permeable soils (like the PO samples), a change in pore water pressure resulted in a more immediate and sharp change in plastic strain (Figure 6.36b) and strain rates (Figure 6.37b) as the increased pore water pressure distributed throughout the sample more quickly. In other words, permeability appears to determine the slope of $\varepsilon - time$ and the $\dot{\varepsilon} - time$ plots. However, the amount of strain and strain rate at each stepped reinflation is more likely to be controlled by the plastic properties of the soils, depending on the stress state.

Regarding both samples, a constant strain rate, which would be expected in perfectly plastic materials under constant stress after yield (Summerfield, 1991), is not common between each step (when pore water pressure is held constant) probably because both the TC and PO samples are not highly permeable, given their high percentage of fines (Table 5.4).

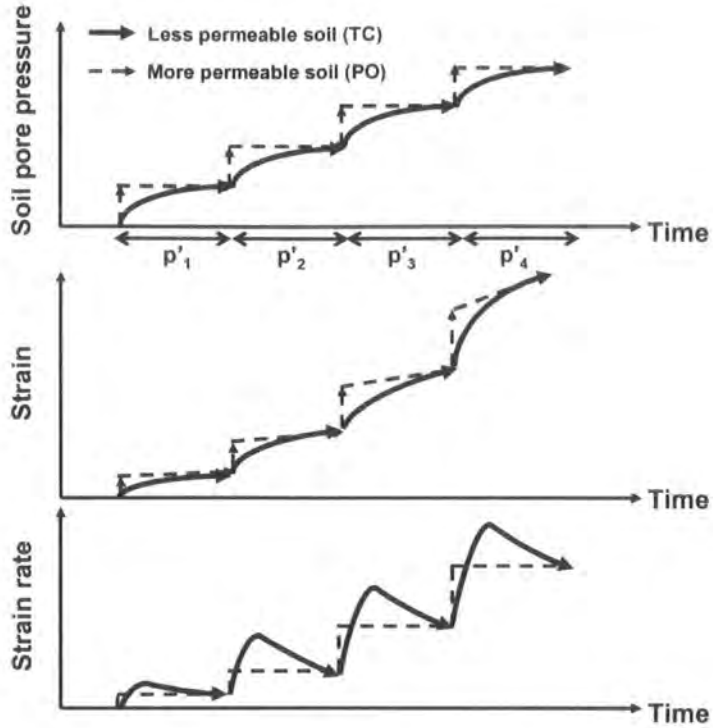

Figure 6.35 Schematic diagrams showing plastic behaviour for soils of higher permeability (dashed lines) and lower permeability (solid lines) under stepped rate reinflation tests

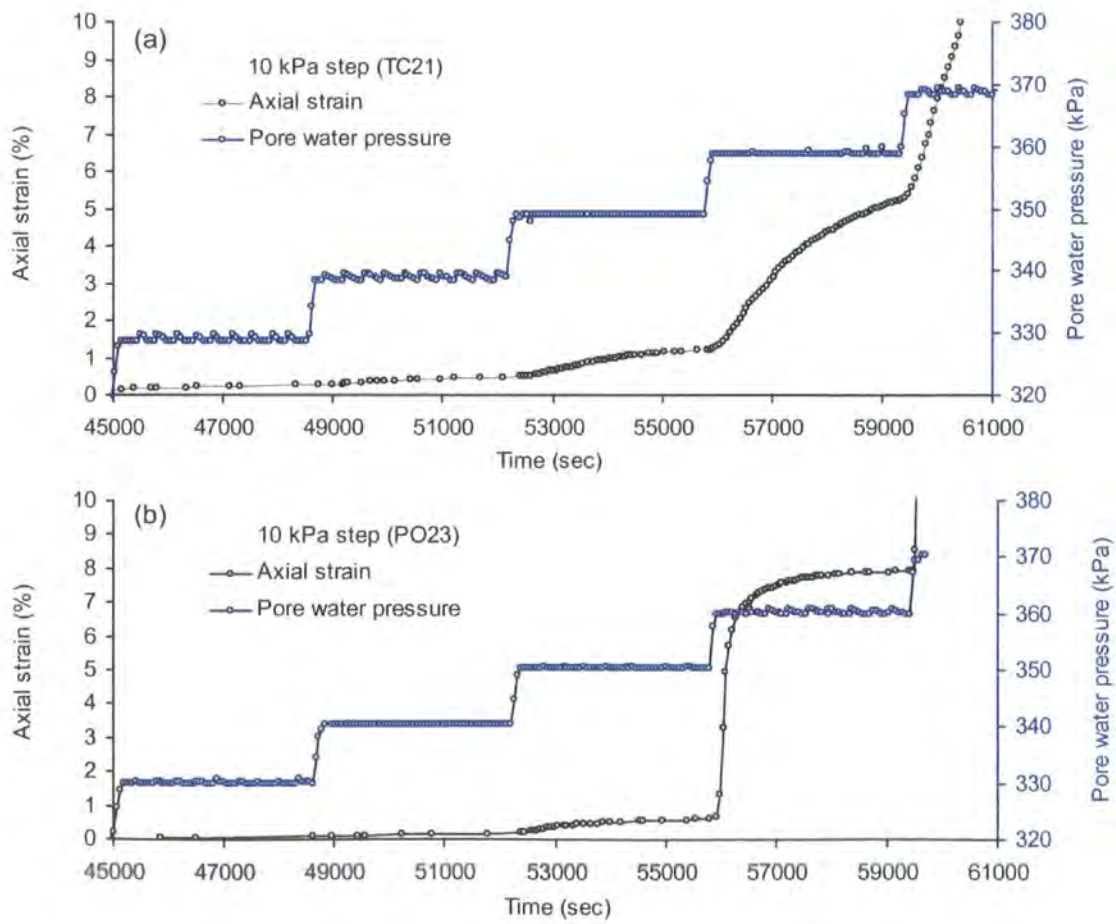

Figure 6.36 Typical strain development over time during the stepped reinflation tests for (a) the less permeable TC and (b) the more permeable PO samples

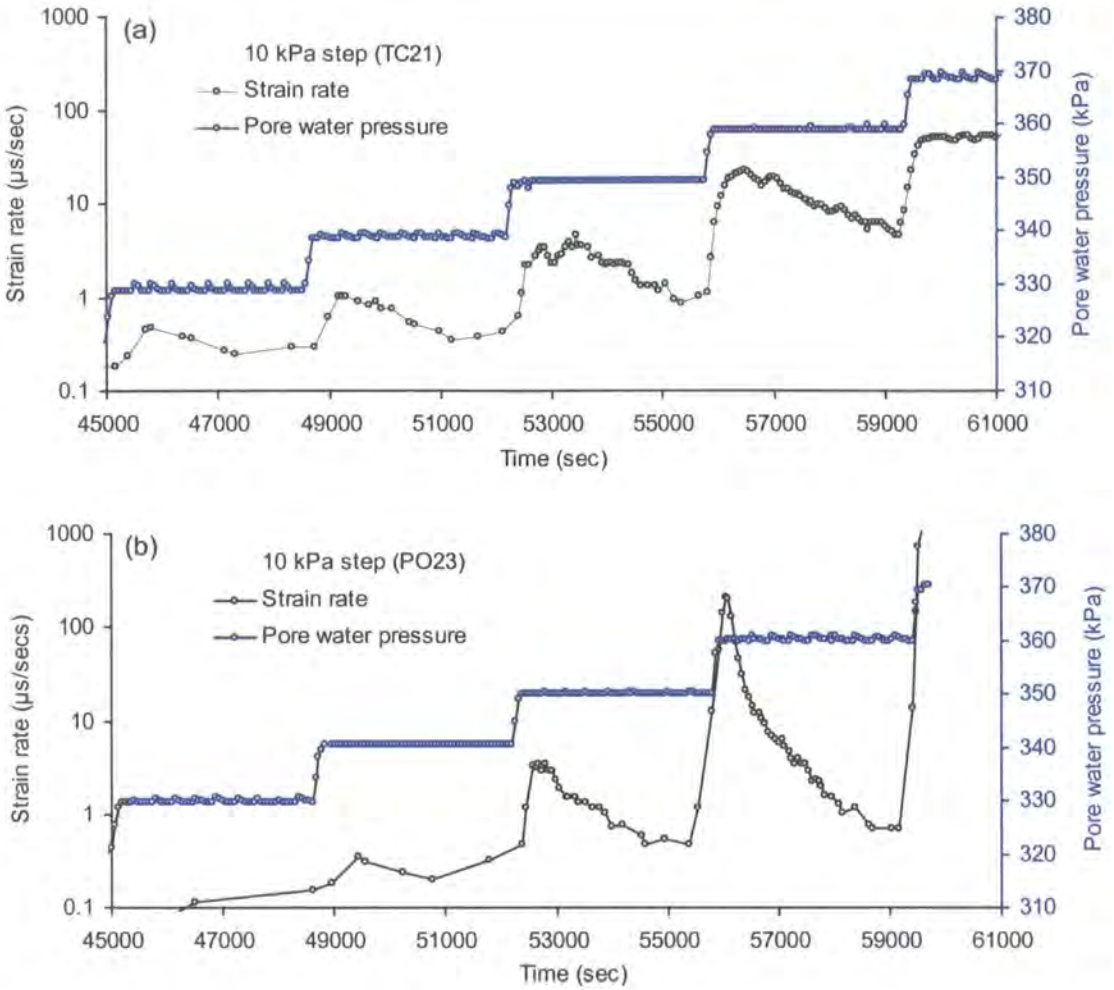

Figure 6.37 Typical strain rate development over time during the stepped reinflation tests for (a) the less permeable TC and (b) the more permeable PO samples

However, as the pore water pressure increases, the sample dilates (section 6.2) and becomes increasingly permeable. As a result, a sharper change in strain and constant strain rates in response to the change in mean effective stress becomes more apparent. Such a transition has been observed in Figure 6.38 for both the TC and PO samples. The transition of the $\varepsilon - t$ patterns is particularly remarkable in sample PO38 as the axial strain becomes increasingly responsive to the change of pore water pressure towards failure (Figure 6.39). This is also evident in the changing pattern of strain rate (i.e. from "decreasing" to being "constant") which has been clearly observed during the reinflation process in the TC and PO samples (Figure 5.50). The transition patterns in $\varepsilon - time$ and $\dot{\varepsilon} - time$ in association with the increasing level of permeability are schematically presented in Figure 6.40.

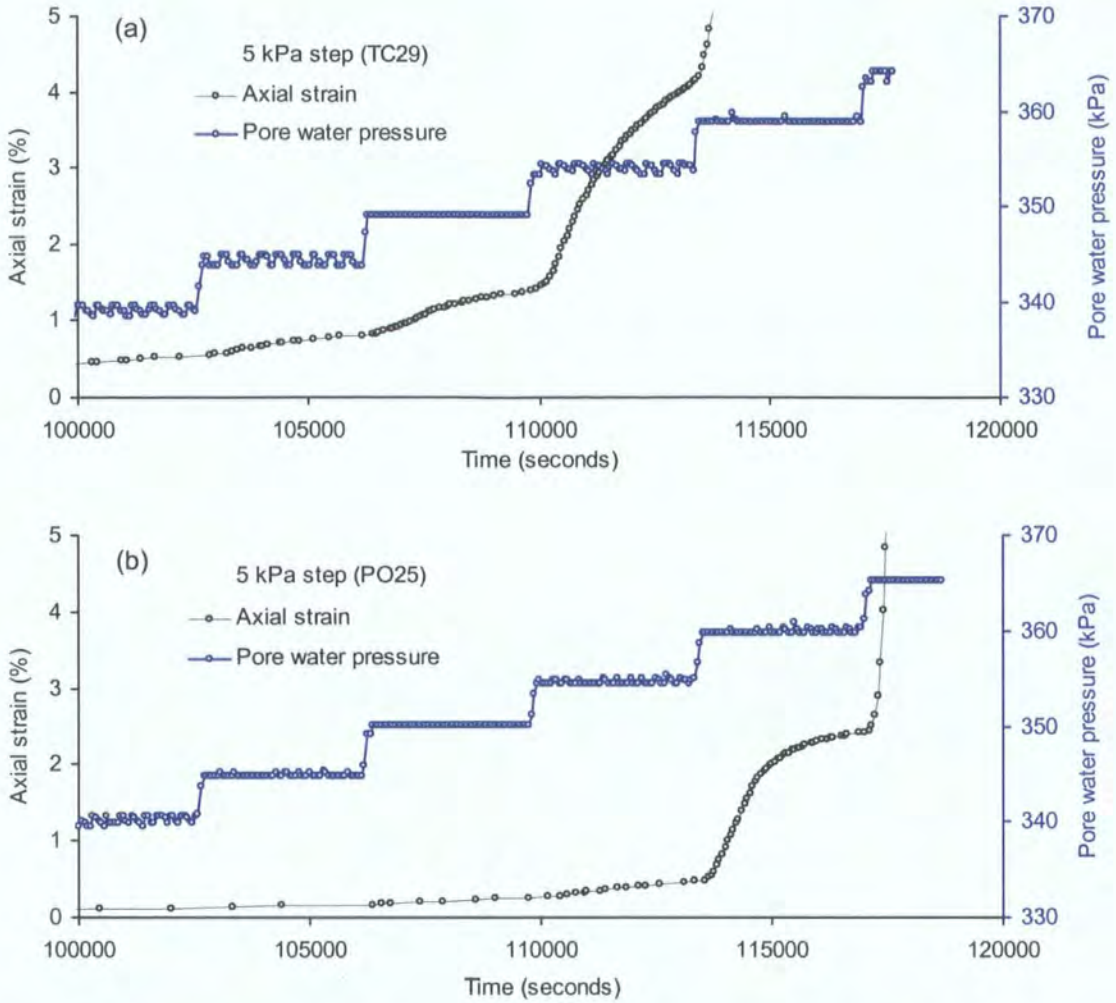

Figure 6.38 The transition from the humpy to more rectangular $\varepsilon - time$ pattern under stepped reinflation test for (a) TC and (b) PO samples

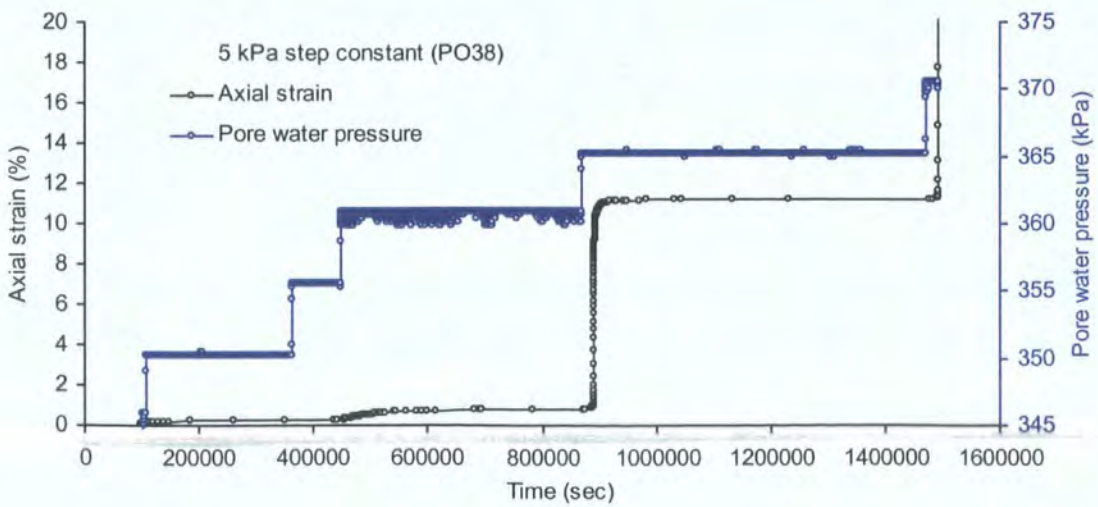

Figure 6.39 The transition from the humpy to more rectangular $\varepsilon - time$ pattern under stepped reinflation test for sample PO38

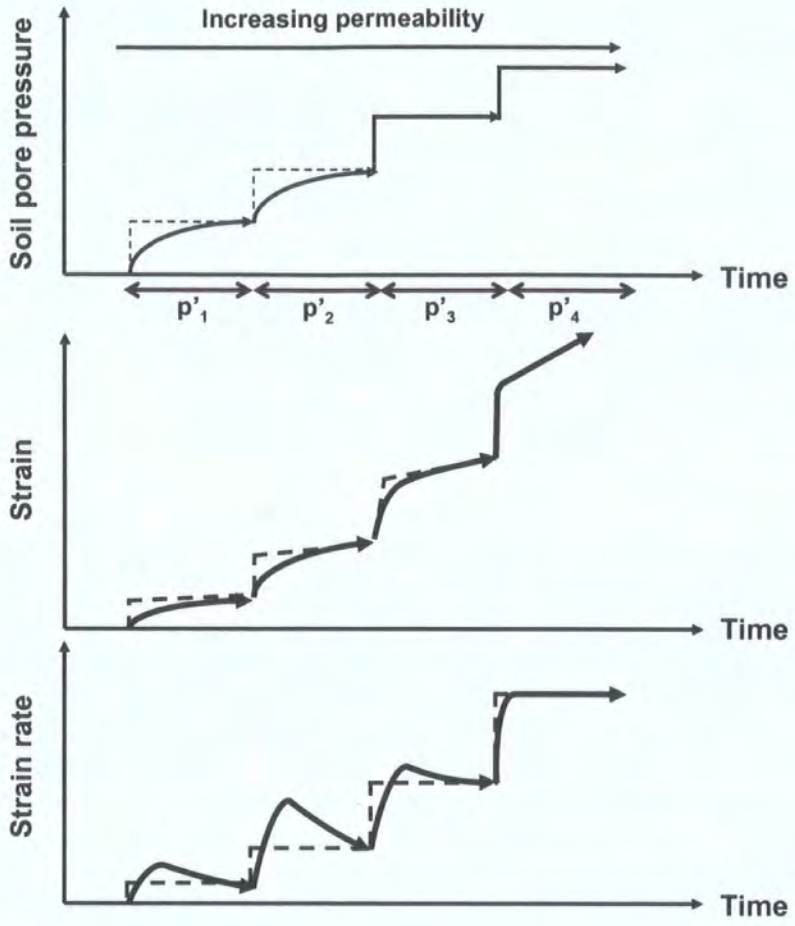

Figure 6.40 Schematic diagrams showing the transition pattern of plastic behaviour with increasing permeability under stepped reinflation test for an individual soil sample

6.3.3 The role of creep

6.3.3.1 Comparison between plastic deformation and creep

A clear distinction has to be made between plastic deformation and creep before evaluating the possibility of the latter in contributing the accumulated strain or strain rate. Figure 6.41 and Figure 6.42 show the fundamental differences and similarities between plastic and creep deformation on the basis of time, under constant stress state. The time dimension also allows examination of the evolution of soil behaviour during the reinflation test.

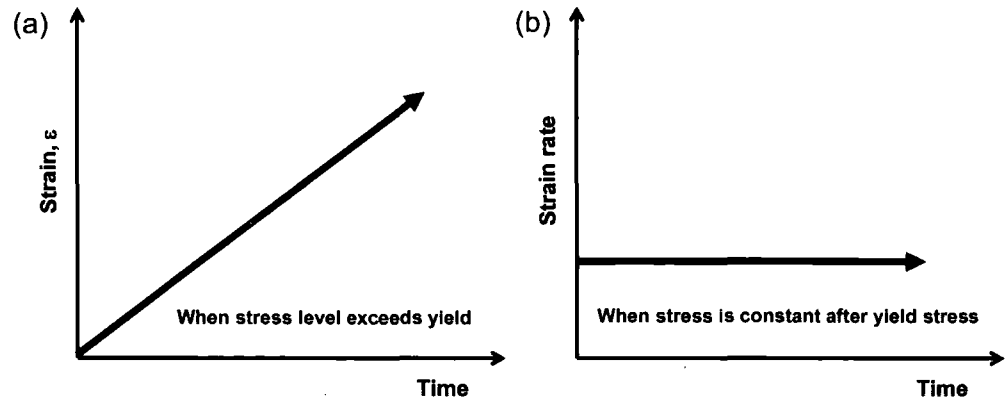

Figure 6.41 Plastic deformation at constant stress, expressed in plots of (a) ε - time and (b) $\dot{\varepsilon}$ - time (after Summerfield, 1991)

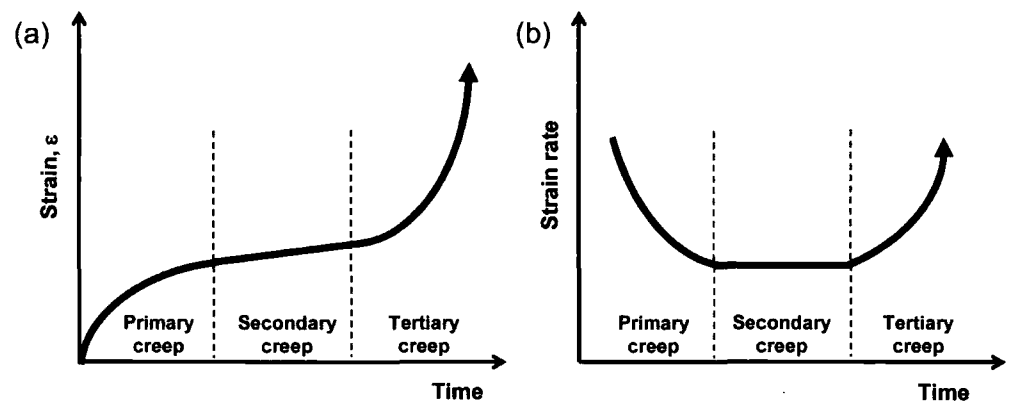

Figure 6.42 Three phase creep at constant stress in plots of (a) $\varepsilon - time$ and (b) $\dot{\varepsilon} - time$ (after Varnes, 1983)

For plastic deformation, plastic strain increases at a constant rate after reaching the yield stress when the stress is constant (Summerfield, 1991) (Figures 6.41). In contrast, creep deformation involves an increase of strain at a decreasing rate (primary creep) and increasing strain rate (tertiary creep) respectively (Varnes, 1983; Fell *et al.*, 2000) (Figures 6.42), features which are not found in plastic deformation.

However, secondary creep is characterised by a constant strain rate, similar to plastic deformation under constant stress conditions. Hence, a constant strain rate could well be the result of either plastic deformation or secondary creep or both under constant stress conditions. Nevertheless, the existence of secondary creep may be subjected to debate as the typical creep curves derived from some of the previous research show an inflection point instead, characterized by relatively constant strain and strain rate for a very short period of time (Varnes, 1983). This is particularly true for soils, which rarely show a long period of secondary creep (Kuhn and Mitchell, 1993).

This period has been regarded as the result of the combination of primary and tertiary creep processes (Fell *et al.*, 2000).

In short, the above discussion demonstrates that, under constant stress conditions, it is theoretically possible to identify the unique contribution of primary and tertiary creep by noting the decreasing and increasing strain rates respectively. However, the contribution of constant strain rates from secondary creep and plastic deformation is indistinguishable.

6.3.3.2 Testing for creep under the stepped reinflation test

Having noted the possibilities and limitations, there was one more complexity which made the evaluation of creep from the reinflation process particularly challenging: the change of mean effective stress during the reinflation process, meaning that the required constant stress conditions for the evaluation were not always present. In other words, it would be misleading to test for the presence of creep using the $\varepsilon - time$ or $\dot{\varepsilon} - time$ data directly from the reinflation tests, because the time dimension also incorporates an increase of pore water pressure (i.e. changes in the stress state).

However, the reinflation test has indeed provided a classic testing condition similar to the standard creep test, which is, testing below the maximum strength of the sample. Moreover, the evaluation of creep is possible for the stepped reinflation tests at the time periods where both p' and q are kept at the same level (i.e. constant stress conditions). In fact, the stepped reinflation test can be regarded as a "multi-stage creep test", as the soil sample has been subjected to constant stress conditions over time at more than one level of its maximum strength (or peak stress).

6.3.3.3 The hypothesis

The evaluation of creep under the stepped reinflation test is illustrated in Figure 6.43. At the start of the reinflation (p'_{dis} , q), or point (a), the sample was subjected to the lowest amount of load, say, deviatoric stress at 20% of its maximum strength (or peak stress). The stress conditions were held constant at (p'_{dis} , q) over a fixed period of time (1 hour), before the next stepped increase in pore water pressure. This was the first time period which allowed the evaluation of creep. At this low stress level, primary creep was most likely to occur and the strain rate might decrease to zero (Varnes, 1983) (Figure 6.44a). After one hour, pore water pressure was increased instantly in

step and reached point (b). At this point, the magnitude of the applied maximum stress was increased, say to 40%, as it was closer to the failure envelope, although the deviatoric stress remained unchanged. Therefore, the creep phase might change from primary to secondary showing an increase of strain at a constant strain rate under the constant stresses at p'_1, q_1 over the hour (Figure 6.44b). At point (c), the sample was under a higher percentage of peak strength, say 80%, which might facilitate the occurrence of tertiary creep with accelerating strain rates (Figure 6.44c) towards the final failure at point (d). This hypothetical model illustrated the ideal presence of three phase creep in relation to the magnitude of the applied stress during the reinflation test. However, some earth materials may exhibit one or two creep phases only (Varnes, 1983; Fell *et al.*, 2000).

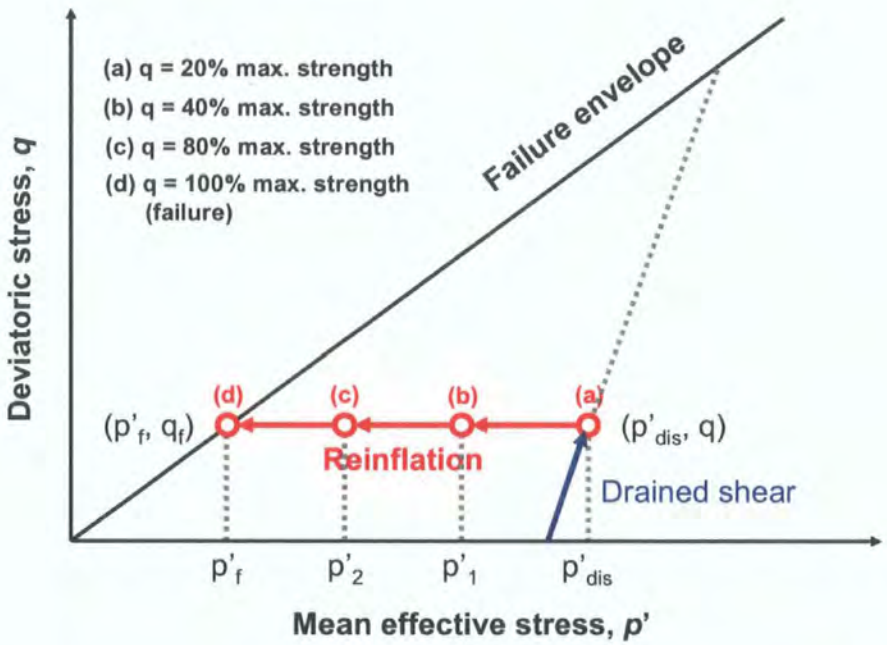

Figure 6.43 The evaluation of creep under the stepped reinflation process: (a)-(d) represent the constant stress conditions between each stepped reinflation with different levels of maximum peak strength of the sample

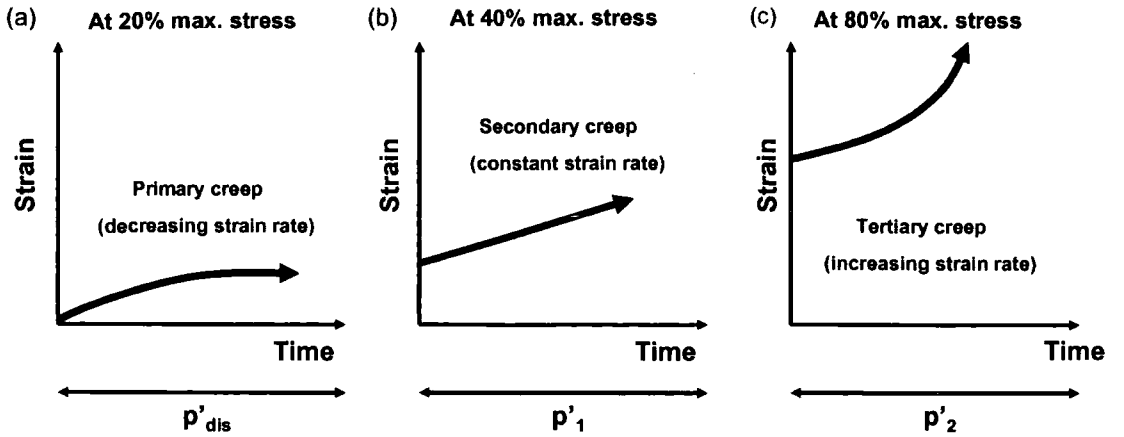

Figure 6.44 The ideal development of the three creep phase at constant stress conditions over time under stepped reinflation: (a) primary creep; (b) secondary creep; (c) tertiary creep

6.3.3.4 The analyses

The typical $\varepsilon - time$ and $\dot{\varepsilon} - time$ behaviour and the corresponding void ratios of the TC and PO samples during the time periods under constant stress conditions (i.e. constant p', q) at various p' levels towards failure are shown in Figures 6.45 and 6.46 respectively. Strain and strain rates are presented in logarithmic scale for clarity. The figures do not include the strain and strain rate development during the time periods when the pore water pressure was increasing stepwise, as this involved a change in the stress state which was not relevant for the evaluation of creep. The time periods at $p' \geq 93$ kPa (TC sample) and $p' \geq 83$ kPa (PO sample) were not included as almost no strain developed.

A complicated strain behaviour was revealed in both the TC and the PO samples under the constant stress conditions, which could not be fully explained by the three phase creep theory. However, it may be largely explained with reference to the soil permeability conditions and plastic behaviour, as suggested in section 6.3.2, instead of creep deformation.

Firstly, the larger extent of decreasing strain rate (the "primary creep" behaviour) was more likely to relate to the increasing permeability within the sample through the reinflation process, as indicated by the non-linear increase in the void ratio (Figures 6.45c, 6.46c). The "primary creep", therefore, was an indicator of the effectiveness of the pore pressure equalisation process, but not the underlying cause for the strain development.

Secondly, the initial increase of strain rate (the "tertiary creep") preceding the "primary creep" could be a direct result of the stepped increase of pore water pressure which had not yet been fully equalised within the sample, even after the target constant stress state was reached. This may explain why this phenomenon was more often found in TC samples which were less permeable (Figure 6.45b). Hence, the "tertiary creep" observed in both samples appears to be a permeability indicator as well.

As for the fluctuating but relatively constant strain rates just before failure within samples TC29 (at p' = 73 kPa) (Figures 5.50a, 6.45b) and TC21 (at p' = 63 kPa) (Figure 5.50b), their behaviour was likely to be related to secondary creep and/or plastic strain exhibited under a permeable condition.

The increasing strain rates towards the final failure exhibited within most of the TC and PO samples were probably a result of the stepped reinflation reaching a critical pore water pressure threshold. Typical examples include samples TC27 (Figure 5.45a), TC29 (Figure 5.50a), PO23 (Figure 5.47) and PO12 (Figure 5.49b), in which the samples accelerated to failure shortly after the stepped reinflation. However, this explanation could not fully explain the intriguing behaviour of samples TC21 (Figure 5.50b) and PO38 (Figure 5.53), as their strain rate were kept initially constant (secondary creep/plastic strain) when the critical pore water pressure level was reached (i.e. p' = 63 kPa), followed by acceleration towards failure under constant stress conditions (p' = 63 kPa, q = 100 kPa). The increasing strain rates under constant stress conditions towards failure appear to be true tertiary creep (section 2.5.1) which is associated with the internal remoulding within the samples. The tertiary creep phase for samples TC21 and PO38 initiated at around 61000 seconds (Figure 5.50b) and at time 11:50:03 (Figure 5.53) respectively under constant stress state.

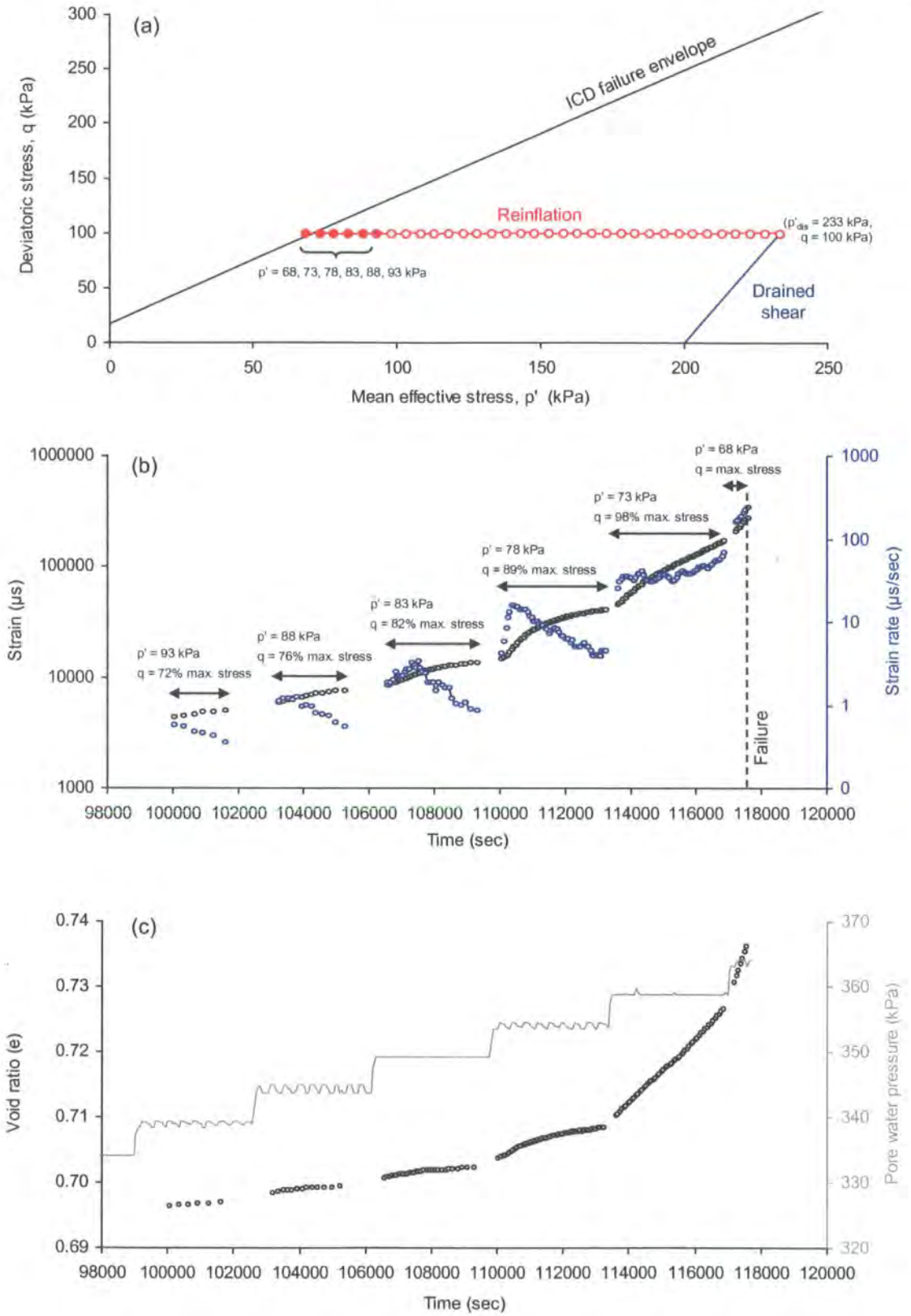

Figure 6.45 Typical strain development at constant stress conditions under stepped reinflation exhibited within TC samples (shown by TC29), in plots of: (a) $p'-q$; (b) $\varepsilon-time$ and (c) $e-time$ at p' = 68, 73, 78, 83, 88, 93 kPa respectively (back pressure = 200 kPa)

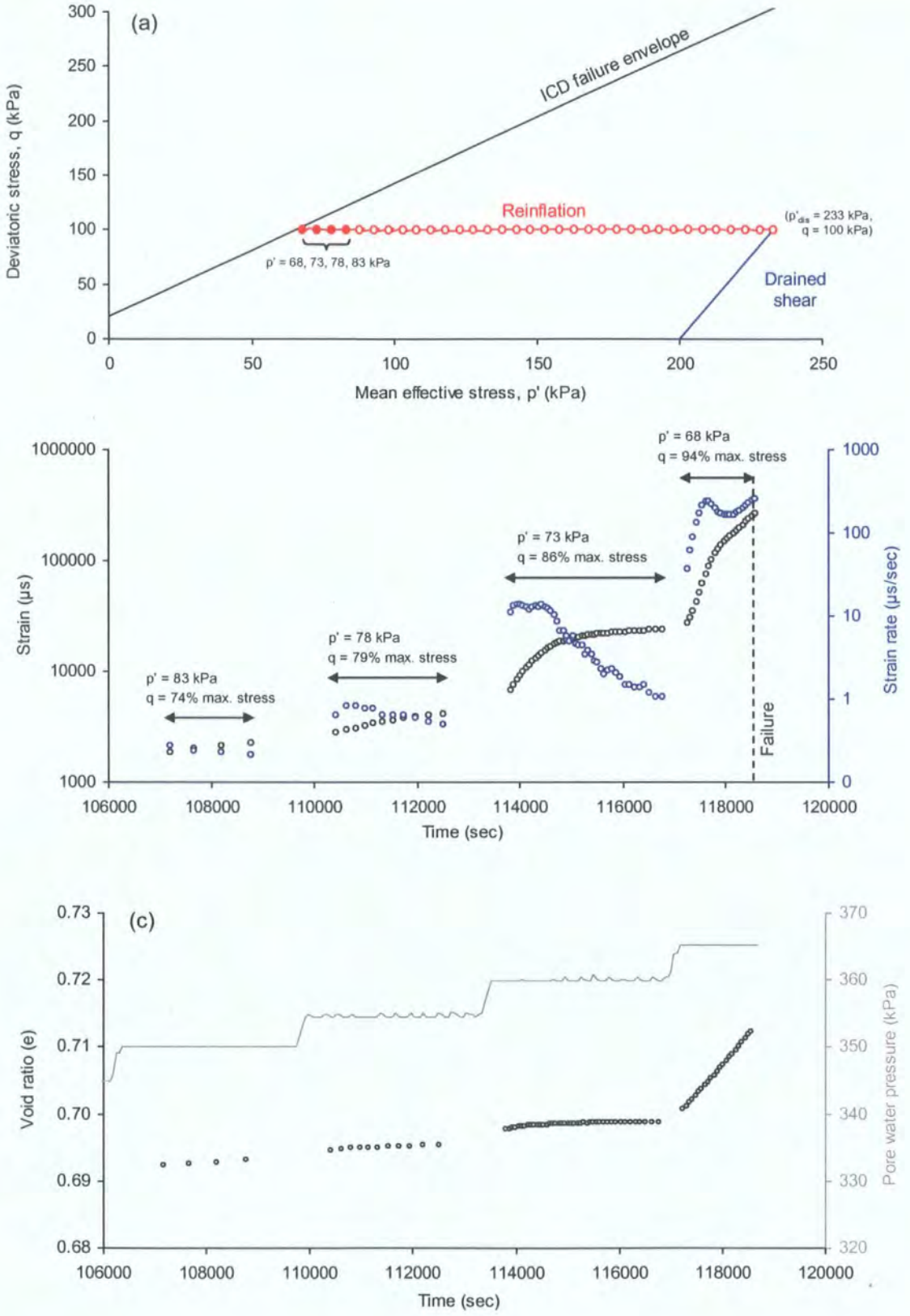

Figure 6.46 Typical strain development at constant stress conditions under stepped reinflation exhibited within PO samples (shown by PO25), in plots of: (a) $p'-q$; (b) $\varepsilon-time$ and (c) $e-time$ at p' = 68, 73, 78, 83 kPa respectively (back pressure = 200 kPa)

6.3.3.5 Evaluating the creep models through the reinflation process

The reinflation test process appears to have clarified the creep phenomenon of landslides observed in Terzaghi (1950). The results from the reinflation tests on the weathered samples suggest that progressive failure observed by Bjerrum (1967) is not applicable. The three phase creep model (Varnes, 1983) in material science also needs to be modified to represent the deformation mechanism for plastic materials. The slider-block friction model for landslides (Helmstetter *et al.* 2004) cannot explain the fluctuating strain rates exhibited by the samples under the constant stress state.

(a) Terzaghi's (1950) creep model

The evaluation of creep through the stepped reinflation process may have clarified the underlying deformation mechanism for the creep phenomenon of landslides described by Terzaghi (1950) (Figure 6.47).

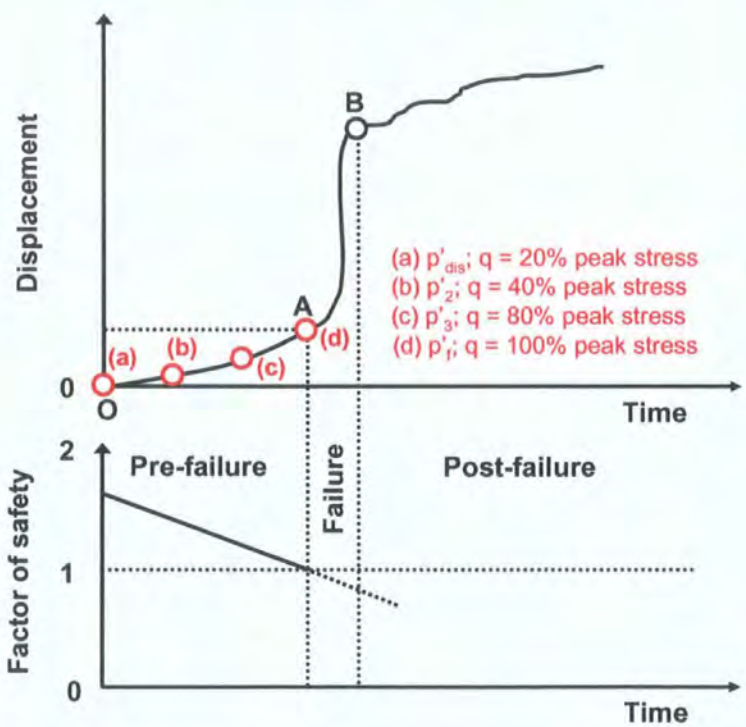

Figure 6.47 Synthesis of the stepped reinflation and Terzaghi's (1950) model

The stress conditions at points (a) to (c) during the reinflation process (Figure 6.43), are likely to represent "creep" period OA in Terzaghi's (1950) model (Figure 6.47) where the Factor of Safety is above 1. At point (a), the start of the reinflation process, no displacement is shown. This is probably because the soil is subjected to very low stress (e.g. 20%) relative to its maximum strength. The corresponding Factor of Safety

is the highest given the highest ratio of mean effective stress to shear stress (p'_{dis}/q). However, an increased pore water pressure under constant shear stress (the field condition) would result in displacement leading to points (b) and (c), as the soils are subjected to a higher load, for example, 40-80%. During this pre-failure period, deformation would be either brittle or plastic depends on the material property, which can be revealed by the respective linear and asymptotic trend in $\Lambda - p'$ or $\Lambda - t$ space. The final failure occurs at point (d) where the Factor of Safety is 1, as the sample reaches its maximum strength (i.e. 100% peak stress). The analyses demonstrate that the mechanism underlying Terzaghi's (1950) pre-failure creep phase appears to be deformation-dependent rather than time-dependent as misleadingly implied from Figure 6.47.

(b) Bjerrum's (1967) progressive failure model

The progressive failure described by Bjerrum (1967) in cohesive materials/ overconsolidated slopes, associated with a significant drop of resistance from peak to residual strength, was not observed within the intensely weathered TC and PO samples. The weathered samples did not show a lack of drop of resistance from the peak to residual strength (Figures 5.13, 5.17). This could be due to the low cohesive strength, as revealed from the small c' intercept of the failure envelopes (Figures 5.9, 5.15, 5.27). Shear surface development was not evident (Appendices 1c, 2). Moreover, the "elastic strain energy" required to advance progressive failure (Bjerrum, 1967) was absent for the weathered samples, as evident from the elasticity evaluation (section 6.3.1). Instead, plastic behaviour has been clearly reflected by the asymptotic trend in $\Lambda - t$ space during the reinflation tests, exhibiting acceleration without catastrophic movement (Figures 5.37, 5.43, 5.57), which are consistent with observations in shallow landslides (Kilburn and Petley, 2003). The findings imply that strain development within the weathered samples is unlikely to be related to the progressive failure mechanism.

(c) Varnes (1983) three phase creep model

The classic form of the three phase creep curve fails to fully characterise the movement patterns within the plastic weathered samples during the reinflation tests. The primary creep phase, which was dominated by the local hardening mechanism of crack growth (Main, 2000), was absent. The associated development of microcracks is not necessary for plastic deformation within the intensely weathered TC and PO materials, as they are probably already highly microfractured or become structureless

by the weathering process. The weathering-induced microcracking process was confirmed by Irfan (1999), who observed that the residual volcanic soils in Hong Kong showed a complete loss of the rock fabric with microcracks and secondary pores. The initial zero strain rate or little strain development is more likely to be attributed to the interlocked inter-particle contacts below the plastic yield stress (Type 1) (section 6.2.1).

The secondary creep phase characterised by relatively constant strain rates over time, which may also well be the plastic deformation process (as they are indistinguishable under constant stress conditions), appears to dominate throughout the reinflation process after the yield stress is reached. The associated strain and strain rate development in the light of plastic deformation mechanism has been evaluated in section 6.3.2. However, it may also be explained with reference to the interactions between soil particles (section 6.2.1). This phase appeared to be characterised by the stepped-like increase in void ratio, indicating localised sliding (Type 2). The sliding process was facilitated by shear as the increased pore water pressure reduced the contacts between soil particles. Similar to the micro-cracking process, the localised sliding could be advanced as the stress would transfer to the remaining interlocked contacts between the particles leading to a generalised sliding.

The rapid acceleration towards failure under constant stress conditions is likely to be associated with generalised interparticle sliding (Type 3) associated with the internal remoulding within the soil sample under shear (section 6.2.1). Pore water pressure plays a less significant role. This appears to provide an explanation for the intriguing accelerating behaviour for sample TC21 (Figure 5.50b) and PO38 (Figure 5.53), which occurred long after the pore water pressure was increased and could not be readily explained by the increasing permeability or plastic strain. The explanation appears to be supported by the creep theory proposed by Kuhn and Mitchell (1993) who attribute creep phenomenon to the rearrangement or alignment of the soil structure by a viscofrictional sliding mechanism.

Therefore, the pre-failure movements for plastic materials are likely to be characterised by secondary creep/plastic deformation in association with localised sliding, and the tertiary creep phase dominated by generalised sliding. Primary creep is absent which appears to be more related to brittle failure processes.

(d) Helmstetter *et al.* (2004) slider-block friction model

The state- and velocity-dependent friction law-based slider-block model may have suggested an alternative physical explanation for the accelerating phase for brittle failures (e.g. Vaiont landslide) but its application in ductile material is unclear (Helmstetter *et al.*, 2004).

A major limitation of the slider-block model is that the friction parameters alone cannot explain the fluctuating (acceleration/deceleration) landslide behaviour (e.g. La Clapière), particularly regarding the deceleration phase which is regarded as a "stable velocity-strengthening sliding regime" (Helmstetter *et al.*, 2004: 1; Sornette *et al.*, 2004). Similarly, Iverson's (2005) model also did not consider the stick-slip movements. The results from the stepped reinflation experiments showed that the decelerating behaviour was unlikely to be explained by an increase in friction (as implied from the slider-block model) or the "negative pore pressure feedback" associated with diminishing pore water pressure due to dilation (Iverson, 2005: 1) as the stress state was held constant. In addition, deceleration could occur just before the final failure, particularly within the less permeable plastic materials (e.g. Figure 5.51). Therefore, the deceleration behaviour is more likely to imply a "conditionally stable" regime. It was also evident that accelerating behaviour could occur under the constant stress state (i.e. state independent) towards the final failure (e.g. Figures 5.50b, 5.53).

The mechanism of subcritical crack growth suggested in the rotational slider-block model for the accelerating creep behaviour (Brückl and Parotidis, 2005), which is similar to the crack growth model for cohesive materials proposed by Petley *et al.* (2005b), is not evident within the plastic TC and PO residual soils. No clear shearing surface has been formed by the crack growth process as the stress is distributed throughout the samples during the reinflation (Appendices 1c, 2).

Iverson's (2005) slider-block model has comprehensively incorporated the effects of pore pressure and volumetric behaviour to explain the changing rate and styles of landslide motion. However, it could not explain how the normally consolidated (i.e. loose) TC and PO residual soils, which exhibited contractive behaviour under shear (Figure 5.18), could dilate under constant stress conditions (section 6.2.2).

6.4 Implications for landslide movement

The analyses of the behaviour of plastic residual soils from the laboratory tests suggest that rainfall-induced landslides in these materials undergo three stages towards failure, namely Stage 1 (stable), Stage 2 (conditionally stable) and Stage 3 (unstable), which parallels the scheme proposed by Crozier (1986). The results from this research further indicate that the underlying mechanics of the stages are determined by the inter-relationships between the external stresses (pore pressure level, rate of pore pressure increase) and the soil properties (strength, plasticity, permeability). The process is presented in Figure 6.48. Most importantly, each stage is characterised by a distinctive style and rates of movements. The implications of the results are supported by field observations of shallow rainfall-induced landslide movements in plastic materials.

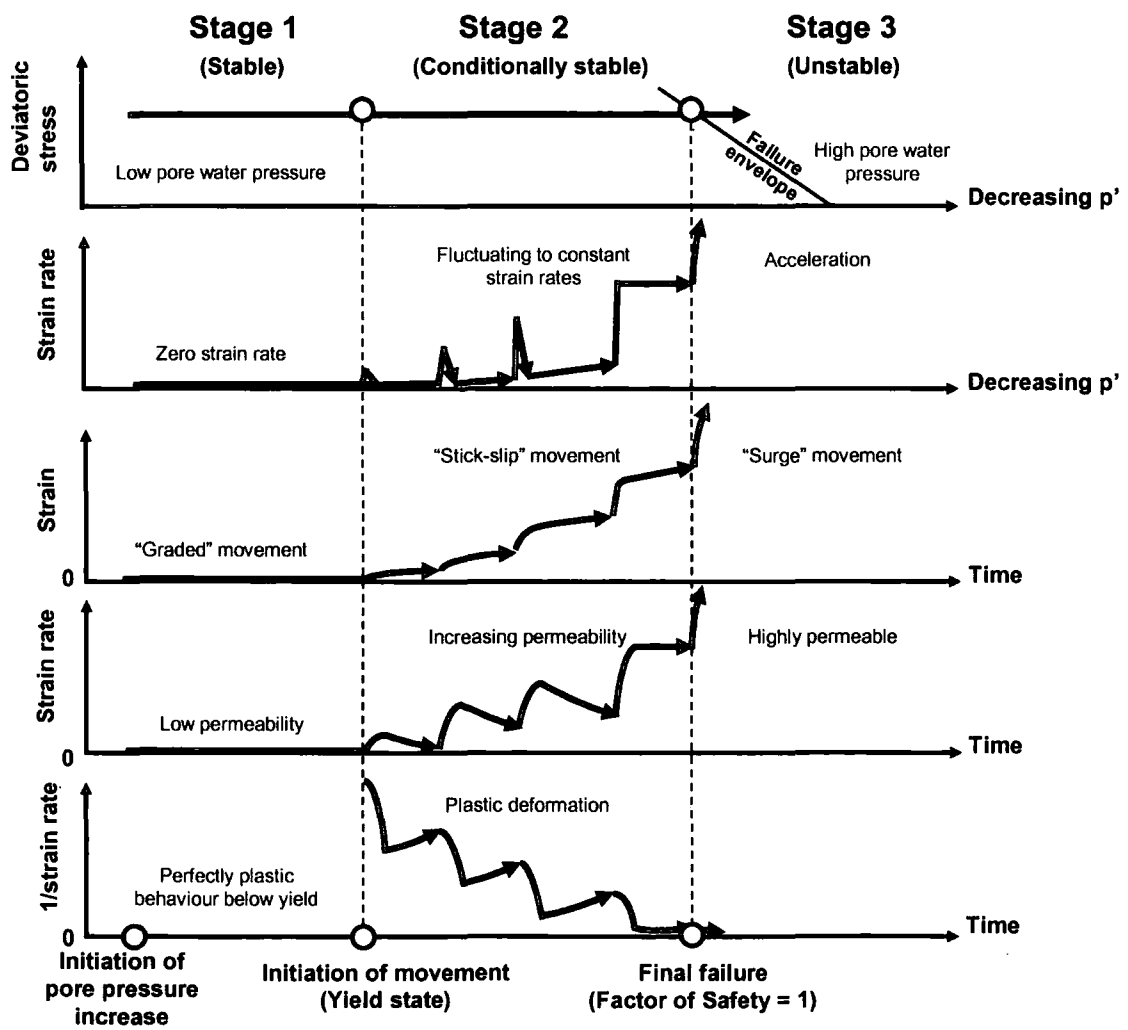

Figure 6.48 Schematic diagrams illustrating plastic deformation mechanisms underlying rainfall-induced landslide movements towards failure on residual soils, at different stress state through time with increasing permeability

6.4.1 Stage 1

Stage 1 represents the stable state of the slope in plastic materials. As pore water pressure increases, the resultant increase of pore fluid begins to push apart the interparticle contacts within the soil and enables them to push and climb over each other (Type 1 behaviour) (Figures 6.16, 6.17a). Slope movement is close to zero, and velocity is too low to be detected. This is probably because the soil strength (which is indicated by the mean effective stress), though decreased, remains high relative to the shear stress. In other words, the yield strength (or yield stress) has not been reached (Selby, 1993). The soil particles are largely interlocked and the slope is highly resistant to deformation (i.e. non-responsive) under any rates of pore water pressure increase.

The experimental implications are supported by the non-responsive slope movement behaviour observed in the field under rainfall (Table 6.2). For example, recorded surface movements were less than 1 cm from January to June in 2003 (the dry season) at the 626 slope failure in Taiwan during the period before reaching the threshold groundwater level (Chang *et al.*, 2005) (Figure 6.49a). Little cumulative displacement was found in July, 2000 at the Tsubayama landslide in Japan (Hong *et al.*, 2005) (Figure 6.49b). Interestingly, zero displacement was reported in a field experiment on a natural slope at Mt. Kaba-san in Japan which was being subjected to artificial rainfall for 4.5 hours at an intensity of 78 mm/hr (Hong *et al.*, 2005) (Figure 6.49c). The common cause for the lack of deformation could be related to the low level of pore water pressure which was below the yield stress of the slopes. This is indicated by the low amount of daily rainfall during the non-responsive period (Figures 6.49a, 6.49b). The presence of the yield threshold is very likely because the soil materials involved appear to be plastic due to their highly weathered nature (Table 6.2).

Table 6.2 Field examples of rainfall-induced landslides indicating Stage 1 movement behaviour

Landslide	Location	Materials	Movement period (Stage 1)	Reference
626 slope failure	Taiwan	Weathered sandstone, siltstone and shale or colluvium with fractured geologic structure	1/1/2003 - early-June, 2003	Chang *et al.* (2005)
Tsubayama landslide	Japan	Weathered and fractured psammitic and pelitic schist	7/7/2000-11/8/2000	Hong *et al.* (2005)
Mt Kaba-san landslide	Japan	Weathered disintegrated granite sand	Elapsed time 24620 – 24627 sec	Ochiai *et al.* (2004)

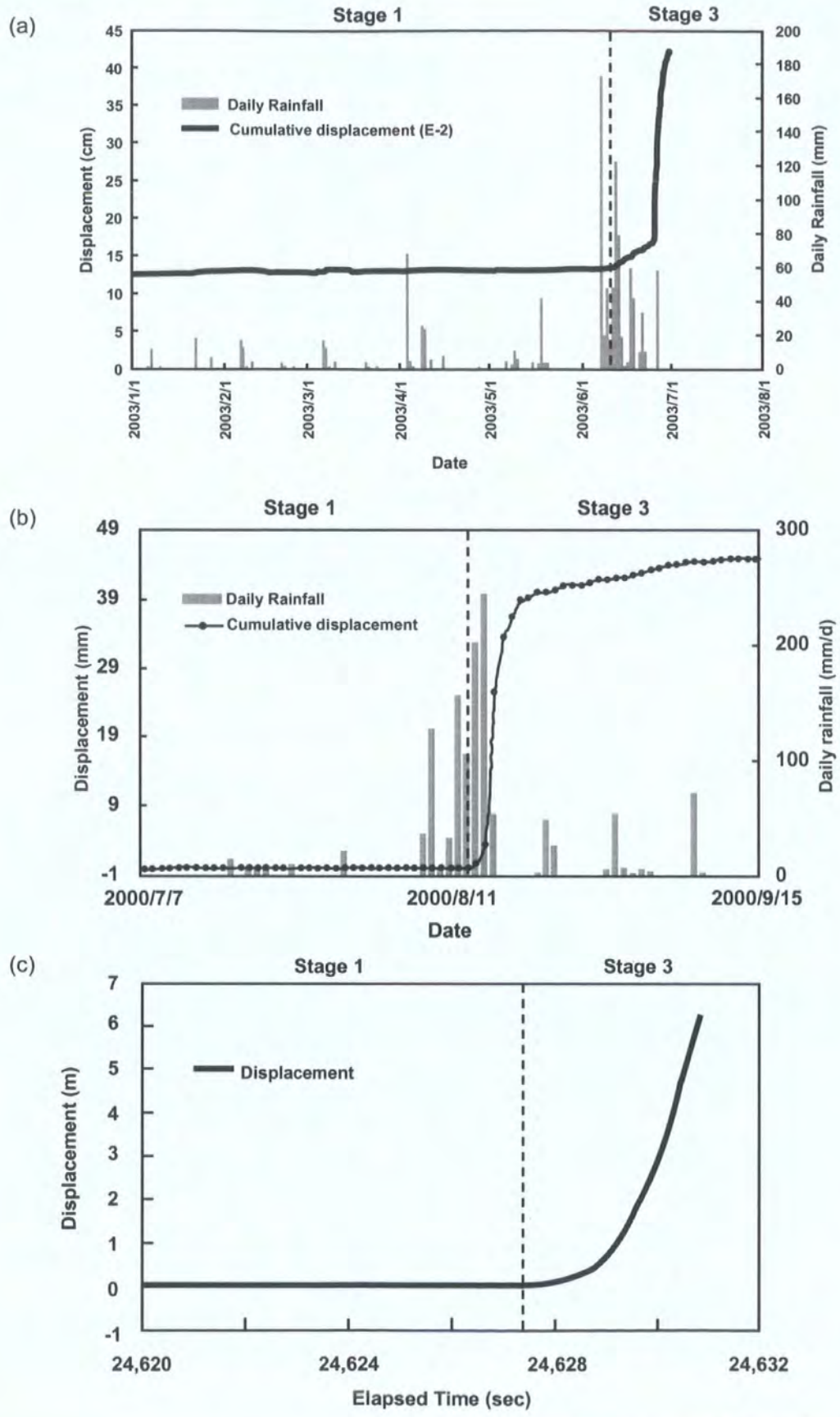

Figure 6.49 Graphs showing Stage 1 movements against time at (a) the 626 slope failure in Taiwan (after Chang *et al.*, 2005); (b) the Tsubayama landslide in Japan (after Hong *et al.* 2005); and (c) Mt Kaba-san fluidized landslide in Japan (after Ochiai *et al.*, 2004)

6.4.2 Stage 2

Stage 2 represents a conditionally stable slope. As the pore water pressure level increases and causes the plastic yield stress to be exceeded, the larger volume of pore fluid causes further rearrangements and weakening of the soil structure through dilation. "Localised sliding" becomes pre-dominant (Figures 6.16, 6.17b) as more particles are moved by shear stress which leads to further increase of plastic strain. The accumulation and the increase of strain rate are likely to be facilitated by the rate of pore pressure increase as well as soil permeability. The deformation behaviour can be best described by the exponential relationship in $\Lambda - p'$ and $\Lambda - t$ space.

Two key plastic strain processes are dominant at Stage 2: (1) a small increase of pore water pressure (i.e. decrease in mean effective stress, p') will result in a more than proportional increase in plastic strain (Figure 6.26) and strain rate (Figure 5.40); and (2) keeping the increased pore water pressure level constant or at zero rate of increase will lead to an increase of strain at constant strain rate (Figure 5.50). Such plastic behaviour seems to explain the well-known "stick-slip" movement pattern of landslides (Allison and Brunsden, 1990). The former process appears to correspond to the "slip" and the latter relates to the "stick" style of movement.

These processes are validated by field observations from plastic materials which show a close correlation between groundwater level (or indirectly by the rainfall amount) and displacement (Table 6.3), including the Higashi-yama Hill earth slide (Matsukura, 1996) (Figure 6.50) and the Jiannosuke-dani landslide (Wang *et al.*, 2007) (Figure 6.51) in Japan, and the Xintan landslide in China (Qin *et al.*, 2001, 2002; He and Wang, 2006; Zhang *et al.*, 2006) (Figure 6.52). The highly plastic nature of the clayey soil at Higashi-yama Hill is indicated by the Atterberg limits (liquid limit: 53.8%, plasticity index: 29.2%) and the presence of swelling minerals (Matsukura, 1996). The Jiannosuke-dani landslide exhibited plastic failure without a clear shear plane (Wang *et al.*, 2006). Plastic deformation of the Xintan landslide is revealed by the asymptotic trend in plots of inversed velocity against time ($\Lambda - t$) (Figure 6.53)

Table 6.3 Field examples of rainfall-induced landslides indicating Stage 2 movement behaviour

Landslide	Location	Materials	Movement period (Stage 2)	Reference
Higashi-yama Hill earth slide	Japan	Highly plastic clayey soil (colluvium) derived from weathered gabbro	07/1977 - 10/1977	Matsukura (1996)
Jiannosuke-dani landslide	Japan	Weathered sandstone and shale	01/07/1997 - 01/07/2001	Wang *et al.* (2007)
Xintan landslide	China	Mixed alluvial and colluvial deposits derived from limestone	03/1978 – 05/1985	Qin *et al.* (2001, 2002); He and Wang (2006); Zhang *et al.* (2006)

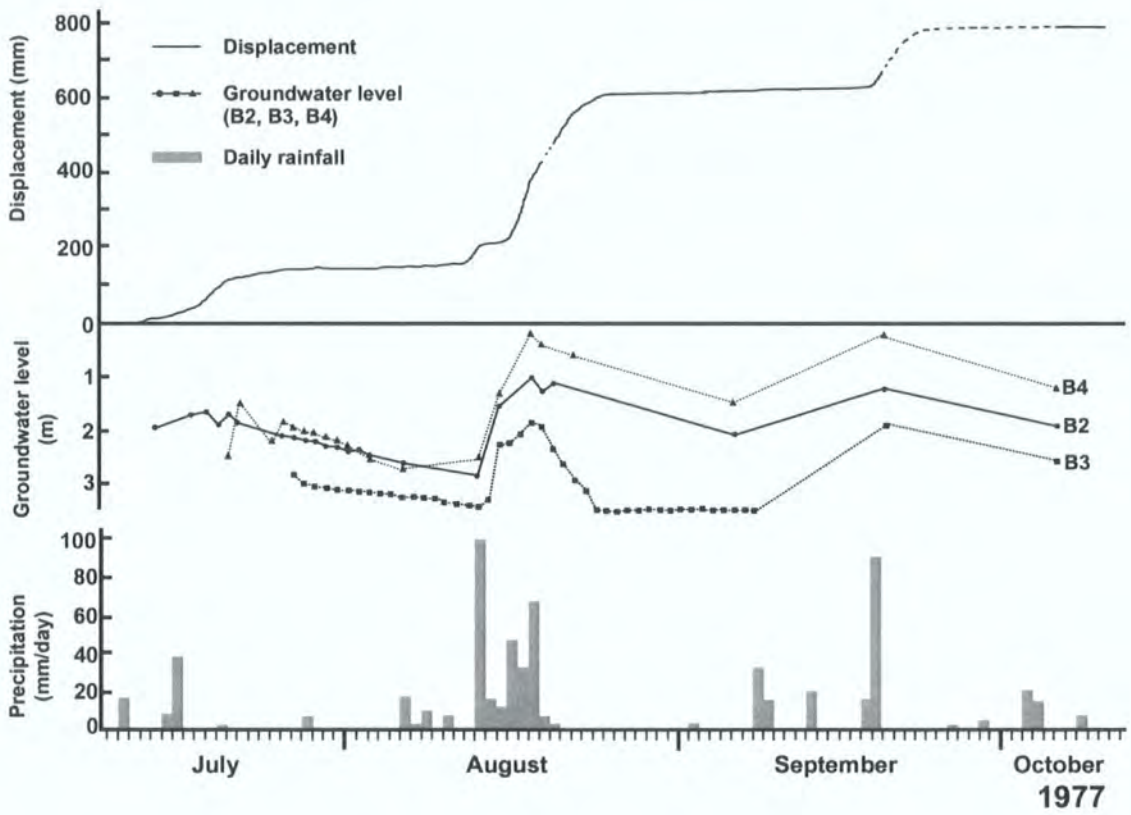

Figure 6.50 Relationship between displacement and groundwater level, at Higashi-yama Hill earth slide, Japan (after Matsukura, 1996)

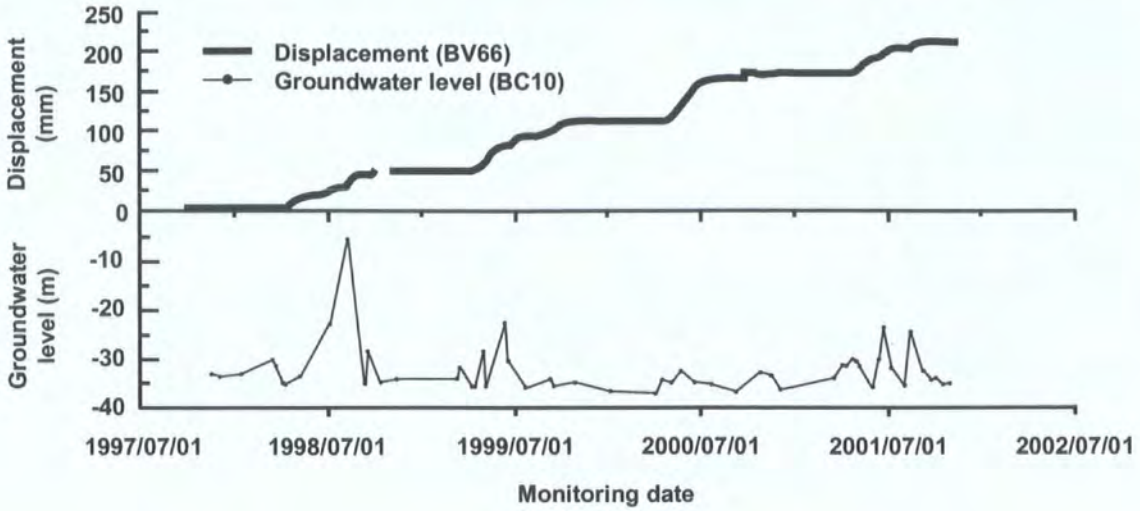

Figure 6.51 Relationship between displacement and groundwater level, at Jiannosuke-dani landslide, Japan (after Wang *et al.*, 2007)

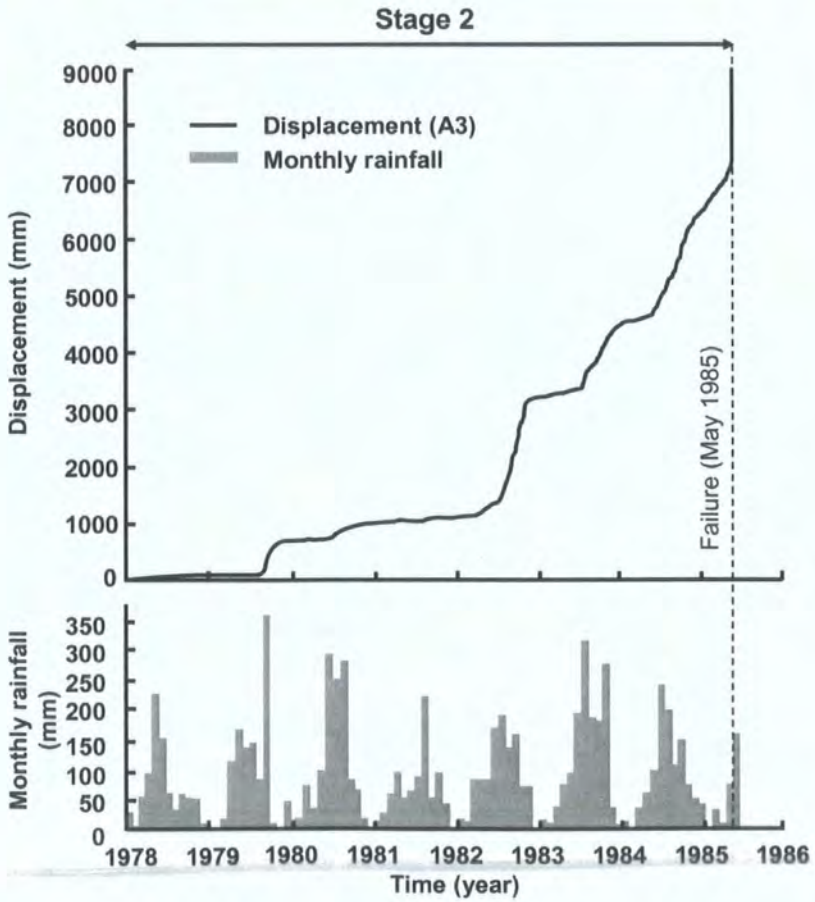

Figure 6.52 Relationship between displacement and monthly rainfall at Xintan landslide, China (after He and Wang, 2006; Zhang *et al.*, 2006)

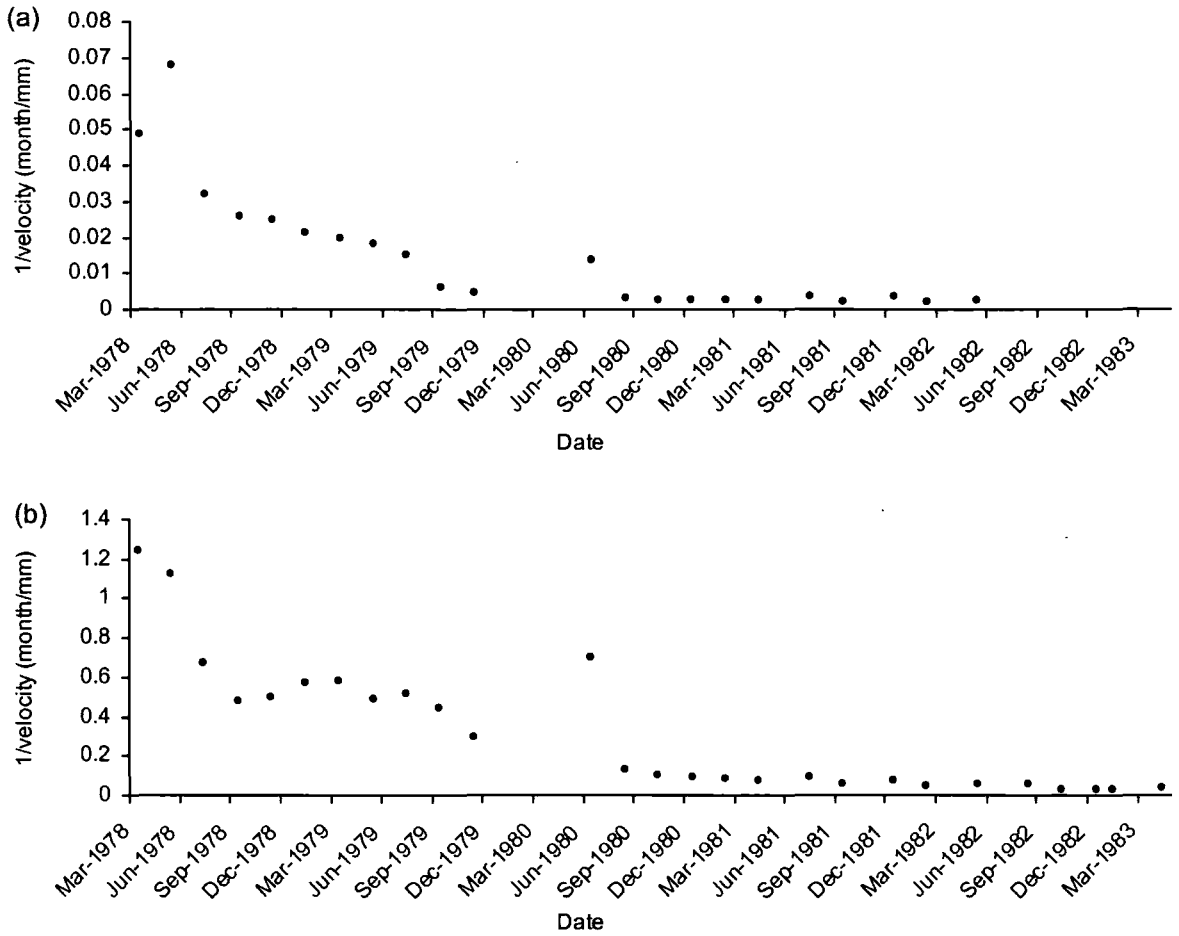

Figure 6.53 Plastic deformation indicated by $\Lambda - t$ plots at (a) main body and (b) toe of Xintan landslide at the Three Gorges, China (data source: He and Wang, 2006)

First of all, the presence of the yield state is a distinctive characteristic of plastic behaviour. This appears to resemble the critical groundwater level noted by Wang *et al.* (2007) for the Jiannosuke-dani landslide, above which displacements are triggered (Figure 6.54). Other notable examples which demonstrate such movement-activating groundwater or pore pressure thresholds include the Alverà mudslide near Cortina d' Ampezzo in the Eastern Dolomites in Italy (Angeli *et al.*, 1996, 1999, 2004), and the Fosso San Martino slide in central Italy which occurs in softened stiff clays (Piccarelli *et al.*, 2004).

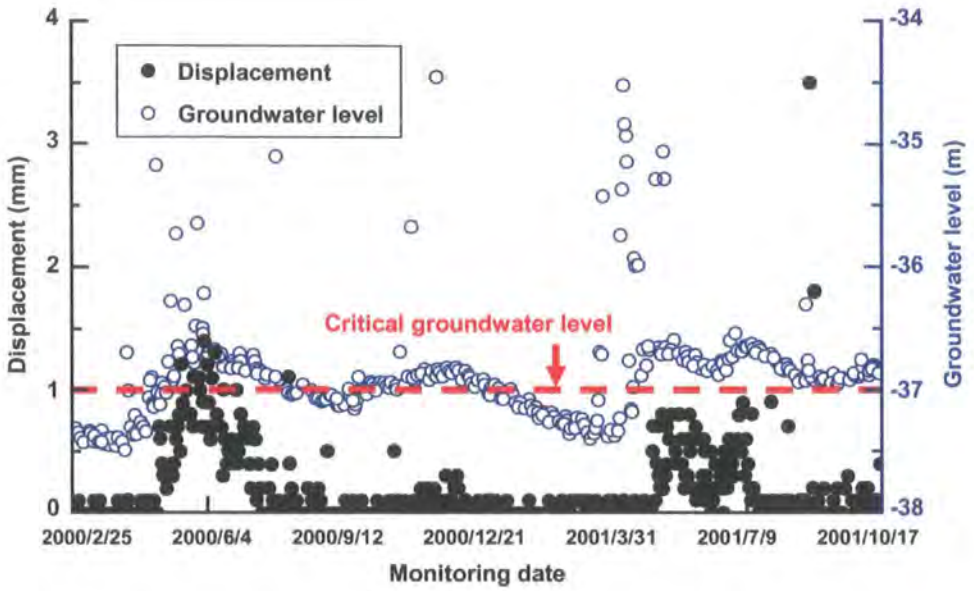

Figure 6.54 The "critical groundwater level" observed at the depth of 37 m in the Jinnosuke-dani landslide, Japan (after Wang *et al.*, 2006)

Once the yield stress is exceeded, stick-slip movements are associated with the plastic strain processes. The "slip" movements are revealed by the increasingly large and rapid displacement in all of the aforementioned field studies (Figures 6.50 to 6.52) as a result of the successive periods of high and rapid change of groundwater levels or rainfall amount. The "stick" movements, which are characterised by the gradual increase of displacement at a constant rate, could be attributed to the relatively constant groundwater level or rainfall amount under a highly permeable state. The generally constant rates of displacements noted at the Jiannosuke-dani landslide in Japan (3-15 mm/year in lower the slide block, 80-170 mm/year in the upper slide block) (Wang *et al.*, 2006) (Figure 6.55a), and at the Slumgullion landslide in Colorado (0.1-1.8 cm/day from 1998 to 2002) (Coe *et al.*, 2003) (Figure 6.55b) appear to demonstrate plastic processes within the landslide.

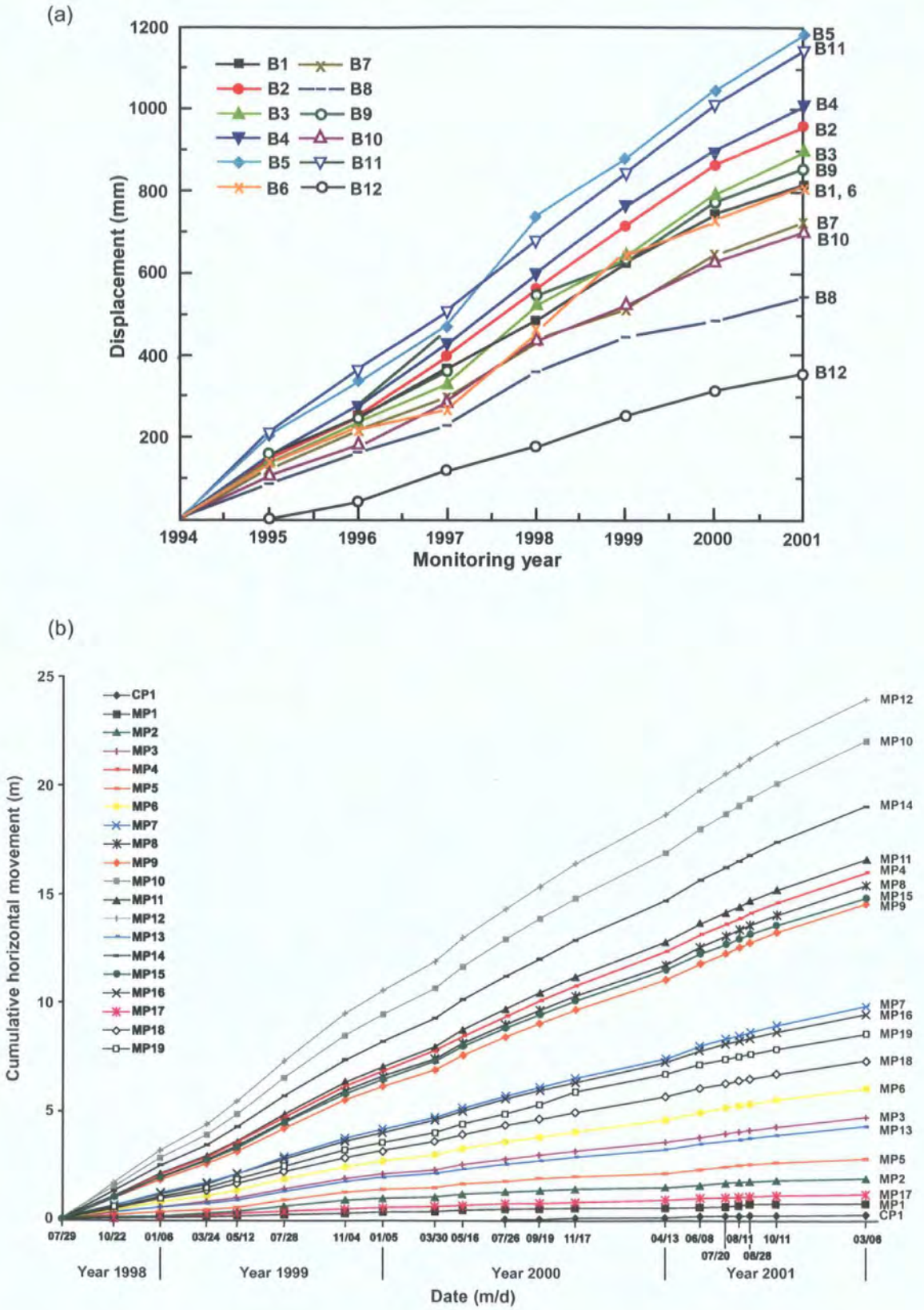

Figure 6.55 Constant displacement rates recorded at the (a) upper block of Jinnosuke-dani landslide in Japan (monitoring points B1-B12) (after Wang *et al.*, 2007), and (b) Slumgullion landslide in Colorado (after Coe *et al.*, 2003)

Moreover, the stepped-like displacement against time plots derived from these field studies and the immediate response after groundwater or rainfall increase further indicate that the soils are permeable, which has been conceptually presented in Figure 6.35. The degree of permeability has been suggested by weak-structured soils of the monitored landslides, which involve colluvium of weathered hornblende-gabbro at Higashi-yama Hill (Matsukura, 1996), and strongly-weathered sandstones and shales at Jinnosuke-dani (Wang *et al.*, 2007) in Japan. Permeable limestone colluvium deposits comprise the main body of the Xintan landslide in China (He and Wang, 2006; Zhang *et al.*, 2006).

For less permeable soil slopes, however, plastic strain development during a rainfall event is more likely to be affected by the pore water equalisation process (section 6.3.2.4). The pore pressure equalisation tests have demonstrated that the pore pressure within the soil increases at a decreasing rate as time is required for the equalisation. This is indicated by the more gentle gradients in $\varepsilon - time$ following the sudden increase of pore water pressure. Therefore, the resultant strain rate would be decreasing. The plots of $\dot{\varepsilon} - time$ are characterised by the fluctuating strain rate in a series of peaks and troughs. The effect of permeability appears to be revealed at Tessina landslide in Italy which comprises marly-clayey and calcarenite strata of low permeability (Angeli *et al.*, 2000). Increasing permeability is indicated by the change of shape in $\varepsilon - time$ plots and the associated variations of velocity from Type I to Type IV movement patterns (Petley *et al.*, 2005b) (Figure 2.20). Permeability appears to play an important role in the increasingly rapid strain response to the rising of pore water pressures.

Most importantly, the resultant movement patterns indicate the state of stability within a highly plastic slope. A pattern with decreasing strain rate could indicate that the slope is conditionally stable. During this period, soil movement could be slow under constant or decreasing rates of pore water pressure. However, a pattern with constant strain rate could mean that the plastic soil is very responsive to the rate of pore water pressure (i.e. highly permeable state) and is about to fail, as indicated from the reinflation tests (Figure 5.50).

6.4.3 Stage 3

Stage 3 represents the unstable state at which rapid acceleration to failure occurs (Table 6.4). The pore water pressure has been increased to the extent that the soil strength is reduced to smaller than the constant shear stress. The particles within

the soil have been largely restructured. The strain rate no longer decreases as the soil is more permeable, even though pore water pressure level may be decreasing (Figure 6.56). The general remoulding process is characterised by the "surge" movement (Allison and Brunsden, 1990), with large and rapidly increasing strain and strain rate. Surge processes are evident in the 626 slope failure in Taiwan (Chang *et al.*, 2005) (Figure 6.49a), Tsubayama landslide (Figure 6.49b) and the Mt. Kaba-san natural slope experiment in Japan (Ochiai *et al.*, 2004) (Figure 6.49c).

Table 6.4 Field examples of rainfall-induced landslides indicating Stage 3 movement behaviour

Landslide	Location	Materials	Movement period (Stage 3)	Reference
626 slope failure	Taiwan	Weathered sandstone, siltstone and shale or colluvium with fractured geologic structure	26/06/2003	Chang *et al.* (2005)
Tsubayama landslide	Japan	Weathered and fractured psammitic and pelitic schist	11/08/2000	Hong *et al.* (2005)
Mt Kaba-san landslide	Japan	Weathered disintegrated granite sand	Elapsed time 24628 -24632 sec	Ochini *et al.* (2004)

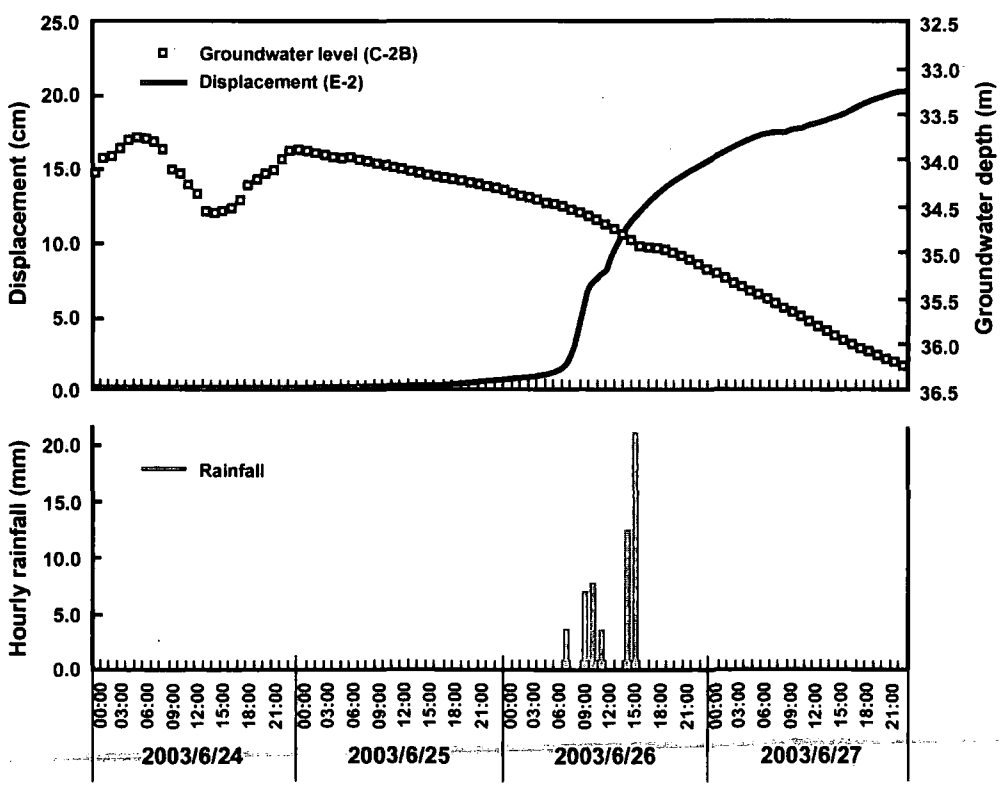

Figure 6.56 An example from Taiwan showing that landslide movements are no longer controlled by the change of pore water pressure at Stage 3 (after Chang *et al.*, 2005)

6.4.4 Random patterns?

The research findings have provided insights on some of the previous observations of seemingly "random" rainfall-induced landslide movements in the field. The unresolved questions mainly involve three aspects: (1) why was there no soil movement at high rainfall intensity? (e.g. Ochiai *et al.*, 2004); (2) why did the movement accelerate and decelerate? (e.g. Allison and Brunsden, 1991); and (3) why did a landslide occur after rainfall had stopped or at a lower groundwater level? (e.g. Chang *et al.*, 2005). A typical example was noted at the 626 landslide in Taiwan, where there was no rainfall record three days before the final failure event and it did not happen at the peak groundwater level (Chang *et al.*, 2005) (Figure 6.56).

The first phenomenon probably lies in the fact that the pore water pressure level has not yet reached the yield state. The second observation is likely to be associated with low soil permeability which slows down the pore pressure equalisation process (and hence leads to a decreasing strain rate). The time delay in the third case appears to be related to tertiary creep instead of being influenced by the external stress (i.e. rainfall), as the soil becomes highly permeable and largely remoulded. Most soil particles are aligned under shear and generalised interparticle sliding is likely to be dominant. Keeping the pore water pressure at the same high level or decreasing pore water pressure might not necessarily decrease velocity, and the landslide is inevitable.

Regarding the whole rainfall-induced landslide process, it logically follows that the soils probably undergo a transition from the initially relatively "less permeable" state of high strength to the "highly permeable" state with low strength as a result of the increase of pore fluid and remoulding processes driven by shear. The transition can be reflected by the associated strain and strain rate behaviour. Marked changes of the steepness of the $\varepsilon - t$ slopes in mid-July and mid-August at Higashi-yama Hill (Figure 6.50); and around mid-1979 and mid-1983 at Xintan (Figure 6.52) suggest increased permeability. Increasing permeability also appears to explain the cause of the pressure dissipation noted during the "multiple stick-slip" movements and the transition to a more significant and rapid "graded" response at a coastal mudslide in Dorset (Allison and Brunsden, 1990) (Figures 6.57). Nevertheless, plastic deformation remains largely the key mechanism for the movement behaviour.

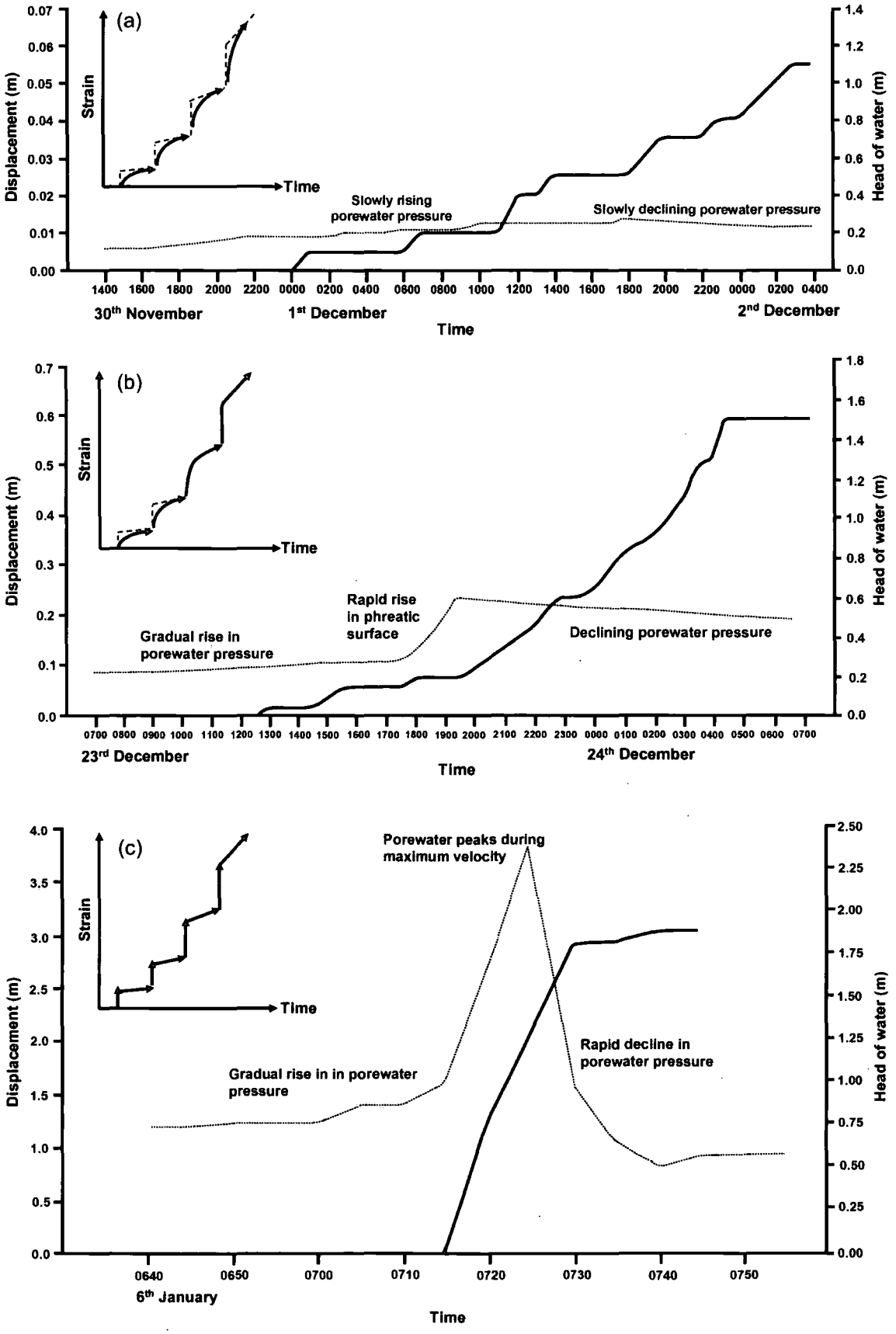

Figure 6.57 The change of shape in $\varepsilon - t$ during the (a) "multiple stick-slip", (b) "graded" and (c) "surge" stage showing an increasing permeability with time, as schematically represented by the plastic behaviour identified in this research (see inset), suggesting an increasing permeability within the landslide (modified from Allison and Brunsden, 1990)

Hence the observed movements are not random (Table 6.5). Instead, they represent plastic behaviour under different stress state, rate of change of pore water pressure and soil permeability. This is demonstrated by the systematic transition of movement patterns noted in natural landslides, for example, the Wealden Beds mudslide at Dorset (Allison and Brunsden, 1990) and the Tessina landslide in Italy (Petley *et al.*, 2005b). The transition involves the "multiple stick-slip", "graded" and "surge" patterns observed by Allison and Brunsden (1990) and the "Type I" to "Type IV" movements illustrated by Petley *et al.* (2005b). The progression of these movement patterns, as indicated from this research, is likely to be attributed to an increasing amount as well as rate of pore water pressure. The corresponding more abrupt change of slope in cumulative displacement against time further suggests an increase in permeability.

Table 6.5 Field examples of rainfall-induced landslides showing systematic movement patterns

Landslide	Location	Materials	Movement patterns	Reference
Tessina landslide	Italy	Tertiary molasse deposits (rhythmic sequence of marlstones, clay shales and calcarenite layers)	Type I to Type IV	Petley *et al.* (2005b)
Wealden Beds mudslide	United Kingdom	Soft, plastic sands, grits, mottled clays and shales	Multiple stick-slip, graded, surge	Allison and Brunsden (1990)

6.4.5 Understanding landslide behaviour on Lantau Island, Hong Kong

There is no detailed field monitoring record of the initiation of landslide movements on natural hillslopes on Lantau island (Evans and Lam, 2003) or debris movement rates in Hong Kong (Au, 1998). However, the asymptotic trend in $\Lambda - p'$ and $\Lambda - t$ space presented in this research (section 5.7.5) indicates that the movement of the shallow landslides on intensely weathered soil slopes on Lantau island is likely to be generated through ductile deformation processes (Petley *et al.*, 2002). The dominance of ductile failure is probably related to the low cohesion and the weakened structure of the residual soil materials as a result of intense weathering (section 6.1). The resulting plastic deformation within the shear zone appears to involve interparticle sliding movements facilitated by dilation and shear (section 6.2). The associated rates of deformation are likely to undergo three stages towards failure, depending on the stress state, the rate of reinflation as well as soil permeability (Figure 6.48).

The weathered slopes on Lantau island may not exhibit any signs of movement during a rainstorm event unless the mean effective stress has reached the plastic yield state (Stage 1). The presence of the yield state for the plastic materials implies the essential role of antecedent rainfall in the development of a landslide to bring the slope to Stage 2. The associated rainfall threshold appears to be below 400 mm (24-hr rolling maximum), as above this would likely cause widespread rainfall-induced natural landslides in the Tung Chung area (Franks, 1998) and over Hong Kong ($\geq$ 10 landslides/ km^2) (Evans *et al.*, 1999).

Plastic deformation/secondary creep is likely to dominate within the weathered hillslopes when the pore water pressure increases beyond the yield state (Stage 2). The associated soil movement would tend to increase to a constant rate under a constant stress state as most weathered soils in Hong Kong are highly permeable (section 2.4.1.1). However, the strain rate may fluctuate initially as the materials are not perfectly permeable, showing a "stick-slip" movement pattern with periods of acceleration and deceleration. The role of rainfall intensity appears to become more important in this stage. A sudden increase of pore water pressure as a result of high rainfall intensity could lead to acceleration due to plastic strain. Deceleration would probably occur under a constant stress state within the less permeable slopes (section 6.3.2.4). These findings appear to clarify the presence of creep in weathered volcanic soils (Irfan, 1994; Duzgoren-Aydin *et al.*, 2002) and the "slow-moving, ductile instability" on some natural hillslopes in Hong Kong (Wong and Ho, 2000: 210) in terms of its nature and movement patterns. Moreover, based on the experimental results (Figures 5.50b, 5.52, 5.53), the change from the fluctuating to the constant strain rate under a constant stress state is likely to be a warning sign indicating that the slope is about to fail (onset of Stage 3). However, the lack of field monitoring on the movements of small rainfall-induced landslides in Hong Kong could mean that the precursory movements are not detected. This may have led to the impression that most landslides occur catastrophically without prior warning (Au, 1998).

The research findings also suggest that tertiary creep (Stage 3) may have contributed to the final failure phase of landslides on Lantau Island, exhibited by an accelerating or "surge" movement pattern towards failure under a constant stress state (Figures 5.50b, 5.53). However, the deformation behaviour is not associated with progressive failure which involves crack growth within brittle materials (Petley *et al.*, 2005b) as no clear shear plane development has been observed within the TC and PO samples (Appendices 1c, 2). Instead, the failure appears to be primarily driven by the internal restructuring of the weathered materials through generalised interparticle

sliding (section 6.2). The contribution of particle rearrangement to shear deformation has been validated by a microstructural study within a natural slip zone of a landslide in Hong Kong through optical microscopy and backscattered electron microscopy techniques (Wen and Aydin, 2003). That study further shows that fine silts, which form a high particle size proportion of both the TC and PO samples (Table 5.4), have the highest degree of alignment and shape preferred orientation (Wen and Aydin, 2003). Hence, particle sliding seems to be a possible mechanism for the final shear phase and may have provided an alternative explanation (to the change of pore water pressure) for the time lag between rainfall and landslides reported in some weathered slopes in Hong Kong (Au, 1998; Irfan, 1998b).

6.5 Limitations

Care should be undertaken in the interpretation of the experimental results for the behaviour of natural landslides in the field, with particular consideration of the following potential limitations:

The landslide development stages and the corresponding movement patterns suggested in this research have described the behaviour of undisturbed, plastic residual soil materials derived from intense weathering of volcanic rocks. However these development stages do not seem to apply to brittle failures which are more likely to be associated with progressive failure involving crack growth processes (Petley *et al.*, 2002, 2005b; Kilburn and Petley, 2003; Petley and Petley, 2006).

The small size of the samples (38 mm in diameter x 76 mm in height), which represents a soil element in the ground (Head, 1998), may mean that some of the larger-scale geological features of weathered rock such as relict discontinuities/joints (Lumb, 1975; Irfan, 1998b) have not been included in the analysis. However, this is not likely to affect the behaviour of the residual soils at shallow depths as no relict mass structure is retained in this most intensely weathered grade (Irfan, 1999). The deformation behaviour within the shear zone with geological discontinuities in the less weathered grades, which may serve as pre-existing shear planes (Irfan, 1994), is likely to be ductile (Petley *et al.*, 2002) although further investigation would be required for verification. Moreover, despite the small size of the samples, they have demonstrated the typical characteristics of residual soils in the humid tropics (section 6.1).

The stress conditions within the triaxial stress path cell are not truly three-dimensional as the intermediate principal stress (σ_2) and the minor principal stress (σ_3)

are not controlled independently, but are assumed to be equal (Head, 1998; Alshibli and Williams, 2005). The field stress on a slope could also be anisotropic (Anderson and Sitar, 1995; Zhu and Anderson, 1998). The mean effective stress and the reinflation rates applied may be higher than the actual values at the sampling sites (chapter 4). Moreover, the vertical displacement (axial strain) in the triaxial cell may differ from the shear displacement measured within a landslide. Within the sample, the stress distribution is likely to be non-uniform, as indicated by the decrease of strain rate during the stepped reinflation tests and the barrelling effect exhibited by both the TC and PO samples. The former was probably caused by the time lag of stress redistribution (seepage) from the top and bottom ends to the middle part of the sample, as revealed by the pore pressure equalisation tests (Figure 6.34). The latter was related to the higher friction between the porous disc and the top and bottom ends of the sample respectively.

The standard design of triaxial stress path testing could not reflect the inhomogeneous stress within the sample. The displacement transducer, which is attached to the piston at the bottom of the sample, can only measure the total axial strain during the tests. Moreover, during the reinflation tests, the pore and back pressures were measured at the bottom and top of the samples (both valves were open), thus the stress conditions in the middle of the samples were unknown. However, the process of stress redistribution within the sample can be measured by adding strain gauges and pore pressure transducers to the main body of the sample.

The non-uniform stress within the sample may cause difficulties in clearly distinguishing the contribution of the volumetric strain (due to decreasing p') and shear strain (due to interparticle movements) to the dilative soil behaviour during the constant stress (p', q) periods after each stepped reinflation. This could have more effect on the less permeable samples because the pore water pressure in the middle of the sample may still be increasing due to the redistribution process. The delayed volumetric strain may be misinterpreted as shear strain under the constant stress state periods. However, the contribution of the volumetric and shear strain can be distinguished by undertaking PPR tests (at the same rates) at q = 0 kPa, as these tests will result in volumetric strain only (Dixon, 2007).

Nevertheless, the practical isotropic assumption and the stresses applied for the reinflation tests do seem to be representative and the resulting deformations (section 5.7) are consistent with field observations of landslide behaviour within plastic materials in general (section 6.4). The systematic measurement error from the

transducers, ranging from 0.11-0.46%, has been taken into account. Area correction has been made for the effect of barrelling. The comparable findings suggest that the stress-controlled reinflation test design on the undisturbed samples has closely, though not perfectly, replicated the actual processes of rainfall-induced landslides.

6.6 Chapter summary

This chapter discussed and evaluated the research findings under three main themes: (1) the nature of the weathered volcanics (TC and PO samples), (2) their volumetric behaviour upon reinflation and (3) the associated deformation mechanism with reference to the accelerating movements towards failure. A synthesis of these key themes suggests that the processes of rainfall-induced landslide initiation on weathered slopes undergo three stages, corresponding to "stable" (Stage 1), "conditionally stable" (Stage 2) and "unstable" (Stage 3), parallel to the scheme proposed by Crozier (1986).

6.6.1 Physical and behavioural characteristics of weathered volcanics

Analyses of the physical properties of the TC and PO samples (section 6.1) demonstrate the typical characteristics of tropical soils. The particle size distribution indicates that they represent the most intensely weathered (Grade VI) or residual soils of fine ash tuff and coarse ash tuff respectively. Their fine-grained and well-graded nature has been attributed to the high degree of chemical weathering typically active under tropical climates. The dominant clay mineral appears to be kaolinite of low swelling capacity. The medium to high Atterberg limits further reveal their plastic nature. The undisturbed TC and PO samples have exhibited a weakly bonded structure, with a heterogeneous nature. The coefficient of permeability further indicates that the looser PO samples are relatively more permeable, possibly due to their higher gravel and sand contents.

In terms of strength properties (c', ϕ'), a new criterion using the strain contours has been proposed which enables consistent comparison between the strain-controlled ICU, ICD tests and the stress-controlled PPR tests. Based on this cross-referenced criterion, the results highlight two important implications for the landslide initiation processes. Firstly, failure involves a mobilisation of friction (as indicated by the increase of the frictional angle throughout the strain development) which can be associated with resistance to the shear force. Secondly, the failure mechanism by compression (the ICU, ICD tests) is different from the reinflation process in the field

(the PPR tests), in that the former generates an initial increase in cohesion but the latter shows a continuous loss in cohesion as strain develops. Nevertheless, the effective strength envelopes derived from the ICU, ICD and PPR tests are linear, implying that the weathered samples might be looser and weaker in their natural state on the shallow hillslopes.

6.6.2 Dilative behaviour in relation to interparticle movements

Three patterns of dilative behaviour have been identified under the reinflation process in terms of $e - p'$ relationships, which can be explained with reference to the interparticle movements within the samples (section 6.2).

Type 1 was characterised by a linear $e - p'$ relationship which dominated the beginning of the reinflation tests undertaken at all rates and styles. This was attributed to the increasing pore fluid which pushed apart the strongly interlocked soil particles and enabled them to climb over each other under shear. The dilative behaviour might be disturbed by slight contractions as some particles might fill up the void space previously occupied by another particle during the "push and climb" process.

Type 2 was marked by a stepped $e - p'$ relationship which showed a sudden increase of void ratio, followed by a gentle increase during the reinflation process. This occurred at the latter part of the 1 kPa/hr linear and the stepped reinflation tests as effective stress was decreased further. Rapid dilation was attributed to "localised sliding", where the inter-particle contacts were reduced to the extent that some particles began sliding past each other. However, as the majority of particles remained interlocked, the slip movements were restricted.

Type 3 involved a non-linear $e - p'$ relationship towards failure, with a rapid and continuous increase in the void ratio in relation to low effective stresses. "Generalised sliding" was most likely, as the soil particles were rearranged and destructured under shear, facilitated by the increasing amount of pore fluid.

6.6.3 The deformation mechanism for shallow rainfall-induced landslides

Three fundamental components of soil behaviour in relation to the stress-strain-time relationship have been discussed, including elasticity, plasticity and creep, to investigate the underlying deformation mechanism of shallow rainfall-induced landslides in the weathered soils (section 6.3).

Elasticity fails to explain the deformation behaviour for the weathered samples as a linear stress-strain relationship has not been found. However, the strain development of the weathered soils during the reinflation process can be largely explained by plastic deformation as well as permeability conditions. The initial zero movement reflect the stress state below yield, as the soil particles are mostly interlocked. After reaching the yield stress, the strain development in $\Lambda - p'$ and $\Lambda - t$ space shows an asymptotic trend (exponential relationship) suggesting the dominance of plastic deformation. The slope of $\Lambda - p'$ and $\Lambda - t$ space decreases under a higher reinflation rate, consistent with the results reported in Petley *et al.* (2005b). This is probably because the stresses with the sample cannot be localised under a quickly destructured state. The stepped reinflation tests further reveal the influence of permeability, which is particularly apparent in the less permeable TC samples. The intriguing decrease in strain rate at constant stress state can be attributed to the pore water pressure equalisation process.

Creep has been evaluated with reference to the models proposed by Terzaghi (1950), Bjerrum (1967), Varnes (1983) and Helmstetter *et al.* (2004). The creep analyses under the constant stress conditions over time during the stepped reinflation test appear to suggest that the underlying mechanism for the creep phase under Terzaghi's (1950) model is deformation dependent. The stepped reinflation can be considered as a "multi-stage creep" test as the sample underwent constant stress state at more than one level of its peak stress. The progressive failure proposed by Bjerrum (1967) was not observed in the weathered samples as no shear surface was developed. The contribution of creep (Varnes, 1983) for the development of landslides in plastic materials may be best explained by inter-particle sliding. Primary creep, which might involve a brittle process, did not occur within the plastic TC and PO samples. Constant strain rates under constant stress state could be associated with secondary creep and/or plastic deformation with localised sliding. The fluctuating strain rates, however, are likely to be associated with permeability within the samples. The deceleration phase under constant stress state cannot be explained by the slider-block friction model (Helmstetter *et al.*, 2004). The rapid acceleration towards failure or

tertiary creep suggests generalised interparticle sliding upon remoulding under constant shear.

6.6.4 Implications for shallow rainfall-induced landslide movements

The analyses of the plastic deformation behaviour of the weathered soils under the reinflation process suggest that shallow rainfall-induced landslides undergo three key stages of strain development towards failure (section 6.4). Stage 1 represents a stable slope below the yield state without signs of movements. Stage 2 is marked by fluctuating strain rates where the slope is conditionally stable depending on the rate of increasing pore water pressure and soil permeability, as the pore water pressure level gets higher. Stage 3 is characterised by accelerating strain rates as the slope fails. All of these stages are consistent with the notable "non-responsive", "stick-slip" and "surge" movement patterns observed in other shallow rainfall-triggered landslides occurred in plastic materials. This research further suggests that "random" movement patterns can be explained in the light of the mechanisms exhibited by the different stages.

Chapter 7 Conclusion

7.1 Principal findings

The deformation behaviour of shallow rainfall-induced landslides is, in part, material dependent. The dominance of plastic behaviour in the undisturbed soil materials collected from two shallow landslides on volcanic tuff slopes on Lantau Island, Hong Kong, is likely to be related to their loose, weakly-bonded structure with a low cohesive strength as a result of the intense degree of chemical weathering typical in the humid tropics. This is reflected by their reddish-brown colour (presence of iron oxides), large proportion of silt and clay particles (probably kaolinite), a medium to high plasticity, and their heterogeneous nature.

A process of interparticle rearrangement/alignment could provide a physical explanation for the development of plastic failures. This is contributed by various interparticle movements from "push and climb" (Type 1) to "localised sliding" (Type 2) and "generalised sliding" (Type 3) towards the final failure. These movement types are revealed from the irregularities in the volumetric behaviour during pore water pressure reinflation testing and the dilative behaviour under constant shear conditions.

Plastic deformation is the key underlying mechanisms and processes of shallow rainfall-induced landslides within the residual soils, as suggested by the initial zero/little strain movement and the asymptotic trend in $\Lambda - t$ space under the reinflation tests. An elastic stress-strain relationship has not been observed. The dominance of plastic deformation could imply that the rates of movement would increase to a steady-state (Petley *et al.*, 2002). Interestingly, the research results further show that the plastic strain rates could be affected by the reinflation rate and soil permeability, resulting in a "stick-slip" movement pattern. Deceleration appears to be an indicator of the efficiency of the pore water pressure equalisation process within plastic materials.

The relationship between creep models and the initiation of plastic failures has been evaluated through analyses of the deformation behaviour during the stepped reinflation tests at constant stress state. The analyses indicate that the creep phenomenon for plastic failures appears to be deformation-dependent (Terzaghi, 1950), but not driven by a progressive failure mechanism (Bjerrum, 1967) or by state and rate dependent friction (Helmstetter *et al.*, 2004). The development of plastic failures does not have a primary creep phase involving crack growth (Main, 2000). However, the samples do appear to undergo the secondary creep (although indistinguishable from

the plastic deformation) and tertiary creep phases, in association with localised and generalised interparticle sliding respectively.

The analyses of the behaviour of the plastic residual soils from the reinflation tests suggest that a rainfall-induced landslide in these materials undergoes three stages towards failure. Each stage can be characterised by a movement pattern, representing the state of stability in the slope: graded movements at zero or very low strain rate (Stage 1), stick-slip movements with fluctuating (accelerating/decelerating) strain rates (Stage 2) and the surge or accelerating movements (Stage 3).

Most interestingly, the changing rates of axial strain development in the plastic failures appear to be not only controlled by the stress state, but also affected by the rate of reinflation as well as soil permeability, generated through dilation and interparticle sliding under constant shear. The interrelationships have largely explained the distinctive movement patterns observed in the development of landslides within plastic materials during a rainfall event in different environmental settings, including some of the random movements. These findings have enhanced current understanding of landslide systems in plastic materials and demonstrate that the steady state behaviour could be a precursor for the accelerating phase towards failure. Monitoring of the changes of strain rate and the identification of their evolving patterns would therefore be essential for an effective landslide warning system.

7.2 Recommendations for further research

Based on this research, recommendations are made for future research to advance the knowledge on the processes and mechanisms of rainfall-induced landslides on residual soil slopes:

The design of the testing programme in this research aims to simulate the field conditions. One of the methods achieved has been the application of a representative low confining pressure, p'_{dis} = 233 kPa, at the start of the reinflation tests on the weathered samples, with consideration of the minimum capacity of the triaxial stress path cell. However, the normally consolidated behaviour of the samples during the ICU and ICD tests suggests that a lower confining pressure (i.e. $p'_c \leq$ 200 kPa) would be ideal for studying shallow landslides within residual soils. This can be made possible given that specially designed triaxial apparatus for low stress testing are currently commercially available. Other recently developed testing equipment such as the back-

pressured shear box (Petley *et al.*, 2007) and the ring shear apparatus (Sassa *et al.*, 2004) would allow more direct and precise measurement of displacement at the shear zone and at large shear displacements respectively.

This research has been focused on examining the relationship between the different rate and style of increasing pore water pressure and the strain rate development from an initial stress state (p'_{dis} = 233 kPa, q = 100 kPa). It would provide a more comprehensive understanding of landslide behaviour including the role of slope inclination by conducting the same set of tests at different deviatoric stress levels. This additional stress dimension could also clarify the determination of the reinflation failure envelopes, as well as the changes of pre-failure strain / strain rate development at a wider range of stress states.

The application of the field referenced rates and styles of increasing pore water pressure has been useful in revealing the complex strain development towards failure. Another interesting aspect, which has not been covered by the reinflation tests, is whether the accelerating behaviour just before failure (Stage 3) can be stopped if the pore water pressure decreases (and at what rates). This might provide further implications for landslide management.

This research has also attempted to integrate the reinflation process and pre-failure creep phase in Terzaghi's (1950) model of progressive failure for landslides. The reinflation process, indeed, satisfies one of the conditions of the standard creep test as it is undertaken below the maximum shear stress. Another condition, the constant stress state, has been involved in the stepped reinflation. However, the link between strain development as a result of the reinflation and strain development under constant stress conditions requires further investigation in detail by increasing the length of time under constant stress state. This would potentially be a way to clarify the underlying mechanism for the intriguing acceleration at constant stress state which currently seems to be a "mixed" result of increased pore water pressure and tertiary creep (e.g. Figure 5.53).

The use of undisturbed samples is probably the most direct way to reproduce the in-situ soil characteristics in the laboratory. This is the latest development of field stress simulation research, and shows prospects for revealing shear zone movement mechanisms (Petley *et al.* 2005b; Petley and Petley, 2006). Quantification of factors which are unique for undisturbed residual soils such as fabric (e.g. Wen and Aydin, 2003, 2005), heterogeneity and the associated permeability (e.g. Vieira and Fernandes,

2004) would be beneficial to develop a numerical model to assess their influence on the landslide initiation processes.

This research yields some insights on shallow rainfall-induced landslide behaviour of the most intensely weathered tropical soils (Grade VI) derived from fine-ash and coarse-ash volcanic tuff. A more comprehensive view of landslide mechanisms on tropical weathered soils should include an examination of movement behaviour within Grade IV and V materials derived from other bedrock types, where rainfall-triggered landslides are also commonly found. It would be interesting to explore if the less weathered soils deform differently and therefore change the identified three stages and distinctive patterns of strain development.

An ideal method which could enhance further understanding of the actual rainfall-induced landslide processes and mechanisms on weathered slopes (Grade IV – Grade VI) is to set up a field monitoring programme with pore pressure recording instruments as well as precise movement detecting devices on distressed slopes. Information on the material behaviour (brittle / ductile) is also essential. Surprisingly, such programmes are scarce in tropical regions. The capability of identifying the precursory landslide movement patterns equipped with the analytical tools revealing the underlying mechanisms would be very valuable towards establishing an effective landslide warning system.

References

Agriculture, Fisheries and Conservation Department (AFCD), 2004. *Lantau Country Park*. http://parks.afcd.gov.hk/newsparks/eng/country/cps/cp_lantau.htm. Accessed on April 21, 2005.

Agriculture, Fisheries and Conservation Department (AFCD), 2006. *South Lantau Country Park*. http://www.afcd.gov.hk/english/country/cou_vis/cou_vis_cou/cou_vis_cou_ls/cou_vis_cou_ls.html Accessed on March 26, 2007.

Alcantara-Ayala, I., 2004. Hazard assessment of rainfall-induced landsliding in Mexico. *Geomorphology*, 61(1-2): 19-40.

Allison, R. and Brunsden, D., 1990. Some mudslide movement patterns. *Earth Surface Processes and Landforms*, 15: 297-311.

Alshibli, K.A. and Williams, H.S., 2005. A true triaxial apparatus for soil testing with mixed boundary conditions. *Geotechnical Testing Journal*, 28(6): 534-543.

Anderson, S.A. and Riemer, M.F., 1995. Collapse of saturated soil due to reduction in confinement. *Journal of Geotechnical Engineering*, 121(2): 216-220.

Anderson, S.A. and Sitar, N., 1995. Analysis of rainfall-induced debris flows. *ASCE Journal of Geotechnical Engineering*, 121(7): 544-552.

Angeli, M.-G., Gasparetto, P., Menotti, R.M., Pasuto, A. and Silvano, S., 1996. A visco-plastic model for slope analysis applied to a mudslide in Cortina d'Ampezzo, Italy. *Quarterly Journal of Engineering Geology*, 29: 233-240.

Angeli, M.-G., Gasparetto, P., Pasuto, A. and Silvano, S., 1989. Examples of landslide instrumentation (Italy). *Proceedings of the 12th Conference on Soil Mechanics and Foundation Engineering, Rio de Janeiro*, pp. 1531-1534.

Angeli, M.G., Pasuto, A. and Silvano, S., 1999. Towards the definition of slope instability behaviour in the Alvera mudslide (Cortina d'Ampezzo, Italy). *Geomorphology*, 30: 201-211.

Angeli, M.-G., Pasuto, A. and Silvano, S., 2000. A critical review of landslide monitoring experiences. *Engineering Geology*, 55: 133-147.

Atkinson, J.H., 1993. *The Mechanics of Soils and Foundations through Critical State Soil Mechanics*. McGraw-Hill, London, 337 pp.

Atkinson, J.H. and Bransby, P.L., 1978. *The Mechanics of Soils : An Introduction to Critical State Soil Mechanics*. McGraw-Hill, London, 375 pp.

Au, S.W.C., 1998. Rain-induced slope instability in Hong Kong. *Engineering Geology*, 51: 1-36.

Aung, K.K., Rahardjo, H., Toll, D.G. and Leong, E.C., 2000. Minerology and microfabric of unsaturated residual soil. In: D.G. Toll and E.C. Leong (Editors), *Unsaturated Soils for Asia*. Balkema, Rotterdam, pp. 317-321.

Babu, G.L.S. and Murthy, D.S.N., 2005. Reliability analysis of unsaturated soil slopes. *Journal of Geotechnical and Geoenvironmental Engineering*, 131(11): 1423-1428.

Baum, R.L. and Reid, M.E., 1995. Geology, hydrology, and mechanics of a slow-moving, clay-rich landslide, Honolulu, Hawaii. In: W.C. Haneberg and S.A. Anderson (Editors), *Clay and Shale Slope Instability*. Geological Society of America, Boulder, Colorado, pp. 79-105.

Bell, F.G., 2000. *Engineering Properties of Soils and Rocks*. Blackwell Science, Oxford, 482 pp.

Bennett, J., 1984. *Review of Superficial Deposits and Weathering in Hong Kong*. Geotechnical Control Office, Engineering Development Dept., Hong Kong, 51 pp.

Bhandari, R.K., 1988. Special lecture: some practical lessons in the investigation and field monitoring of landslides. *Proceedings of the 5th International Symposium on Landslides*. Balkema, pp. 1435-1457.

Bhasin, R., Grimstad, E., Larsen, J.O., Dhawan, A.K., Singh, R., Verma, S.K. and Venkatachalam, K., 2002. Landslide hazards and mitigation measures at Gangtok, Sikkim Himalaya. *Engineering Geology*, 64(4): 351-368.

Bishop, A.W. and Henkel, D.J., 1962. *The Measurement of Soil Properties in the Triaxial Test.* Edward Arnold, London, 228 pp.

Bishop, A.W. and Wesley, L.D., 1975. A hydraulic triaxial apparatus for controlled stress path testing. *Geotechnique*, 25(4): 657-670.

Bjerrum, L., 1967. Progressive failure in slopes of overconsolidated plastic clay and clay shales. *Journal of the Soil Mechanics and Foundation Division of the ASCE*, 93: 1-49.

Blight, G.E., 1997. Origin and formation of residual soils. In: G.E. Blight (Editor), *Mechanics of Residual Soils: A Guide to the Formation, Classification and Geotechnical Properties of Residual Soils, with Advice for Geotechnical Design.* A.A. Balkema, Rotterdam, pp. 1-15.

Boonsinsuk, P. and Yong, N., 1982. Analyses of Hong Kong residual soil slopes, Engineering and Construction in Tropical and Residual Soils. *Proceedings of the ASCE Geotechnical Engineering Division Specialty Conference, Honolulu, Hawaii, January 11-15.* American Society of Civil Engineers, pp. 463-482.

Brand, E.W., 1981. Some thoughts on rain-induced slope failures. *Proceedings of the 10th International Conference on Soil Mechanics and Foundation Engineering, Stockholm, 15-19 June*, pp. 373-376.

Brand, E.W., 1985. Predicting the performance of residual soil slopes. *Proceedings of the 11th International Conference on Soil Mechanics and Foundation Engineering, San Francisco.* Balkema, pp. 2541-2578.

Brand, E.W., 1994. Landslides in Hong Kong during the rainfall event of 4-5 November 1993. *Landslide News*, 8: 35-36.

Brand, E.W., 1995. Keynote paper: slope instability in tropical areas. In: D.H. Bell, *Landslides : Proceedings of the Sixth International Symposium, 10-14 February 1992, Christchurch.* Rotterdam : A. A. Balkema, pp. 2031-2051.

Brand, E.W., Phillipson, H.B., Borrie, G.W. and Clover, A.W., 1983. In situ shear tests on Hong Kong residual soil. *Proceedings of International Symposium on Soil and Rock Investigations by In Situ Testing, Paris*, 2: 13-17.

Brand, E.W., Premchitt, J. and Phillipson, H.B., 1984. Relationship between rainfall and landslides in Hong Kong. *Proceedings of the 4th International Symposium on Landslides, Toronto, 1*, pp. 377-384.

Brenner, R.P., Garga, V.K. and Blight, G.E., 1997. Shear strength behaviour and the measurement of shear strength in residual soils. In: G.E. Blight (Editor), *Mechanics of Residual Soils: A Guide to the Formation, Classification and Geotechnical Properties of Residual Soils, with Advice for Geotechnical Design*. A.A. Balkema, Rotterdam, pp. 155-220.

Brenner, R.P., Tam, H.K. and Brand, E.W., 1985. Field stress path simulation of rain-induced slope failure. *Proceedings of the 11th International Conference on Soil Mechanics and Foundation Engineering*, pp. 991-996.

British Standards Institution (BSI), 1981. *Code of Practice for Site Investigations*. BS 5930: 1981, 192 pp.

British Standards Institution (BSI), 1990a. *British Standard Methods of Test for Soils for Civil Engineering Purposes. Part 1: General Requirements and Sample Preparation*. BS 1377: Part 1: 1990, 28 pp.

British Standards Institution (BSI), 1990b. *British Standard Methods of Test for Soils for Civil Engineering Purposes. Part 2: Classification Tests*. BS 1377: Part 2: 1990, 61 pp.

British Standards Institution (BSI), 1990c. *British Standard Methods of Test for Soils for Civil Engineering Purposes. Part 3: Chemical and Electro-chemical Tests*. BS 1377: Part 3: 1990.

British Standards Institution (BSI), 1990d. *British Standard Methods of Test for Soils for Civil Engineering Purposes. Part 8: Shear strength tests (effective stress)*. BS 1377: Part 8: 1990, 28 pp.

Brückl, E. and Parotidis, M., 2005. Prediction of slope instabilities due to deep-seated gravitational creep. *Natural Hazards and Earth System Sciences*, 5: 155-172.

Burland, J.B., 1989. Small is beautiful: the stiffness of soils at small strains. *Canadian Geotechnical Journal*, 26: 499-516.

Burland, J.B., 1990. On the compressibility and shear strength of natural clays. *Geotechnique*, 40(3): 329-378.

Campanella, R.G. and Vaid, Y.P., 1974. Triaxial and plane strain creep rupture of an undisturbed clay. *Canadian Geotechnical Journal*, 11, 1-10.

Campbell, S.D.G. and Koor, N.P., 1999. *Assessment of Geological Features Related to Recent Landslides in Volcanic Rocks of Hong Kong Phase 2A : Chai Wan Study Area.* GEO Report no. 60. Geotechnical Engineering Office, Civil Engineering Dept., Hong Kong, 78 pp.

Capra, L., Lugo-Hubp, J. and Borselli, L., 2003. Mass movements in tropical volcanic terrains: the case of Teziutlan (Mexico). *Engineering Geology*, 69(3-4): 359-379.

Carson, M., 1971. *The Mechanics of Erosion.* Pion, London, 174 pp.

Carson, M. and Kirkby, M., 1972. *Hillslope Form and Process.* University Press, Cambridge, 475 pp.

Casagrande, A., 1936, Characteristics of cohesionless soils affecting the stability of slopes and earth fills. *Journal of the Boston Society of Civil Engineers*, 23, 13–32.

Catt, P., 1986. Vegetation. In: T. Chiu and C. So (Editors), *A Geography of Hong Kong.* Oxford University Press, Hong Kong, pp. 118-147.

Chang, M., Chiu, Y., Lin, S. and Ke, T.-C., 2005. Preliminary study on the 2003 slope failure in Woo-wan-chai Area, Mt. Ali Road, Taiwan. *Engineering Geology*, 80(1-2): 93-114.

Chen, C.Y., Chen, T.C., Yu, F.C. and Lin, S.C., 2005a. Analysis of time-varying rainfall infiltration induced landslide. *Environmental Geology*, 48(4-5): 466-479.

Chen, H., Lee, C.F. and Law, K.T., 2004. Causative mechanisms of rainfall-induced fill slope failures. *Journal of Geotechnical and Geoenvironmental Engineering*, June: 593-602.

Chen, H., Lee, C.F. and Shen, J.M., 2000. Mechanisms of rainfall-induced landslides in Hong Kong. In: G.F. Wieczorek and N.D. Naeser (Editors), *Debris-flow Hazards Mitigation : Mechanics, Prediction, and Assessment : Proceedings of the 2nd International Conference on Debris Flows, Taipei.* Rotterdam: Balkema, Taipei, pp. 53-60.

Chen, P.W.M., 1996. *Methods of Test for Soils in Hong Kong for Civil Engineering Purposes (Phase I Tests).* GEO report ; no. 36. Geotechnical Engineering Office, Civil Engineering Dept., Hong Kong, 90 pp.

Chen, R.H. and Yang, S.C., 2000. Study on debris-flow triggered by pore water pressure. In: G.F. Wieczorek and N.D. Naeser (Editors), *Debris-flow Hazards Mitigation : Mechanics, Prediction, and Assessment : Proceedings of the 2nd International Conference on Debris Flows, Taipei.* Rotterdam: Balkema, Taipei, pp. 61-65.

Chin, P., 1986. Climate and weather. In: T. Chiu and C. So (Editors), *A Geography of Hong Kong.* Oxford University Press, Hong Kong, pp. 69-85.

Chu, J., Leroueil, S. and Leong, W.K., 2003. Unstable behaviour of sand and its implication for slope instability. *Canadian Geotechnical Journal*, 40(5): 873-885.

Coe, J.A., Ellis, W.L., Godt, J.W., Savage, W.Z., Savage, J.E., Michael, J.A., Kibler, J.D., Powers, P.S., Lidke, D.J. and Debray, S., 2003. Seasonal movement of the Slumgullion landslide determined from Global Positioning System surveys and field instrumentation, July 1998-March 2002. *Engineering Geology*, 68(1-2): 67-101.

Cooper, M.R., Bromhead, E.N., Petley, D.J. and Grant, D.I., 1998. The Selborne cutting stability experiment. *Geotechnique*, 48: 83-101.

Cornelius, R.R. and Scott, P.A., 1993. A materials failure relation of accelerating creep as empirical description of damage accumulation. *Rock Mechanics and Rock Engineering*, 26(3): 233-252.

Craig, R.F., 1997. *Soil Mechanics*. Spon Press, London, 485 pp.

Cristescu, N.D., Cazacu, O. and Cristescu, C., 2002. A model for slow motion of natural slopes. *Canadian Geotechnical Journal*, 39(4): 924-937.

Crozier, M.J., 1986. Landslides : Causes, Consequences and Environment. Croom Helm, London, 252 pp.

Cruden, D. and Varnes, D., 1996. Landslide types and processes. In: A. Turner and R. Schuster (Editors), *Landslides : Investigation and Mitigation*. National Academy Press, Washington, D.C., pp. 36-75.

Dai, F., Lee, C., Li, J. and Xu, Z., 2001. Assessment of landslide susceptibility on the natural terrain of Lantau Island, Hong Kong. *Environmental Geology*, 40(3): 381-391.

Dai, F.C. and Lee, C.F., 2002. Landslide characteristics and slope instability modeling using GIS, Lantau Island, Hong Kong. *Geomorphology*, 42(3-4): 213-228.

Dai, F.C., Lee, C.F., Tham, L.G., Ng, K.C. and Shum, W.L., 2004. Logistic regression modelling of storm-induced shallow landsliding in time and space on natural terrain of Lantau Island, Hong Kong. *Bulletin of Engineering Geology and the Environment*, 63(4): 315-327.

Dai, F.C., Lee, C.F. and Wang, S., 1999a. Analysis of rainstorm-induced slide-debris flows on natural terrain of Lantau Island, Hong Kong. *Engineering Geology*, 51(4): 279-290.

Dai, F.C., Lee, C.F., Wang, S.J. and Feng, Y.Y., 1999b. Stress-strain behaviour of a loosely compacted volcanic-derived soil and its significance to rainfall-induced fill slope failures. *Engineering Geology*, 53: 359-370.

De la Cruz-Reyna, S. and Reyes-Davila, G.A., 2001. A model to describe precursory material-failure phenomena: applications to short-term forecasting at Colima volcano, Mexico. *Bulletin of Volcanology*, 63(5): 297-308.

Deutscher, M.S., Gasmo, J.M. and Leong, E.C., 2000. Field measurements of pore-water pressure profiles in residual soil slopes of the Bukit Timah Granite Formation, Singapore. In: H. Rahardjo, D.G. Toll and E.C. Leong (Editors), *Unsaturated soils for Asia : Proceedings of the Asian Conference on Unsaturated Soils UNAT-ASIA 2000, Singapore, 18-19 May 2000.* A.A. Balkema, Rotterdam, pp. 777-782.

Dietrich, W. and Sitar, N., 1997. Geoscience and geotechnical engineering aspects of debris-flow hazard assessment. In: C. Chen (Editor), *Debris-flow Hazards Mitigation : Mechanics, Prediction, and Assessment : Proceedings of First International Conference: San Francisco, California, August 7-9, 1997.* American Society of Civil Engineers, New York, pp. 656-676.

Dixon, N., 2007. *Personal communication.*

Duncan, J., 1996b. Soil slope stability analysis. In: A. Turner and R. Schuster (Editors), *Landslides : Investigation and Mitigation.* National Academy Press, Washington, D.C., pp. 337-371.

Duncan, J.M., 1992. State of the art – static stability and deformation analysis in stability and performance of slopes and embankments II. *ASCE Geotechnical Special Publication*, 31, 222-266.

Duncan, J.M., 1996a. State of the art: Limit equilibrium and finite-element analysis of slopes. *Journal of Geotechnical Engineering*, 122(7): 577-596.

Duzgoren-Aydin, N., Aydin, A. and Malpas, J., 2002. Distribution of clay minerals along a weathered pyroclastic profile, Hong Kong. *Catena*, 50: 17-41.

Dykes, A.P. and Thornes, J.B., 2000. Hillslope hydrology in tropical rainforest steeplands in Brunei. *Hydrological Processes*, 14: 215-235.

Eberhardt, E., Stead, D. and Coggan, J.S., 2004. Numerical analysis of initiation and progressive failure in natural rock slopes--the 1991 Randa rockslide. *International Journal of Rock Mechanics and Mining Sciences*, 41(1): 69-87.

Ebuk, E.J., 1991. *Influence of Fabric on the Shear Strength Characteristics of Weathered Granites*. PhD Thesis, University of Leeds, 486 pp.

ELE International, 2004. *Online Instruction Manuals - Soil test.* http://eleusa.com/ Accessed on November 7, 2004

Evans, N.C., 1998. The natural terrain landslide study. In: K.S. Li, J.N. Kay and K.K.S. Ho (Editors), *Slope Engineering In Hong Kong*. A.A. Balkema, Rotterdam, pp. 137-144.

Evans, N.C., King, J.P. and Huang, S.W., 1999. *The Natural Terrain Landslide Study : Phases I and II*. GEO report ; no. 73. Geotechnical Engineering Office, Civil Engineering Dept., Hong Kong, 128 pp.

Evans, N.C. and Lam, K.C., 2003. *Tung Chung East Natural Terrain Study Area-Ground Movement and Groundwater Monitoring Equipment and Preliminary Results*. GEO report ; no. 142. Geotechnical Engineering Office, Civil Engineering Dept., Hong Kong, 105 pp.

Faisal, H.A., 2000. Unsaturated tropical residual soils and rainfall induced slope failures in Malaysia. In: D.G. Toll and E.C. Leong (Editors), *Unsaturated Soils for Asia*. Balkema, Rotterdam, pp. 41-52.

Fan, C.H., Allison, R.J. and Jones, M.E., 1994. The effects of tropical weathering on the characteristics of Argillaceous rocks. In: D.A. Robinson and R.B.G. Williams (Editors), *Rock Weathering and Landform Evolution*. Wiley, Chichester, pp. 339-354.

Fan, C.H., Allison, R.J. and Jones, M.E., 1996. Weathering effects on the geotechnical properties of argillaceous sediments in tropical environments and their geomorphological implications. *Earth Surface Processes and Landforms*, 21: 49-66.

Farooq, K., Orense, R. and Towhata, I., 2004. Response of unsaturated sandy soils under constant shear stress drained condition. *Soils and Foundations*, 44(2): 1-13.

Federico, A., Fidelibus, C. and Interno, G., 2002. The prediction of landslide time to failure - a state of the art. *3th International Conference for Landslides, Slope Stability & the Safety of Infra-Structure: 11-12 July 2002, Singapore*, pp. 167-180.

Federico, A., Popescu, M., Fidelibus, C. and Internò, G., 2004. On the prediction of the time of occurrence of a slope failure: a review. In: W.A. Lacerda, M. Ehrlich, S.A.B. Fontoura and A.S.F. Sayão (Editors), *Landslide: Evaluation and Stabilization. Proceedings of the 9th International Symposium on Landslides, Rio de Janeiro, June 28-July 2, 2004.* Leiden : A. A. Balkema, pp. 979-1188.

Fell, R., Hungr, O., Leroueil, S. and Riemer, W., 2000. Keynote lecture - geotechnical engineering of the stability of natural slopes, and cuts and fills. *Proceedings of the Geoengineeing Conference, Melbourne*, pp. 21-120.

Fookes, P.G., 1997. *Tropical Residual Soils: A Geological Society Engineering Group Working Party Revised Report*. The Geological Society, London, 184 pp.

Foss, I. 1973. Red soils from Kenya as a foundation material. *Proceedings of the Eighth International Conference on Soil Mechanics and Foundation Engineering, Moscow*, 2, 73-80.

Franks, C.A.M., 1998. *Study of Rainfall-induced Landslides on Natural Slopes in the Vicinity of Tung Chung New Town, Lantau Island.* GEO report ; no. 57. Geotechnical Engineering Office, Civil Engineering Dept., Hong Kong, 102 pp.

Franks, C.A.M., 1999. Characteristics of some rainfall-induced landslides on natural slopes, Lantau Island, Hong Kong. *Quarterly Journal of Engineering Geology*, 32(3): 247-259.

Franks, C.A.M., Campbell, S.D.G. and Shum, W.W.L., 1999. *Assessment of Geological Features Related to Recent Landslides in Volcanic Rocks of Hong Kong Phase 2B : Aberdeen Study Area.* GEO report ; no. 67. Geotechnical Engineering Office, Civil Engineering Dept., Hong Kong, 106 pp.

Franks, C.A.M. and Woods, N.W., 1993. Engineering geology of North Lantau, Hong Kong. *Quarterly Journal of Engineering Geology*, 26: 81-98.

Fredlund, D.G. and Rahardjo, H., 1993. *Soil Mechanics for Unsaturated Soils*. Wiley, New York ; Chichester, 517 pp.

Fukuzono, T., 1985. A new method for prediciting the failure time of a slope. *Proceedings of the 4th International Conference and Field Workshop on Landslides, 1985, Tokyo*, pp. 145-150.

Fukuzono, T., 1990. Recent studies on time prediction of slope failure. *Landslide News*, 4: 9-12.

Fukuzono, T.,1996. Creep model of Kanto loam and its application to time prediction of landslide. *Proceedings of the 8th International Conference and Field Trip on Landslides, Granada, Spain*. Balkema, pp. 221-233.

Fyfe, J.A., Shaw, R., Campbell, S.D.G., Lai, K.W. and Kirk, P.A., 2000. *The Quaternary Geology of Hong Kong*. Hong Kong Geological Survey, Geotechnical Engineering Office, Civil Engineering Dept., Hong Kong, 209 pp.

Gabet, E.J. and Mudd, S.M., 2006. The mobilization of debris flows from shallow landslides. *Geomorphology*, 74(1-4): 207-218.

Gan, J.K.M. and Fredlund, D.G., 1996. Shear strength characteristics of two saprolitic soils. *Canadian Geotechnical Journal*, 33: 595-609.

Gasmo, J.M., Rahardjo, H. and Leong, E.C., 2000. Infiltration effects on stability of a residual soil slope. *Computers and Geotechnics*, 26: 145-165.

Geotechnical Control Office (GCO), 1982. *Mid-Levels Study : Report on Geology, Hydrology and Soil Properties*. Government Printer, Hong Kong, 264 pp.

Geotechnical Control Office (GCO), 1988a. *North Lantau*. Geotechnical Area Studies Programme (GASP) Report. Government Printer, Hong Kong, 124 pp.

Geotechnical Control Office (GCO), 1988b. *South Lantau.* Geotechnical Area Studies Programme (GASP) Report XI. Government Printer, Hong Kong, 148 pp.

Geotechnical Engineering Office (GEO), 1994a. *Report on the Kwun Lung Lau landslide of 23 July 1994. Volume 2: Findings of the Landslide Investigation, Hong Kong*, 379 pp.

Geotechnical Engineering Office (GEO), 1994b. *Tung Chung: Sheet 9, Solid and Superficial Geology.* Series HGM20. 1: 20000 scale. Hong Kong Geological Survey, Hong Kong.

Geotechnical Engineering Office (GEO), 1996. *Fung Wong Shan (Lantau Peak): Sheet 9-SE-C, Solid and Superficial Geology.* Series HGP5. 1: 5000 scale. Hong Kong Geological Survey, Hong Kong.

Geotechnical Engineering Office (GEO), 2000. *Guide to Rock and Soil Descriptions.* Geoguide 3. Geotechnical Engineering Office, Civil Engineering Department, Hong Kong, 186 pp.

Geotechnical Engineering Office (GEO), 2004. Planning Division. *Personal communication.*

Geotechnical Observations Limited (GOL), 2002. *Shallow Pore Pressure Measurements in a Natural Terrain Slope, Tung Chung, Lantau Island, Hong Kong.* Department of Civil & Environmental Engineering, Imperial College of Science, Technology & Medicine, London, 8 p plus appendices.

Gerscovich, D.M.S., Vargas, J., E.A. and de Campos, T.M.P., 2006. On the evaluation of unsaturated flow in a natural slope in Rio de Janeiro, Brazil. *Engineering Geology*, 88(1-2): 23-40.

He, K. and Wang, S., 2006. Double-parameter threshold and its formation mechanism of the colluvial landslide: Xintan landslide, China. *Environmental Geology*, 49(5): 696 - 707.

Head, K.H., 1998. *Manual of Soil Laboratory Testing, Volume 3: Effective Stress Tests.* John Wiley & Sons, Chichester, 428 pp.

Helmstetter, A., Sornette, D., Grasso, J.R., Andersen, J.V., Gluzman, S. and Pisarenko, V., 2004. Slider block friction model for landslides: Application to Vaiont and La Clapiere landslides. *Journal of Geophysical Research-Solid Earth*, 109(B2), 15pp.

Hong, Y., Hiura, H., Shino, K., Sassa, K., Suemine, A., Fukuoka, H. and Wang, G.H., 2005. The influence of intense rainfall on the activity of large-scale crystalline schist landslides in Shikoku Island, Japan. *Landslides*, 2(2): 97-105.

Hong Kong Geological Survey, 1999. *Geological Map of Hong Kong*. Series AR/3/G. Geotechnical Engineering Office, Civil Engineering Department.

Hong Kong Observatory (HKO), 2003. *Monthly Normals of Meteorological Elements for Hong Kong, 1971-2000.* http://www.hko.gov.hk/cis/normal/1971_2000/enormal.htm. Accessed on March 22, 2007.

Hong Kong Special Administrative Region (HKSAR) Government, 2006. *Hong Kong in Brief*. http://www.info.gov.hk/info/hkbrief/eng/ahk.htm
Accessed on January 10, 2007.

Hutchinson, J., 2001. Landslide risk - to know, to foresee, to prevent. *Geologica Tecnica & Ambientale*, 9: 3-24.

Hutchinson, J.N., 1988. General report: morphological and geotechnical parameters of landslides in relation to geology and hydrogeology. *Proceedings of the 5th International Symposium of Landslides.* Balkema, pp. 3-35.

Hutchinson, J.N., 1995. Keynote paper: landslide hazard assessment. *Landslides: Proceedings of the 6th International Symposium, 10-14 February, 1992.* A.A.Balkema, Rotterdam, pp. 1805-1841.

Irfan, T., 1999. Characterization of weathered volcanic rocks in Hong Kong. *Quarterly Journal of Engineering Geology*, 32: 317-348.

Irfan, T.Y., 1994. Mechanism of creep in a volcanic saprolite. *Quarterly Journal of Engineering Geology*, 27: 211-230.

Irfan, T.Y., 1996. *Mineralogy and Fabric Characterization and Classification of Weathered Granitic Rocks in Hong Kong.* GEO report ; no. 41. Geotechnical Engineering Office, Civil Engineering Department, Hong Kong, 158 pp.

Irfan, T.Y., 1998a. *Mineralogical and Fabric Characterization and Classification of Weathered Volcanic Rocks in Hong Kong.* GEO report ; no. 66. Geotechnical Engineering Office, Civil Engineering Dept., Hong Kong, 113 pp.

Irfan, T.Y., 1998b. Structurally controlled landslides in saprolitic soils in Hong Kong. *Geotechnical and Geological Engineering*, 16: 215-238.

Iverson, R.M., 2000. Landslide triggering by rain infiltration. *Water Resources Research*, 36(7): 1897-1910.

Iverson, R.M., 2005. Regulation of landslide motion by dilatancy and pore pressure feedback. *Journal of Geophysical Research-Earth Surface*, 110(F2): Article no.-F02015.

Jiao, J.J., Wang, X.-S. and Nandy, S., 2005. Confined groundwater zone and slope instability in weathered igneous rocks in Hong Kong. *Engineering Geology*, 80(1-2): 71-92.

Junaideen, S.M., 2005. *Failure of Saturated Sandy Soils due to Increase in Pore Water Pressure.* PhD Thesis, The University of Hong Kong, Hong Kong, 244 pp.

Kalaugher, P.G., Hodgson, R.L.P. and Grainger, P., 2000. Pre-failure strains as precursors of sliding in a coastal mudslide. *Quarterly Journal of Engineering Geology and Hydrogeology*, 33: 325-334.

Karintzis, V., 2005. *Mechanisms of Deep-seated Landslides.* Unpublished MSc Thesis, Durham University, United Kingdom, 86 pp.

Kenney, C., 1984. Properties and behaviours of soils relevant to slope instability. In: D. Brunsden and D. Prior (Editors), *Slope Instability.* John Wiley & Sons Ltd., Chichester, pp. 27-65.

Kilburn, C.R.J. and Petley, D.N., 2003. Forecasting giant, catastrophic slope collapse: lesson from Vajont, Northern Italy. *Geomorphology*, 54: 21-32.

King, J.P., 1999. *Natural Terrain Landslide Study : the Natural Terrain Landslide Inventory*. GEO report ; no. 74. Geotechnical Engineering Office, Civil Engineering Dept., Hong Kong, 127 pp.

Kuhn, M.R. and Mitchell, J.K., 1993. New perspectives on soil creep. *Journal of Geotechnical Engineering-Asce*, 119(3): 507-524.

Kwong, J., Spengler, S., Wong, N. and Wan, A., 1999. Some important engineering geological and hydrogeological factors influencing slope stability in Hong Kong and Hawaii. In: B. Clarke (Editor), *Urban Ground Engineering : Proceedings of the International Conference organized by the Institution of Civil Engineers and held in Hong Kong, China, on 11-12 November 1998*. Thomas Telford, London, pp. 235-252.

Lan, H.X., Lee, C.F., Zhou, C.H. and Martin, C.D., 2005. Dynamic characteristics analysis of shallow landslides in response to rainfall event using GIS. *Environmental Geology*, 47(2): 254-267.

Langford, R., James, J., Shaw, R., Campbell, S., Kirk, P. and Sewell, R., 1995. *Geology of Lantau district : 1:20000 Sheets 9,10,13 & 14. Hong Kong Geological Survey Memoir* ; no. 6. Geotechnical Engineering Office, Civil Engineering Dept., Hong Kong, 173 pp.

Larsen, M. and Torres-Sánchez, A., 1998. The frequency and distribution of recent landslides in three montane tropical regions of Puerto Rico. *Geomorphology*, 24: 309-331.

Lee, S. and Talib, J.A., 2005. Probabilistic landslide susceptibility and factor effect analysis. *Environmental Geology*, 47(7): 982-990.

Leroueil, S. and Vaughan, P.R., 1990. The general and congruent effects of structure in natural soils and weak rocks. *Geotechnique*, 40(3): 467-488.

Li, A.G., Yue, Z.Q., Tham, L.G., Lee, C.F. and Law, K.T., 2005. Field-monitored variations of soil moisture and matric suction in a saprolite slope. *Canadian Geotechnical Journal*, 42(1): 13-26.

Lim, T.T., Rahardjo, H., Chang, M.F. and Fredlund, D.G., 1996. Effect of rainfall on matric suctions in a residual soil slope. *Canadian Geotechnical Journal*, 33: 618-628.

Lourenço, S.D.N., Sassa, K. and Fukuoka, H., 2006. Failure process and hydrologic response of a two layer physical model: Implications for rainfall-induced landslides. *Geomorphology*, 73(1-2): 115-130.

Lumb, P., 1962. General nature of the soils of Hong Kong. In: P. Lumb (Editor), *Proceedings of the Symposium on Hong Kong soils, May 1962*. Local Property & Printing Co., Hong Kong, pp. 19-31.

Lumb, P., 1965. The residual soils of Hong Kong. *Geotechnique*, 15: 180-194.

Lumb, P., 1975. Slope failures in Hong Kong. *Quarterly Journal of Engineering Society*, 8: 31-65.

Lumb, P. and Lee, C.F., 1975. Clay mineralogy of the Hong Kong soils. *Proceedings of the 4th Southeast Asian Conference on Soil Engineering*, Kuala Lumpur, Malaysia, 7th - 10th April, 1975, pp. 1-41.

Maail, S., Huat, B.B.K. and Jamaludin, S., 2004. Index, engineering properties and classification of tropical residual soils. In: B.B.K. Huat, G. See-Sew and F.H. Ali (Editors), *Tropical Residual Soils Engineering*. A.A. Balkema, London, pp. 37-55.

Maharaj, R., 1993. Landslide processes and landslide susceptibility analysis from an upland watershed: a case study from St. Andrew, Jamaica, West Indies. *Engineering Geology*, 34: 53-79.

Main, I.G., 1999. Applicability of time-to-failure analysis to accelerated strain before earthquakes and volcanic eruptions. *Geophysical Journal International*, 139: F1-F6.

Main, I.G., 2000. A damage mechanics model for power-law creep and earthquake aftershock and foreshock sequences. *Geophysical Journal International*, 142: 151-161.

Matsukura, Y., 1996. The role of the degree of weathering and groundwater fluctuation in landslide movement in a colluvium of weathered hornblende-gabbro. *Catena*, 27: 63-78.

McFeat-Smith, I., Workman, D., Burnett, A. and Chau, E., 1989. Geology of Hong Kong. *Bulletin of the Association of Engineering Geologists*, XXVI(1): 23-107.

Menzies, B.K., 1988. A computer controlled hydraulic triaxial testing system. In: R.T. Donaghe, R.C. Chaney and M.L. Silver (Editors), *Advanced Triaxial Testing of Soil and Rock, ASTM STP 977*. American Society for Testing and Materials, Philadelphia, pp. 82-94.

Mitchell, J.K. and Sitar, N., 1982. Engineering properties of tropical residual soils. *Proceedings of the Conference on Engineering and Construction in Tropical and Residual Soils*, ASCE, Honolulu, Hawaii, January 11-15, 1982, pp. 30-57.

Mitchell, J.K. and Soga, K., 2005. *Fundamentals of Soil Behaviour*. John Wiley & Sons, Hoboken, New Jersey, 577 pp.

National Meteorological & Hydrological Services (NMHSs), 2007. *World Weather Information Service*. http://worldweather.wmo.int/
Accessed on April 1, 2007.

Nemat-Nasser, S., 2004. *Plasticity : A Treatise on the Finite Deformation of Heterogeneous Inelastic Materials*. Cambridge University Press, Cambridge, 730 pp.

Ng, C.W.W. and Pang, Y.W., 2000. Influence of stress state on soil-water characteristics and slope stability. *Journal of Geotechnical and Geoenvironmental Engineering*, 126(2): 157-166.

Ng, C.W.W., Wang, B. and Tung, Y.K., 2001. Three-dimensional numerical investigations of groundwater responses in an unsaturated slope subjected to various rainfall patterns. *Canadian Geotechnical Journal*, 38(5): 1049-1062.

Ng, K.C., Parry, S., King, J.P., Franks, C.A.M. and Shaw, R., 2002. *Guidelines for Natural Terrain Hazard Studies*. Special Project Report ; SPR 1/2002. Geotechnical Engineering Office, Civil Engineering Dept., Hong Kong, 136 pp.

Ng, K.Y., 2001. Factors affecting the spatial distribution of landslides on Lantau Island-A statistical approach. *Hong Kong Geologist*, 7: 9-17.

Nicholson, P.G., Russell, P.W. and Fujii, C.F.,1996. Soil creep and creep testing of highly weathered tropical soils. In: T.C. Sheahan and V.N. Kaliakin (Editors), *Measuring and Modeling Time Dependent Soil Behavior : Proceedings of Sessions. Geo-Institute of the American Society of Civil Engineers in conjunction with the ASCE Convention in Washington, D.C., November 10-14, 1996.* American Society of Civil Engineers, pp. 195-213.

Ochiai, H., Okada, Y., Furuya, G., Okura, Y., Matsui, T., Sammori, T., Terajima, T. and Sassa, K., 2004. A fluidized landslide on a natural slope by artificial rainfall. *Landslides*, 1: 211-219.

Ohtsuka, S. and Miyata, Y., 2001. Consideration on landslide mechanism based on pore water pressure loading test. *Proceedings of the Fifteenth International Conference on Soil Mechanics and Geotechnical Engineering : Istanbul, 27-31 August 2001.* Lisse : Balkema, pp. 1233-1236.

Okamoto, T., Larsen, J.O., Matsuura, S., Asano, S., Takeuchi, Y. and Grande, L., 2004. Displacement properties of landslide masses at the initiation of failure in quick clay deposits and the effects of meteorological and hydrological factors. *Engineering Geology*, 72(3-4): 233-251.

Parry, R.H.G. (Editor), 2004. *Mohr Circles, Stress Paths and Geotechnics.* Spon Press, London, 264 pp.

Petley, D., 1996. The mechanics and landforms of deep-seated landslides. In: M. Anderson and S. Brooks (Editors), *Advances in Hillslope Processes*, pp. 823-835.

Petley, D.N., 2004. The evolution of slope failures: mechanisms of rupture propagation. *Natural Hazards and Earth System Sciences*, 4: 147-152.

Petley, D.N. and Allison, R.J., 1997. The mechanics of deep-seated landslides. *Earth Surface Processes and Landforms*, 22: 747-758.

Petley, D.N. and Bulmer, M.H., 2004. The application of Earth observation technologies for landslide disaster mitigation. *Proceedings of the CEOS Workshop, November 2004*, Beijing.

Petley, D.N., Bulmer, M.H. and Murphy, W., 2002. Patterns of movement in rotational and translational landslides. *Geology*, 30(8): 719-722.

Petley, D.N., Carey, J., Rosser, N.J. and Dunning, S.A., 2007. Temporal prediction in landslides – understanding the Saito effect. Geophysical Research Abstracts, vol. 9, 07977. SRef-ID: 1607-7962/gra/EGU2007-A-07977.

Petley, D.N., Dunning, S.A. and Rosser, N.J., 2005a. The analysis of global landslide risk through the creation of a database of worldwide landslide fatalities. *Landslide risk management : Proceedings of the International Conference on Landslide Risk Management, Vancouver, Canada, 31 May-3 June 2005.* Taylor & Francis, London, pp. 367-373.

Petley, D.N., Higuchi, T., Petley, D.J., Bulmer, M.H. and Carey, J., 2005b. Development of progressive landslide failure in cohesive materials. *Geology*, 33(3): 201-204.

Petley, D.N., Mantovani, F., Bulmer, M.H. and Zannoni, A., 2005c. The use of surface monitoring data for the interpretation of landslide movement patterns. *Geomorphology*, 66: 133-147.

Petley, D.N. and Petley, D.J., 2006. On the initiation of large rockslides: perspectives from a new analysis of the Vaiont movement record. In: S.G. Evans, G.S. Mugnozza, A. Strom and R.L. Hermanns (Editors), *Landslides from Massive Rock Slope Failure. NATO Science Series IV: Earth and Environmental Sciences*. Springer, Dordrecht, pp. 77-84.

Picarelli, L., 2000. Mechanisms and rates of slope movements in fine grained soils. In: *GEO2000: an International Conference on Geotechnical & Geological Engineering, 19-24 November 2000, Melbourne, Australia*. Lancaster, Pa. : Technomic Publishing Co., pp. 1618-1670.

Picarelli, L., Urciuoli, G. and Russo, C., 2004. Effect of groundwater regime on the behaviour of clayey slopes. *Canadian Geotechnical Journal*, 41(3): 467-484.

Qin, S.Q., Jiao, J.J. and Li, Z.G., 2006. Nonlinear evolutionary mechanisms of instability of plane-shear slope: Catastrophe, bifurcation, chaos and physical prediction. *Rock Mechanics and Rock Engineering*, 39(1): 59-76.

Qin, S.Q., Jiao, J.J. and Wang, S.J., 2001. The predictable time scale of landslides. *Bulletin of Engineering Geology and the Environment*, 59(4): 307-312.

Qin, S.Q., Jiao, J.J. and Wang, S.J., 2002. A nonlinear dynamical model of landslide evolution. *Geomorphology*, 43(1-2): 77-85.

Queiroz de Carvalho, J.B. and Simmons, J.V., 1997. Mineralogy and microstructure. In: G.E. Blight (Editor), *Mechanics of Residual Soils: A Guide to the Formation, Classification and Geotechnical Properties of Residual Soils, with Advice for Geotechnical Design*. A.A. Balkema, Rotterdam, pp. 30-40.

Rahardjo, H., Aung, K.K., Leong, E.C. and Rezaur, R.B., 2004. Characteristics of residual soils in Singapore as formed by weathering. *Engineering Geology*, 73: 157-169.

Rahardjo, H., Lee, T., Leong, E. and Rezaur, R., 2005. Response of a residual soil slope to rainfall. *Canadian Geotechnical Journal*, 42(2): 340-351.

Rahardjo, H., Leong, E.C., Gasmo, J.M. and Tang, S.K., 1998. Assessment of rainfall effects on stability of residual soil slopes. *Proceedings of the Second International Conference on Unsaturated Soils, 27-30 August 1998, Beijing, China*. International Academic Publishers, Beijing, pp. 280-285.

Rahardjo, H., Lim, T.T., Chang, M.F. and Fredlund, D.G., 1995. Shear-strength characteristics of a residual soil. *Canadian Geotechnical Journal*, 32: 60-77.

Ranalli, G., 1995. *Rheology of the Earth*. Chapman & Hall, London, 413pp.

Rao, S.M., 1996. Role of apparent cohesion in the stability of Dominican allophane soil slopes. *Engineering Geology*, 43(4): 265-279.

Rao, S.M. and Revanasiddappa, K., 2002. Collapse behaviour of a residual soil. *Geotechnique*, 52(4): 259-268.

Reid, M.E., Nielsen, H.P. and Dreiss, S.J., 1988. Hydrologic factors triggering a shallow hillslope failure. *Bulletin of the Assoication of Engineering Geologists*, XXV(3): 349-361.

Rezaur, R.B., Rahardjo, H. and Leong, E.C., 2002. Spatial and temporal variability of pore-water pressures in residual soil slopes in a tropical climate. *Earth Surface Processes and Landforms*, 27: 317-338.

Rezaur, R.B., Rahardjo, H., Leong, E.C. and Lee, T.T., 2003. Hydrologic behavior of residual soil slopes in Singapore. *Journal of Hydrologic Engineering*, 8(3): 133-144.

Rosenfeld, C., 1994. The geomorphological dimensions of natural disasters. *Geomorphology*, 10: 27-36.

Saito, M., 1965. Forecasting the time of occurrence of a slope failure. *Proceedings of the 6th International Conference on Soil Mechanics and Foundation Engineering, Montreal*, pp. 537-541.

Saito, M., 1969. Forecasting time of slope failure by tertiary creep. *Proceedings of the 7th International Conference Soil Mechanics Foundation Engineering, Mexico*, pp. 677-683.

Saito, M. and Uezawa, H., 1961. Failure of soil due to creep. *Proceedings of the 5th International Conference on Soil Mechanics and Foundation Engineering, Paris, July 17-22*, pp. 315-319.

Salt, G.A. 1985. Aspects of landslide mobility. *Proceedings of the 11th International Conference on Soil Mechanics and Foundation Engineering, San Francisco*, 3, pp. 1167-1172.

Santos, O.F., Lacerda, W.A. and Ehrlich, M., 1996. Collapse of saturated soil due to reduction in confinement - Discussion. *Journal of Geotechnical Engineering*, 122(6): 505-506.

Sassa, K., Fukuoka, H., Wang, G. and Ishikawa, N., 2004. Undrained dynamic-loading ring-shear apparatus and its application to landslide dynamics. *Landslides*, 1: 7-19.

Schuster, D., 1996. Socioeconomic significance of landslides. In: A. Turner and R. Schuster (Editors), *Landslides : Investigation and Mitigation*. National Academy Press, Washington, D.C., pp. 12-35.

Selby, M., 1993. *Hillslope Materials and Processes*. Oxford University Press, Oxford, England, 451 pp.

Sewell, R. and Fletcher, C., 2000. *Pilot Study on Regolith Mapping in Hong Kong*. Geological Report GR1/2000. Planning Division, Geotechnical Engineering Office, Hong Kong, 45 pp.

Sharpe, C.F.S. 1938. *Landslides and the Related Phenomena: A Study of Mass Movements of Soil and Rock*. Pageant, New Jersey, 137pp.

Shaw-Shong, L., 2004. Slope failures in tropical residual soils. In: Huat, B.B.K., Sew, G.S., Ali, F.Hj. (Editors). *Tropical Residual Soils Engineering*. A.A. Balkema, Leiden, pp. 73-100.

Shroder, J.F., Cverckova, L. and Mulhern, K.L., 2005. Slope-failure analysis and classification: review of a century of effort. *Physical Geography*, 26(3): 216-247.

Shuzui, H. 2001. Process of slip-surface development and formation of slip-surface clay in landslides in Tertiary volcanic rocks, Japan. *Engineering Geology*, 61, 199-220.

Singh, B. and Mitchell, J.K., 1968. General stress-strain-time function for soils. Journal of the Soil Mechanics and Foundation Division. *Proceedings of the American Society of Civil Engineers*, 94: 21-46.

Sitar, N., MacLaughlin, M.M. and Doolin, D.M., 2005. Influence of kinematics on landslide mobility and failure mode. *Journal of Geotechnical and Geoenvironmental Engineering*, 131(6): 716-728.

Skempton, A.W. and Hutchinson, J.N., 1969. Stability of natural slopes and embankment foundations, state-of-the-art report. *Proceedings of the 7th International Conference on Soil Mechanics and Foundation Engineering, Mexico*, 4, pp. 291-340.

Smith, G.N. and Smith, I.G.N. (Editors), 1998. *Elements of Soil Mechanics*. Blackwell Science, Oxford, 494 pp.

Sornette, D., Helmstetter, A., Andersen, J.V., Gluzman, S., Grasso, J.R. and Pisarenko, V., 2004. Towards landslide predictions: two case studies. *Physica A-Statistical Mechanics and Its Applications*, 338(3-4): 605-632.

Springman, S.M., Jommi, C. and Teysseire, P., 2003. Instabilities on moraine slopes induced by loss of suction: a case study. *Geotechnique*, 53(1): 3-10.

Summerfield, M.A., 1991. *Global Geomorphology : An Introduction to the Study of Landforms*. Longman Scientific & Technical, Harlow, Essex, 537 pp.

Terlien, M.T.J., 1998. The determination of statistical and deterministic hydrological landslide-triggering thresholds. *Environmental Geology*, 35(2-3): 124-130.

Ter-Stepanian, G., 1980. Creep on natural slopes and cuttings. *Proceedings of the 3rd International Symposium of Landslides, Sarita Prakashan*, pp. 95-108.

Terzaghi, K., 1936. The shearing resistance of saturated soils. *Proceedings of the 1st International Conference on Soil Mechanics, Cambridge, MA*, 1, 54-56.

Terzaghi, K., 1950. Mechanism of landslides. In: Geological Society of America (Editor), *Application of Geology to Engineering Practice : Berkley Volume*. Geological Society of America, New York, pp. 83-123.

Terzaghi, K., 1953. Discussion on stability and deformation of slopes and earth dams. *Proceedings Third International Conference on Soil Mechanics*, Zurich, 3, pp. 217-218.

Terzaghi, K., Peck, R.B. and Mesri, G., 1996. *Soil Mechanics in Engineering Practice*. John Wiley and Sons, New York, 549 pp.

Thomas, M., 1994. *Geomorphology in the Tropics : A Study of Weathering and Denudation in Low Latitudes.* John Wiley & Sons Ltd., Chichester, 460 pp.

Toll, D.G., 1999. A data acquisition and control system for geotechnical testing. In: B. Kumar and B.H.V. Topping (Editors), *Computing developments in civil and structural engineering.* Civil-Comp, Edinburgh, pp. 237-242.

Toll, D.G., 2001. Rainfall-induced landslides in Singapore. *Proceedings of the Institution of Civil Engineers-Geotechnical Engineering*, 149(4): 211-216.

Toll, D.G., 2002. *TRIAX User Manual. Version 4.2.* Geotechnical Systems Group, Durham University, 33 pp.

Tsaparas, I., Rahardjo, H., Toll, D.G. and Leong, E.C., 2002. Controlling parameters for rainfall-induced landslides. *Computers and Geotechnics*, 29(1): 1-27.

Tsaparas, I., Rahardjo, H., Toll, D. and Leong, E.C., 2003. Infiltration characteristics of two instrumented residual soil slopes. *Canadian Geotechnical Journal*, 40(5): 1012-1032.

Tsutiya, A.M., Tanaka, A., Campos, H.C.N.S., Ciacheti, H.L., Santos Jr, O.F., Macedo, E.S. and Cerri, L.E.S.,1992. Mechanism of natural slope instability in Guaratinguetá city, Brazil. In: D.H. Bell, *Landslides: Proceedings of the Sixth International Symposium on Landslides, 10-14 February 1992, Christchurch.* Rotterdam : A. A. Balkema, pp. 1429-1433.

Van Asch, T.W., 1984. Creep processes in landslides. *Earth Surface Processes and Landforms*, 9: 573-583.

Varnes, D., 1978. Slope movement types and processes. In: R. Schuster and R. Krizek (Editors), *Landslides, Analysis and Control.* Special Report 176. National Research Council (U.S.). Transportation Research Board., National Academy of Sciences, Washington, D.C., pp. 11-33.

Varnes, D.J., 1983. Time-deformation relations in creep to failure of earth materials. *Proceedings of the 7th Southeast Asian Geotechnical Conference, 22-26 November 1982, Hong Kong*, pp. 107-1302.

Vaughan, P.R.,1988. Keynote paper: characterising the mechanical properties of in-situ residual soil. *International Conference on Geomechanics in Tropical Soils. Singapore*. Rotterdam: Balkema, pp. 469-487.

Vieira, B.C. and Fernandes, N.F., 2004. Landslides in Rio de Janeiro: The role played by variations in soil hydraulic conductivity. *Hydrological Processes*, 18(4): 791-805.

Voight, B., 1988a. A method for prediction of volcanic eruptions. *Nature*, 332: 125-130.

Voight, B., 1988b. Material science law applies to time forecasts of slope failure. *Proceedings of the 5th International Symposium of Landslides. Balkema, Lausanne*, pp. 1471-1472.

Voight, B., 1989a. Materials science law applies to time forecasts of slope failure. *Landslide News*, 3: 8-11.

Voight, B., 1989b. A relation to describe rate-dependent material failure. *Science*, 243: 200-203.

Wang, F., Okuno, T. and Matsumoto, T., 2007. Deformation characteristics and influential factors for the giant Jinnosuke-dani landslide in the Haku-san Mountain area, Japan. *Landslides*, 4(1): 19-31.

Wen, B.P. and Aydin, A., 2003. Microstructural study of a natural slip zone: quantification and deformation history. *Engineering Geology*, 68(3-4): 289-317.

Wen, B.P. and Aydin, A., 2004. Deformation history of a landslide slip zone in light of soil microstructure. *Environmental & Engineering Geoscience*, 10(2): 123-149.

Wen, B.P. and Aydin, A., 2005. Mechanism of a rainfall-induced slide-debris flow: constraints from microstructure of its slip zone. *Engineering Geology*, 78(1-2): 69-88.

Wong, H., Chen, Y. and Lam, K., 1997. *Factual Report on the November 1993 Natural Terrain Landslides in Three Study Areas on Lantau Island*. GEO Report ; no. 61. Geotechnical Engineering Office, Civil Engineering Dept., Hong Kong, 42 pp.

Wong, H. and Ho, K., 1995. *General Report on Landslips on 5 November 1993 at Man-made Features in Lantau.* GEO report ; no. 44. Geotechnical Engineering Office, Civil Engineering Department, Hong Kong, 78 pp.

Wong, H.N. and Ho, K.K.S., 2002. Observations from studies of natural hillside failures in Hong Kong, *Symposium on Slope Hazards and Their prevention : 8-10 May, 2000, Hong Kong, PRC.* Jockey Club Research & Information Centre for Landslip Prevention and Land Development, The University of Hong Kong; CAS-HKU Centre for Slope Engineering Research, Comprehensive Institute of Geotechnical Investigation and Surveying, Ministry of Construction, Hong Kong, pp. 207-212.

Wong, H.N., Lam, K.C. and Ho, K.K.S., 1998. *Diagnostic Report on the November 1993 Natural Terrain Landslides on Lantau Island.* GEO Report ; no. 69. Geotechnical Engineering Office, Civil Engineering Dept., Hong Kong, 98 pp.

Wood, D.M., 1990. *Soil Behaviour and Critical State Soil Mechanics.* Cambridge University Press, Cambridge, 462 pp.

Yau, H.Y., 2001. *Natural Terrain Landslides and Drainage Network Development in Hong Kong: A Geomorphological Perspective.* MPhil Thesis, The University of Hong Kong, Hong Kong, 157 pp.

Yu, F.C., Chen, T.C., Lin, M.L., Chen, C.Y. and Yu, W.H., 2006. Landslides and rainfall characteristics analysis in Taipei City during the Typhoon Nari event. *Natural Hazards*, 37(1-2): 153-167.

Yu, H.S., 2006. *Plasticity and Geotechnics.* Springer, New York, 522 pp.

Zhang, L.L., Fredlund, D.G., Zhang, L.M. and Tang, W.H., 2004. Numerical study of soil conditions under which matric suction can be maintained. *Canadian Geotechnical Journal*, 41(4): 569-582.

Zhang, W.J., Chen, Y.M. and Zhan, L.T., 2006. Loading/unloading response ratio theory applied in predicting deep-seated landslides triggering. *Engineering Geology*, 82: 234-240.

Zhou, C., Lee, C., Li, J. and Xu, Z., 2002. On the spatial relationship between landslides and causative factors on Lantau Island, Hong Kong. *Geomorphology*, 43: 197-207.

Zhu, J.-H. and Anderson, S.A., 1998. Determination of shear strength of Hawaiian residual soil subjected to rainfall-induced landslides. *Geotechnique*, 48(1): 73-82.

Appendix 1

Failure mode at different stress conditions: (a) ICU; (b) ICD and (c) PPR tests

(a) ICU tests (p'_c at 100 kPa, 200 kPa, 300 kPa; strain rate at 0.1% mm/min)

Soil \ p'_c	100 kPa	200 kPa	400 kPa
TC samples	 TC11	 TC09	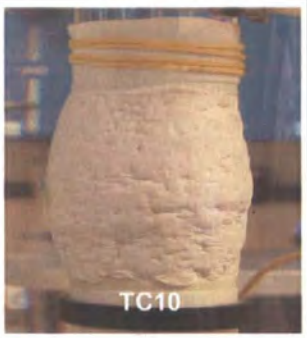 TC10
PO samples	 PO27	 PO34	 PO29

(b) ICD tests (p'_c at 50 kPa, 100 kPa, 200 kPa; strain rate at 0.01% mm/min)

Soil \ p'_c	50 kPa	100 kPa	200 kPa
TC samples	 TC39	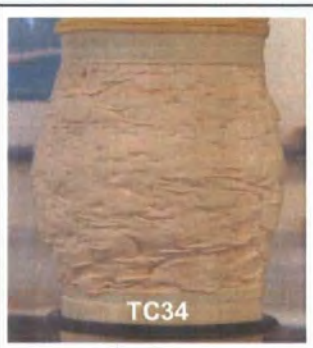 TC34	 TC33
PO samples	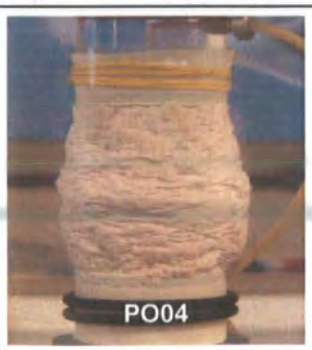 PO04	 PO06	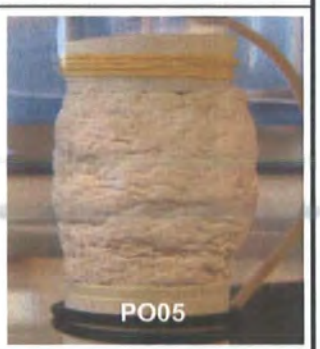 PO05

Appendix 1 (continued)

(c) PPR tests (q at 100 kPa, 200 kPa, 300 kPa; PPR rate at 10 kPa/hr)

Soil \ q	100 kPa	200 kPa	300 kPa
TC samples	 TC28	 TC24	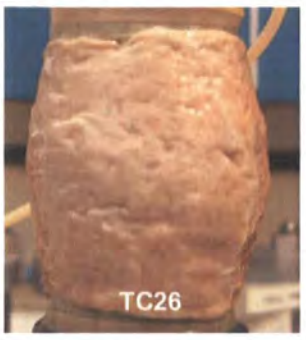 TC26
PO samples	 PO07	 PO19	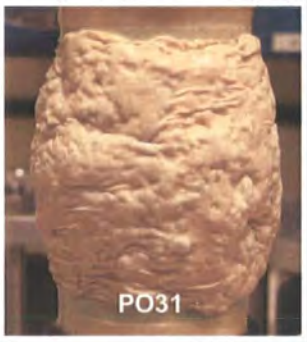 PO31

Appendix 2

Failure mode at different PPR rates: (a) linear; (b) stepped and (c) logarithmic

(a1) PPR tests at linear rates (0.5, 1, 5, 10 kPa/hr; q at 100 kPa)

Soil \ Rate	0.5 kPa/hr	1 kPa/hr	5 kPa/hr	10 kPa/hr
TC samples				
PO samples			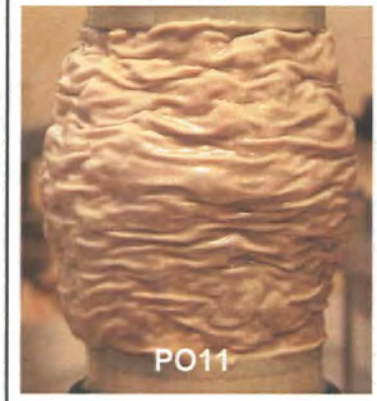	

Appendix 2 (continued)

(a2) PPR tests at linear rates (15, 50, 100 kPa/hr; q at 100 kPa)

Rate / Soil	15 kPa/hr	15 kPa/hr (2nd test)	50 kPa/hr	100 kPa/hr
TC samples				
PO samples				

Appendix 2 (continued)

(b) PPR tests at stepped rates (5, 10, 15, 50 kPa/hr; q at 100 kPa)

Rate / Soil	5 kPa step	5 kPa step	10 kPa step	15 kPa step	50 kPa step
TC samples	 TC29		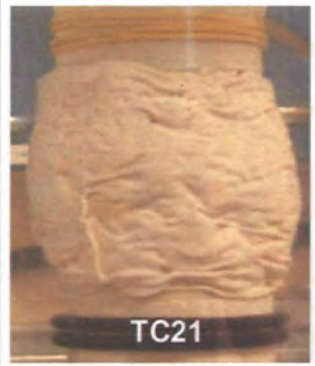 TC21	 TC31	 TC22
PO samples	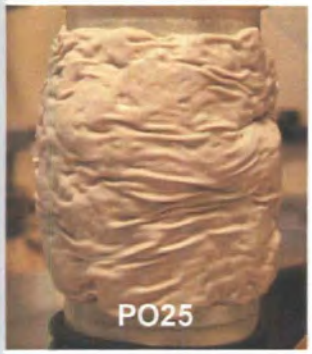 PO25	 PO38	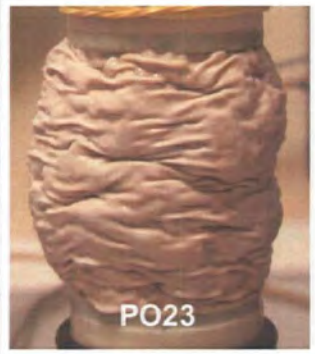 PO23	 PO30	

Appendix 2 (continued)

(c) PPR tests at logarithmic rates (54, 67, 77 kPa/hr; q at 100 kPa)

Rate / Soil	54Ln kPa/hr	67Ln kPa/hr	77Ln kPa/hr
TC samples	 TC30	 TC36	 TC37
PO samples (undisturbed)	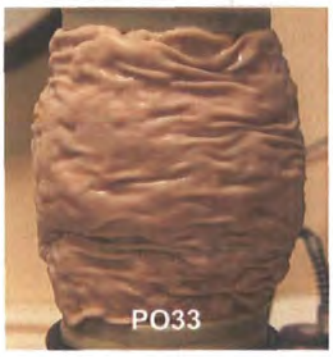 PO33	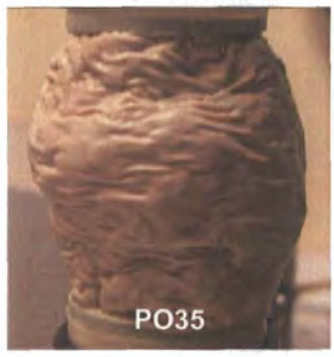 PO35	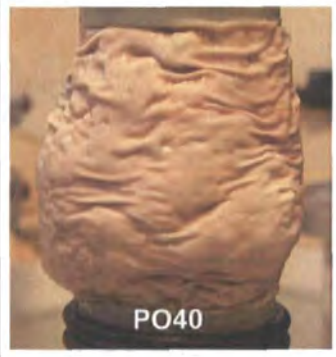 PO40
PO samples (disturbed)	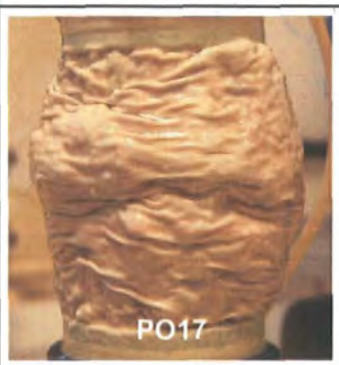 PO17	 PO14	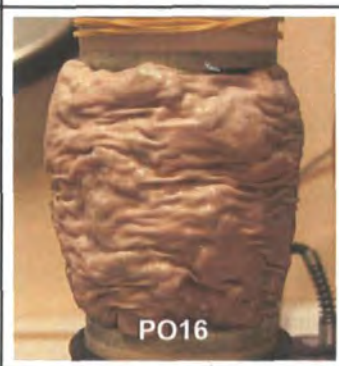 PO16